

**DISPERSIVE TIME-DOMAIN
BEAM PROPAGATION METHOD FOR
ANALYZING OPTICAL DEVICES**

BY

MOHAMMAD SHAHED AKOND

A Dissertation Presented to the
DEANSHIP OF GRADUATE STUDIES

KING FAHD UNIVERSITY OF PETROLEUM & MINERALS

DHAHRAN, SAUDI ARABIA

In Partial Fulfillment of the
Requirements for the Degree of

DOCTOR OF PHILOSOPHY

In

ELECTRICAL ENGINEERING

March 2011

KING FAHD UNIVERSITY OF PETROLEUM & MINERALS

DHAHRAN, SAUDI ARABIA

DEANSHIP OF GRADUATE STUDIES

This Dissertation, written by **MOHAMMAD SHAHED AKOND** under the direction of his dissertation advisor and approved by his dissertation committee, has been presented to and accepted by the Dean of Graduate Studies, in partial fulfillment of the requirements for the degree of **DOCTOR OF PHILOSOPHY** in **ELECTRICAL ENGINEERING**.

Thesis Committee

H. Masoudi 26/3/2011

Dr. Husain M. Masoudi (Chairman)

[Signature] 9/3/2011

Dr. Hussain A. Al-Jamid (Member)

[Signature] March 23, 2011

Dr. Mohammad A. Al-Sunaidi (Member)

[Signature]
27 MAR 2011
Dr. Samir H. Abdul Jauwad
Department Chairman

[Signature]
Dr. Salam A. Zummo
Dean of Graduate Studies



[Signature] March 23, 2011
Dr. Sheikh Sharif Iqbal (Member)

1/4/11
Date

[Signature] March 26, 2011
Dr. Khurram Karim Qureshi (Member)

ACKNOWLEDGMENT

Praise and gratitude be to ALLAH, almighty, without whose gracious help it would have been impossible to accomplish this work. Acknowledgement is due to King Fahd University of Petroleum and Minerals for extending the facilities to carry out this research.

I am extremely obliged to my advisor, Dr. Husain M. Masoudi, for guiding and supporting me throughout the thesis work. I thank him for being so patient and tolerant with me, and more importantly for being like a friend to me. I also would like to thank him for his strenuous efforts in refining this thesis work. I am thankful to my committee members Dr. Hussain A. Al-Jamid, Dr. Mohammad A. Al-Sunaidi, Dr. Sheikh S. Iqbal and Dr. Khurram K. Qureshi for their encouragement and support. Their comments and positive feedback helped me improve my thesis.

I owe my family an expression of gratitude for their patience and understanding during my study in KFUPM.

Thanks also to all my friends and colleagues for their support.

List of Symbols

B	Vector magnetic flux density	-	T
c_0	Light speed in free space	2.9979×10^8	m/s
*	Complex Conjugate	-	-
D	Vector electric flux density	-	C/m ²
δ	Damping coefficient	-	s ⁻¹
Δz	The mesh spacing in the z-direction	-	m
Δx	The mesh spacing in the x-direction	-	m
E	Vector electric field	-	V/m
e	Electron charge	$1.6021765 \times 10^{-19}$	C
ϵ	Permittivity	-	F/m
ϵ_0	Free space permittivity	8.85412×10^{-12}	F/m
ϵ_r	Relative permittivity, Dielectric Constant	-	-
ϵ_∞	Relative permittivity at infinite frequency	-	-
ϵ_s	Static relative permittivity	-	-
f	Femto	10^{-15}	prefix
H	Vector magnetic field	-	A/m
J	Current Density	-	A/m ²
j	Complex number	$\sqrt{-1}$	-
χ	Linear susceptibility	-	-
$\chi^{(2)}$	Second order nonlinear Susceptibility	-	m/V
$\chi^{(3)}$	Third order nonlinear Susceptibility	-	m ² /V ²
L_c	Coupling length	-	m
λ	Wavelength	-	M
∇^2	Laplacian Operator	-	-
M_x	Number of spatial discrete point along x-direction	-	-
M_t	Number of temporal discretization point	-	-
n	Refractive index	-	-
n_0	Reference refractive index	-	-
μ_0	Free space permeability	$4\pi \times 10^{-7}$	H/m
μ	Permeability	-	H/m
μ	Micro	10^{-6}	prefix
φ	Scalar flux density	-	-
ψ	Scalar electric field	-	-
σ_{t0}	Initial temporal Gaussian pulse width	-	s
σ_{x0}	Initial spatial Gaussian pulse width	-	m
t	time	-	s
τ	Characteristic relaxation time	-	s
ω	Angular frequency	-	rads ⁻¹
ω_0	Resonant angular frequency	-	rad/s

List of Abbreviations

1-D	One Dimensions
2-D	Two Dimensions
ABC	Absorbing Boundary Condition
ADE	Auxiliary Differential Equation
ADI	Alternating Direction Implicit
BCG	Bi-Conjugate Gradient
Bi-CGSTAB	Bi-conjugate Gradient Stabilized
BPM	Beam Propagation Method
CE	Complex Envelope
CFL	Courant-Friedrich-Levy
CGS	Conjugate Gradient Squared
CN	Crank-Nicholson
CW	Continuous Wave
DC	Directional Coupler
EFD	Explicit Finite Difference
FD	Finite Difference
FE	Finite Element
FFT	Fast Fourier Transform
GaAs	Gallium Arsenide
GHz	Giga Hertz
GS	Gauss Siedel
IC	Integrated Circuit
InP	Indium Phosphate
LED	Light Emitting Diode
LOD	Locally One Dimensional
LSI	Large Scale Integration
LSQR	Least Square
MoL	Method of Lines
PML	Perfectly Matched Layer
PSTD	Pseudo Spectral Time Domain
QMR	Quasi Minimal Residual
RS	Real Space
SOR	Successive Over Relaxation
SSI	Small Scale Integration
TBC	Transparent Boundary Condition
TD	Time Domain
TE	Transverse Electric
TM	Transverse Magnetic
VLSI	Very Large Scale Integration
WG	Wave Guide
WSI	Wafer Scale Integration

Table of Contents

Acknowledgement	iii
List of Symbols	iv
List of Abbreviations	v
List of Tables	xi
List of Figures	xii
Dissertation Abstract.....	xviii
CHAPTER 1	
INTRODUCTION	
1.1 General.....	- 1 -
1.2 Time-Domain Methods.....	- 4 -
1.3 The Objective of the Thesis	- 8 -
1.4 Thesis Organization	- 9 -
References.....	- 11 -
CHAPTER 2	
MODELING OPTICAL DEVICES	
2.1 Introduction.....	- 17 -
2.2 The Wave Equation.....	- 17 -
2.3 The Slab Waveguide.....	- 20 -
2.3.1 Transverse Electric (TE) Guided Modes	- 21 -
2.3.2 Transverse Magnetic (TM) Guided Modes.....	- 22 -
2.4 The Method of Lines (MoL).....	- 23 -
2.4.1 MoL Formulation.....	- 24 -
2.5 The Beam Propagation Method	- 27 -
2.5.1 The BPM Formulation	- 28 -
2.6 Perfectly Matched Layer.....	- 32 -

2.7 Implementations.....	- 34 -
2.7.1 Homogeneous Media	- 34 -
2.7.2 Slab Waveguide	- 35 -
2.7.3 Directional Coupler.....	- 37 -
2.8 Summary.....	- 39 -
References.....	- 40 -

CHAPTER 3
THE FINITE DIFFERENCE TIME DOMAIN METHOD

3.1 Introduction.....	- 44 -
3.2 Maxwell's Equations	- 45 -
3.2.1 TE Polarized Fields.....	- 46 -
3.2.2 TM Polarized Fields.....	- 47 -
3.3 The Implicit FDTD	- 48 -
3.4 The Explicit FDTD	- 50 -
3.5 The Scalar FDTD	- 53 -
3.6 Numerical Implementation	- 54 -
3.7 Perfectly Matched Layer (PML).....	- 55 -
3.8 Implementation of Bérenger's PML.....	- 59 -
3.9 Summary.....	- 62 -
References.....	- 62 -

CHAPTER 4
THE TIME DOMAIN BEAM PROPAGATION METHOD

4.1 Introduction.....	- 66 -
4.2 The TD-BPM Formulation	- 68 -
4.2.1 Padé Approximant	- 71 -
4.2.2 The TD-BPM Operator	- 74 -

4.2.3 Iterative Methods for Sparse Systems.....	- 74 -
4.3 TD-BPM Implementation	- 75 -
4.3.1 Implementation: 1-D	- 76 -
4.3.2 Implementation: 2-D- Free Space	- 80 -
4.3.3 Implementation: 2-D- Waveguide	- 82 -
4.3.4 Performance Tests.....	- 84 -
4.3.4.1 Time Step (Δt)	- 85 -
4.3.4.2 Propagation Step (Δz)	- 88 -
4.3.4.3 Padé Order	- 89 -
4.3.4.4 Computational Requirements.....	- 90 -
4.4 Conclusion	- 95 -
References.....	- 95 -
CHAPTER 5	
MATERIAL DISPERSION MODELS	
5.1 Introduction.....	- 98 -
5.2 Material Dispersion.....	- 98 -
5.2.1 Debye Model.....	- 100 -
5.2.2 Lorentz Model.....	- 103 -
5.2.2.1 Lorentz Model of GaAs	- 106 -
5.2.2.2 Ultra Short Pulses in GaAs	- 109 -
5.2.3 Drude Model	- 112 -
5.3 Summary	- 112 -
References.....	- 112 -
CHAPTER 6	
DISPERSIVE TIME-DOMAIN NUMERICAL TECHNIQUES	
6.1 Introduction.....	- 115 -
6.2 The Dispersive FDTD.....	- 116 -
6.3 The Dispersive TD-BPM	- 120 -

6.4 Implementations.....	- 125 -
6.4.1 One Dimensional Implementation	- 125 -
6.4.2 Two Dimensional Implementation	- 127 -
6.4.2.1 Homogeneous Medium	- 127 -
6.4.2.2 Slab Waveguide.....	- 129 -
6.5 Performance of the TD-BPM.....	- 131 -
6.5.1 Time step (Δt)	- 133 -
6.5.2 Propagation step (Δz).....	- 135 -
6.5.3 Padé Order	- 136 -
6.6 The Performance of the FDTD	- 138 -
6.7 Computational Resource Requirement	- 140 -
6.8 Conclusion	- 146 -
References.....	- 147 -
 CHAPTER 7	
DISPERSIVE DIRECTIONAL COUPLER ANALYSIS	
7.1 Introduction.....	- 150 -
7.2 Background.....	- 152 -
7.3 Numerical Implementations.....	- 154 -
7.4 Material and Intermodal Dispersions Analysis.....	- 159 -
7.5 Pulse Spread Due to Material and Intermodal Dispersions	- 164 -
7.6 Conclusion	- 168 -
References.....	- 169 -
 CONCLUSION AND FUTURE WORK PLAN	
8.1 Conclusion	- 171 -
8.2 Future Work Plan.....	- 173 -
References.....	- 174 -

APPENDIX

A.1 Conjugate Gradient Squared (CGS) - 176 -
A.2 Least Square (lsqr) - 177 -
A.3 Quasi-Minimal Residual (QMR) - 178 -
References - 179 -
VITA.....- 180 -

List of Tables

Table 4.1 Convergence of the Iterative Solvers of the TD-BPM operator for optical slab waveguide at minimum residual of 10^{-6}	- 92 -
Table 5.1 Debye parameters of several dispersive materials.....	- 101 -
Table 6.1 Coefficients of Debye, Lorentz and Drude model used for $E_y \Big _{i,k}^{n+1/2}$ calculation in FDTD of Eq. 6.4.....	- 119 -
Table 6.2: The coefficients of Q and R matrices for the Debye model.	- 122 -
Table 6.3: The coefficients of Q and R matrices for the Lorentz model	- 122 -
Table 6.4: The Coefficients of Q and R matrices for the Drude model	- 123 -

List of Figures

Figure 2.1 The dielectric slab waveguide	20 -
Figure 2.2 Discretization of a waveguide with PML.....	33 -
Figure 2.3 The evolution of a Gaussian field in air using (a) the MoL, the EFD-BPM, and the CN-BPM, (b) Effect of implementing the PML in MoL.....	35 -
Figure 2.4 Propagated fields at $z = 40 \mu\text{m}$ inside a slab waveguide (a) the TE_0 mode (b) the TE_1 mode using the three techniques: the MoL, the EFD-BPM and the CN-BPM.	36 -
Figure 2.5 The directional coupler geometry.....	37 -
Figure 2.6 The propagation of the TE_0 guided mode of the isolated slab waveguide inside a directional coupler with a separation distance $s = 1\mu\text{m}$. The total propagation distance used is equal to one coupling length, $L_c = 358.8 \mu\text{m}$	38 -
Figure 2.7 Normalized power versus distance along the directional coupler.	39 -
Figure 3.1 The flow diagram of the FDTD leap-frog integrator. Multiplicative constants have been omitted. (b) Position of the electric field vector components useful for calculating magnetic field vector components (c) Position of the magnetic field vector components useful for calculating electric field vector components.....	52 -
Figure 3.2 The temporal pulse of a propagated Gaussian optical pulsed beam in a slab waveguide at (a) $z = 25 \mu\text{m}$ and (b) $z = 50 \mu\text{m}$ using the scalar FDTD and the vector FDTD (c) and (d) are absolute differences between the scalar and vector fields.	55 -
Figure 3.3 Computational main grid and the conductivities in PML region of the FDTD problem space.....	58 -
Figure 3.4 The spatial pulse profile at a) $z = 4 \mu\text{m}$ b) $z = 8 \mu\text{m}$ c) $z = 12 \mu\text{m}$ and d) $z = 16$ μm in air obtained by the FDTD for using PML and for not using PML compared with the actual field.....	60 -

Figure 3.5 The temporal pulse profile at a) $z = 4 \mu\text{m}$ b) $z = 8 \mu\text{m}$ c) $z = 12 \mu\text{m}$ and d) $z = 16 \mu\text{m}$ in air obtained by the FDTD for using PML and for not using PML compared with the actual field.	- 61 -
Figure 4.1 The propagation of a 50 fs Gaussian pulse in a homogenous medium using the TD-BPM over a distance of $z = 100 \mu\text{m}$ using (a) no moving time window (b) a moving time window.....	- 80 -
Figure 4.2 Comparison between the TD-BPM and the FDTD for the propagation of a 50 fs pulse.	- 80 -
Figure 4.3 The propagation of a pulsed Gaussian beam of $\sigma_{t0} = 50 \text{ fs}$ in free space using the non-paraxial TD-BPM at several distances.	- 81 -
Figure 4.4 A comparison between the TD-BPM and the FDTD results for 2-D free space implementation. The figure shows the temporal profile at (a) $z = 12.5 \mu\text{m}$ and (b) $z = 25 \mu\text{m}$ and the spatial profile (c &d) of the pulse at the same distances.....	- 82 -
Figure 4.5 The propagation of the fundamental guided mode pulsed optical beam of $\sigma_{t0} = 50 \text{ fs}$ in the slab waveguide using the TD-BPM at several distances along the propagation direction.	- 83 -
Figure 4.6 Comparison between the TD-BPM and the FDTD for the propagation of the fundamental guided mode pulsed optical beam in the slab waveguide at several distances along the propagation.	- 84 -
Figure 4.7 The effect of changing the time step size (Δt) on the convergence of the TD-BPM technique in comparison with the FDTD for a time pulse width of 25 fs (a) The percentage maximum difference (b) The percentage of root mean square of the difference (c) The percentage difference at peak, (d) the Group Velocity Ratio.	- 87 -
Figure 4.8 The same as of Figure 4.7 but with initial pulse width of $\sigma_{t0} = 100 \text{ fs}$	- 87 -
Figure 4.9 The effect of changing the propagation steps size (Δz) on the percentage root mean square difference of the technique in comparison with the FDTD for the propagation of a pulsed beam of 25 fs, 50 fs and 100 fs initial temporal waist inside a non-dispersive slab waveguide.	- 88 -
Figure 4.10 The same as of Figure 4.9 with the variation of the Padé order.....	- 89 -

Figure 4.11 The total computational time of the FDTD and the TD-BPM using direct and iterative solvers for (a) 25 fs and (b) 100 fs pulsed beams as a function of propagation distance z	91 -
Figure 4.12 Computer memory requirement of the FDTD and the TD-BPM using direct and iterative solvers with (a) 25 fs and (b) 100fs initial pulsed beam widths. -	94 -
Figure 5.1 Frequency dependence of the real and imaginary part of the dielectric constant (a and b) and the same for refractive index (c and d) of human muscle tissue approximated by Debye model.	102 -
Figure 5.2 Forces affecting a free electron in Lorentz model.....	103 -
Figure 5.3 Wavelength λ dependence (a and b) and its corresponding frequency dependence (c and d) of the real and imaginary part of the relative permittivity of <i>GaAs</i> using Lorentz Model.	108 -
Figure 5.4 Operating refractive index of <i>GaAs</i> for Gaussian pulse with spread of (a) 120 fs, (b) 50 fs, (c) 25 fs, (d) 10 fs and their frequency spectrum (inset figures).	111 -
Figure 6.1 The flow chart of the dispersive FDTD algorithm.	120 -
Figure 6.2 The propagation of the Gaussian pulse at (a) $z = 55 \mu\text{m}$ and (b) $z = 126 \mu\text{m}$ in a 1-D dispersive medium represented by Lorentz model using the MoL, the TD-BPM and the FDTD.....	126 -
Figure 6.3 The evolution of the pulsed Gaussian optical beam in a homogeneous 2D dispersive medium using the non-paraxial TD-BPM for an initial pulse width of $\sigma_{t0} = 20$ fs.....	128 -
Figure 6.4 The temporal profile of the propagated pulsed beam in a homogeneous 2D dispersive medium at $z = 25.0 \mu\text{m}$ and $z = 50.0 \mu\text{m}$ using the non-paraxial TD-BPM and the FDTD.	128 -
Figure 6.5 Propagation of the TE_0 pulsed optical beam in the dispersive slab waveguide using the TD-BPM at several propagation distances. The two horizontal lines show the positions of the core layer of the slab.	130 -
Figure 6.6 Comparison between the TD-BPM and the FDTD results of the temporal profile of the propagated pulse with $\sigma_{t0} = 50$ fs at several distances along the direction of z inside the dispersive slab waveguide.....	131 -

Figure 6.7 The effect of changing the time step size (Δt) on the accuracy of the technique in comparison with the FDTD (a) The percentage maximum difference (b) The percentage of root mean square of the difference (c) The percentage difference at peak, (d) Group Velocity Ratio for the propagation of a pulsed beam of 25 fs temporal waist inside a *GaAs* dispersive slab waveguide.- 134 -

Figure 6.8 The same as in Figure 6.7 but with an initial temporal pulse waist of $\sigma_{t0} = 100$ fs.- 134 -

Figure 6.9 The same as in Figure 6.7 but with *AlGaAs* dispersive core waveguide whose Lorentz model parameters were given in the text.- 135 -

Figure 6.10 The effect of changing the propagation step size (Δz) on the percentage root mean square difference of the technique in comparison with the FDTD for the propagation of a pulsed beam of 25 fs and 100 fs temporal waist inside a strongly dispersive *GaAs* and a weakly dispersive *AlGaAs* dispersive slab waveguide.- 136 -

Figure 6.11 The effect of changing Padé order on the accuracy of the TD-BPM in comparison with the FDTD for the propagation of a pulsed beam of 25 fs and 100 fs temporal waist inside a strongly dispersive *GaAs* and a weakly dispersive *AlGaAs* dispersive slab waveguide.- 137 -

Figure 6.12 The effect of changing the time step size Δt on the accuracy of the FDTD in comparison with the TD-BPM (a) The percentage maximum difference (b) The percentage of root mean square of the difference (c) The percentage difference at peak, (d) Group Velocity Ratio for the propagation of a pulsed beam of 25 fs temporal waist inside a *GaAs* dispersive slab waveguide.- 139 -

Figure 6.13 The same as of Figure 6.12 with the variation of the FDTD mesh size Δz- 140 -

Figure 6.14 Computational time of the dispersive FDTD and the dispersive TD-BPM using the direct and the iterative solvers for the propagation of 100 fs pulsed beam in *GaAs* dispersive slab waveguide.- 141 -

Figure 6.15 Computational time of the dispersive FDTD and the dispersive TD-BPM using the direct and the iterative solvers for the propagation of 25 fs pulsed beam in dispersive <i>AlGaAs</i> slab waveguide.	142 -
Figure 6.16 Memory usage by the dispersive FDTD and the dispersive TD-BPM using direct and iterative solvers with (a) 25 fs and (b) 100 fs pulsed beam.	143 -
Figure 6.17 The effect on the percentage difference between the FDTD and the TD-BPM using the exact operator (a and c) and an approximated operator (b and d) at $z = 50 \mu\text{m}$ (a and b) and at $z = 100 \mu\text{m}$ (c and d) for the propagation of a pulsed beam of 100 fs temporal waist inside a <i>GaAs</i> dispersive slab waveguide.	145 -
Figure 7.1 The Dispersive Directional Coupler Geometry	155 -
Figure 7.2 Evolution of the pulsed optical beam with an initial pulse width of 50 fs inside the dispersive directional-coupler structure of Figure 7.1 at several distances along the longitudinal direction. The horizontal lines show the position of the two waveguide boundaries.	156 -
Figure 7.3 Temporal profiles at two distances along the z direction in the two waveguides of a directional coupler for an initial pulse-width of 25 fs using the TD-BPM and the FDTD. WG_1 is the waveguide where the input has been launched.....	157 -
Figure 7.4 The same as of Figure 7.3 but for an input beam of 120 fs temporal pulse-width.	158 -
Figure 7.5 Normalized power inside the upper and lower waveguides of the directional coupler along the direction of propagation for CW and 120 fs initial pulse-width. Solid lines belong to the upper waveguide (WG_1) where the input was launched and dashed lines belong to the lower waveguide (WG_2). D means dispersive and ND means non-dispersive.....	160 -
Figure 7.6 The same as in Figure 7.5 but for an initial pulse width of 50 fs.	161 -
Figure 7.7 The same as in Figure 7.6 but for an initial pulse width of 25 fs.	162 -
Figure 7.8 The same as in Figure 7.6, but for $\delta = 0$	163 -
Figure 7.9 The same as in Figure 7.7, but for $\delta = 0$	164 -

Figure 7.10 Relative pulse width increase in percent for the propagation of 50 fs and 25 fs pulses in dispersive and non-dispersive directional couplers. - 165 -

Figure 7.11 Frequency Spectrum of the input of 25 fs temporal pulse and the pulsed beams of a *GaAs* directional coupler having non-dispersive medium (ND) and Lorentz dispersive medium at $z = 5L_c = 285.5 \mu\text{m}$ - 167 -

Figure 7.12 The same as in Figure 7.11 with temporal pulse of 50 fs. - 168 -

Dissertation Abstract

Name: MOHAMMAD SHAHED AKOND
Title: DISPERSIVE TIME DOMAIN BEAM PROPAGATION METHOD FOR ANALYZING OPTICAL DEVICES
Degree: DOCTOR OF PHILOSOPHY
Major Field: ELECTRICAL ENGINEERING
Date of Degree: MARCH 2011

The work in this thesis aims at developing an efficient unidirectional Time-Domain technique for modeling the propagation of short and ultra short pulsed optical beams in devices containing dispersive material. The non-paraxial Time-Domain Beam Propagation Method (TD-BPM) has been developed and used for this purpose. The method relies on the classical BPM style of expanding the wave equation as a one-way longitudinal operator while retaining the time variation as another variable along with the other transverse spatial variables. This arrangement allows the numerical time window to follow the propagation of the pulse and hence minimizes computer resource requirements. To account for the fast variation of short and ultra short pulses, the method uses higher order rational Padé approximants to overcome the paraxial limitation. The use of several iterative numerical techniques, to solve the complex sparse matrix operator of the TD-BPM, showed a remarkable speed up factors compared to the direct matrix solver in both implementations of non-dispersive and dispersive applications. In order to verify and assess the results of the TD-BPM, the explicit FDTD has been formulated and implemented. In this thesis, Lorentz dispersive model of *GaAs* and *AlGaAs* has been used in all implementations. Being an implicit method, the TD-BPM converges using large time and longitudinal step sizes

compared to the explicit FDTD step sizes. The assessment of the TD-BPM includes application to 1-D and 2-D of dispersive material and structures. Full numerical analysis of important numerical parameters and dispersive coefficients has been carried out to assess the relationship between these variables. It has been noticed that the developed TD-BPM is very stable, accurate and efficient in modeling short and ultra short pulse propagation in structures containing dispersive materials. The aim of second part of this thesis is to study the propagation of short and ultra short optical pulses in directional coupler structures containing dispersive materials. Pulse spread due to material dispersion and intermodal dispersion of directional couplers has been modeled accurately. As the initial pulse duration decreases the pulse spread increases during power exchange mechanism between the two waveguides along the longitudinal direction. Eventually the pulse breaks up which gives rise to distortion. It was found that the existence of material dispersion speeds up the pulse break-up phenomena in a shorter distance. Thus, the efficient TD-BPM was implemented and compared with the existing FDTD technique for the observation of the complex optical behavior inside various photonic device structures containing dispersive and non-dispersive material.

ملخص بحث درجة الدكتوراه في الفلسفة

الاسم : محمد شاهد اكوند

العنوان : طريقة إتباع الومضات الضوئية في المواد ذات التبعثر الضوئي TD-BPM

الدرجة العلمية : دكتوراه في الفلسفة

مجال التخصص : الهندسة الكهربائية

تاريخ الدرجة العلمية : 2011 مارس.

الرسالة تهدف لتطوير طريقة جديدة لدراسة الومضات الضوئية المتناهية الصغر في المواد ذات التبعثر الضوئي TD-BPM. هذه الطريقة هي طريقة محدثة من الطريقة القديمة لدراسة الومضات الضوئية ذي الاتجاه الأحادي والتي أثبتت أنها ليست كافية لدراسة الومضات الضوئية المتناهية الصغر. الطريقة الجديدة تعتمد بشكل أساسي على مفكوكات بادي (Pade) للتغلب على قيود (Praxial). إن استعمال تحريك النافذة الوقتية لمتابعة الومضات أثبتت فعالية كبيرة من حيث الوقت والسعة المطلوبة من الحواسب الآلية المستعملة. أيضا تم إضافة واستعمال عدة طرق جديدة لمعالجة المصفوفة الرئيسية باستخدام تقنيات تكرارية. وقد تم استخدام الطريقة المعروفة (FDTD) لتقييم نتائج الطريقة المطروحة (TD-BPM) من حيث الدقة وكفاءة استعمال الكمبيوتر. في هذه الرسالة لقد تم استخدام نموذج اللورينتز (Lorentz) لمحاكاة المواد ذات التبعثر الضوئي. إن دراسة الطريقة الجديدة تطلب تغيير ومراقبة عدد من المتغيرات لتطبيقات المواد ذات البعد الأحادي والثنائي. أثبتت النتائج أن الطريقة الجديدة (TD-BPM) هي مستقرة وفعالة ودقيقة لدراسة الومضات المتناهية الصغر في المواد ذات التبعثر الضوئي. الجزء الثاني من الرسالة يهدف إلى استخدام الطرق (TD-BDM) و (FDTD) لدراسة إنتشار الومضات المتناهية الصغر في جهاز (Directional Coupler) الذي يحتوي على مواد ذي تبعثر ضوئي. لوحظ في هذه الدراسة أن الومضة الضوئية المتناهية الصغر تتعرض إلى انقسام في مسافات أقصر مقارنة مع عدم وجود مواد ذات تبعثر ضوئي.

CHAPTER 1

INTRODUCTION

1.1 General

The current trend of "high-technology" foresees what will take place in the near future. After the invention of the transistor in 1947 at Bell laboratories [1], the miniaturization of microelectronic devices paved the way of devices to be smaller-and-smaller which eventually brought the small scale integration (SSI), medium-scale-integration (MSI), large scale integration (LSI) and very-large-scale-integration (VLSI) of the Integrated Circuit (IC) systems. The IC industries were dreaming to produce IC's on a silicon wafer with 100% yield that will take the era to wafer scale- integration (WSI) [2]. But till now the concept could not pass the hypothesis level. Flaws on the surface of the wafers and problems during the deposition or layering process are impossible to avoid, and cause some of the individual chips to be defective. The achievable yields are typically 30%-50%. The tunneling current [3], parasitic inductance of a heterostructured transistor, reliability-related problems associated with the thermal stress and thermal management limits the miniaturization of the ICs [4 - 5]. Increase of the clock rate is also limited in the GHz range due to the transit time of the electron [4]. The characteristic transit time is determined by the structure and material

used in the transistors. Few of the reasons behind the development of the multiprocessor or parallel processor in computational systems are mentioned above.

Photonic devices, on the other hand, operate at optical frequencies, with very low transmission losses, without dissipation of heat and are immune to electromagnetic interference and cross-talk. Therefore, it is very likely that in the near future microelectronics will be largely replaced by optoelectronics and photonics. Photonic devices, such as laser sources, optical fibers, optical couplers and switches have already been incorporated in telecommunication and computer systems. The advantages of photonic devices arise from the fact that the carriers are photons, rather than electrons. Transmission of photons is at the speed of light, not limited by the transit time as happens in the case of electrons. Unfortunately, photonic devices are much larger than their microelectronic counterparts because of the diffraction limit. The transmission efficiency of multimode fiber decreases with the decreasing of the core-diameter until a cut-off is reached [6]. For single mode fiber, which has no cut-off, the guided mode field becomes less confined with the decreasing of the core-diameter [7]. This causes the evanescent fields to spread further out of the cladding into the surrounding and interfere with the other nearby devices. Therefore, to prevent cross-talk, fibers have to be coated with extra layer or be separated by a larger distance with the result of further increase of the device size in the transverse direction [7]. In the longitudinal direction, design of photonics devices should be done in such a way that excessive loss due to bends and interfaces within the devices are minimized. The reduction of the total loss requires the devices to be made adiabatic, i.e., with very slow branching angles. Typical branching angle in these devices, such as directional coupler and power splitter are within 1° [8 - 9] for better

performance. This can make the branching section of the device to be hundreds of wavelengths in length. In addition, the weakly guiding nature of the optical structures cause the waveguides to be separated sufficiently apart to be isolated from each other. These factors cause the optical length of common optical devices to be in the order of thousands of wavelengths.

Most of photonic devices rely on compound semiconductor technology that is based on the III-V semiconducting materials, such as Gallium Arsenide (*GaAs*) and Indium Phosphide (*InP*) [10]. A large family of them has a direct band gap. They are ideally suited for light generation, such as, laser diodes and light emitting diodes (LEDs) and in light detection. Doped fiber amplifier, where silica is commonly doped with Erbium, is used for laser amplification [11]. The refractive index of these materials and other optical materials used in different applications shows dispersive properties in the optical region of the spectrum. Plasmonics is a rapidly emerging photonics discipline that enables unusual dispersion engineering, and it has an important impact on the development of metamaterials and active nanophotonic devices. Dispersion control and active material integration have yielded plasmonic components, such as three-dimensional single layer plasmonic metamaterials, all-optical, electro-optic and field effect modulation of plasmon propagation, plasmon-enhanced absorption in solar cells, etc [12]. The dispersive nature of these materials is commonly expressed by well-known models, such as Debye, Lorentz, and Drude [13] models. Ultrashort or femtosecond optical pulses, which have a broad frequency spectrum, interact and are strongly affected by the dispersive nature of these materials. Therefore, modeling techniques of photonic devices should consider all the challenges mentioned above.

This is because accurate and realistic numerical simulation of photonic devices and systems is important for investigating innovative basic and engineering concepts, materials, and device configurations before they are fabricated. These provide a framework in which one can interpret complex experimental results and suggest further diagnostics or alternate protocols. On the other hand, modeling techniques have to be very accurate, efficient and must run easily on ordinary computer resources; otherwise, they are less useful if they require a special computer, such as a supercomputer to which very few people have access.

Time Domain (TD) analysis of ultrashort pulses in dispersive structures of photonic devices is much more complicated than Continuous Wave (CW) analysis due to the involvement of a large number of frequencies in the spectrum. This adds another dimension of challenge to modeling techniques. After understanding the challenges of simulating optical devices, extensive knowledge of existing numerical methods have to be explored and implemented to show their effectiveness in overcoming these challenges. The following paragraph gives an overview and literature survey of these challenges and the available techniques to handle them effectively.

1.2 Time-Domain Methods

The Finite Difference Time Domain (FDTD) is one of the most widely used numerical techniques for modeling photonic devices. The primitive form of the FDTD algorithm, introduced by Yee in 1966 [14], was to choose a geometric relation for the spatial sampling of the vector components of the electric and magnetic fields that robustly represents both the differential and integral forms of Maxwell's equations. The nonphysical dispersion

error arose from the numerical parameters of the FDTD is proportional to the length of the wave propagation [15 - 16]. Depending upon the required application and accuracy, the numerical dispersion of the method restricts the mesh gridding of at least 10 to 20 cells per minimum wavelength in every direction [17]. In the full vector FDTD, six unknowns have to be solved by solving six Maxwell's first order equations for 3-D problems that throws a challenge of providing enough computational resources for finely meshed grids. In the scalar FDTD [18 - 19], the amount of required memory is reduced to one third and to two thirds of the vector FDTD scheme for 3-D and 2-D problems, respectively. But this scalar version is only suitable for weakly guided waves and it is not widely used [20]. Courant–Friedrichs–Lewy (CFL) condition on the time step [21 - 22] puts a restriction on both of these methods. Thus these methods require large computational resources for pulse propagation in long optical devices. This renders a further modification of the FDTD algorithm. Various techniques have been proposed to make the FDTD method more efficient by relaxing the fineness of the mesh grid including nonuniform [23], adaptive mesh refinement [24] and pseudospectral time-domain (PSTD) techniques [25 – 26], etc. The nonuniform and adaptive mesh refinement is limited to specific geometries that conform to specialized grid [23]. For short pulses, the temporal pulse sampling density must be increased with the electrical size of the problem in PSTD, to avoid the unwanted cumulative numerical dispersion. Thus, even though PSTD provides a large reduction in computer resources relative to Yee's algorithm for electrically large problems, it is not suitable for short pulses. Therefore, recently there is tendency to modify the FDTD algorithm by overcoming the second limitation of the CFL stability criterion. This is done by converting the traditional explicit FDTD to an implicit one. To name two of these methods: the Alternating Direct Implicit (ADI) FDTD [27 - 32] and the

Locally One-Dimensional (LOD) FDTD [33 - 36]. Although both techniques, being implicit, succeeded in removing the CFL stability criterion of the explicit FDTD, however the numerical dispersion is inherent to both of these methods where it increases with the increase of the time step size. Moreover, the methods exhibit a splitting error proportional to the square of the time step size [37], which limits the accuracy of the methods. An effort to reduce the splitting error makes the method lose unconditional stability [38]. So the time step size is limited for a desired accuracy and excitation spectrum [39 - 41]. Some envelope implicit FDTD have been developed which have better numerical dispersion than the conventional implicit FDTD, such as the Complex Envelop (CE) ADI-FDTD [42] and the envelope LOD-FDTD [43]. The normalized phase velocities of both envelope versions remain close to unity at the center wavelength, even for a large time step. This means that these methods have better performance over the conventional ADI/LOD-FDTD. Moreover, some artifacts for the CE-ADI-FDTD have been found of having the time-harmonic spurious charges that produces secondary radiation and anomalous mode propagation [44]. The memory requirements for the implicit and the envelope implicit FDTDs, which do not depend on the choice of the time step size, are increased compared to the explicit FDTD due to the solution of the tridiagonal matrix in addition to the solution of several explicit numerical equations. Even though many implicit and envelope FDTDs have been proposed which provides comparable results to those of the explicit FDTD, their advantages are not clear [43]. However, as the FDTD can model photonic device problems with dispersive media, even though with high computational cost for long devices, it can be used as a reference tool for a comparison of other newly developed numerical tools. The frequency domain constitutive relations in dispersive media can be converted to the time domain either

using the recursive convolution integral [45 - 46] or by a direct integration approach [47 – 48]. As discrete time series representation has a natural representation in terms of z-transform, use of z-transform approach is also possible to perform this conversion [49 – 50].

Another attractive method to analyze a number of structures of integrated optics is the Beam Propagation Method (BPM). This one-way propagation technique is well-suited for long device interaction [51 – 52]. The main advantage of the BPM over the coupled mode analysis, for example, is that it accounts both for guided and radiation modes in the same formalism and its propagational ability makes it a good tool in the analysis of longitudinally varying devices. The original BPM was based on the Fast Fourier Transform (FFT). To improve the accuracy and efficiency, the Finite Difference (FD) approximation was later used successfully in the formulation of the BPM, resulting in the so called FD-BPM. The FD-BPM can be classified either as implicit or explicit. The Crank-Nicholson (CN) implicit FD proved to be a very stable and accurate method. On the other hand, explicit methods, such as the Real Space (RS) or the explicit FD showed improved convergence and efficiency in comparison with their implicit counterpart. The explicit RS method depends on splitting the finite-difference matrix operator into two matrix operators where each matrix contains small sub-matrices that are solved analytically. Explicit FD-BPM is another simple and attractive method to implement. Both of these approaches were also used efficiently in modeling long CW and nonlinear wave interaction [53 – 54]. However, most BPMs were developed for CW operations. Recent developments on Time Domain (TD) BPM techniques to model pulsed optical beam propagation in waveguide structures proved to be very efficient in modeling long device interaction [55 - 56]. The advent of this method occurred with

paraxial approximation in narrowband applications and solved explicitly under a conditionally stability limit. Then this method was improved to make it unconditionally stable [56] for certain class of problems. Limited wideband application of similar method was shown in [57] based on the finite element method and the application of CN scheme in [58] made the technique implicit. Recently the application of Padé approximants made the TD-BPM method applicable to model ultra short pulse interaction in non-dispersive devices [59 - 60]. A comparative study between this technique and the existing FDTD counterparts remains unchecked. In addition, the applicability and the efficiency of this method is yet to be examined for material dispersion and nonlinear parametric optical interactions of $\chi^{(2)}$ and $\chi^{(3)}$ [60].

1.3 The Objective of the Thesis

The main objective of this work is to study the implementation of the Time Domain numerical techniques for modeling the propagation of short and ultra short optical pulse propagation in dispersive materials. The TD-BPM and the FDTD techniques will be implemented and tested to model two dimensional devices containing dispersive material. Lorentz model will be used as a dispersive model for the representation of dispersion of the material. The outcome of this work will be used to model ultra short pulse propagation in a directional coupler made of dispersive material. To accomplish these objectives, several numerical issues have to be resolved. Therefore, the work of this thesis is divided mainly into three phases. In the first phase, the two techniques will be initially implemented, tested and compared for non-dispersive devices. Several tests will be performed to show the applicability of these methods to model ultra short pulse propagation in 2-D structures.

Comparison of convergence, accuracy, stability and efficiency of the techniques will be performed rigorously. In this phase, important numerical parameters of the TD-BPM, such as the time step size, the Padé order and the longitudinal step size will be tested. Similar tests for the FDTD numerical parameters will be performed. Part of the objective of this phase is to explore the possibility of speeding up gains by using different iterative numerical solvers for the TD-BPM operator. The second phase involves the application of these two methods to model short and ultra short optical pulse propagation in dispersive 2-D material. In addition to the tuning of numerical parameters for the two techniques, the study in this phase involves the effect of material dispersion on the convergence and the accuracy of the two techniques. The third phase involves the study of the propagation of short and ultra short pulse in directional couplers made of dispersive material.

1.4 Thesis Organization

The starts with basics of electromagnetic and progressively develops to an advanced stage of ultra short pulse propagation in dispersive optical devices. This is done to facilitate understanding of the thesis work. This chapter (Chapter one) gives a general overview of the literature survey of important issues in photonics technology and the numerical techniques used to model short pulse propagation in dispersive material. It is to be mentioned that the following chapters also give supplementary literature survey and detailed information for the techniques used. The chapter also gives the motivation of this work in detail. Chapter two starts with Maxwell's equations, and then shows the derivation of Helmholtz equation and its numerical solution with different propagation methods. It was mentioned in the introduction that most propagation methods were devised for continuous wave (CW) application. For this

reason some applications with the existing methods on different optical devices have been demonstrated. The chapter shows the main differences between CW and TD implementations. Chapter three shows the formulation and the implementation of the FDTD technique. The chapter also gives a literature survey of common implicit FDTD techniques that have been developed over the last few years. In addition, this chapter shows the application of Bérenger PML as an absorbing boundary condition for the FDTD. Chapter four contains the derivation and the implementation of the TD-BPM for non-dispersive materials. It gives detailed numerical convergence and accuracy results when applied to different geometries. Iterative numerical techniques are also introduced in this chapter to enhance the efficiency of the TD-BPM. Chapter five gives an overview of material dispersion and the commonly used model that represents practical dispersive materials. The chapter also discusses the difficulty of incorporating these models in numerical techniques and the impact of the propagation of short pulse in such materials. Chapter six basically contains extension of the two main techniques presented in chapters three and four to dispersive material. This chapter shows the numerical implementation of short and ultra short pulse propagation in dispersive material using the FDTD and the TD-BPM. Comparative study of these two methods has been done for one and two dimensions. In two dimensions, the implementations in homogeneous dispersive medium as well as a slab waveguide are considered. The accuracy, stability and performance of the dispersive TD-BPM have also been studied and the results were compared with those of the FDTD results. Chapter seven shows the analysis in modeling short and ultra short pulse propagation in dispersive directional coupler structures. The effect of the initial pulse width on the mechanism of

power switching between the two coupled waveguides is analyzed in detail. The thesis ends with a concluding chapter for the whole work as well as future work.

References

- [1] Arns, R.G. "The other transistor: early history of the metal–oxide–semiconductor field-effect transistor", *Engineering Science and Education Journal*, vol. 7, Iss. 5, pp. 233 – 240, Oct 1998.
- [2] Ephraim Suhir, "Microelectronics and Photonics-the Future "Proc. 22nd International Conference on Microelectronics (MIEL 2000), vol. 1, NIS, Serbia, May, 2000.
- [3] W. R. Fahrner, "Nanotechnology and Nanoelectronics", 1st edition, Springer, 2005.
- [4] Serge Luryi, Jimmy Xu, Alexander Zaslavsky, "Future trends in microelectronics: up the nano- creek", John Wiley & Sons, 2007.
- [5] Satoshi Kawat, M. Ohtsu, M. Irie, "Nano-Optics", Springer Berlin Heidelberg, Jun 2002.
- [6] Yeh, C., Shimabukuro, F., "The Essence of Waveguides", Springer 2008.
- [7] Casimer DeCusatis, Carolyn J. Sher DeCu, "Fiber optic essentials", Academic Press, 2006.
- [8] Pranabendu Ganguly, Juran Chandra Biswas, Samir Kumar Lahiri, "Analysis of Ti:LiNbO₃ zero-gap directional coupler for wavelength division multiplexer/demultiplexer" *Optics Communications* 281, 3269–3274, 2008.
- [9] Tzyy-Jiann Wang, Chih-Feng Huang, and Way-Seen Wang, *Member, IEEE*, Wide-Angle Optical Power Divider in LiNbO₃ for Variable Power Splitting, *IEEE Photonics Technology Letters*, vol. 15, no. 10, October 2003.
- [10] Saleh, Bahaa E. A. and Teich, Malvin Carl, "Fundamentals of Photonics", New York, John Wiley & Sons, 1991.
- [11] M. J. Connelly, "Semiconductor Optical Amplifiers", Boston, MA: Springer-Verlag, 2002.
- [12] Harry Atwater, "Active Plasmonic Components and Metamaterials" International Conference on Materials for Advance Technologies, Singapore,

July 3, 2009.

- [13] A. R. Von Hippel, "Dielectrics and Waves", 2nd ed., Boston MA: Artech House, 1994.
- [14] K. S. Yee, "Numerical solution of initial boundary value problems involving Maxwell's equations in isotropic media," *IEEE Trans. Antennas Propagat.*, vol. AP-14, pp. 302–307, May 1966.
- [15] Jeffrey L. Young, Ronald O. Nelson, "A Summary and Systematic Analysis of FDTD Algorithms for Linearly Dispersive Media", *IEEE Transactions on Antennas and Propagation* vol. 43, no. 1, pp. 61 – 77, Feb. 2001.
- [16] A. Taflove, Computational Electrodynamics: *The Finite-Difference Time-Domain Method*. Norwood, MA: Artech House, 2005.
- [17] C. D. Moss, Fernando L. Teixeira, and Jin Au Kong, "Analysis and Compensation of Numerical Dispersion in the FDTD Method for Layered, Anisotropic Media", *IEEE Transactions on Antennas and Propagation*, vol. 50, no. 9, pp. 1174-1184, sep. 2002.
- [18] S . T. Chu and S. K. Chaudhuri, "A finite-difference time-domain method for the design and analysis of guided-wave optical structures", *IEEE/OSA J. Lightwave Technol.*, vol. LT-7, pp. 2033-2038, 1989.
- [19] W. P. Huang, S. T. Chu, A. Goss, and S. K. Chaudhuri, "A scalar finite-difference time-domain approach to guided-wave optics", *IEEE Photon. Technol. Lett.*, vol. 3, pp. 524-526, June 1991.
- [20] S . T. Chu and S. K. Chaudhuri and W. P. Huang "Analysis of Optical Guided-Wave Devices with the Finite-Difference Time-Domain Method", *IEEE Antennas and Propagation International Symposium*, AP-S, pp. 257-260, 1992.
- [21] R. Courant, K. Friedrichs and H. Lewy, Über die partiellen Differenzengleichungen der mathematischen Physik, *Mathematische Annalen*, vol. 100, no. 1, pages 32–74, 1928.
- [22] R. Courant, K. Friedrichs and H. Lewy, "On the partial difference equations of mathematical physics", *IBM Journal*, pp. 215-234, English translation of the 1928 German original, March 1967.
- [23] Monk P., "Error estimates for Yee's method on non-uniform grids," *IEEE Trans. Magnetics*, vol. 30, pp.3200-3203, 1994.
- [24] Sheen, D. Numerical Modeling of Microstrip Circuits and Antennas, Ph. D. Dissertation, Massachusetts Institute of Technology, Cambridge, MA, June

1991.

- [25] Liu, Q. H. The pseudospectral time-domain (PSTD) method: A new algorithm for solutions of Maxwell's equations," *Proc. IEEE Antennas and Propagation Society Intl. Symposium*, (IEEE catalog no. 97CH36122), Montreal, Canada, vol. 1, pp. 122-125, July 13-18, 1997.
- [26] Liu, Q. H. "The PSTD Algorithm: A Time-Domain Method Requiring only Two Grids Per Wavelength", New Mexico State Univ., Las Cruces, NM, Technical Report NMSU-ECE96-013, Dec. 1996.
- [27] F. Zheng, Z. Chen, and J. Zhang, "Toward the development of a three-dimensional unconditionally stable finite-difference time-domain method," *IEEE Trans. Microw. Theory Tech.*, vol. 48, no. 9, pp. 1550–1558, Sept. 2000.
- [28] S. González García, A. Rubio Bretones, R. Gómez Martín and Susan C. Hagness, "Accurate Implementation of Current Sources in the ADI-FDTD Scheme *IEEE Transaction on Antennas & Propagation*, vol. 3, pp. 141-144, 2004.
- [29] Shumin Wang, Fernando L. Teixeira, and Ji Chen, "An Iterative ADI-FDTD with Reduced Splitting Error", *IEEE Microwave & Wireless Components Letters*, vol. 15, no. 2, Feb. 2005.
- [30] Juan Chen and Jianguo Wang, "PEC Condition Implementation for the ADI-FDTD Method", *Microwave and Optical Technology Letters*, vol. 49, no. 3, pp. 526 – 530, March 2007.
- [31] Kyung-Young Jung and Fernando L. Teixeira, "Multispecies ADI-FDTD Algorithm for Nanoscale Three-Dimensional Photonic Metallic Structures", *IEEE Photonics Technology Letters*, vol. 19, no. 8, pp. 586-588, April, 2007.
- [32] T. Namiki, "3-D ADI-FDTD method—Unconditionally stable time domain algorithm for solving full vector Maxwell's equations," *IEEE Trans. Microw. Theory Tech.*, vol. 48, no. 10, pp. 1743–1748, Oct. 2000.
- [33] J. Shibayama, M. Muraki, J. Yamauchi, and H. Nakano, "Efficient implicit FDTD algorithm based on locally one-dimensional scheme," *Electron. Lett.*, vol. 41, no. 19, pp. 1046–1047, Sep. 2005.
- [34] Eng Leong Tan, "Fundamental Schemes for Efficient Unconditionally Stable Implicit Finite-Difference Time-Domain Methods", *IEEE Transactions on Antennas and Propagation*, vol. 56, no. 1, pp. 170 – 177, January 2008.
- [35] Kyung-Young Jung and F. L. Teixeira, "An Iterative Unconditionally Stable LOD-FDTD Method", *IEEE Microwave & Wireless Components Letters*, vol.

18, no. 2, pp. 76-78, Feb. 2008.

- [36] J. Shibayama, A. Nomura, R. Ando, J. Yamauchi, and H. Nakano, "A frequency dependent LOD-FDTD Method and its application to the analyses of plasmonic waveguide devices", *IEEE Journal of Quantum Electronics*, vol. 46, no. 1, pp. 40–49, January, 2010.
- [37] Garcí'a, S.G., Lee, T.W., and Hagness, S.C. "On the accuracy of the ADI-FDTD method", *IEEE Antennas Wirel. Propag. Lett.*, 1, pp. 31–34, 2002.
- [38] J. Chen and J.G. Wang, "Weakly conditionally stability FDTD scheme with reduced split error", *Electronics Letters*, vol. 42 no. 18, pp. 1017-1018, August 2006.
- [39] F. Zheng and Z. Chen, "Numerical dispersion analysis of the unconditionally stable 3-D ADI-FDTD method," *IEEE Trans. Microw. TheoryTech.*, vol. 49, no. 5, pp. 1006–1009, May 2001.
- [40] S. Ju, H. Kim, and H.-H. Kim, "A study of the numerical dispersion relation for the 2-D ADI-FDTD method," *IEEE Microw. Wireless Compon. Lett.*, vol. 13, no. 9, pp. 405–407, Sep. 2003.
- [41] Qi-Feng Liu, Zhizhang Chen, Wen-Yan Yin, " An Arbitrary-Order LOD-FDTD Method and its Stability and Numerical Dispersion", *IEEE Transactions on Antennas and Propagation*, vol. 57, Issue 8 pp. 2409 – 2417, Aug. 2009.
- [42] Hongling Rao, Robert Scarmozzino, and Richard M. Osgood, "An Improved ADI-FDTD Method and Its Application to Photonic Simulations", *IEEE Photonics Tech. Letters*, vol. 14, no. 4, pp. 477-479, April 2002.
- [43] J. Shibayama, M. Muraki, R. Takahashi, J. Yamauchi, and H. Nakano, "Performance evaluation of several implicit FDTD methods for optical waveguide analysis," *Journal of Lightwave Technology*, vol. 24, no. 6, pp. 2465–2471, Sep. 2006.
- [44] K.Y. Jung, F. L. Teixeira, S. G. Garcia, and R. Lee, "On Numerical Artifacts of the Complex Envelope ADI-FDTD Method" *IEEE Transaction on Antennas & Propagation*, vol. 57, no. 2, pp. 491-498, Feb. 2009.
- [45] R. J. Luebbers and F. Hunsberger, "FDTD for nth-order dispersive media," *IEEE Trans. Antennas Propagat.*, vol. 40, no. 11, pp. 1297-1301, Nov. 1992.
- [46] D. F. Kelley and R. J. Luebbers, "The piecewise linear recursive convolution method for incorporating dispersive media into FDTD," in *11th Ann. Rev. of Progress in Applied Computational Electromagnetics*, Monterey, CA, vol. 1, pp. 526-533, Mar. 1995.

- [47] Kashiwa, T., and I. Fukai, "A treatment by FDTD method of dispersive characteristics associated with electronic polarization," *Microwave and Optics Technology Letters*, vol. 3, pp.203-205, 1990.
- [48] R. M. Joseph, S. C. Hagness, and A. Taflove, "Direct time integration of Maxwell's equations in linear dispersive media with absorption of scattering and propagation of femtosecond electromagnetic pulses," *Opt. Lett.*, vol. 17, pp. 1412-1414, 1991.
- [49] D. M. Sullivan, "Frequency dependent FDTD methods using Z transforms," *IEEE Trans. Antennas Propag.*, vol. 40, pp. 1223-1230, 1992.
- [50] D. M. Sullivan, "Z-transform theory and the FDTD method," *IEEE Trans. Antennas Propag.*, vol. 44, pp. 28-34, 1996.
- [51] M. D. Feit and J. A. Fleck, "Light propagation in graded-index optical fibers," *Appl. Opt.*, vol. 17, no. 24, pp. 3990-3998, Dec. 1978.
- [52] Y. Chung and N. Dagli, "Analysis of Z-invariant and Z-variant semiconductor rib waveguides by explicit finite difference beam propagation method with nonuniform mesh configuration," *IEEE J. Quantum Electron.*, vol. 27, no. 10, pp. 2296-2305, 1991.
- [53] H. M. Masoudi and J. M. Arnold, "Parallel beam propagation method for the analysis of second harmonic generation," *IEEE Photon. Technol. Lett.*, vol. 7, no. 4, pp. 400-402, Apr. 1995.
- [54] H. M. Masoudi and J. M. Arnold, "Modeling second-order nonlinear effects in optical waveguides using a parallel-processing beam propagation method," *IEEE J. Quantum Electron.*, vol. 31, no. 12, pp. 2107-2113, Dec. 1995.
- [55] H. M. Masoudi, M. A. AlSunaidi, and J. M. Arnold, "Time-domain finite-difference beam propagation method," *IEEE Photon. Technol. Lett.*, vol. 11, no. 10, pp. 1274-1276, Oct. 1999.
- [56] H. M. Masoudi, M. A. AlSunaidi, and J. M. Arnold, "Efficient time-domain beam propagation method for modeling integrated optical devices," *J. Lightw. Technol.*, vol. 19, no. 5, pp. 759-771, May 2001.
- [57] M. Koshiha, Y. Tsuji, and M. Hikari, "Time-domain beam propagation method and its application to photonics crystal circuits," *J. Lightw. Technol.*, vol. 18, no. 1, pp. 102-110, Jan. 2000.
- [58] M. Koshiha and W. P. Huang, "An efficient split step time domain propagation method for modeling of optical waveguide devices," *J. Lightw. Technol.*, vol.

23, no. 6, pp. 2186 – 2191, Jan. 2005.

- [59] H. M. Masoudi, "A novel non-paraxial time domain beam propagation method for modeling ultra short pulses in optical structures" *J. Lightw. Technol.*, vol. 25, no. 10, Oct. 2007.
- [60] H. M. Masoudi, "A Stable Time-Domain Beam Propagation Method for Modeling Ultrashort Optical Pulses" *IEEE Photonics Technology Letters*, Vol. 19, No. 10, pp. 786-788, May 15, 2007.

CHAPTER 2

MODELING OPTICAL DEVICES

2.1 Introduction

This chapter presents the basic equations needed in modeling optical devices starting with Maxwell's equations. It gives a review of the slab waveguide theory for the Transverse Electric (TE) and the Transverse Magnetic (TM) polarized electromagnetic fields. The chapter, then, continues to give an overview for the common techniques used in modeling optical devices, namely, the Method of Lines (MoL) and the Beam Propagation Method (BPM). The Perfectly Matched Layer (PML) used as an absorbing numerical technique to attenuate unwanted radiation fields at the edge of the numerical window is formulated and implemented. The chapter ends with the numerical implementations for both the MoL and the BPM for two dimensional devices.

2.2 The Wave Equation

Starting with Maxwell's equations in differential form which can be written as

$$\nabla \times \mathbf{E} = -\frac{\partial \mathbf{B}}{\partial t} \quad (2.1)$$

$$\nabla \times \mathbf{H} = \frac{\partial \mathbf{D}}{\partial t} + \mathbf{J} \quad (2.2)$$

$$\nabla \cdot \mathbf{D} = \rho_v \quad (2.3)$$

$$\nabla \cdot \mathbf{B} = 0 \quad (2.4)$$

where $\mathbf{E}(\mathbf{r},t)$ and $\mathbf{H}(\mathbf{r},t)$ are respectively the electric and the magnetic field vectors, $\mathbf{D}(\mathbf{r},t)$ and $\mathbf{B}(\mathbf{r},t)$ are respectively the electric and magnetic flux density vectors and $\mathbf{J}(\mathbf{r},t)$ and $\rho_v(\mathbf{r},t)$ represent the current and the charge density sources. In isotropic materials, the magnetic flux density vector \mathbf{B} has a direct relation with the magnetic field vector \mathbf{H} through the scalar magnetic permeability μ and can be written as

$$\mathbf{B} = \mu \mathbf{H} \quad (2.5)$$

where $\mu = \mu_0 \mu_r$, μ_r is the relative permeability taken to be unity for non-magnetic materials and μ_0 is the free space permeability. Also for isotropic electrically non-linear materials the electric displacement \mathbf{D} can be written, in general, as a function of \mathbf{E} , as

$$\mathbf{D}(\mathbf{r},t) = \varepsilon_0 \left[\mathbf{E}(\mathbf{r},t) + \chi \mathbf{E}(\mathbf{r},t) + \chi^{(2)} \mathbf{E}^2(\mathbf{r},t) + \chi^{(3)} \mathbf{E}^3(\mathbf{r},t) + \dots \right] \quad (2.6)$$

where ε_0 is the free space permittivity. χ is the scalar linear susceptibility, $\chi^{(2)}$ and $\chi^{(3)}$ are the second and third order nonlinear susceptibilities, respectively. For dielectrics, the value of $\varepsilon = \varepsilon_0 \varepsilon_r$ is greater than ε_0 , and contains a material part characterized by a dipole moment density or polarization, \mathbf{P} (C/m²). It can again be split as linear and nonlinear part by the following equation

$$\mathbf{D}(\mathbf{r},t) = \varepsilon_0 (1 + \chi) \mathbf{E}(\mathbf{r},t) + \varepsilon_0 \mathbf{P}^{\text{NL}}(\mathbf{r},t) \quad (2.7)$$

A medium is linear if its properties do not depend on the amplitude of the fields and thus $\mathbf{P}^{\text{NL}} = 0$. Considering a non-magnetic ($\mu = \mu_0$), linear and source free set of Maxwell's equations ($\mathbf{J} = 0$ and $\rho_v = 0$), while taking the curl ($\nabla \times$) of Eq. 2.1 and using Eq. 2.2, the following can be obtained

$$\begin{aligned}\nabla \times \nabla \times \mathbf{E} &= -\mu_0 \frac{\partial}{\partial t} \{ \nabla \times \mathbf{H} \} \\ &= -\mu_0 \frac{\partial^2 \mathbf{D}}{\partial t^2}\end{aligned}\tag{2.8}$$

Using the vector identity,

$$\nabla \times \nabla \times \mathbf{E} = \nabla (\nabla \cdot \mathbf{E}) - \nabla^2 \mathbf{E}\tag{2.9}$$

For a locally homogeneous medium, where ϵ is locally space independent, the first term on the right hand side of the above vector identity can be set to zero (using Eq. 2.3) [1 - 5] to the wave equation

$$\nabla^2 \mathbf{E} - \mu_0 \frac{\partial^2 \mathbf{D}}{\partial t^2} = 0\tag{2.10}$$

If the medium is linear and non-dispersive, then Eq. 2.10 can be written as

$$\nabla^2 \mathbf{E} - \mu_0 \epsilon_0 \epsilon_r \frac{\partial^2 \mathbf{E}}{\partial t^2} = 0\tag{2.11}$$

For a monochromatic field that oscillates with an angular frequency ω , the electric and the magnetic fields can be described as

$$\begin{bmatrix} \mathbf{E}(\mathbf{r}, t) \\ \mathbf{H}(\mathbf{r}, t) \end{bmatrix} = \begin{bmatrix} \tilde{\mathbf{E}}(\mathbf{r}) \\ \tilde{\mathbf{H}}(\mathbf{r}) \end{bmatrix} e^{j\omega t}\tag{2.12}$$

Then the second derivative with respect to t in Eq. 2.11 can be replaced by $-\omega^2$, leading to the following vectorial wave equation, as

$$\nabla^2 \tilde{\mathbf{E}} + k_0^2 n^2 \tilde{\mathbf{E}} = 0\tag{2.13}$$

where $n = \sqrt{\epsilon_r}$ is the refractive index, $k_0 = \omega/c_0$ is the free space wave number. Eq. 2.13 is

the well-known Helmholtz equation.

2.3 The Slab Waveguide

The slab waveguide consists of three layers with different dielectric constants, extending infinitely in the directions parallel to their interfaces. A schematic diagram of a three layer planar waveguide is shown in Figure 2.1. It consists of a superstrate, a core and a substrate with refractive indices n_1 , n_2 and n_3 respectively, where $n_2 > n_3 > n_1$ which satisfies the guidance condition.

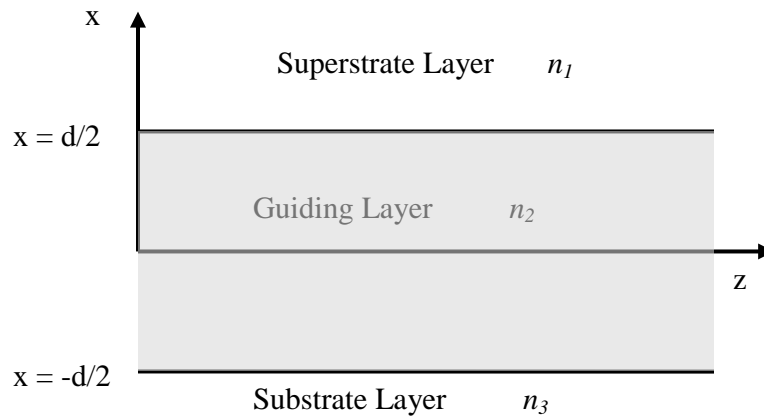


Figure 2.1 The dielectric slab waveguide

In order to simplify the analysis, the structure is assumed to be uniform and infinitely stretched along the y direction, so that the field can be assumed not to vary along the y -axis. This allows to set $\frac{\partial}{\partial y} = 0$. The direction of propagation is assumed to be the z -direction.

The wave equation in Eq. 2.13 can be written for each region as [6]

$$\frac{\partial^2 \mathbf{E}}{\partial x^2} + \frac{\partial^2 \mathbf{E}}{\partial z^2} + k_0^2 n_r^2 \mathbf{E} = 0, \quad r = 1, 2, 3 \quad (2.14)$$

Moreover, assuming the variation of the fields in the positive z-direction as $\exp(-jk_z z)$, where k_z is the propagation constant, Eq. 2.14 can be written region wise separately as

$$\frac{\partial^2 \mathbf{E}}{\partial x^2} - (k_z^2 - k_0^2 n_r^2) \mathbf{E} = 0, \quad r = 1, 3 \quad (2.15a)$$

$$\frac{\partial^2 \mathbf{E}}{\partial x^2} + (k_0^2 n_2^2 - k_z^2) \mathbf{E} = 0 \quad (2.15b)$$

Eq. 2.15a is valid for the substrate and superstrate regions and Eq. 2.15b is applicable for the guiding region. There are two types of polarizations that can be supported in slab waveguide structure- the Transverse Electric (TE) field and the Transverse Magnetic (TM) field polarizations.

2.3.1 Transverse Electric (TE) Guided Modes

For TE-polarized waves, the electric field points in the y-direction, namely $\mathbf{E} = E_y \mathbf{a}_y$ and the magnetic field has two components $\mathbf{H} = H_x \mathbf{a}_x + H_z \mathbf{a}_z$. By solving Eq. 2.15 in each layer of the slab waveguide along with the application of the boundary conditions for the continuity of E_y at the interface, E_y can be expressed as [6]

$$E_y = \begin{cases} \left[A \cos(r_g d / 2) + B \sin(r_g d / 2) \right] e^{-r_c(x-d/2)} & x \geq d/2 \\ A \cos(r_g x) + B \sin(r_g x) & -d/2 \leq x \leq d/2 \\ \left[A \cos(r_g d / 2) - B \sin(r_g d / 2) \right] e^{r_s(x+d/2)} & x \leq -d/2 \end{cases} \quad (2.16)$$

where $r_g^2 = k_0^2 n_2^2 - k_z^2$, $r_c^2 = k_z^2 - k_0^2 n_1^2$ and $r_s^2 = k_z^2 - k_0^2 n_3^2$. Using Maxwell's equations, the corresponding two non-zero components of the magnetic field H_x and H_z , can be written as

$$H_x = -\frac{k_z}{\omega\mu_0} E_y \quad (2.17a)$$

$$H_z = -\frac{j}{\omega\mu_0} \frac{\partial E_y}{\partial x} \quad (2.17b)$$

Under guiding condition most of the power is confined in the core with oscillatory behavior in the middle layer and exponential decaying (evanescent) behavior in the outer regions. This feature requires that r_c^2 , r_g^2 and $r_s^2 > 0$ and can be combined to get the following inequalities (for $n_3 > n_1$)

$$k_0 n_1 \leq k_0 n_3 \leq k_z \leq k_0 n_2 \quad (2.18)$$

Substituting Eq. 2.16 into Eq. 2.17 and applying the boundary conditions for H_z we get [6]

$$\tan(dr_g) = \frac{r_g(r_s + r_c)}{r_g^2 - r_s r_c} \quad (2.19)$$

Eq. 2.19 is the analytical eigenvalue (characteristic) equation for the TE guided modes where the only unknown quantity is the propagation constant k_z . The eigenvalue equation determines the allowed values of the propagation constant k_z , i.e., the guided modes.

2.3.2 Transverse Magnetic (TM) Guided Modes

The same approach described in the previous section can be applied to obtain the guided modes for the TM polarization. For TM-polarized waves, the magnetic field has a single component in the y-direction, namely $\mathbf{H} = H_y \mathbf{a}_y$. The electric field \mathbf{E} has two components so that $\mathbf{E} = E_x \mathbf{a}_x + E_z \mathbf{a}_z$. By solving Eq. 2.16 in each layer of the slab waveguide along with the application of the boundary conditions for the continuity of H_y , H_y can then be written as

$$H_y = \begin{cases} \left[A \cos(r_g d/2) + B \sin(r_g d/2) \right] e^{-r_c(x-d/2)} & x \geq d/2 \\ A \cos(r_g x) + B \sin(r_g x) & -d/2 \leq x \leq d/2 \\ \left[A \cos(r_g d/2) - B \sin(r_g d/2) \right] e^{r_s(x+d/2)} & x \leq -d/2 \end{cases} \quad (2.20)$$

Using Maxwell's equations, the corresponding two non-zero components of the electric field E_x and E_z can be also obtained in terms of H_y

$$E_x = \frac{k_z}{\omega \epsilon_0 n_r^2} H_y \quad (2.21a)$$

$$E_z = -\frac{j}{\omega \epsilon_0 n_r^2} \frac{\partial H_y}{\partial x} \quad (2.21b)$$

Substituting Eq. 2.20 in Eq. 2.21 and applying boundary conditions for E_z , we get [6]

$$\tan(dr_g) = \frac{r_g n_2^2 (n_1^2 r_s + n_3^2 r_c)}{n_1^2 n_3^2 r_g^2 - n_2^4 r_s r_c} \quad (2.22)$$

Eq. 2.22 is the analytical eigenvalue equation for the TM guided modes with the only unknown quantity being again the propagation constant k_z .

2.4 The Method of Lines (MoL)

The Method of Lines (MoL) [7-14] solves partial differential equations (PDE) by transforming it into an ordinary differential equation (ODE) whereby all the independent variables are discretized except one. Therefore, $(n - 1)$ variables are discretized of a PDE with n independent variables, resulting in an ODE which can then be solved analytically in terms of the remaining variable [16]. Computation of eigenvalues and eigenvectors (eigenpairs) of the system matrix are employed in the analytical solution. The eigenpairs calculation requires a numerical effort proportional to M^3 , where M is the number of discrete points used in the

field representation. Even though the MoL has been applied to several types of planar longitudinally uniform optical and microwave waveguide problems, interface conditions can also be easily employed in this method. It has been used to analyze single [17] and multiple longitudinal discontinuities in optical waveguides [9], non-linear waveguide problems [11] and diffraction problems from waveguide ends [10]. The MoL has been successfully used also to model 3D problems [14-15] for both optical and microwave waveguides. The MoL has a high numerical precision and an acceptable computational expense [8]. However, if the size of the problem is exceedingly large, the computation of the eigenpairs becomes computationally expensive and even prohibitive in some cases.

2.4.1 MoL Formulation

In this section, we discuss the formulation of the MoL for 2-D slab waveguide structure. The wave is assumed to propagate in z -direction and the time dependence is assumed, as before, to be $e^{j\omega t}$. For the waveguide structure shown in Figure 2.1, the waveguide geometry is discretized in the x -direction and the boundary layers are parallel to the y - z plane. The computational window is bounded in all direction by an electric wall ($E_y = 0$) or a magnetic wall ($H_y = 0$). The two dimensional wave equation obtained from Eq. 2.14 is given by

$$\frac{\partial^2 \psi(x, z)}{\partial z^2} + \frac{\partial^2 \psi(x, z)}{\partial x^2} + k_0^2 n^2 \psi(x, z) = 0 \quad (2.23)$$

where ψ represents either E_y or H_y , depending on whether we have TE or TM polarized waves, respectively. Upon discretization, the second term in Eq. 2.23 is replaced by the three-point central Finite Difference (FD) approximation

$$\frac{\partial^2 \psi}{\partial x^2} = \frac{\psi_{i+1} - 2\psi_i + \psi_{i-1}}{\Delta x^2} \quad (2.24)$$

Then Eq. 2.23 becomes

$$\frac{d^2 \psi_i}{dz^2} + \frac{\psi_{i+1} - 2\psi_i + \psi_{i-1}}{(\Delta x)^2} + k_0^2 n_i^2 \psi_i = 0 \quad (2.25)$$

where the subscript i refers to the field at the i -th mesh line in the discretized space as shown in Figure 2.2 (in section 2.6). For transverse discretization points Eq. 2.25 assumes to the following matrix equation

$$\begin{aligned} \frac{d^2}{dz^2} \begin{bmatrix} \psi_1(z) \\ \psi_2(z) \\ \psi_3(z) \\ \vdots \\ \vdots \\ \psi_M(z) \end{bmatrix} + \frac{1}{(\Delta x)^2} \begin{bmatrix} -2 & 1 & & & \\ 1 & -2 & 1 & & 0 \\ & 1 & -2 & 1 & \\ & & \ddots & \ddots & \ddots \\ 0 & & & 1 & -2 & 1 \\ & & & & 1 & -2 \end{bmatrix} \begin{bmatrix} \psi_1(z) \\ \psi_2(z) \\ \psi_3(z) \\ \vdots \\ \vdots \\ \psi_M(z) \end{bmatrix} + \\ k_0^2 \begin{bmatrix} n_1^2 & & & & \\ & n_2^2 & & & 0 \\ & & n_3^2 & & \\ & & & \ddots & \\ 0 & & & & \ddots \\ & & & & & n_M^2 \end{bmatrix} \begin{bmatrix} \psi_1(z) \\ \psi_2(z) \\ \psi_3(z) \\ \vdots \\ \vdots \\ \psi_M(z) \end{bmatrix} = \begin{bmatrix} 0 \\ 0 \\ 0 \\ \vdots \\ \vdots \\ 0 \end{bmatrix} \end{aligned} \quad (2.26)$$

or equivalently,

$$\frac{d^2}{dz^2} \Psi_i + C \Psi_i + k_0^2 N \Psi_i = 0 \quad (2.27)$$

where $\Psi_i = [\psi_1(z) \ \psi_2(z) \ \psi_3(z) \ \cdots \ \psi_M(z)]^T$ is the column vector representing the discretized field, C is a tri-diagonal matrix, N is a diagonal matrix with elements being the

square of the refractive indices $(n_1^2 \ n_2^2 \ n_3^2 \ \dots \ n_M^2)$ at the mesh points. Finally, Eq. 2.27 can be written as

$$\frac{d^2\psi_i}{dz^2} + Q\psi_i = 0 \quad (2.28)$$

where $Q = C + k_0^2 N$. The general solution of the ordinary second order matrix differential equation is given by [10]

$$\psi_i = e^{j\sqrt{Q}z} \mathbf{A} + e^{-j\sqrt{Q}z} \mathbf{B} \quad (2.29)$$

The first term on the right hand side of Eq. 2.29 represents fields propagation in the $-z$ direction and the second term represents fields propagation in the $+z$ direction. \mathbf{A} and \mathbf{B} represent the field propagating in $\mp z$ at $z = 0$, respectively. Both \mathbf{A} and \mathbf{B} are column vectors of size $M \times 1$, and $e^{j\sqrt{Q}z}$ (or $e^{-j\sqrt{Q}z}$) is a square matrix of size $M \times M$ which can be evaluated using eigenvalue decomposition of the matrix Q . The square matrix Q is first expressed in terms of its eigenpairs in the form

$$Q = UVU^{-1} \quad (2.30)$$

and thus

$$\sqrt{Q} = U\sqrt{V}U^{-1} \quad (2.31)$$

where the diagonal matrix V contains the eigenvalues of Q and the square matrix contains the corresponding eigenvectors. The matrix exponentials $e^{\pm j\sqrt{Q}z}$ can then be found using the following relation

$$e^{\pm j\sqrt{Q}z} = Ue^{\pm j\sqrt{V}z}U^{-1} \quad (2.32)$$

The procedure of adopting the eigenpair calculation for the evaluation of \sqrt{Q} and $e^{\pm j\sqrt{Q}z}$ is a fundamental feature of the MoL.

2.5 The Beam Propagation Method

The Beam Propagation Method (BPM) is a numerical technique used to solve the wave equation in optical waveguides. This technique was invented for simulating the propagation of light using slowly varying optical fields. The BPM was first introduced in the 1970's by Feit and Fleck [18 - 19], and it relied on the approximate differential equation having first order derivatives along z (the waveguide axis). The BPM decomposes the initial field into superposition of plane waves each travelling in different directions. The first order derivative equation in z can be solved as an "initial" value problem whereby the "initial" value refers to the input field. After a one-way model is obtained, the variable z still has to be discretized. The main advantage of the BPM over the traditional mode approach is that it computes both guided and radiation modes of linear z -variant devices, in the same formalism; no special arrangement is needed to account for radiation modes. In addition, optical devices containing nonlinear effects are very difficult to analyze using the conventional mode theory. On the other hand, it is very simple to include the nonlinear part in the formulation of the BPM by a proper adjustment of the linear version.

Various kinds of the BPMs, such as the fast Fourier Transform (FFT-BPM) [19 - 22], the Finite Difference (FD-BPM) [23 - 30], and the Finite Element (FE-BPM) [31], have been developed based on how the derivative with respect to the lateral direction is handled. The classical BPM is mainly an approximation to the scalar wave equation in its parabolic form using the Fast Fourier Transform and thus it is called FFT-BPM. The FD-BPM, which is a

powerful numerical tool, uses Finite Difference (FD) approximations to replace the partial derivatives in the wave equation. There are two ways to perform the FD-BPM formalism- explicit and implicit approaches. The explicit scheme is only conditionally stable which restricts the propagation step to very small values. The implicit scheme developed by Chung and Dagli [23] is the state-of-the-art in terms of accuracy, numerical efficiency and stability. Its unconditional stability is particularly another advantage which allows setting the propagation step relatively large. A Wide-Angle (WA) scheme using Padé approximant operators [24], [25] has been developed by Hadley. The limitation of the Slowly Varying Envelope Approximation (SVEA) of having the accuracy only for the waves propagating in a small angle in the waveguide axis is overcome in the WA-BPM. These contributions made the BPM capable of being used even in the design of optical waveguides made of high-contrast-index materials, such as semiconductor based optical waveguides.

2.5.1 The BPM Formulation

This section shows the formulation of the FD-BPMs based on the solution of the parabolic equation. For this purpose the formulation of the parabolic equation from Helmholtz equation is derived first. We extract a rapidly changing phase factor in the direction of propagation z and write the field E_y , for the TE case as an example, as

$$E_y(x, y, z) = \phi(x, y, z) e^{-jk_0 n_0 z} \quad (2.33)$$

where n_0 is the reference refractive index number and k_0 is the vacuum wave number. Substituting Eq. 2.33 in Eq. 2.13, we get

$$\begin{aligned} \frac{\partial^2 \phi}{\partial x^2} e^{-jk_0 n_0 z} + \frac{\partial^2 \phi}{\partial y^2} e^{-jk_0 n_0 z} + \frac{\partial^2 \phi}{\partial z^2} e^{-jk_0 n_0 z} - 2jk_0 n_0 \frac{\partial \phi}{\partial z} e^{-jk_0 n_0 z} \\ - k_0^2 n_0^2 \phi e^{-jk_0 n_0 z} + k_0^2 n^2 \phi e^{-jk_0 n_0 z} = 0 \end{aligned} \quad (2.34)$$

With the parabolic (the slowly varying envelope) approximation, where it is assumed that the rate of change of the field in the direction of propagation is very small over a wavelength, i.e., $\left| \frac{\partial^2 \phi}{\partial z^2} \right| \ll \left| 2k_0 n_0 \frac{\partial \phi}{\partial z} \right|$, the equation can be simplified resulting in the following parabolic or Fresnel wave equation

$$2jk_0 n_0 \frac{\partial \phi}{\partial z} = \frac{\partial^2 \phi}{\partial x^2} + \frac{\partial^2 \phi}{\partial y^2} + k_0^2 (n^2 - n_0^2) \phi \quad (2.35)$$

All the methods based on the finite difference BPM can be divided into two main categories implicit and explicit techniques. Here we give a short formulation of the widely used methods. The parabolic equation Eq. 2.35 can be written as

$$j \frac{\partial \phi(x, y, z)}{\partial z} = G \phi(x, y, z) \quad (2.36)$$

where

$$G = \frac{1}{2k_0 n_0} \left[\frac{\partial^2}{\partial x^2} + \frac{\partial^2}{\partial y^2} + k_0^2 (n^2 - n_0^2) \right] \quad (2.37)$$

The solution of Eq. 2.36 can be written formally as [32 – 34]

$$\phi(x, y, z + \Delta z) = e^{(-j\Delta z G)} \phi(x, y, z) \quad (2.38)$$

where Δz is the propagation step along the z-axis which should be sufficiently small. In order to develop Eq. 2.38 into a computational form, the equation can be written in the following well-known symmetrized operator which is accurate up to second order as [35 - 38]

$$\phi(x, y, z + \Delta z) = e^{\left(-j \frac{\Delta z}{a_0} \nabla_x^2\right)} e^{\left(-j \frac{\Delta z}{a_0} d_0\right)} e^{\left(-j \frac{\Delta z}{a_0} \nabla_y^2\right)} \phi(x, y, z) + O\left((\Delta z)^3\right) \quad (2.39)$$

where

$$\begin{aligned}
 a_0 &= 2k_0 n_0 \\
 d_0(x, y, z) &= k_0^2 [n^2(x, y, z) - n_0^2] \\
 \nabla_\alpha^2 &= \frac{\partial^2}{\partial \alpha^2}, \quad (\alpha = x, y)
 \end{aligned}
 \tag{2.40}$$

In the Alternating Direction Implicit BPM (ADI-BPM), the split operator of Eq. 2.39 can be approximated using Cayley form representation, which is second order accurate [33 - 34]

$$e^{\left(-j \frac{\Delta z}{a_0} \nabla_\alpha^2\right)} = \frac{\left[1 - j \frac{\Delta z}{2a_0} \frac{\partial^2}{\partial \alpha^2}\right]}{\left[1 + j \frac{\Delta z}{2a_0} \frac{\partial^2}{\partial \alpha^2}\right]}, \quad (\alpha = x, y)
 \tag{2.41}$$

The form of Eq. 2.39 could be used to operate on any field at any stage of the split operator equation as

$$\left[1 + j \frac{\Delta z}{2a_0} \frac{\partial^2}{\partial \alpha^2}\right] F^{s+\Delta}(\alpha) = \left[1 - j \frac{\Delta z}{2a_0} \frac{\partial^2}{\partial \alpha^2}\right] F^s(\alpha)
 \tag{2.42}$$

where $s + \Delta$ is an intermediate stage for F in the split operator. The partial derivatives in Eq. 2.42 can be replaced by their finite-difference approximations; if the second order central FD approximation is used, then the right hand side of Eq. 2.42 involves a direct multiplication of the discretized field with a tridiagonal matrix, and the operator on the left side involves an inversion of a tridiagonal matrix. This method is unconditionally stable. The 2-D version of the ADI-BPM is known as the Crank-Nicholson BPM (CN-BPM). Its formulation is obtained by combining Equations (2.38) and (2.41) for two-dimensions which can be expressed in matrix form as

where i and m represent the discretization of the transverse co-ordinates x and y , respectively.

This algorithm is stable with the following condition [35]

$$\Delta z < 2k_0 n_0 \left[\frac{4}{\Delta x^2} + \frac{4}{\Delta y^2} + k_0^2 |n_{i,m}^2 - n_{0\max}^2| \right]^{-1} \quad (2.47)$$

2.6 Perfectly Matched Layer

The computational window in the above mentioned methods is normally terminated either by an electric or a magnetic wall. These types of walls cause total reflection of the radiated field back into the computational window. Thus, this necessitates an absorbing boundary to be placed so that the radiated field is absorbed. This objective can be achieved by use of the so called Perfectly Matched Layer (PML). PML layers are added on both ends of the computational window as shown in Figure 2.2.

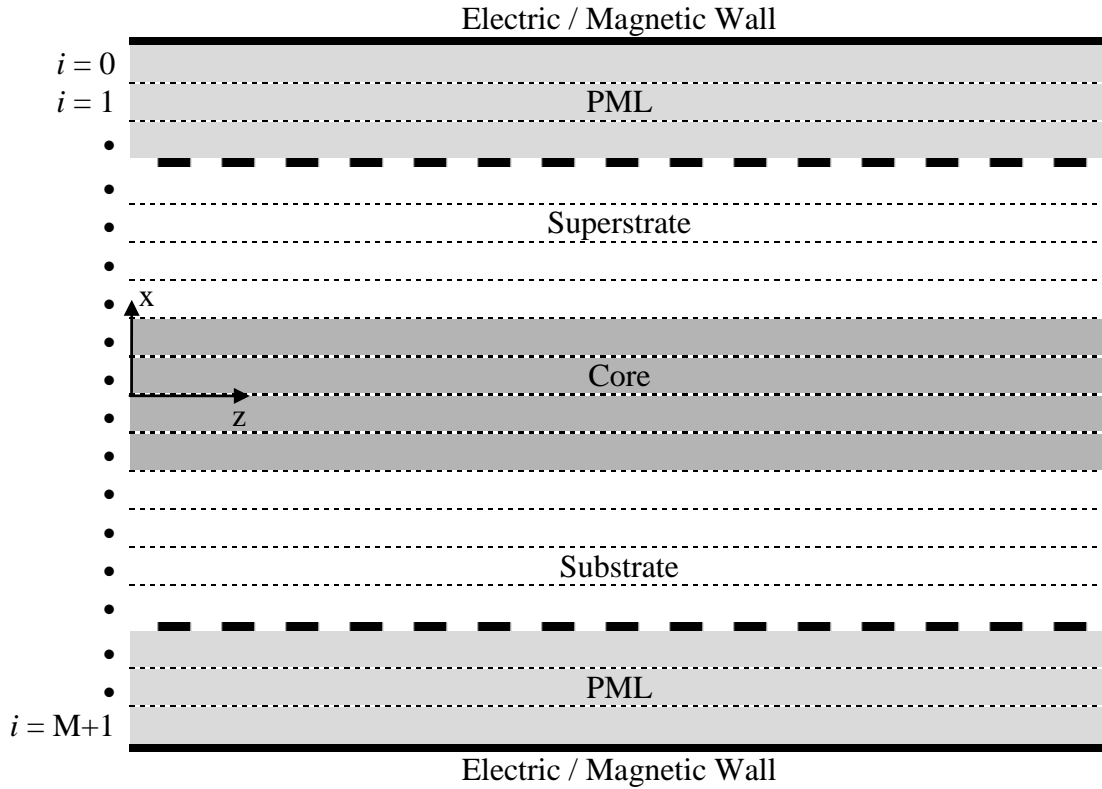


Figure 2.2 Discretization of a waveguide with PML

PML layers cause gradual attenuation of the radiated field by converting space into the complex domain. In the PML, the real space is transformed to complex space, i.e., $x \rightarrow x(1+j\sigma)$ and $\Delta x \rightarrow \Delta x(1+j\sigma)$, using the attenuation or decay parameter σ . Thus, with this type of transformation, the wave propagating in the +x-direction becomes

$$e^{-j k x (1+j\sigma)} = e^{-j k x} e^{k \sigma x} \quad (2.48)$$

The resulting exponential decay factor causes the field to be attenuated gradually. The value of σ and the number of points in the PML layer is chosen in such a way that the field becomes significantly low whenever it reaches the electric or magnetic wall at the extreme end of the computational window

2.7 Implementations

This section shows the implementations of the MoL, the CN-BPM and the EFD-BPM to model practical optical problems and devices of free space and slab waveguide.

2.7.1 Homogeneous Media

The propagation of the field in air is analyzed using previously described three methods, namely the MoL, the CN-BPM and the EFD-BPM. The methods have been used to propagate a Gaussian field in air with an input with half beam width of $w_0 = 2.0 \mu\text{m}$ and a wavelength of $\lambda = 1.0 \mu\text{m}$. The field propagated to a distance of $z = 50 \mu\text{m}$ with $\Delta x = 0.1 \mu\text{m}$, $\Delta z = 0.025 \mu\text{m}$ and a total window size of $40 \mu\text{m}$. As shown in Figure 2.3 (a), the three methods predict equal beam spread. Figure 2.3 (b) depicts the effect of the perfectly matched layer (PML) employed in the numerical solution of the MoL. The ripple seen in the figure at $z = 40 \mu\text{m}$ could be removed by enlarging the window size; however this will result in more computational cost. Introducing a PML with the same window size significantly reduces the ripple as shown in the figure.

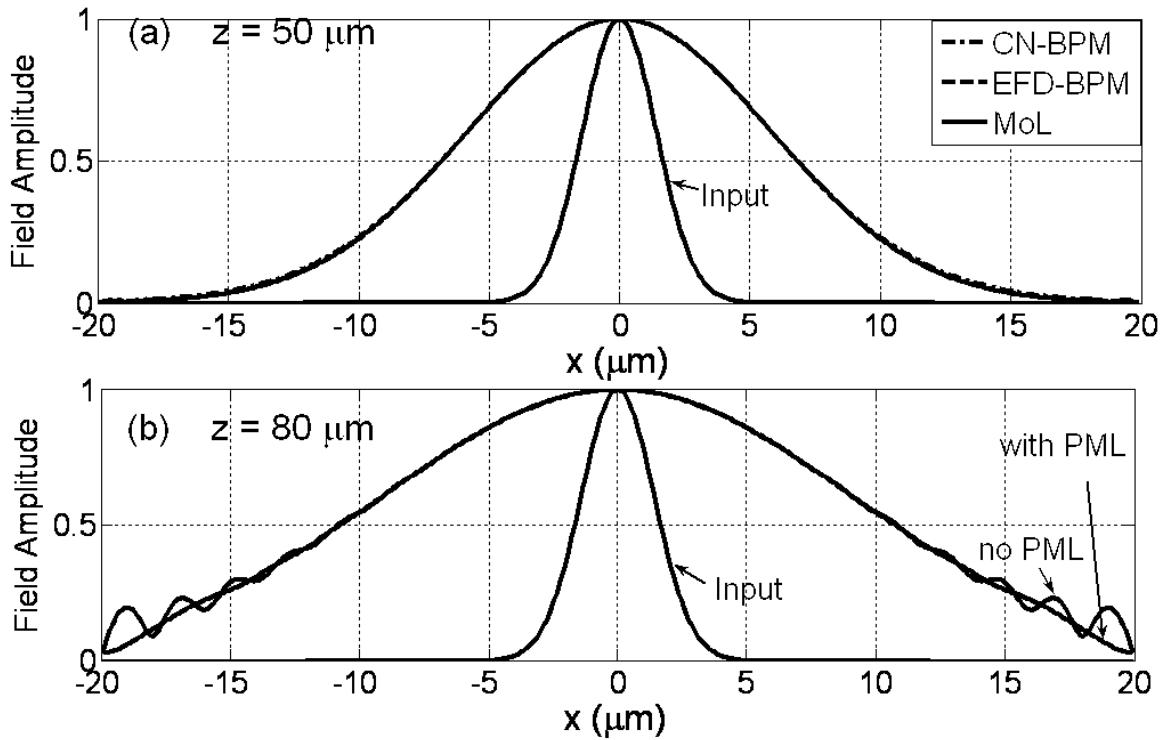


Figure 2.3 The evolution of a Gaussian field in air using (a) the MoL, the EFD-BPM, and the CN-BPM, (b) Effect of implementing the PML in MoL.

2.7.2 Slab Waveguide

This section shows the propagation of the TE_0 and TE_1 modes through a symmetric waveguide using the EFD-BPM, the CN-BPM and the MoL. The widths of the substrate, the guiding and the superstrate of the waveguide are $20\ \mu\text{m}$, $10\ \mu\text{m}$ and $20\ \mu\text{m}$ with refractive indices of 3.5, 3.6 and 3.5, respectively and a wavelength of $\lambda = 1.55\ \mu\text{m}$ is taken. Different propagation steps have been chosen for different methods as the EFD-BPM requires a stability condition to be fulfilled. A lateral mesh size $\Delta x = 0.1\ \mu\text{m}$ was used for all techniques. The TE_0 mode of the slab was launched as an input and the field was allowed to propagate to a distance of $40\ \mu\text{m}$ using the three techniques. Figure 2.4 (a) shows the input

field and the fields at $z = 40 \mu\text{m}$. Figure 2.4 (b) shows the propagated fields of the TE_1 mode using the three techniques under the same condition. The figures show the close agreement among the three techniques.

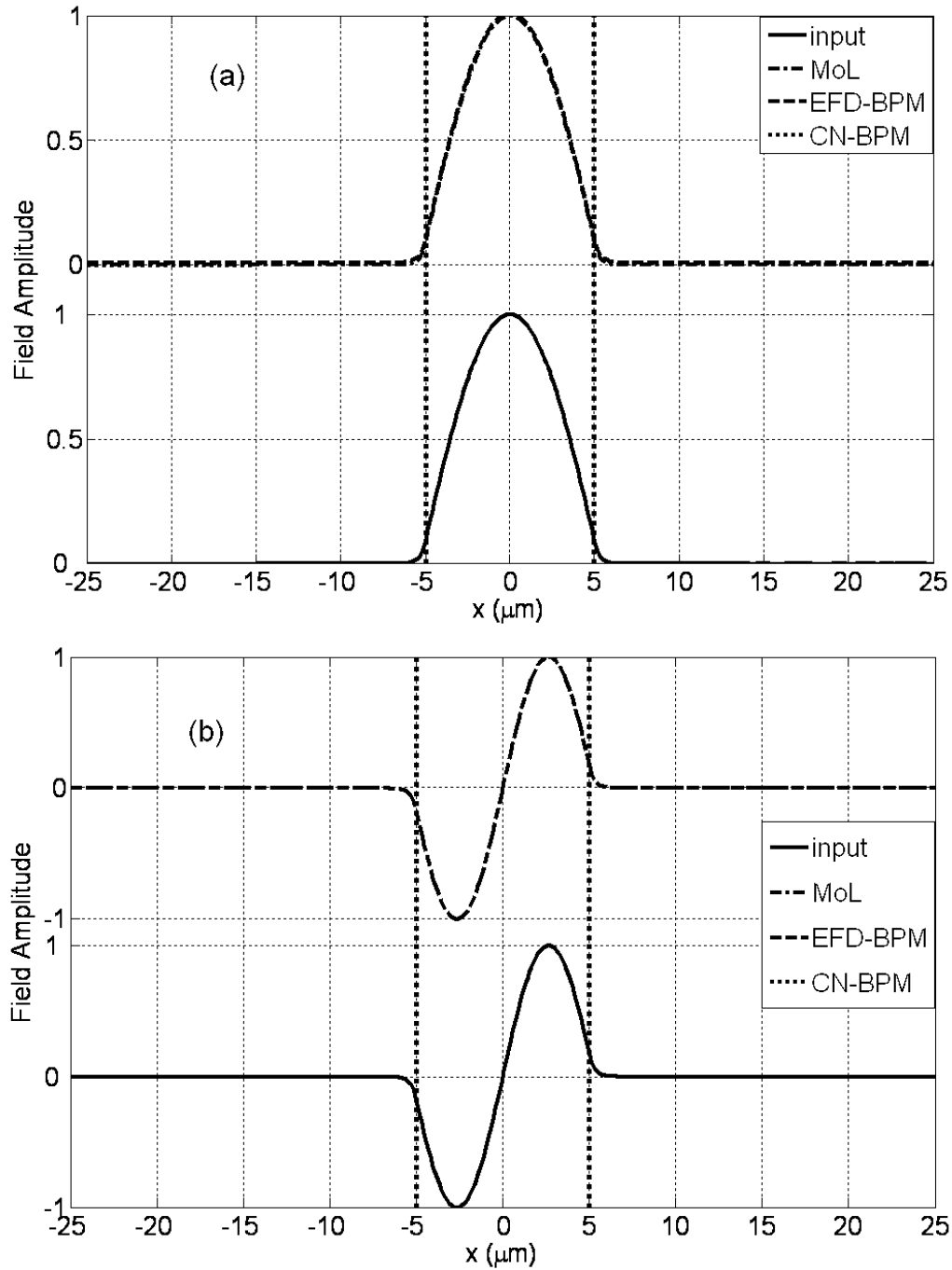


Figure 2.4 Propagated fields at $z = 40 \mu\text{m}$ inside a slab waveguide (a) the TE_0 mode (b) the TE_1 mode using the three techniques: the MoL, the EFD-BPM and the CN-BPM.

2.7.3 Directional Coupler

The basic structure of a Directional Coupler (DC) is constructed by placing two waveguides in close proximity so that the energy can be coupled from one waveguide to the other after a longitudinal distance. Figure 2.5 shows the geometry of the directional coupler structure with a separation of s .

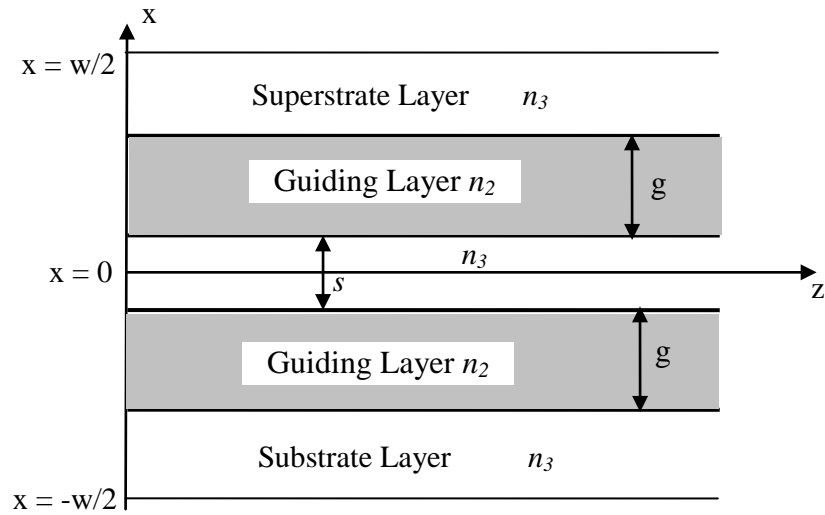


Figure 2.5 The directional coupler geometry

The coupling length L_c is the distance at which the excited energy in one waveguide is transformed completely to the other waveguide. L_c can be computed using the relation [43 - 44]

$$L_c = \frac{\pi}{\beta^e - \beta^o} \quad (2.49)$$

where β^e and β^o are the propagation constants for the even and odd modes of the DC structure. One of the key factors that govern the coupling length is the spacing s between the two cores.

The three numerical techniques, the MoL, the EFD-BPM and the CN-BPM were used to model optical field propagation inside a *GaAs* directional coupler structure. The parameters of the *GaAs* coupler are as follows: the core width = 1.0 μm and both the substrate and the superstrate are taken as 5.0 μm , the gap between the guiding region is $s = 1.0 \mu\text{m}$, and the refractive index of the core is 3.6 and that of the substrate and the superstrate is 3.5 and a wavelength $\lambda = 1.55 \mu\text{m}$. A lateral mesh size $\Delta x = 0.1 \mu\text{m}$ and propagation step size $\Delta z = 0.1 \mu\text{m}$ is used for all techniques. The DC structure was excited with the TE_0 mode of an isolated waveguide and the field was followed numerically for one coupling length.

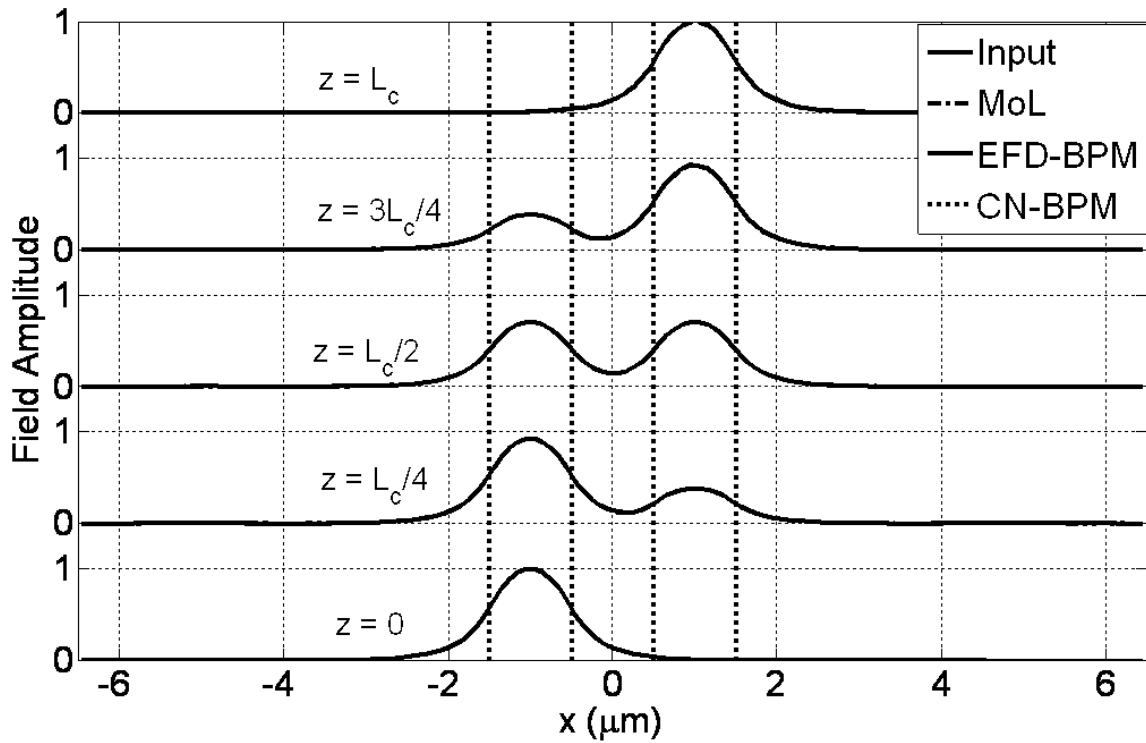


Figure 2.6 The propagation of the TE_0 guided mode of the isolated slab waveguide inside a directional coupler with a separation distance $s = 1 \mu\text{m}$. The total propagation distance used is equal to one coupling length, $L_c = 358.8 \mu\text{m}$.

Figure 2.6 shows the propagation of the TE_0 guided mode of the isolated waveguide using the three techniques. The left hand side waveguide is excited by the TE_0 mode. The

field is seen to couple to the adjacent waveguide with the complete transfer of energy in one coupling length, $L_c = 359.7 \mu\text{m}$ which agrees with the theoretical value.

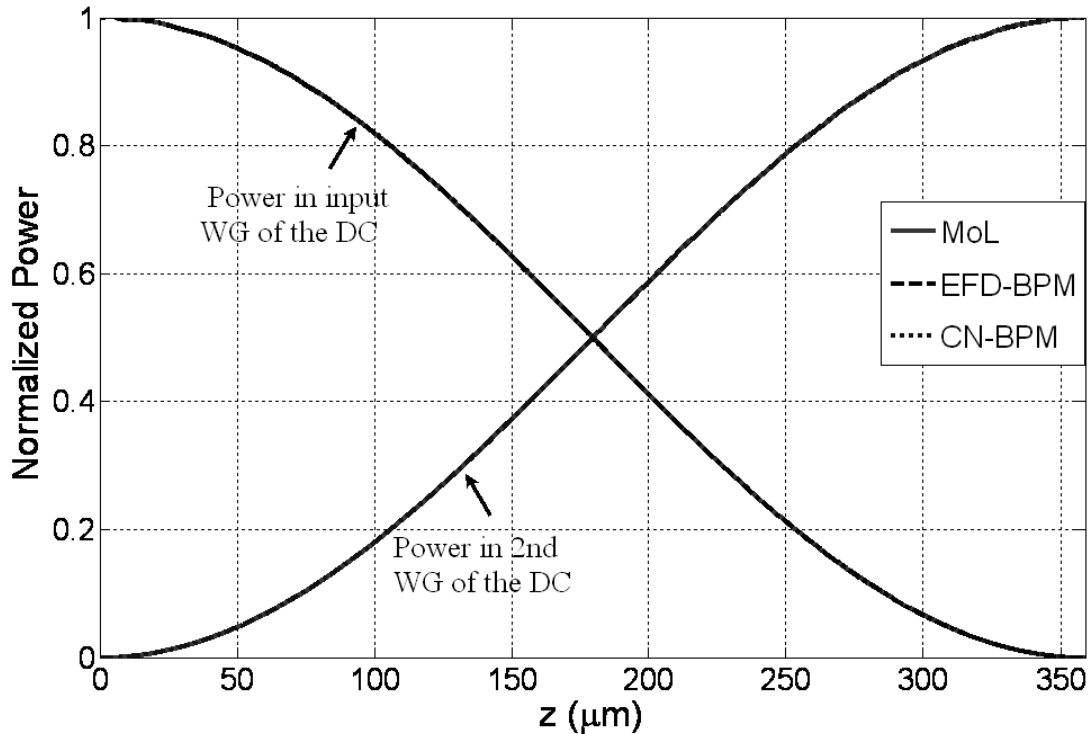


Figure 2.7 Normalized power versus distance along the directional coupler.

Figure 2.7 shows the exchange of power between the two waveguides of the DC structure for all the three methods. The two figures show the close agreement among the three implemented techniques.

2.8 Summary

Basic equations useful for modeling optical devices have been formulated from Maxwell's equations. Detailed mathematical formulations for the implicit (CN), the explicit (EFD) BPM and the MoL were shown. These numerical techniques have been implemented

for CW applications in a homogeneous medium, a slab waveguide and a directional coupler structure. The results obtained using all three methods showed close agreement.

References

- [1] Saad, M.S., "Review of Numerical Methods for the analysis of Arbitrary-Shaped Microwave and Optical Dielectric Waveguides", *IEEE Trans. MTT*, 33, 894-899, 1985.
- [2] Stern, M.S. "Semivectorial Polarized Finite Difference Method for Optical Waveguides with Arbitrary Index Profiles", *IEE Proc. Pt.J.*, 135, 56-63, 1988.
- [3] Robertson, M.J., Ritchie, S., and Dayan, P., "Semiconductor Waveguides: Analysis of Optical Propagation in Single Rib Structures and Dielectric Couplers", *IEE Proc. Pt. J.*, 132, 336-342, 1985.
- [4] Schweig, E., and Bridges, W., "Computer Analysis of Dielectric Waveguides: A finite Difference Method", *IEEE Trans. MTT*, 32, 531-541, 1984.
- [5] Henry C.H., and Verbeck, B.H., "Solution of the Scalar Wave Equation for Arbitrarily Shaped Dielectric Waveguides by using Two-Dimensional Fourier Analysis", *J. Lightwave Techn.*, 7, 308-313, 1989.
- [6] Kenji Kawano, Tsutomu Kitoh, *Introduction Optical Waveguide Analysis: Solving Maxwell's Equations and the Schrodinger Equation*, John Wiley & Sons, 2001.
- [7] A. Barcz, S. F. Helfert, and R. Pregla, "The method of lines applied to numerical simulation of 2D and 3D bandgap structures," *Transparent Optical Networks*, vol. 1, pp. 126 – 129, July 2003.
- [8] H. A. Jamid and M. N. Akram, "A new higher order finite-difference approximation scheme for the Method of lines," *Journal of Lightwave Technology*, vol. 19, 2001.
- [9] W. D. Yang and R. Pregla, "Method of lines for analysis of waveguide structures with multidiscontinuities," *Electronics Letters*, vol. 31, pp. 892, May 1995.
- [10] R. Pregla and W. Yang, "Method of lines for analysis of multilayered dielectric waveguides with bragg gratings," *Electronics Letters*, vol. 29, pp. 1962, October 1993.

- [11] S. J. Al-Bader and H. A. Jamid, "Method of lines applied to non-linear guided waves," *Electronics Letters*, vol. 31, pp. 79-85, February 1995.
- [12] S. J. Al-Bader and H. A. Jamid, "Perfectly matched layer absorbing boundary conditions for the Method of lines modeling scheme," *IEEE Microwave and Guided Waves Letters*, vol. 8, pp. 357-359, November 1998.
- [13] H. A. Jamid and M. N. Akram, "Analysis of Deep Waveguide Gratings: An efficient Cascading and Doubling Algorithm in the Method of Lines Framework," *Journal of Lightwave Technology*, vol. 20, pp. 1204-1208, July 2002.
- [14] W. D. Yang and R. Pregla, "The method of lines for analysis of integrated optical waveguide structures with arbitrary curved interfaces," *Journal of Lightwave Technology*, vol. 14, pp. 879-884, May 1996.
- [15] F. H. Al-Harbi, "Implementation of a full vectorial method of lines analysis in the study of metal clad rib waveguide," *M. S. Thesis*, KFUPM, Saudi Arabia, Dec. 2000.
- [16] V. Vemuri and W. J. Karplus, "Digital computer treatment of partial differential equations," *Series in Computational Mathematics*, 1981.
- [17] J. C. W. Jiang and M. Fontaine, "Analysis of ARROW waveguides," *Optics Communications*, vol. 72, pp. 180-186, July 1989.
- [18] F. D. Tappert, The parabolic approximation method, in: J. B. Keller and J. S. Papadakis (Eds.), *Wave Propagation and Underwater Acoustics*, Springer-Verlag, Berlin, pp. 224-287, 1977.
- [19] M. D. Feit and J. A. Fleck, "Light propagation in graded-index optical fibers," *Appl. Opt.*, vol. 17, no. 24, pp. 3990-3998, Dec. 1978.
- [20] P. L. Ho and Y. Y. Lu, "A stable bidirectional propagation method based on scattering operators", *IEEE Photon. Technol. Lett.*, vol. 13, pp. 1316-1318, Dec., 2001.
- [21] Y. Chung and N. Dagli, "Analysis of Z-invariant and Z-variant semiconductor rib waveguides by explicit finite difference beam propagation method with nonuniform mesh configuration," *IEEE J. Quantum Electron.*, vol. 27, no. 10, pp. 2296-2305, 1991.
- [22] L. Thylen, "The beam Propagation method: An analysis of its applicability," *Opt. Quantum Electron* vol. 15, pp. 433-439, 1983.
- [23] Y. Chung and N. Dagli, "Assessment of Finite Difference Beam Propagation

- Method," *IEEE J. Quantum Electron.*, vol. 26, no. 10, pp. 1335–1339, Oct. 1990.
- [24] G. R. Hadley, "Wide-angle beam propagation using Padé approximant operators", *Opt. Lett.*, vol. 17, pp. 1426-1428, 1992.
- [25] G. R. Hadley, "A multistep method for wide angle beam propagation", *Integrated Photon. Res.*, vol. ITU 15-1, pp. 387-391, 1993.
- [26] J. Yamauchi, J. Shibayama, and H. Nakano, "Modified finite difference beam propagation method on the generalized Douglas scheme or variable coefficients" *IEEE Photon. Technol. Lett.* Vol. 7, pp. 661-663, 1995.
- [27] J. Yamauchi, T. Ando, and H. Nakano, "Beam-propagation analysis of optical fibers by alternating direction implicit method" *Electron. Lett.*, vol., 27, pp. 1663-1665, 1991.
- [28] J. Yamauchi, T. Ando, and H. Nakano, "Propagating beam analysis by alternating-direction implicit finite-difference method", *Trans. IEICE Jpn.*, vol. J75-C-I, pp. 145-154, 1992 (in Japanese).
- [29] W. P. Huang, S. Chu, A. Goss, and K. Chaudhuri, "A scalar finite difference time-domain approach to guided-wave optics," *IEEE Photon. Technol. Lett.*, vol. 3, no. 6, pp. 524–526, Jun. 1991.
- [30] W. P. Huang and C. L. Xu, "Simulation of three-dimensional optical waveguides by a full-vector beam propagation method", *IEEE J. Quantum Electron.*, vol. 29, pp. 2639-2649, 1993.
- [31] M. Koshiba and Y. Tsuji, "A wide-angle finite element beam propagation method", *IEEE Photon. Technol. Lett.*, vol. 8, pp. 1208-1210, 1996.
- [32] Mitchell, A. R., and Griffiths, D. F., "The Finite Difference Method in Partial Differential Equations", John Wiley & Sons, 1980.
- [33] Goldberg, A., Schey, H. M. and Schwarz, J. L., "Computer Generated Motion Pictures of One-Dimensional Quantum-Mechanical Transmission and Reflection Phenomena", *Am. J. Phys.*, 35, 177-186, 1967.
- [34] Press, W. H., Teukolsky, S. A., Vetterling, W. T., Flannery, B. P., "The art of scientific computing: numerical recipes in FORTRAN", Cambridge Uni. Press, 1992.
- [35] M. D. Feit and J. A. Fleck, "Calculation of Dispersion in Graded-Index Multimode Fibers by a Propagating Beam Method" *Appl. Opt.*, vol. 18, pp. 2843-2851, 1979.

- [36] M. D. Feit and J. A. Fleck, "Computation of Mode Properties in Optical Fiber Waveguides by a Propagating Beam Method," *Appl. Opt.*, vol. 19, pp. 1154–1164, 1980.
- [37] M. D. Feit and J. A. Fleck, "Computation of Mode Eigen functions in Graded-Index Optical Fibers by the Propagating Beam Method," *Appl. Opt.*, vol. 19, pp. 2240–2246, 1980.
- [38] M. D. Feit and J. A. Fleck, "Analysis of Rib Waveguides and Couplers by the Beam Propagation Method," *J. Opt. Soc. Am. A*, 71, pp. 73–79, 1990.
- [39] Hendew, S. T. and Shaker, S. A., "Recursive Numerical Solution for the Nonlinear Wave Propagation in Fibers and Cylindrically Symmetric System", *App. Opt.*, 1759-1764, 25, 1986.
- [40] H. M. Masoudi, "Parallel Numerical Methods for Analyzing Optical Devices with the BPM," *Ph.D Dissertation*, pp. 75–78, 1995.
- [41] Marcuse, D. *Theory of Dielectric Waveguides*, Academic Press, San Diego, 1991.
- [42] Snyder, A. W., Love, J. D., *Optical Waveguide Theory*, Chapman and Hall, London, 1983.

CHAPTER 3

THE FINITE DIFFERENCE

TIME DOMAIN METHOD

3.1 Introduction

The Finite Difference Time Domain (FDTD) [1] is one of the most powerful numerical techniques for modeling photonic devices which accounts for all aspects of optical wave behavior by virtue of direct discretization of Maxwell's equations. Originally, the scheme was created to discretize Maxwell's equations under the assumption of isotropic, non-dispersive and linear media. As the method grew in popularity and was successfully applied in scattering, diffraction, and propagation problems, many researchers devised ways that the algorithm could be applied to problems for which the device was no longer simple in structure. This chapter gives a description of the FDTD with emphasis on its application to model optical devices. The chapter shows the basic equations used for 3D and 2D of TE and TM polarizations. The chapter also discusses the implicit, the explicit and the scalar FDTD techniques reported in the literature over the years to model optical devices. The implementations of the TE polarized and the scalar FDTD to model 2-D structures are also

shown. In addition, PML implementation, as an absorbing boundary condition, is presented at the end of the chapter.

3.2 Maxwell's Equations

The time dependent Maxwell's curl equations in general form are (given in Eqs. 2.3 and 2.4)

$$\frac{\partial \mathbf{H}}{\partial t} = -\frac{1}{\mu} \begin{vmatrix} \hat{x} & \hat{y} & \hat{z} \\ \partial & \partial & \partial \\ \partial x & \partial y & \partial z \\ E_x & E_y & E_z \end{vmatrix} \quad (3.1)$$

$$\mathbf{D} = \varepsilon_0 \varepsilon_r \mathbf{E} \quad (3.2)$$

$$\frac{\partial \mathbf{D}}{\partial t} = \begin{vmatrix} \hat{x} & \hat{y} & \hat{z} \\ \partial & \partial & \partial \\ \partial x & \partial y & \partial z \\ H_x & H_y & H_z \end{vmatrix} \quad (3.3)$$

The above vector equations yield the following system of six coupled scalar equations [2]

$$\frac{\partial H_x}{\partial t} = \frac{1}{\mu} \left(\frac{\partial E_y}{\partial z} - \frac{\partial E_z}{\partial y} \right) \quad (3.4a)$$

$$\frac{\partial H_y}{\partial t} = \frac{1}{\mu} \left(\frac{\partial E_z}{\partial x} - \frac{\partial E_x}{\partial z} \right) \quad (3.4b)$$

$$\frac{\partial H_z}{\partial t} = \frac{1}{\mu} \left(\frac{\partial E_x}{\partial y} - \frac{\partial E_y}{\partial x} \right) \quad (3.4c)$$

$$\frac{\partial D_x}{\partial t} = \frac{\partial H_z}{\partial y} - \frac{\partial H_y}{\partial z} \quad (3.4d)$$

$$\frac{\partial D_y}{\partial t} = \frac{\partial H_x}{\partial z} - \frac{\partial H_z}{\partial x} \quad (3.4e)$$

$$\frac{\partial D_z}{\partial t} = \frac{\partial H_y}{\partial x} - \frac{\partial H_x}{\partial y} \quad (3.4f)$$

These coupled partial differential equations form the basis of the FDTD numerical algorithm for electromagnetic wave interactions with general three-dimensional objects. The FDTD space grid must be structured so that constitutive relation (Eq. 3.2) is implicit in the positions of E and H field vector components in the grid.

3.2.1 TE Polarized Fields

Assuming the structure being modeled extends to infinity and uniform in the y -direction. All partial derivatives with respect to y may be set to zero. Thus, the 2D equations for the TE field can be obtained from the above coupled partial differential equations for the field components E_y , D_y , H_x and H_z as

$$\frac{\partial H_x}{\partial t} = \frac{1}{\mu} \frac{\partial E_y}{\partial z} \quad (3.5a)$$

$$\frac{\partial H_z}{\partial t} = -\frac{1}{\mu} \frac{\partial E_y}{\partial x} \quad (3.5b)$$

$$\frac{\partial D_y}{\partial t} = \left(\frac{\partial H_x}{\partial z} - \frac{\partial H_z}{\partial x} \right) \quad (3.5c)$$

Eq. 3.5a, 3.5b and 3.5c can be arranged as

$$\frac{\partial \varphi}{\partial t} = ([A] + [B])\varphi \quad (3.6)$$

where

$$\varphi = [H_x \quad H_z \quad E_y]^T,$$

$$[A] = \begin{bmatrix} 0 & 0 & \frac{1}{\mu} \frac{\partial}{\partial z} \\ 0 & 0 & 0 \\ \frac{1}{\varepsilon} \frac{\partial}{\partial z} & 0 & 0 \end{bmatrix} \text{ and } [B] = \begin{bmatrix} 0 & 0 & 0 \\ 0 & 0 & -\frac{1}{\mu} \frac{\partial}{\partial x} \\ 0 & -\frac{1}{\varepsilon} \frac{\partial}{\partial x} & 0 \end{bmatrix} \quad (3.7)$$

3.2.2 TM Polarized Fields

Similarly, the equations for the field components H_y , D_x , D_z , E_x and E_z can be obtained as

$$\frac{\partial D_x}{\partial t} = -\frac{\partial H_y}{\partial z} \quad (3.8a)$$

$$\frac{\partial D_z}{\partial t} = \frac{\partial H_y}{\partial x} \quad (3.8b)$$

$$\frac{\partial H_y}{\partial t} = \frac{1}{\mu} \left(\frac{\partial E_z}{\partial x} - \frac{\partial E_x}{\partial z} \right) \quad (3.8c)$$

It can be observed that the TE and the TM fields contain no common field components and are therefore decoupled. Eq. 3.8a, 3.8b and 3.8c can also be coupled in the form

$$\frac{\partial \varphi}{\partial t} = ([A] + [B])\varphi$$

where

$$\varphi = [E_x \quad E_z \quad H_y]^T,$$

$$[A] = \begin{bmatrix} 0 & 0 & -\frac{1}{\varepsilon} \frac{\partial}{\partial z} \\ 0 & 0 & 0 \\ -\frac{1}{\mu_0} \frac{\partial}{\partial z} & 0 & 0 \end{bmatrix} \text{ and } [B] = \begin{bmatrix} 0 & 0 & 0 \\ 0 & 0 & \frac{1}{\varepsilon} \frac{\partial}{\partial x} \\ 0 & \frac{1}{\mu_0} \frac{\partial}{\partial x} & 0 \end{bmatrix} \quad (3.9)$$

It is to be noted that above mentioned formulation is applicable for non-dispersive media. For dispersive media some additional formulation has to be included. Before we show the implementation of the explicit FDTD, it is useful to show the main equations for the implicit FDTD techniques developed recently to overcome the CFL stability condition of the explicit FDTD.

3.3 The Implicit FDTD

Recently the Courant-Friedrich-Levy (CFL) condition [3] that prevents the use of large time step (Δt) in the discretization of the coupled Maxwell's equations has been overcome using the implicit FDTD. As discussed in chapter 1, the literature contains a number of implicit FDTD developed recently for this purpose. Two of the widely used implicit FDTD methods are the Alternating-Direction-Implicit (ADI) FDTD [4-9] and the Locally One-Dimensional (LOD) FDTD [10-13]. In these methods the Crank-Nicholson (CN) scheme [14-15] is applied to Eq. 3.6 which gives

$$\varphi^{n+1} = \frac{[I] + \frac{\Delta t}{2}([A] + [B])}{[I] - \frac{\Delta t}{2}([A] + [B])} \varphi^n \quad (3.10)$$

where I denotes the identity matrix and φ^n is the field at n -th time step. Eq. 3.10 is factorized as

$$\varphi^{n+1} = \frac{\left([I] + \frac{\Delta t}{2}[A]\right)\left([I] + \frac{\Delta t}{2}[B]\right)}{\left([I] - \frac{\Delta t}{2}[A]\right)\left([I] - \frac{\Delta t}{2}[B]\right)} \varphi^n \quad (3.11)$$

In the ADI-FDTD, Eq. 3.11 is solved in two steps that involve solving two explicit and four implicit equations [13]. In the LOD-FDTD scheme [14] Eq. 3.11 is also solved in two steps whereby two implicit and two explicit equations are needed. An intermediate field of $\phi^{n+1/2}$ is used in the first time step as

$$\phi^{n+1/2} = \frac{[I] + \frac{\Delta t}{2}[B]}{[I] - \frac{\Delta t}{2}[B]} \phi^n \quad (3.12)$$

Then the field at $n+1$ -th time step can be obtained using

$$\phi^{n+1} = \frac{[I] + \frac{\Delta t}{2}[A]}{[I] - \frac{\Delta t}{2}[A]} \phi^{n+1/2} \quad (3.13)$$

In both techniques described before, Eq. 3.11 is solved by two different approaches and they are unconditionally stable. However, while obtaining Eq. 3.11 from Eq. 3.10, a splitting error term $\Delta t^2 [A][B]/4$ is introduced to the main formulation. For this reason, it is observed in [11, 18] that the normalized phase velocity degrades with the increase of the time step size (Δt) as well as with the peak excitation frequency in both of these methods. Although the time step size is longer than that of the explicit FDTD, the techniques showed limitation on their accuracy as Δt is increased [17 - 18]. It is also noted that they are not suited for ultra short pulse propagation due to the splitting error term mentioned before. On the other hand, their envelope FDTD counterparts (the envelope ADI-FDTD [16] and the envelope LOD-FDTD [17]), showed a relaxation on the constraint of the time step by absorbing the fast temporal variation of the field in Eq. 3.6. Applying the time dependence

$\varphi = \phi e^{j\omega_0 t}$, where $\varphi = [H_x \ H_z \ E_y]^T$ is the slowly varying envelope (SVE) for the TE mode, in Eq. 3.6, we get,

$$\frac{\partial \phi}{\partial t} = ([A] + [B] - j\omega_0 [I])\phi \quad (3.14)$$

Similarly, in the envelope LOD-FDTD two equations, obtained from Eq. 3.12, are solved in the half time step [17]. Of the total four equations, two are solved implicitly and the remaining two are solved explicitly. In the envelope ADI-FDTD three equations, obtained from Eq. 3.12, are solved in the half step [16]. Here four implicit and two explicit equations have to be solved. Both envelope versions have lower numerical dispersion and lower computational cost than the original one. However, numerical instability is reported in both of these methods due to the accumulation of the reflection coming from the PML to the computational domain [16, 20]. The larger the time step is, the earlier the appearance of this instability and the faster it builds up. Another limitation of these methods is the creation of time harmonic spurious numerical artifacts, which are detrimental as they produce secondary radiation [21]. Due to the above limitation it was observed that the implicit techniques are not suited for ultra short pulse propagation [22]. As the purpose of the thesis is to investigate ultra short pulses (with wideband spectrum), the formulation of the explicit FDTD has been implemented in the thesis.

3.4 The Explicit FDTD

In the explicit FDTD, direct discretization of the coupled equations (Eq. 3.4) is applied. We denote any function u of space and time evaluated at a discrete point in the grid and at a discrete point in time as [2]

$$u(i \Delta x, j \Delta y, k \Delta z, n \Delta t) = u_{i,j,k}^n \quad (3.15)$$

Here, Δx , Δy , Δz , are respectively, the lattice space increments in the x , y , and z coordinate directions, and i , j , k are integers. Δt is the time interval, assumed uniform over the observation interval and n is an integer. Using these notations, the numerical approximations of Maxwell's curl equations for 2-D non-dispersive problems for TE polarized waves can be obtained from Eq. 3.5c as

$$E_y|_{i,k}^{n+1/2} = E_y|_{i,k}^{n-1/2} + \frac{\Delta t}{\epsilon_{i,k} \Delta z} \left(H_x|_{i,k+1/2}^n - H_x|_{i,k-1/2}^n \right) - \frac{\Delta t}{\epsilon_{i,k} \Delta x} \left(H_z|_{i+1/2,k}^n - H_z|_{i-1/2,k}^n \right) \quad (3.16)$$

The update of the H-fields are obtained from Eq. 3.5a and Eq. 3.5b as

$$H_x|_{i,k+1/2}^{n+1} = H_x|_{i,k+1/2}^n + \frac{\Delta t}{\mu \Delta z} \left(E_y|_{i,k+1}^{n+1/2} - E_y|_{i,k}^{n+1/2} \right) \quad (3.17)$$

$$H_z|_{i+1/2,k}^{n+1} = H_z|_{i+1/2,k}^n - \frac{\Delta t}{\mu \Delta x} \left(E_y|_{i+1,k}^{n+1/2} - E_y|_{i,k}^{n+1/2} \right) \quad (3.18)$$

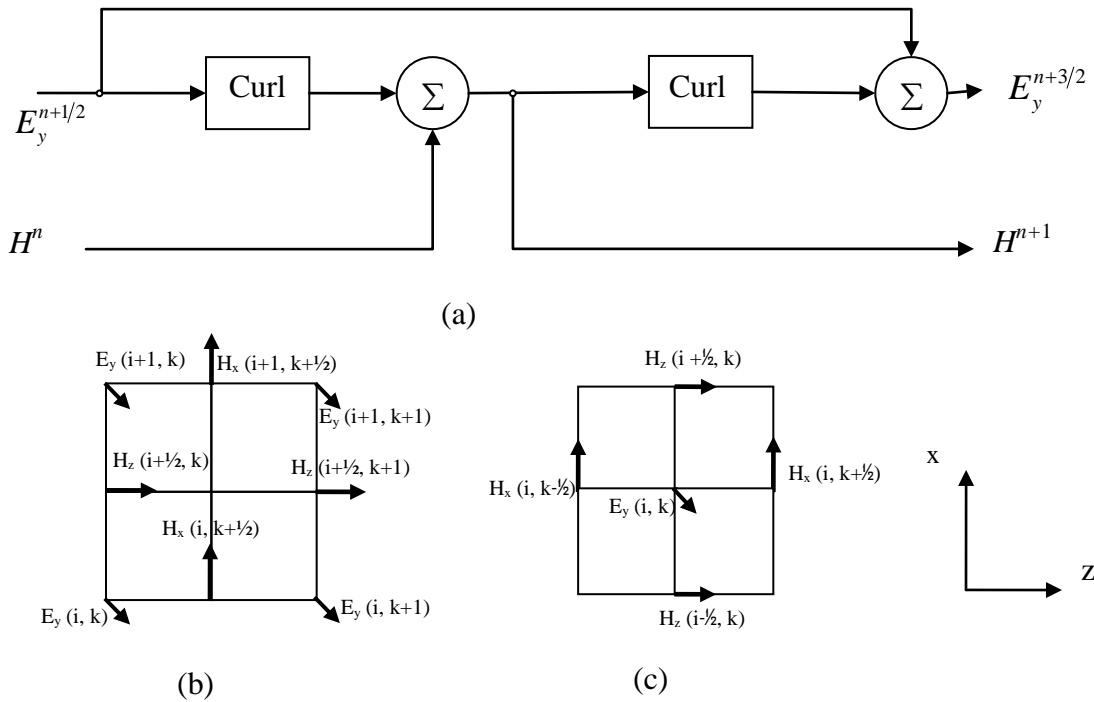


Figure 3.1 The flow chart diagram of the FDTD leap-frog integrator. Multiplicative constants have been omitted. (b) Position of the electric field vector components useful for calculating magnetic field vector components (c) Position of the magnetic field vector components useful for calculating electric field vector components.

These numerical equations are solved sequentially for a finely meshed grid structure. The implementations of the above equations are summarized in the flow chart diagram [3] of Figure 3.1. While implementing the flow diagram, the FDTD space grid must be structured so that the constitutive relation of Eq. 3.2 is implicit in the position of the E and the H field vector components in the grid, and in the numerical space-derivative operations upon these components that model the action of the curl operator.

The velocity of the numerical wave in the explicit FDTD, which is dependent on the space increments Δx , Δz and time-step Δt , is different from the actual analytical wave velocity. The difference is called the numerical dispersion error. This error increases linearly

with the wave propagation distance and with reduction of the grid-sampling density. Another restriction of this method is in the choice of the time-step size which must be bounded to ensure numerical stability. Based on the complex frequency analysis this bound is obtained as [2]

$$\Delta t < \frac{1}{c \sqrt{1/\Delta x^2 + 1/\Delta z^2}} \quad (3.19)$$

where c is the maximum velocity of light in the region of concern.

3.5 The Scalar FDTD

In the scalar FDTD [24 - 26], the amount of required memory is reduced to one third and to two third of the vector FDTD scheme for 3-D and 2-D problems, respectively. Some practical optical waveguides are weakly guiding, therefore the scalar analysis [25] is often sufficient for these applications. In this method, the transverse electric field is solved and assumed to be linearly polarized under the scalar approximations, e.g. $\vec{E}_y = \psi \hat{a}_y$. In comparison to the vector FDTD scheme which solves Maxwell's equations with three unknown field components, only one field is needed to be solved in the scalar FDTD. In this method, the scalar wave equation is solved which can be obtained for 2-D non-dispersive media from Eq. 2.11 as [25]

$$\frac{\partial^2 \psi}{\partial x^2} + \frac{\partial^2 \psi}{\partial z^2} - \frac{n^2}{c_0^2} \frac{\partial^2 \psi}{\partial t^2} = 0 \quad (3.20)$$

Using the central difference FD approximation (Eq. 2.24 of chapter 2), the field value at $t = (n + 1)\Delta t$ and the lattice point $x = i\Delta x$ and $z = k\Delta z$ is expressed explicitly by the field values of two previous time steps at the same point and neighboring lattice points. This

results in second-order accuracy in the time and space increments. The resulting discretized equation is given by

$$\begin{aligned} \psi|_{i,k}^{n+1/2} = 2 \left[1 - \frac{\delta_x^2 + \delta_z^2}{n_{i,k}^2} \right] \psi|_{i,k}^{n-1/2} - \psi|_{i,k}^{n-3/2} + \\ \frac{\delta_z^2}{n_{i,k}^2} \left(\psi|_{i,k+1}^{n-1/2} + \psi|_{i,k-1}^{n-1/2} \right) + \frac{\delta_x^2}{n_{i,k}^2} \left(\psi|_{i+1,k}^{n-1/2} + \psi|_{i-1,k}^{n-1/2} \right) \end{aligned} \quad (3.21)$$

where $\delta_x = c\Delta t/\Delta x$ and $\delta_z = c\Delta t/\Delta z$. Again the scalar FDTD computational scheme is stable if the CFL criterion given in Eq. 3.19 is satisfied.

3.6 Numerical Implementation

In this section, we show the implementation of the scalar and the vectorial FDTD techniques to study the propagation of pulsed optical beams in a slab waveguide. The 1.0 μm thick core is of *AlGaAs* having a refractive index of 2.9697 [27] and the 2.0 μm thick cladding and substrate with a refractive index of 2.706. The operating wavelength is $\lambda_c = 1.064 \mu\text{m}$. A Gaussian pulsed beam in time of the form $\psi(x, z = 0, t) = \psi_0(x) \exp(-t^2/\sigma_{t0}^2)$ is launched as the input field excited at $z = 0$ in the waveguide. Here $\psi_0(x)$ is the spatial profile in the x -direction taken as the TE_0 mode and the initial temporal waist of the Gaussian beam is $\sigma_{t0} = 20$ fs. A hard source excitation technique has been used to launch the input for both methods [28]. The source was assumed at the first numerical line of z . The temporal variation of the pulse at the middle of the waveguide ($x = 0$) at $z = 25 \mu\text{m}$ and $z = 50 \mu\text{m}$ using both the scalar and the vector FDTD is shown in Figures 3.2 (a) and 3.2 (b), respectively. A comparison between the scalar and the vector

FDTD results at these two positions are shown in Figures 3.2 (c) and 3.2 (d) by measuring the absolute difference at each time. The vectorial field is for the E_y component.

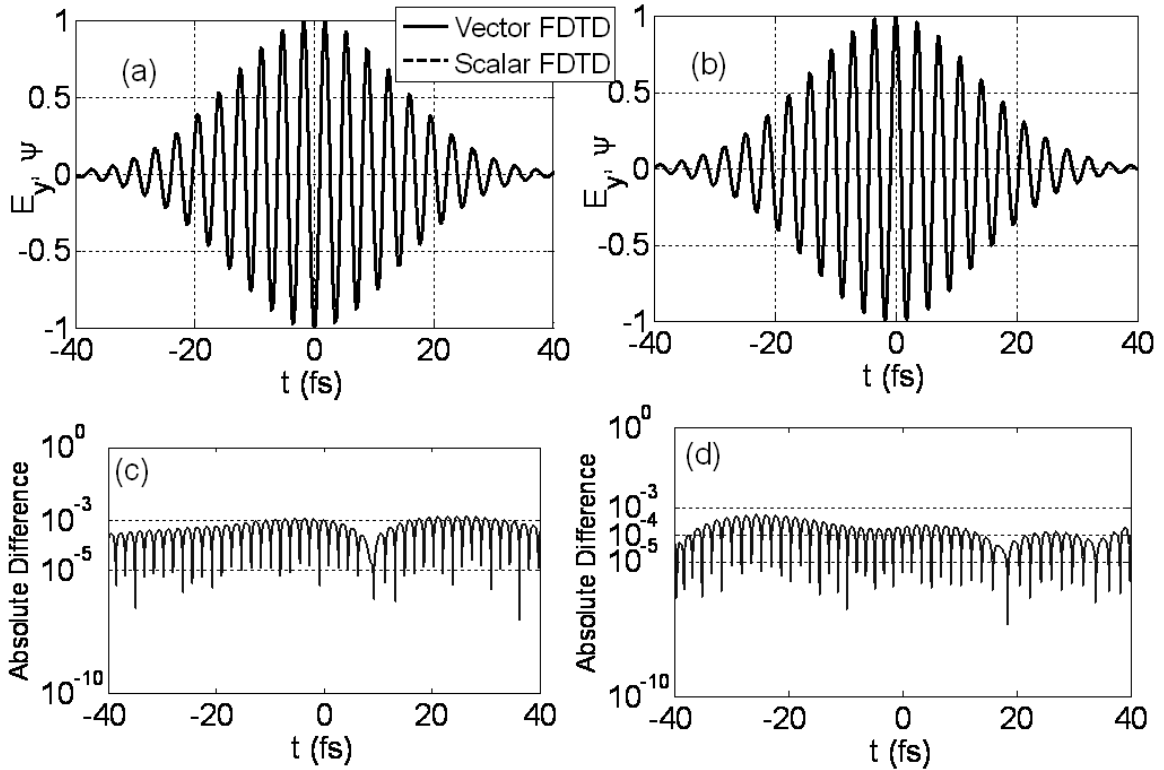


Figure 3.2 The temporal pulse of a propagated Gaussian optical pulsed beam in a slab waveguide at (a) $z = 25 \mu\text{m}$ and (b) $z = 50 \mu\text{m}$ using the scalar FDTD and the vector FDTD (c) and (d) are absolute differences between the scalar and vector fields.

The complete overlap of the pulse using these two methods at two different distances and the very small maximum error (less than 10^{-3}) shown in Figure 3.2 suggests a good agreement of these two implementations.

3.7 Perfectly Matched Layer (PML)

As discussed in chapter 2, whenever a Partial Differential Equation (PDE) numerically is solved by a meshed discretization, the computational grid must be truncated in some way, and the key question is how to perform this truncation without introducing

significant artifacts into the computation. Some problems are naturally truncated, e.g. for periodic structures where periodic boundary conditions can be applied. Some problems involve solutions that are rapidly decaying in space, so that the truncation is irrelevant as long as the computational grid is large enough. The computational window can be truncated either using Absorbing Boundary Conditions (ABC) [29] or by introducing Perfectly Matched Layers (PML) techniques [30 - 31].

The ABC tries to somehow extrapolate from the interior grid points to the edge grid point(s), to fool the solution into “thinking” that it extends forever with no boundary. Elaborately speaking, in calculating the E field, H values need to be known at the surrounding. At the edge of the problem space, even though there is no H at one side, the fields at the edge must be propagating outward. So the value at the end can be estimated by using the value next to it [29]. It turns out that this is possible to do perfectly in one dimension, where waves can only propagate in two directions ($\pm z$). However, the main interest for numerical simulation lies in two and three dimensions, and in these cases the infinite number of possible propagation directions makes the ABC problem much harder.

In 1994, Bérenger [30] proposed an absorbing boundary layer instead of finding an absorbing boundary condition. A brief derivation of Bérenger PML applicable in the optical pulse propagation in 2-D FDTD problem is described here. As discussed earlier, in the TE case, three field components are needed and these are E_y , H_x and H_z . In a PML medium, the electric field E_y component is split into two subcomponents $E_y = E_{yz} + E_{yx}$. The PML medium equations for the TE case are [29]

$$\mu \frac{\partial H_z}{\partial t} + \sigma_x^* H_z = -\frac{\partial E_y}{\partial x} = -\frac{\partial (E_{yz} + E_{yx})}{\partial x} \quad (3.22)$$

$$\mu \frac{\partial H_x}{\partial t} + \sigma_z^* H_x = \frac{\partial E_y}{\partial z} = \frac{\partial (E_{yz} + E_{yx})}{\partial z} \quad (3.23)$$

$$\varepsilon \frac{\partial E_{yz}}{\partial t} + \sigma_z E_{yz} = \frac{\partial H_x}{\partial z} \quad (3.24)$$

$$\varepsilon \frac{\partial E_{yx}}{\partial t} + \sigma_x E_{yx} = -\frac{\partial H_z}{\partial x} \quad (3.25)$$

where σ and σ^* are the electric and magnetic conductivity, respectively. It is to be noted that when $\sigma_x = \sigma_z$, then the last two equations can merge and the above equation reduces to a set of three equations involving the original three components H_z , H_x and E_y . As a result, the PML medium holds as particular cases for all the usual media. Moreover, if the condition,

$$\frac{\sigma}{\varepsilon} = \frac{\sigma^*}{\mu} \quad (3.26)$$

is satisfied, then the impedance of the PML equals that of the computational region and no reflection occurs when a plane wave propagates normally across the interface of the two region. The computational grid and the PML region are shown in the Figure 3.3.

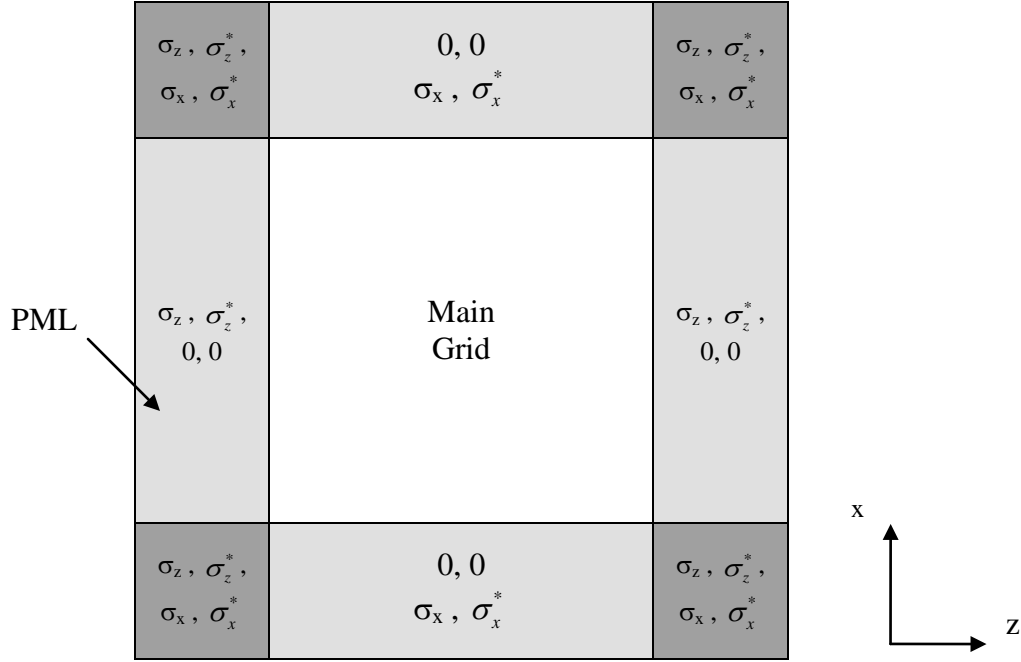


Figure 3.3 Computational main grid and the conductivities in PML region of the FDTD problem space.

It is shown in [30] that at an interface normal to z lying between two matched PML media having the same (σ_x, σ_x^*) , an optical wave is transmitted without reflection at any incidence angle and at any frequency. That is also true, if the first medium is a vacuum and the second one is a $(\sigma_z, \sigma_z^*, 0, 0)$, since a vacuum can be seen as a $(0, 0, 0, 0)$ medium. That's why some conductivities are shown zero in the PML. But at the four corners of the domain, the absorbing layers are made of PML media $(\sigma_z, \sigma_z^*, \sigma_x, \sigma_x^*)$ having the conductivities equal to those of the adjacent media of $(\sigma_z, \sigma_z^*, 0, 0)$ and $(0, 0, \sigma_x, \sigma_x^*)$.

Although it is mentioned zero reflection in the above discussion, in reality a small amount of reflection is produced which is a function of σ and the thickness δ . The thickness

δ can be as thin as needed; even can be reduced to one cell of the FDTD mesh. However, sharp variations of the conductivity create numerical reflections. So, in practical computations the layer has to be a few cells thick with conductivity increasing from zero at the inner layer interface to a value σ_m at the outer side of the layer, where its value is determined by the maximum allowable reflection coefficient $R(\theta)$ using the following expression

$$\sigma_m = -\frac{\epsilon_0 c (p+1)}{2\delta} \log(R(\theta)) \quad (3.27)$$

where p is the order and c is the velocity of light in free space. The space dependent conductivities are calculated using

$$\sigma_v(i) = \frac{1}{\Delta v} \int_{v(i)-\Delta v/2}^{v(i)+\Delta v/2} \sigma_v(v') dv' \quad ; \quad v = x, z \quad (3.28)$$

where the conductivity of a given layer, $\sigma(\rho)$, has the form of

$$\sigma(\rho) = \sigma_m \left(\frac{\rho}{\delta} \right) \quad (3.29)$$

with σ_m being the maximum value. The basic difference in the computation of the PML field components and the main grid field components lies in the evaluation of the conductivities which are absent in the main grid.

3.8 Implementation of Bérenger's PML

To test the PML implementation for the FDTD, homogeneous free space has been used for this purpose. An ultra short pulsed Gaussian beam having a spatial waist of $\sigma_{x0} = 1.0 \mu\text{m}$ and temporal waist of $\sigma_{t0} = 25 \text{ fs}$ is propagated through air using the FDTD. The

transverse width of the computational window is taken as $x = 25 \mu\text{m}$ and the longitudinal length is taken as $z = 20.0 \mu\text{m}$. For calculating the reference field, the transverse width was increased to $x = 50.0 \mu\text{m}$ such that the field does not reach the edge of the computational window. The FDTD computational grids are surrounded by PML around all side of the window, except the pulse entering side, with 8 cells on each sides and a reflection coefficient of 1.0×10^{-5} . Both the spatial and the temporal variation of the field were recorded at $z = 4, 8, 12$ and $16 \mu\text{m}$. Figure 3.4 shows the spatial pulse profile comparison among the FDTD with PML, the FDTD without PML and the reference fields at four propagation distances.

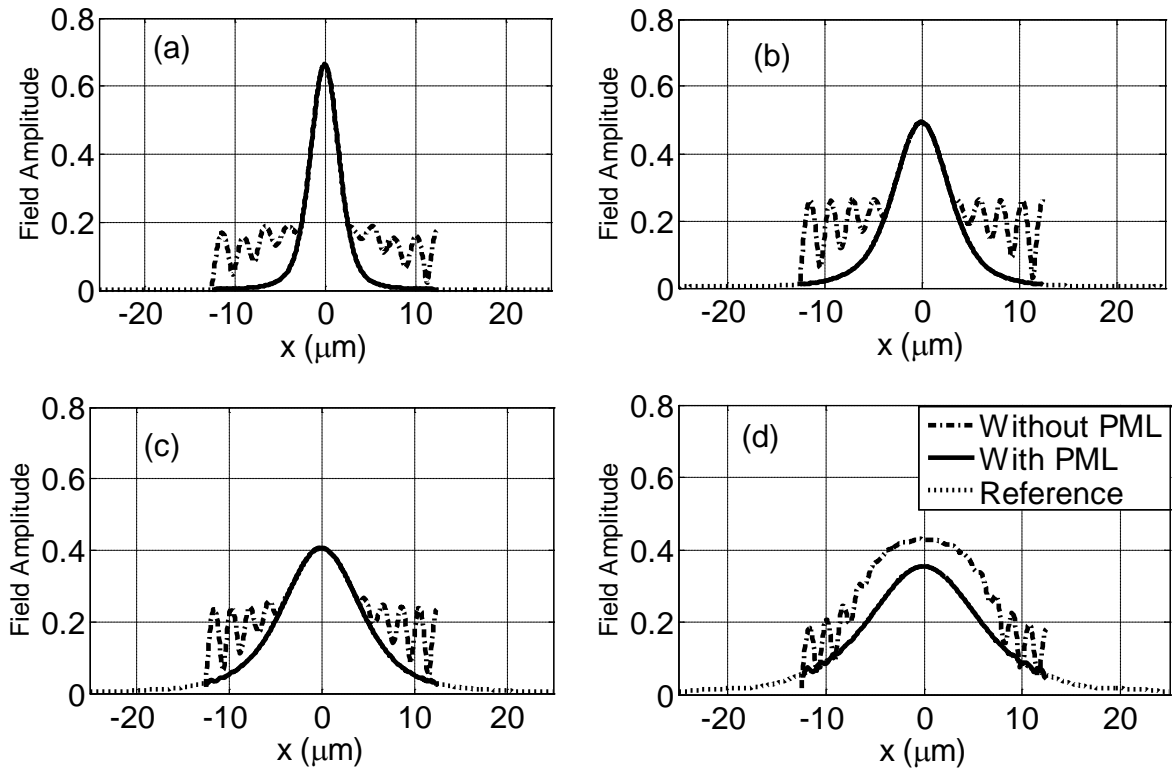


Figure 3.4 The spatial pulse profile at a) $z = 4 \mu\text{m}$ b) $z = 8 \mu\text{m}$ c) $z = 12 \mu\text{m}$ and d) $z = 16 \mu\text{m}$ in air obtained by the FDTD for using PML and for not using PML compared with the reference field.

The figure clearly shows the usefulness of the PML when used at the edge of the numerical window. The reflection from the edge of the window is clearly seen as ripple when there is no PML.

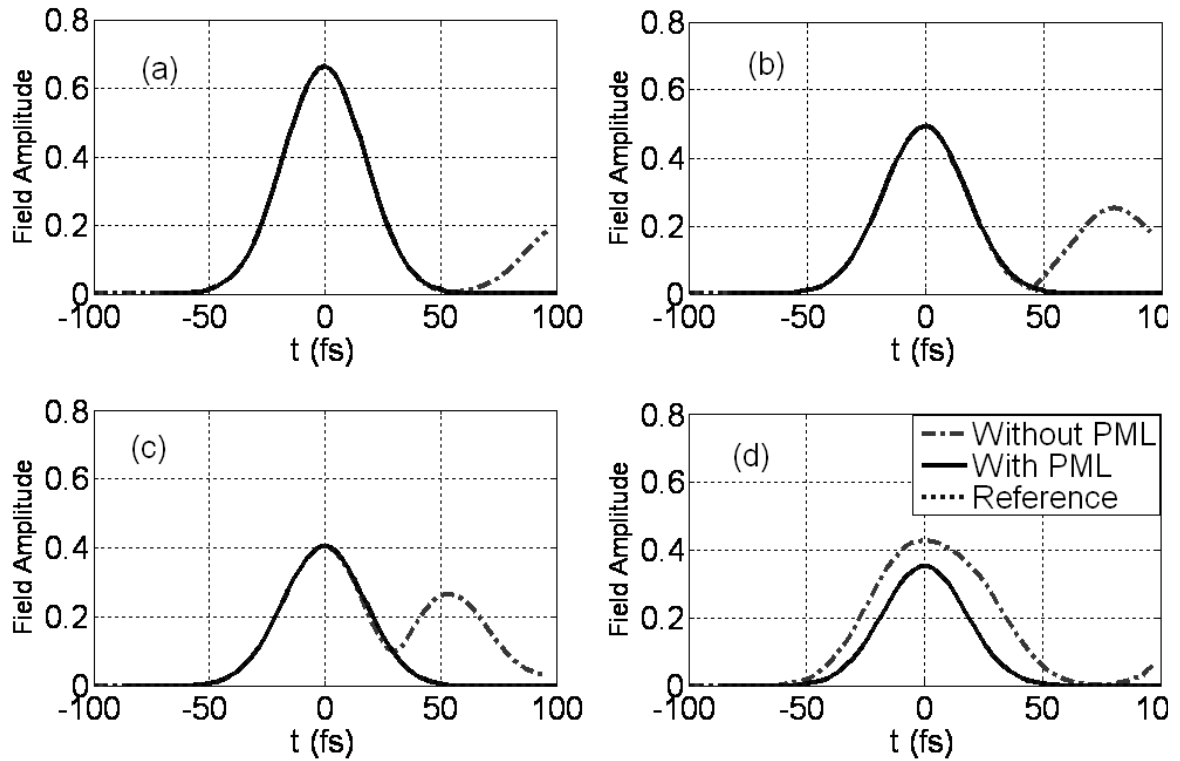


Figure 3.5 The temporal pulse profile at a) $z = 4 \mu\text{m}$ b) $z = 8 \mu\text{m}$ c) $z = 12 \mu\text{m}$ and d) $z = 16 \mu\text{m}$ in air obtained by the FDTD for using PML and for not using PML compared with the reference field.

Figure 3.5 shows the temporal pulse profile for the same distances indicated in Figure 3.4. As shown in the figure, if the PML is not employed several reflected pulses are formed along with the reference pulse, and hence it becomes difficult to distinguish the real propagated pulse from the unwanted reflected pulse.

3.9 Summary

In this chapter, mathematical formulations for the implicit FDTD have been shown along with a literature survey of recent applications and underlying challenges in modeling optical devices. Detailed mathematical formulation of two different types of explicit FDTD namely the vector FDTD and the scalar FDTD have been formulated and implemented. Ultra short pulse propagation inside a slab waveguide has been analyzed using both techniques. The results show good agreement between the techniques. The chapter also presented detailed mathematical formulation of Bérenger PML along with its numerical implementation to a homogeneous medium that demonstrates the importance of the PML.

Reference

- [1] K. S. Yee, "Numerical solution of initial boundary value problems involving Maxwell's equations in isotropic media," *IEEE Trans. Antennas Propagat.*, vol. AP-14, pp. 302–307, May 1966.
- [2] A. Taflove and S. C. Hagness, *Computational Electrodynamics: The Finite-Difference Time-Domain Method*. Norwood, MA: Artech, 2000.
- [3] R. Courant, K. Friedrichs and H. Lewy, "On the partial difference equations of mathematical physics", *IBM Journal*, pp. 215-234, English translation of the 1928 German original, March 1967.
- [4] F. Zheng, Z. Chen, and J. Zhang, "Toward the development of a three-dimensional unconditionally stable finite-difference time-domain method," *IEEE Trans. Microw. Theory Tech.*, vol. 48, no. 9, pp. 1550–1558, Sept. 2000.
- [5] S. González García, A. Rubio Bretones, R. Gómez Martín and Susan C. Hagness, "Accurate Implementation of Current Sources in the ADI-FDTD Scheme *IEEE Transaction on Antennas & Propagation*, vol. 3, pp. 141-144, 2004.
- [6] Shumin Wang, Fernando L. Teixeira, and Ji Chen, "An Iterative ADI-FDTD with Reduced Splitting Error", *IEEE Microwave & Wireless Components Letters*, vol. 15, no. 2, Feb. 2005.

- [7] Juan Chen and Jianguo Wang, "PEC Condition Implementation for the ADI-FDTD Method", *Microwave and Optical Technology Letters*, vol. 49, no. 3, pp. 526 – 530, March 2007.
- [8] Kyung-Young Jung and Fernando L. Teixeira, "Multispecies ADI-FDTD Algorithm for Nanoscale Three-Dimensional Photonic Metallic Structures", *IEEE Photonics Technology Letters*, vol. 19, no. 8, pp. 586-588, April, 2007.
- [9] T. Namiki, "3-D ADI-FDTD method—Unconditionally stable time domain algorithm for solving full vector Maxwell's equations," *IEEE Trans. Microw. Theory Tech.*, vol. 48, no. 10, pp. 1743–1748, Oct. 2000.
- [10] J. Shibayama, M. Muraki, J. Yamauchi, and H. Nakano, "Efficient implicit FDTD algorithm based on locally one- dimensional scheme," *Electron. Lett.*, vol. 41, no. 19, pp. 1046–1047, Sep. 2005.
- [11] Eng Leong Tan, "Fundamental Schemes for Efficient Unconditionally Stable Implicit Finite-Difference Time-Domain Methods", *IEEE Transactions on Antennas and Propagation*, vol. 56, no. 1, pp. 170 – 177, January 2008.
- [12] Kyung-Young Jung and F. L. Teixeira, "An Iterative Unconditionally Stable LOD-FDTD Method", *IEEE Microwave & Wireless Components Letters*, vol. 18, no. 2, pp. 76-78, Feb. 2008.
- [13] J. Shibayama, A. Nomura, R. Ando, J. Yamauchi, and H. Nakano, "A frequency dependent LOD-FDTD Method and its application to the analyses of plasmonic waveguide devices", *IEEE Journal of Quantum Electronics*, vol. 46, no. 1, pp. 40–49, January, 2010.
- [14] A. R. Mithcell and D. F. Griiths, *The Finite-Difference Method in Partial Difference Equations*, Hoboken, NJ: Wiley, 1980.
- [15] Eng Leong Tan, "Efficient Algorithms for Crank–Nicolson-Based Finite-Difference Time-Domain Methods", *IEEE Trans. Microw. Theory Tech.*, vol. 56, no. 2, pp. 408-413, Feb. 2008.
- [16] H. Rao, R. Scarmozzino, and R. M. Osgood, Jr., "An improved ADI-FDTD method and its application to photonic simulations," *IEEE Photon. Technol. Lett.*, vol. 14, no. 4, pp. 477–479, Apr. 2002.
- [17] J. Shibayama, M. Muraki, R. Takahashi, J. Yamauchi, and H. Nakano, "Performance evaluation of several implicit FDTD methods for optical waveguide analysis," *Journal of Lightwave Technology*, vol. 24, no. 6, pp. 2465–2471, Sep. 2006.
- [18] F. Zheng and Z. Chen, "Numerical dispersion analysis of the unconditionally

- stable 3-D ADI-FDTD method,” *IEEE Trans. Microw. TheoryTech.*, vol. 49, no. 5, pp. 1006–1009, May 2001.
- [19] S. Ju, H. Kim, and H.-H. Kim, “A study of the numerical dispersion relation for the 2-D ADI-FDTD method,” *IEEE Microw. Wireless Compon. Lett.*, vol. 13, no. 9, pp. 405–407, Sep. 2003.
- [20] D. Pinto, S. S. A. Obaya, "Improved complex-envelope alternating direction implicit finite difference time domain method for photonic bandgap cavities", *Journal of Lightwave Technology*, vol. 25, no. 1, January 2007.
- [21] K.Y. Jung, F. L. Teixeira, S. G. Garcia, and R. Lee, "On Numerical Artifacts of the Complex Envelope ADI-FDTD Method" *IEEE Transaction on Antennas & Propagation*, vol. 57, no. 2, pp. 491-498, Feb. 2009.
- [22] Mordechai Botton, Simon J. Cooke, Thomas M. Antonsen, Jr., Igor A. Chernyavskiy, Alexander N. Vlasov, and Baruch Levush, "Compact 3-D Envelope ADI-FDTD Algorithm for Simulations of Coherent Radiation Sources", *IEEE Transactions on Plasma Science*, vol. 38, no. 6, June 2010.
- [23] Jeffrey L. Young, Ronald O. Nelson, "A Summary and Systematic Analysis of FDTD Algorithms for Linearly Dispersive Media", *IEEE Transactions on Antennas and Propagation* Aug. 2009 Vol. 43 , no. 1, pp. 61 – 77, Feb. 2001.
- [24] S . T. Chu and S. K. Chaudhuri, "A finite-difference time-domain method for the design and analysis of guided-wave optical structures", *IEEE/OSA J. Lightwave Technol.*, vol. LT-7, pp. 2033-2038, 1989.
- [25] W. P. Huang, S. T. Chu, A. Goss, and S. K. Chaudhuri, "A scalar finite-difference time-domain approach to guided-wave optics", *IEEE Photon. Technol. Lett.*, vol. 3, pp. 524-526, June 1991.
- [26] S . T. Chu and S. K. Chaudhuri and W. P. Huang "Analysis of Optical Guided-Wave Devices with the Finite-Difference Time-Domain Method", *IEEE Antennas and Propagation International Symposium, AP-S*, pp. 257-260, 1992.
- [27] M. A. Alsunaidi, F. S. Alhajiri, and H. M. Masoudi, " A FDTD Algorithm for the analysis of Short Optical Pulse second harmonic Generation in Dispersive Medium”, *Microwave and Optical Techn. Lett.*, vol. 51, no. 4, April 2009
- [28] D. M. Sullivan, *Electromagnetic Simulation using the FDTD Method*, IEEE Press, Piscataway, NJ, 2000.
- [29] G. Mur, "Absorbing boundary conditions for the finite-difference approximation of the time domain electromagnetic field equations" *IEEE Trans. Electromagnetic Compat.* vol. 23, pp. 377-384, 1981.

- [30] J.-P. Bérenger, "A perfectly matched layer for the absorption of electromagnetic waves," *J. Comput. Phys.*, vol. 114, no. 1, pp. 185–200, 1994.
- [31] R. Holland and J. W. Williams, "Total-field versus scattered-field finite-difference codes: a comparative assessment", *IEEE Trans. Nucl. Sci.*, vol. 30, no. 6, pp. 4583 - 4588, 1983.

CHAPTER 4

THE TIME-DOMAIN

BEAM PROPAGATION METHOD

4.1 Introduction

The recent development of ultrashort powerful laser pulses increased the need to study the nonlinear effects by new modeling techniques. With such pulses the hypothesis of monochromatic waves is no longer valid, so there is a need to work in the time domain (TD). The FDTD method [1], described in the previous chapter, is a well-known technique developed and used in many applications to model both TD and CW problems. The method has evolved over the last 40 years in solving a variety of challenging problems and optical structures containing dispersive and nonlinear interaction. However, its computational cost compelled scientists and researchers to search for other methods suitable to model optical devices in the time domain. On the other hand, alternative TD techniques are also useful to investigate and verify new implementations of complicated material response such as dispersion and nonlinearities. As discussed in chapter 2 that the BPM is at present one of the most widely used method for the study of light propagation in longitudinally varying optical waveguides. In the attempts to modify the BPM [2 - 5] in time domain form, slow wave

simulators account for only the slowly time-varying envelope which is not suitable for short pulse propagation. To account for short pulse propagation using the beam propagation method a new development was observed [6] using the Fast Fourier Transform (FFT). In this approach, the spectral domain wave equation is solved using the BPM for each frequency of the pulse and the final shape is reconstructed using the inverse FFT. But this method is restricted only for linear pulse interaction. Recently, efficient TD-BPM techniques for modeling optical pulse propagation in long device interaction were proposed using the Explicit Finite Difference (EFD) [7 - 8]. They involve writing the TD wave equation as a one-way paraxial equation for the propagation along the axial direction while retaining the time variation as another element along with other spatial variables. This arrangement has the advantage of allowing the numerical time window to follow the evolution of the pulse and hence minimize the computational costs. However, due to the paraxial approximation imposed, these techniques showed limitation in modeling ultrashort pulse propagation. Recently, a new wide-angle TD-BPM technique based on finite element has been reported for modeling short pulse propagation [9]. The method was applied under certain approximation by neglecting first-order derivatives of time and longitudinal terms. Another more accurate TD-BPM based on using Padé expansion was proposed and verified [10]. The rational complex coefficient approximation based on the Padé approximant is used in this method as an operator to march the pulse packet along the direction of propagation [11 - 12]. This chapter shows the derivation of the TD-BPM operator and also shows the numerical implementation to model 2-D optical devices.

4.2 The TD-BPM Formulation

The TD wave equation for a non-dispersive medium can be extracted from Eq. 2.13 as

$$\frac{\partial}{\partial z} \left(r \frac{\partial \psi}{\partial z} \right) + \frac{\partial}{\partial x} \left(r \frac{\partial \psi}{\partial x} \right) = \frac{s}{c_0^2} \frac{\partial^2 \psi}{\partial t^2} \quad (4.1)$$

For TE fields, $r = 1$, $s = n^2$, and $\psi = E_y$ represents the electric field; for TM fields, $r = 1/n^2$, $s = 1$, and $\psi = H_y$ represents the magnetic field; c_0 is the wave velocity in free space; z is the propagation direction; and $n = n(x)$ is the position-dependent refractive-index variation. It is more convenient to extract a carrier frequency ω and a propagation factor $k = k_0 n_0$ in the direction of propagation from ψ as

$$\psi = \Psi e^{j(\omega t - k_0 n_0 z)} \quad (4.2)$$

where $k_0 = \omega/c_0$, n_0 is a reference refractive index. The removal of the fast carrier allows one to track a slowly varying envelope of a pulsed wave directly in the time domain and thus, the converged solution could be obtained with moderate time step size [13 - 14]. After substitution, Eq. 4.1 can be written in terms of Ψ for the TE case as

$$\frac{\partial^2 \Psi}{\partial z^2} - 2jk_0 n_0 \frac{\partial \Psi}{\partial z} - n^2 k_0^2 \Psi + \frac{\partial^2 \Psi}{\partial x^2} - \frac{n^2}{c_0} \left[\frac{\partial^2}{\partial t^2} + 2j\omega k_0 \frac{\partial}{\partial t} - \omega^2 \right] \Psi = 0 \quad (4.3)$$

One of the motivating features of the TD-BPM is the application of the moving time window for efficiency purposes. A compact pulse eventually disappears from the window after a certain number of propagation steps, where it requires the computational window to be adjusted in time at each propagation step. Here, to derive the parabolic TD-BPM technique [7 - 8], one can simply neglect the first term in Eq. 4.3 that has the second derivative along the direction of propagation z . On the other hand, to derive the equation for

wide-angle TD-BPM (Broadband) application, we define the pseudodifferential square-root operator L given by Eq. 4.5 as

$$\frac{\partial^2 \Psi}{\partial z^2} - 2jk_0 n_0 \frac{\partial \Psi}{\partial z} - n^2 k_0^2 \Psi + L^2 \Psi = 0 \quad (4.4)$$

where,

$$L = \sqrt{\frac{\partial^2}{\partial x^2} - \frac{n^2}{c_0} \left[\frac{\partial^2}{\partial t^2} + 2j\omega k_0 \frac{\partial}{\partial t} - \omega^2 \right]} \quad (4.5)$$

Eq. 4.4 can be factorized as

$$\left\{ \frac{\partial}{\partial z} - jk_0 n_0 [1-L] \right\} \left\{ \frac{\partial}{\partial z} - jk_0 n_0 [1+L] \right\} \Psi = 0 \quad (4.6)$$

The solution for the forward propagation of Eq. 4.6 can be written as

$$\Psi(z) = e^{-jk_0 n_0 L z} e^{jk_0 n_0 z} \Psi(0) \quad (4.7)$$

where $\Psi(0)$ is the initial field. In principle, the exponential of the square root operator in Eq. 4.7 can be computed using the same way as it was done in Eq. 2.33 of chapter 2 using the MoL approach, but the inversion of the matrix is limited by the size of the matrix. Some inversion techniques may provide reasonable numerical solution along with this approach. Another alternative way is the use of Padé approximant technique to approximate the operator in Eq. 4.7.

To make the TD-BPM efficient, arrangement of the operator is necessary in a proper way. First the use of the central FD approximation to replace partial derivatives in Eq. 4.5, one may write the operator in a discrete form. When the initial field is arranged in column vector, then the matrix operator will be a sparse matrix of the form shown in Eq. 4.8.

$$L^2 = \begin{bmatrix} S_t & S_d & & & \\ S_d & S_t & S_d & 0 & \\ & \ddots & \ddots & \ddots & \\ & & 0 & S_d & S_t & S_d \\ & & & & S_d & S_t \end{bmatrix} \quad (4.8)$$

where S_t and S_d are sparse tri-diagonal and sparse diagonal block matrices, respectively. The size of L is $M_x \times M_t$ by $M_x \times M_t$, where M_x and M_t are the spatial and the temporal discretization points, respectively. Each block matrix given in Eq. 4.8 can be represented by its elements as

$$S_t = \begin{bmatrix} s_0^1 & s_{+1}^1 & & & \\ s_{-1}^2 & s_0^2 & s_{+1}^2 & 0 & \\ & \ddots & \ddots & & \\ & & 0 & s_{-1}^{M_x-1} & s_0^{M_x-1} & s_{+1}^{M_x-1} \\ & & & & s_{-1}^{M_x} & s_0^{M_x} \end{bmatrix}, \quad (4.9)$$

$$S_d = \begin{bmatrix} d & & & & \\ & d & & 0 & \\ & & \ddots & & \\ & & & 0 & d \\ & & & & & d \end{bmatrix} \quad (4.10)$$

The size of S_t and S_d is M_t by M_t . The elements of the S_t and S_d block matrices can be represented as

$$s_0^i = -\frac{2}{\Delta x^2} + \frac{n_i^2}{c_0^2} \left(\frac{2}{\Delta t^2} + \omega^2 \right) \quad (4.11a)$$

$$d = 1/\Delta x^2 \quad (4.11b)$$

$$s_{-1}^i = -\frac{n_i^2}{c_0^2 \Delta t^2} - j \frac{\omega n_i^2}{c_0^2 \Delta t} \quad (4.11c)$$

and

$$s_{+1}^i = -\frac{n_i^2}{c_0^2 \Delta t^2} + j \frac{\omega n_i^2}{c_0^2 \Delta t} \quad (4.11d)$$

4.2.1 Padé Approximant

The introduction of Padé approximant in the TD-BPM enables the method to treat the propagation of ultrashort optical pulses more accurately. Padé Approximants are a particular type of rational fraction approximation to a polynomial. Any function can be approximated by its Maclaurine series expansion as

$$f(x) = \sum_{k=0}^{\infty} c_k x^k \quad (4.12)$$

where $c_k = \frac{f^{<k>(0)}}{k!}$, $f^{<k>(0)}$ is the k -th differentiation of the function at $x = 0$.

Padé proposed [13] finding the closest approximation to the sum by defining a rational fraction $P_m(x)/Q_n(x)$, with

$$P_m(x) = \sum_{k=0}^m a_k^{(m)} x^k \quad (4.13)$$

$$Q_n(x) = 1 + \sum_{k=0}^n b_k^{(n)} x^k \quad (4.14)$$

where $a_k^{(m)}$ is called Padé coefficients of order m for the numerator and $b_k^{(n)}$ is the Padé coefficients of order n for the denominator. For convenience, the order of the numerator and the denominator is assumed to be equal ($m = n$). These coefficients can be real or complex and can be obtained using the Maclaurine series coefficients of Eq. 4.12 as

$$\sum_{k=0}^{\infty} c_k x^k - \frac{P_n(x)}{Q_n(x)} = O(x^{2n+1}) \cong 0 \quad (4.15)$$

Replacing Eq. 4.13 and Eq. 4.14 in Eq. 4.15,

$$\sum_{k=0}^{\infty} c_k x^k - \frac{\sum_{k=0}^m a_k^{(n)} x^k}{1 + \sum_{k=0}^n b_k^{(n)} x^k} = 0 \quad (4.16)$$

Equating the coefficients of x^k for $k = 0, 1, 2, \dots, 2n$ the following set of equations are obtained as

$$\begin{aligned}
c_0 &= a_0 \\
c_1 + c_0 b_1 &= a_1 \\
c_2 + c_1 b_1 + c_0 b_2 &= a_2 \\
&\vdots \\
&\vdots \\
c_n + c_{n-1} b_1 + \dots + c_0 b_n &= a_n \\
c_{n+1} + c_n b_1 + \dots + c_1 b_n &= 0 \\
&\vdots \\
&\vdots \\
c_{2n} + c_{2n-1} b_1 + \dots + c_n b_n &= 0
\end{aligned} \tag{4.17}$$

The last set of n linear equations of Eq. 4.16 is solved to obtain all the b_k coefficients in the first stage. In the second stage, the obtained b_k and Maclaurine series c_k coefficients are utilized to obtain a_k coefficients. The implementation of the Padé approximants into any function minimizes the computational cost while keeping the accuracy level dependent upon the order of the Padé primes [14 - 15]. This means there remains an option to make a trade-off between the accuracy level and the computational cost depending upon the problems to be handled.

The Padé approximant operator was used efficiently in the Bi-directional BPM [16 - 18]. The evanescent field, which propagates in slowly varying or uniform sections of the device, is incorrectly treated if real Padé coefficients are used [16 - 17]. This causes degradation of accuracy and gives rise to serious instability. In contrast, complex-valued Padé approximants treat the evanescent field in a better way and achieves higher accuracy. A complex propagator is necessary using a complex reference wave number to apply the complex-valued Padé approximants [16]. However, the improper treatment of the propagating modes may develop instability and hence this technique is not applicable to the

normal propagating region. It is observed in [18] that the rotated branch cut Padé exhibits better performance than the complex coefficient Padé in approximating the propagator. In such situation a branch cut rotation of the square root function into the complex plane is given by the following equation as [11]

$$L = \gamma^{-1/2} \sqrt{1 + (\gamma L^2 - 1)} = \gamma^{-1/2} \sqrt{1 + X} \quad (4.18)$$

where $X = \gamma L^2 - 1$. The complex factor γ can be written in the form $\gamma = \alpha e^{j\theta}$ where α is the magnitude and θ is the angle of γ . When $\theta \neq 0$, the factor γ causes the branch cut of the square root function to be rotated in the complex plane. The propagation operator can be expressed as

$$\begin{aligned} e^{-jk_0 n_0 L z} &= e^{-jk_0 n_0 \gamma^{-1/2} \sqrt{1 + (\gamma L^2 - 1)} z} \\ &= e^{-jk_0 n_0 \gamma^{-1/2} \sqrt{1 + X} z} \\ &= e^{g \sqrt{1 + X}} \end{aligned} \quad (4.19)$$

where $g = -jk_0 n_0 \gamma^{-1/2} z$. The Taylor series expansion coefficients of $e^{g \sqrt{1 + X}}$ need to be obtained and stored first, then Padé primes are calculated for different parameters. It was shown in [19] that the branch cut amplitude α and the angle θ have optimum values for which best results are obtained with even relatively low number of Padé approximants. The reported optimum values are $\alpha = (1.5k_0)^{-2}$ and $\theta = -\pi/2$.

4.2.2 The TD-BPM Operator

In order to compute the field at the next propagation step, Eq. 4.7 is used to do this. The first exponential term of Eq. 4.7 can be expressed by Padé approximants as

$$e^{g\sqrt{1+X}} = \frac{\prod_{k=1}^p I + d_k^{(p)}X}{\prod_{k=1}^n I + e_k^{(n)}X} \quad (4.20)$$

So, if the field at any transverse plane is known, the field in the next transverse plane can be obtained using the above equation of repeated computation. In Eq. 4.20, the sparse matrix obtained from the numerator is multiplied with the field that results in a column vector. The column vector is then divided using MATLAB operation (left division) by the denominator and the process is repeated. In MATLAB, the matrix left division operation $x = A \backslash b$ solves the symbolic linear equations $Ax = b$, and $A \backslash b$ is roughly equivalent to $A^{-1}B$. There are basically two ways to perform the inversion of the matrix; either by using direct algorithm based on the Gaussian elimination method and its enhancements or by using iterative algorithms in order to approximate the solution by inexpensive (in terms of storage and computational time) repetitive computation. In the next section we discuss a few of such iterative solvers.

4.2.3 Iterative Methods for Sparse Systems

The term “iterative method” refers to a wide range of techniques that use successive approximations to obtain more accurate solutions to a linear system, such as $Ax = b$, at each step [20]. Iterative methods are especially useful when the matrix A is sparse. In theory, infinite number of iterations might be required to converge to exact solution. In practice,

iteration terminates when a residual $r = \|b - Ax\|$, or some other measure of error, is as small as desired. There are several iterative methods, such as, Jacobi, Gauss-Seidel (GS), Successive Over Relaxation (SOR), Conjugate Gradient (CG) methods [20 - 21] and others. In each of these methods the matrix needs to be of a special type. As for example, Jacobi requires strict diagonal dominant elements and its convergence is very slow. GS requires the matrix to be symmetric positive definite. SOR and CG is not directly applicable to nonsymmetric or indefinite systems. However, CG can be generalized to nonsymmetric systems by sacrificing one of the key features of this method of short recurrence and minimum error. Nevertheless, several generalizations have been developed for solving nonsymmetric systems, including Generalized Minimal Residual Method (GMRES), Quasi Minimal Residual (QMR), Conjugate Gradient Stabilized (CGS), Biconjugate Gradient (BiCG), and Biconjugate Gradient Stabilized (Bi-CGSTAB). These tend to be less robust and require more storage than CG, but they can still be very useful for solving large nonsymmetric systems [20 - 21]. More detailed of the methodology of few iterative methods that are used in the TD-BPM implementation can be found in the appendix.

4.3 TD-BPM Implementation

In order to test the performance of the TD-BPM technique described earlier, we apply it to different homogeneous and waveguide optical problems of 1-D (t, z) and 2-D (t, x, z). The results from these implementations will be compared with those of the FDTD. One of the main differences between the TD-BPM and the FDTD is the initial excitation of the input. This difference remains inherent to both techniques due to their different formulations.

One has to note that the TD-BPM considers the input pulse right at $z = 0$, while the excitation of the input for the FDTD requires special techniques. In the following analysis, hard source technique at the edge of the computational window ($z = 0$) has been used. This requires the input pulse to enter gradually from $z = 0$ and to propagate toward the positive z - direction. This difference between the two initial excitations creates a difficulty in the assessment of the forthcoming results. Another important observation in the subsequent comparative results that should be noted is the extraction of the envelope of the pulse from the FDTD results. A computer program has been written to determine the position of the envelope of the pulse out of the oscillatory TD variation of the FDTD data. This technique adds a hidden accuracy concern when comparing the TD-BPM and the FDTD results. Other factors to be mentioned at this point is that most of the time the two methods use different Δt 's which may add errors to the exact position of the peak of the pulse and the rest of the envelope data extracted for the FDTD. In addition, manual shift of the pulse envelope to match each other at the peak might also contribute to the accuracy assessment.

4.3.1 Implementation: 1-D

It is to be noticed that for 1-D implementation, the second derivation with respect to x vanishes in Eq. 4.5. The remaining terms of the L operator of Eq. 4.5 are discretized using the 3-point central FD approximation. Thus, the formed tri-diagonal matrix is the same as the operator L^2 of Eq. 4.8, which can be expressed as

$$L^2 = \begin{bmatrix} d_0^1 & d_{+1}^1 & & & & \\ d_{-1}^2 & d_0^1 & d_{+1}^2 & 0 & & \\ & \ddots & \ddots & \ddots & & \\ & & 0 & d_{-1}^{M_t-1} & d_0^{M_t-1} & d_{+1}^{M_t-1} \\ & & & & d_{-1}^{M_t} & d_0^{M_t} \end{bmatrix} \quad (4.21)$$

where

$$d_0^i = \frac{n_i^2}{c_0^2} \left(\frac{2}{\Delta t^2} + \omega^2 \right) \quad (4.22a)$$

$$d_{+1}^i = -\frac{n_i^2}{c_0^2 \Delta t^2} + j \frac{\omega n_i^2}{c_0^2 \Delta t} \quad (4.22b)$$

$$d_{-1}^i = -\frac{n_i^2}{c_0^2 \Delta t^2} - j \frac{\omega n_i^2}{c_0^2 \Delta t} \quad (4.22c)$$

We consider the propagation of a pulsed optical beam having a temporal Gaussian pulse of the form $G(t) = \exp(-t^2/\sigma_{t0}^2)$ at $z = 0$, where σ_{t0} scales the duration of the initial pulse. This temporal pulse is used as initial condition in all simulations. The wavelength and the reference refractive index were chosen to be unity.

We need to compensate for the displacement of the pulse in the time window as the pulse moves forward, due to the motion of the envelope at the group velocity. There are two methods to use which allows tracking the time window movement. The first is by using the moving time window technique. Simply it is described by setting zero boundary conditions at the edges of the relative time window and moving in the absolute time enclosure with the group velocity of the pulse, such that the relative motion of the pulse in the time window is cancelled. But, in some cases the required group velocity v_g is not known prior to simulation, in which case it has to be computed from the propagation simulation process itself. In this case the second technique can be used, which is based on simple periodic boundary

conditions. The ends of the relative time window in which the pulse exiting at one side simply re-enters at the other side of the time window.

Figure 4.1 shows the propagation of a 50 fs Gaussian pulse using Padé order $p = 2$ and $\Delta t = 0.2$ fs. The pulse was allowed to propagate to a distance of $z = 100$ μm . The figure shows the evolution of the pulse at several distances for comparison purposes. Figure 4.1a shows the simulation in the case of not using “the moving time window”, while Figure 4.1b shows the same simulation in the case of moving the time window at the group velocity of the pulse. If the window is not moved at the group velocity of the pulse, then the pulse will hit the edge of the time window creating a distortion as seen in Figure 4.1a. It is to be noted that all fields of Figure 4.1b are on top of each other, and this is an expected behavior due to the absence of dispersion, thus the pulse does not change shape.

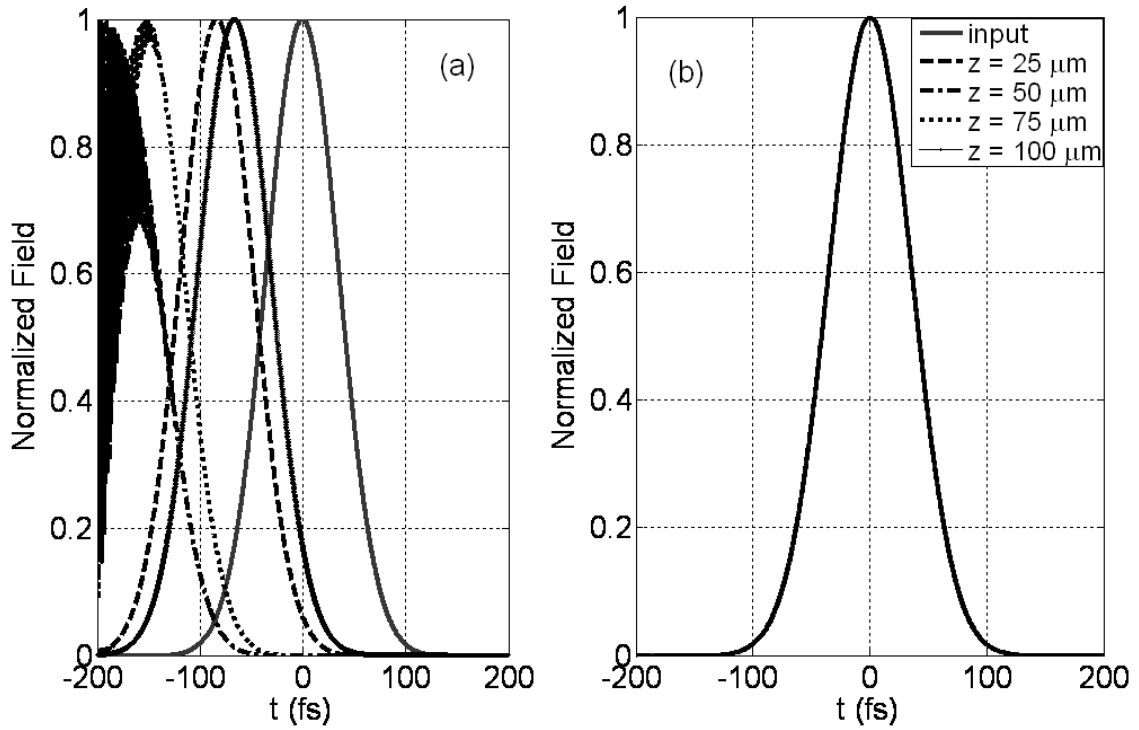


Figure 4.1 The propagation of a 50 fs Gaussian pulse in a homogenous medium using the TD-BPM over a distance of $z = 100 \mu\text{m}$ using (a) no moving time window (b) a moving time window.

Figure 4.2 shows a comparison between the TD-BPM results that appear in Figure 4.1 and the FDTD results. The FDTD parameters used are $\Delta z = \lambda/80$ and $\Delta t = \Delta z/(2c_0) = 0.021$ fs. It is noteworthy to mention that the numerical parameters of Δz and Δt of the TD-BPM are respectively 8 times and 10 times larger than those of the FDTD parameters. This is because the FDTD is restricted by the fine mesh convergence [22] and CFL time stepping criteria [23]. Figure 4.3 shows good agreement of the results obtained by these two methods.

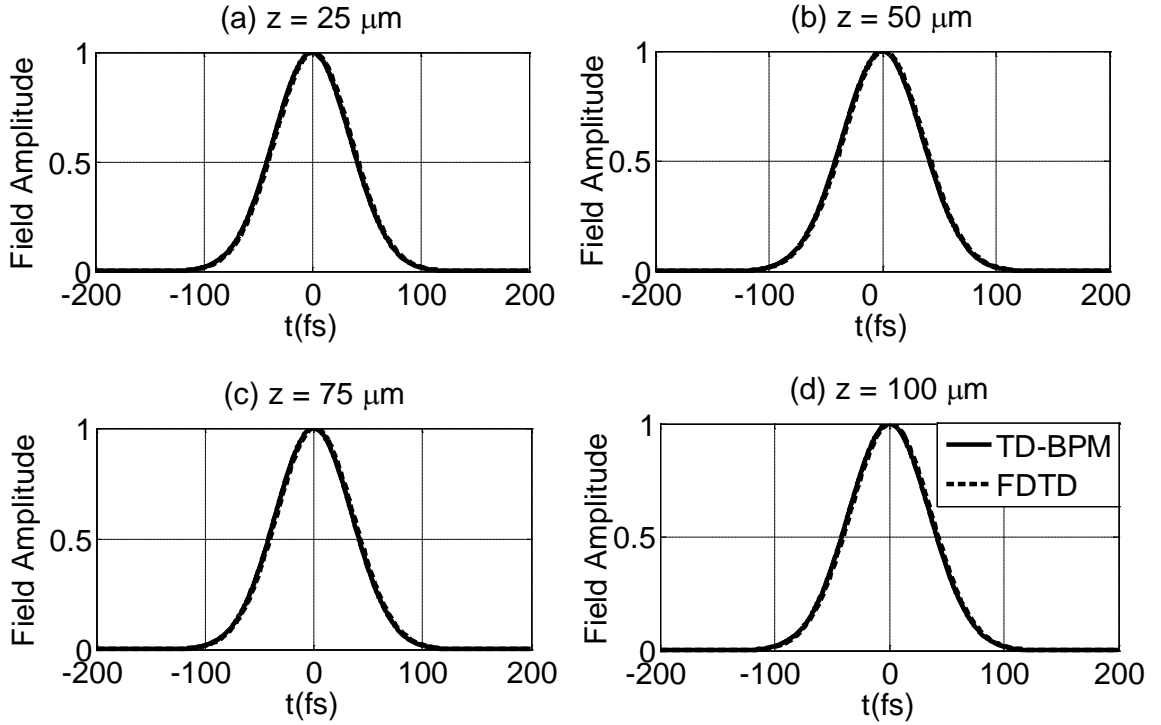


Figure 4.2 Comparison between the TD-BPM and the FDTD for the propagation of a 50 fs pulse.

4.3.2 Implementation: 2-D- Free Space

In this section, we extend the implementation of the TD-BPM to 2-D structures by considering the propagation of a pulsed optical beam in free space. The excited initial pulsed beam considered is $\Psi(x, z = 0, t) = \Psi_0(x)G(t)$, where $G(t)$ is a Gaussian pulsed profile, which is defined as $G(t) = \exp(-t^2/\sigma_{t0}^2)$, and $\Psi_0(x)$ is the transverse spatial profile of the pulsed beam again taken as a Gaussian spatial profile. The parameter σ_{t0} is the width of the initial pulsed beam time profile. We apply the TD-BPM in free space propagation with a wavelength of the carrier frequency of $\lambda_c = 1.0 \mu\text{m}$. The reference refractive index was chosen to be unity, the initial spatial waist $w_0 = 2.5 \mu\text{m}$ and the time pulse width to be $\sigma_{t0} = 50 \text{ fs}$. The pulse was propagated to a distance of $z = 25 \mu\text{m}$ using Padé order of $p = 2$,

propagation step size $\Delta z = 0.05 \mu\text{m}$, and $\Delta x = 0.1 \mu\text{m}$. In this case, the group velocity of the optical pulse $v_g = c_o$.

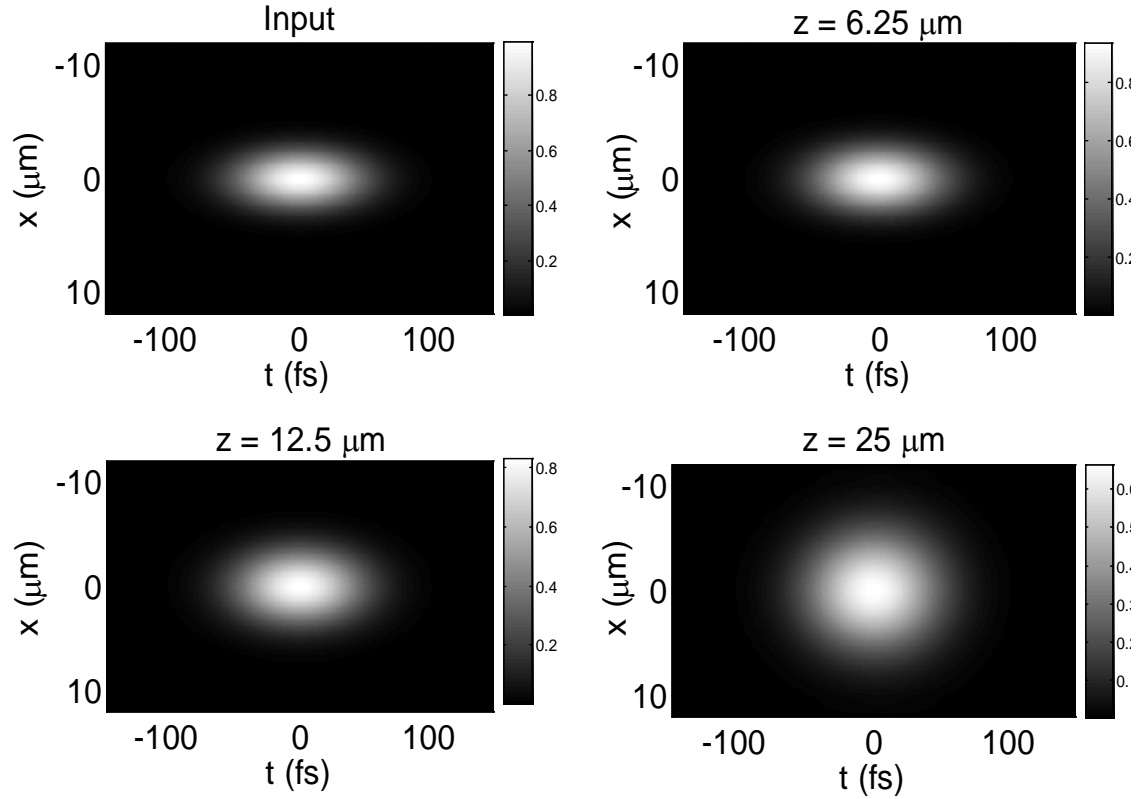


Figure 4.3 The propagation of a pulsed Gaussian beam of $\sigma_{t_0} = 50$ fs in free space using the non-paraxial TD-BPM at several distances.

Figure 4.3 shows the Gaussian pulse spreads along the x -direction while it maintains the time shape of the input due to the non-dispersive nature of the material. A moving time window has been used for the results of Figure 4.3, that is why the pulse is always seen in the middle of the window. We have also verified the results of the TD-BPM with the FDTD results. Figure 4.4 shows a comparison between the TD-BPM and the FDTD results for the diffraction of the pulse along the spatial dimension x for several longitudinal distances. The figure shows the close agreement between the results of the two techniques.

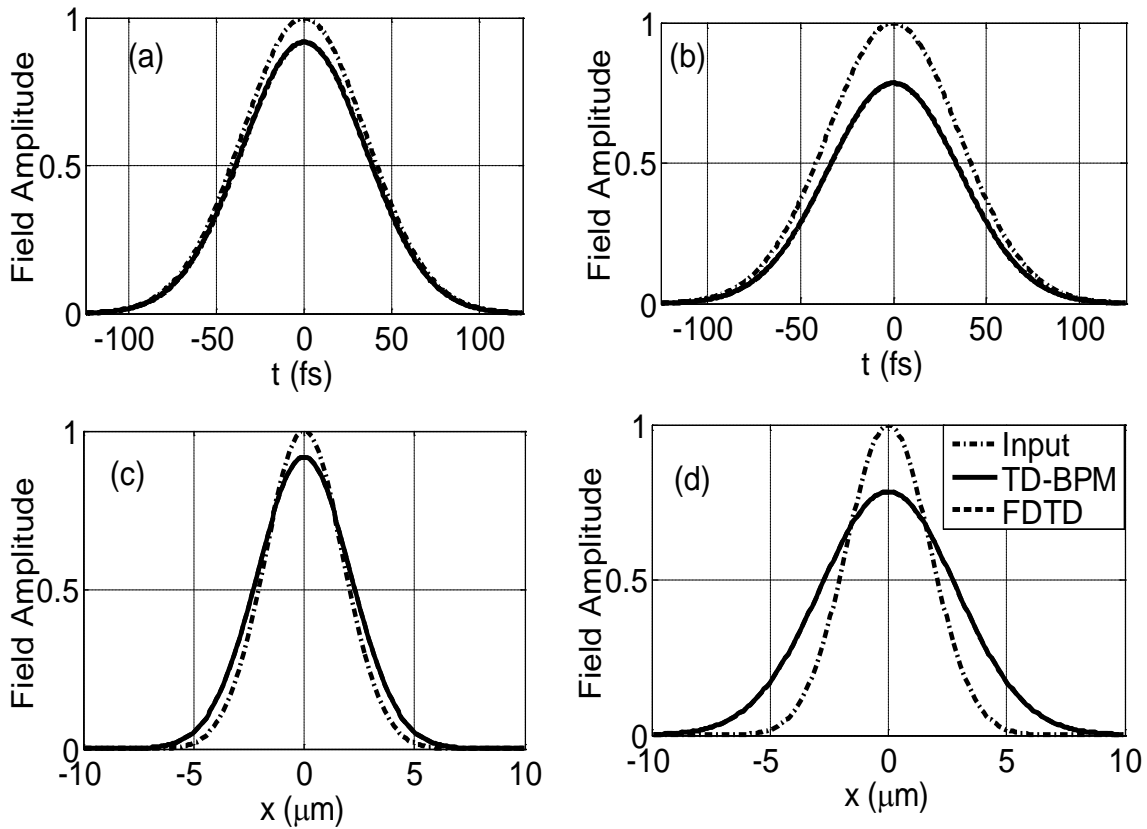


Figure 4.4 A comparison between the TD-BPM and the FDTD results for 2-D free space implementation. The figure shows the temporal profile at (a) $z = 12.5 \mu\text{m}$ and (b) $z = 25 \mu\text{m}$ and the spatial profile (c & d) of the pulse at the same distances.

4.3.3 Implementation: 2-D- Waveguide

In this section, we use the above mentioned techniques to model the propagation of pulsed optical beams in a symmetric *GaAs* slab waveguide structure. The widths of the superstrate, the guiding and the substrate of the waveguide were taken to be respectively $2.50 \mu\text{m}$, $1.0 \mu\text{m}$ and $2.50 \mu\text{m}$. The corresponding refractive indices are 3.4, 3.6 and 3.4, respectively. The wavelength of the carrier was taken as $\lambda_c = 1.55 \mu\text{m}$. The reference refractive index is the effective index of the fundamental guided TE mode which is $n_0 = 3.55984323$. The initial spatial pulse was taken as the TE₀ mode profile and the pulse

duration as $\sigma_{t0} = 50$ fs. The beam was propagated to a distance of $z = 100 \mu\text{m}$ using Padé order, $p = 2$, with a propagation step size $\Delta z = 0.10 \mu\text{m}$ and $\Delta x = 0.1 \mu\text{m}$.

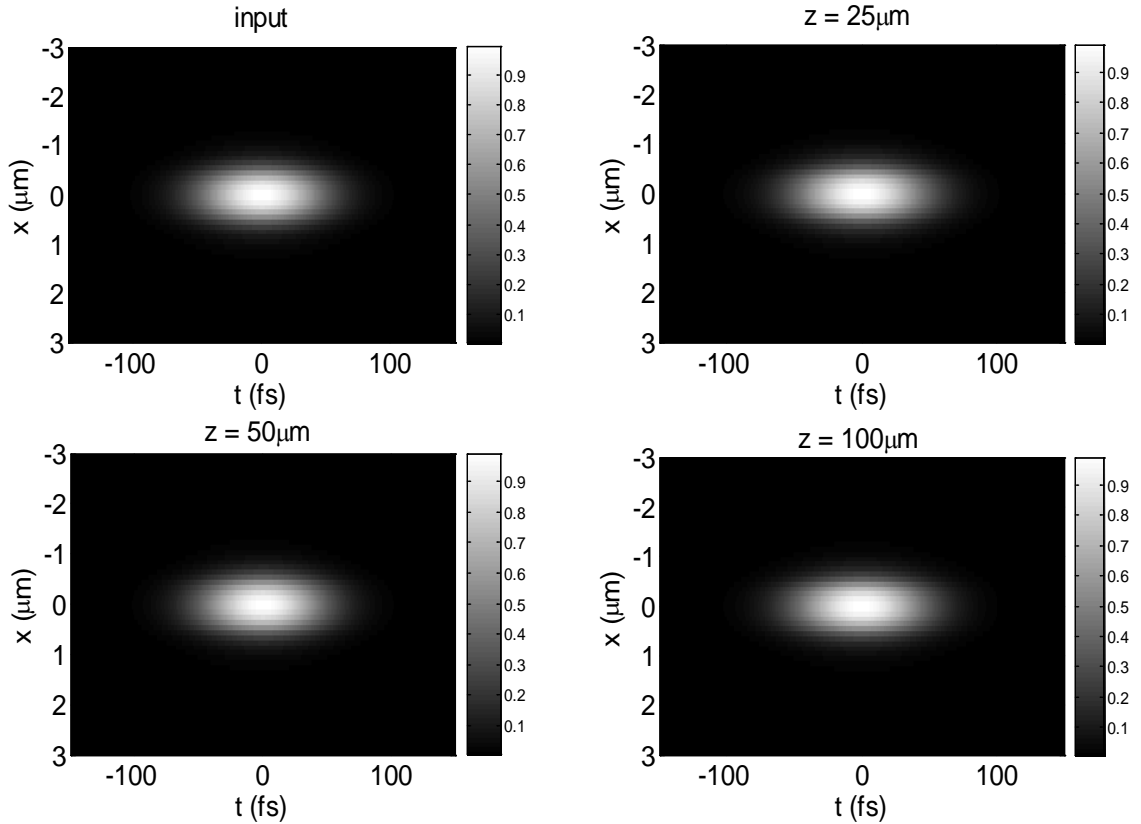


Figure 4.5 The propagation of the fundamental guided mode pulsed optical beam of $\sigma_{t0} = 50$ fs in the slab waveguide using the TD-BPM at several distances along the propagation direction.

Figure 4.5 shows the results of the propagated pulsed beam inside the waveguide at several distances using the TD-BPM. In this case, the group velocity of the optical pulse was calculated from the velocity of the moving time window and found to be $v_g = 0.278c_o$. Figure 4.6 shows that the pulsed beam maintains its spatial shape as a guided mode during propagation. Figure 4.6 shows a comparison between the TD-BPM and the FDTD results for the temporal profile right in the middle of the waveguide for propagation distances $z = 50 \mu\text{m}$ and $100 \mu\text{m}$. The figure shows the close agreement between the results of the two techniques.

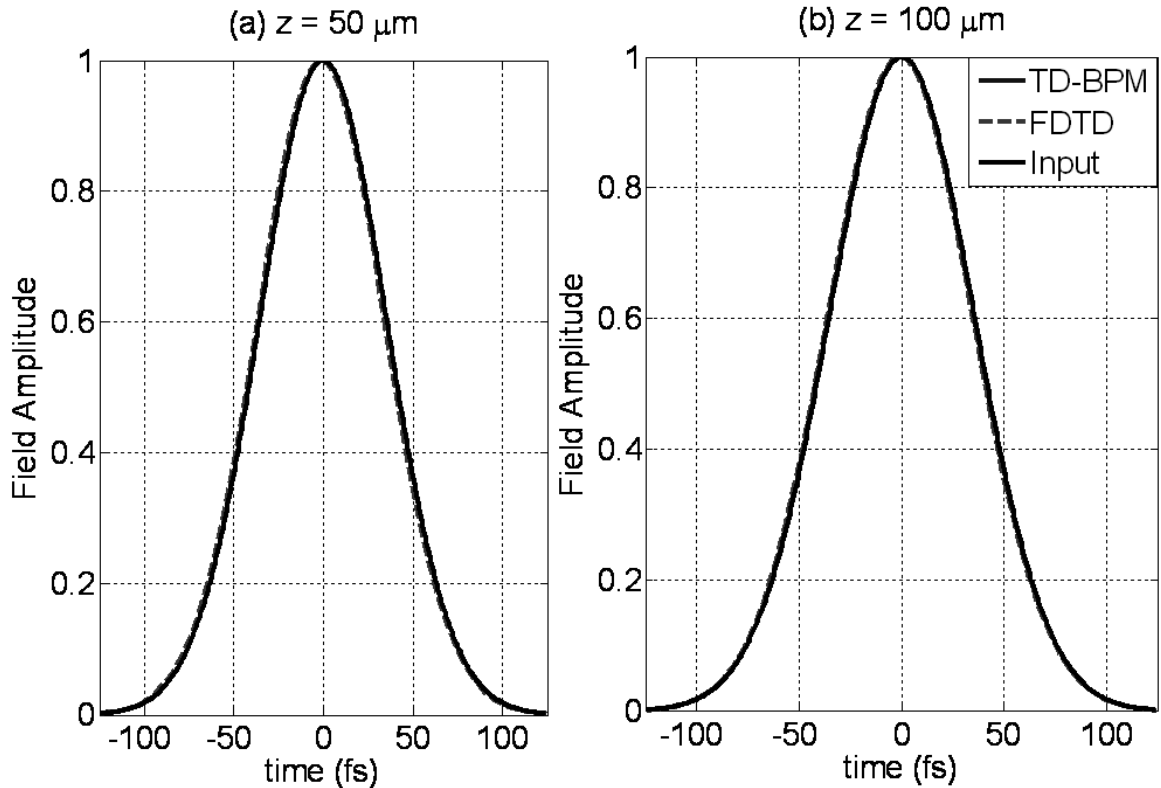


Figure 4.6 Comparison between the TD-BPM and the FDTD for the propagation of the fundamental guided mode pulsed optical beam in the slab waveguide at several distances along the propagation.

4.3.4 Performance Tests

In the previous sections, comparison between the non-paraxial TD-BPM and the FDTD was done based on graphical inspection. In this section, quantitative and detail comparison between the two methods are performed more rigorously. It is to be noted that the results of the FDTD is taken here to be a reference in all the performance tests that follows. The reason for this is that the examples used do not have closed form analytical expressions. For this purpose, the maximum percentage difference, the percentage root mean square of the difference and the percentage difference at the peak of the pulse obtained by these two methods are measured. The maximum percentage difference of the fields is measured as

$$\text{Maximum \% difference} = \text{Max} \left\langle \left| E_y^B(t) \right| - \left| E_y^F(t) \right| \right\rangle \times 100, \quad -T/2 \leq t \leq T/2 \quad (4.23)$$

where $\left| E_y^B(t) \right|$ and $\left| E_y^F(t) \right|$ are the amplitude of the temporal profile of the fields obtained by the TD-BPM and FDTD respectively, taken in the middle of the spatial window. The percentage root mean square difference is defined as [24]

$$\% \text{ r.m.s. difference} = \sqrt{\frac{1}{T} \int_{-T/2}^{T/2} \tilde{\varepsilon}^2(t) dt} \times 100 \quad (4.24)$$

where $\tilde{\varepsilon}(t) = \left| E_y^B(t) \right| - \left| E_y^F(t) \right|$ is the difference of the amplitude of the field measured by the two methods. The percentage difference in the peak is the percentage difference of the fields measured by the two methods at $t = 0$ (the peak of the pulse), which is

$$\% \text{ difference in peak} = \left(\left| E_y^B(0) \right| - \left| E_y^F(0) \right| \right) \times 100 \quad (4.25)$$

The normalized intensity at a particular position along the propagation direction with respect to the input is also measured using the TD-BPM and the FDTD. In some cases we also investigate the group velocity ratio (GVR) of the two methods. In the following, the variations of these assessment parameters with the variation of different numerical parameters for the non-paraxial TD-BPM technique are investigated.

4.3.4.1 Time Step (Δt)

In this section, a symmetric slab waveguide is considered for the following simulation comparison with similar parameters of the structure considered in section 4.3.3. The core of the slab is a non-dispersive *GaAs* with a refractive index of $n = 3.5993$ and a substrate and a superstrate of refractive index of $n = 3.4$ and $\lambda_c = 1.55 \mu\text{m}$. The substrate and superstrate are $2.5 \mu\text{m}$ thick each, while the core width is $1.0 \mu\text{m}$. The calculated effective refractive index is

$n_{eff} = 3.55845$. The parameters for the FDTD are: $\Delta z = \lambda_c/80 = 0.019375 \mu m$, $\Delta x = 0.1 \mu m$ and $\Delta t = \Delta z/(2c_0) = 0.0323$ fs. The initial pulsed beam is formed using the spatial profile of the TE_0 and the temporal pulse of the Gaussian profile with a pulse width of 25 fs. The profile of the pulse in the middle of the waveguide at a propagation distance of $z = 100 \mu m$ is recorded for a comparison between the two techniques.

Figure 4.7 shows the effect of changing the time step size Δt on the assessment parameters defined in Eqs. 4.23, 4.24 and 4.25 for the two techniques. In the TD-BPM, $\Delta z = 0.1 \mu m$ and a Padé order $p = 4$ were used, while Δx is kept the same as that of the FDTD. The figure illustrates that the choice of higher Δt gives a high percentage differences; however the TD-BPM never becomes unstable. As Δt is reduced, the percentage differences are decreased. Figure 4.8 shows the measuring parameters as a function of Δt for an initial pulse width of $\sigma_{t0} = 100$ fs. Similar observations to those of Figure 4.7 can be noted. On the other hand, comparison between the two cases show that as the initial pulse width increases, the required time steps size can be relaxed. It is to be noted that at $\Delta t = 2$ fs, the time step size of TD-BPM is around 62 times that of the FDTD step size when $\sigma_{t0} = 100$ fs and it is around 23 times when $\sigma_{t0} = 25$ fs at $\Delta t = 0.75$ fs.

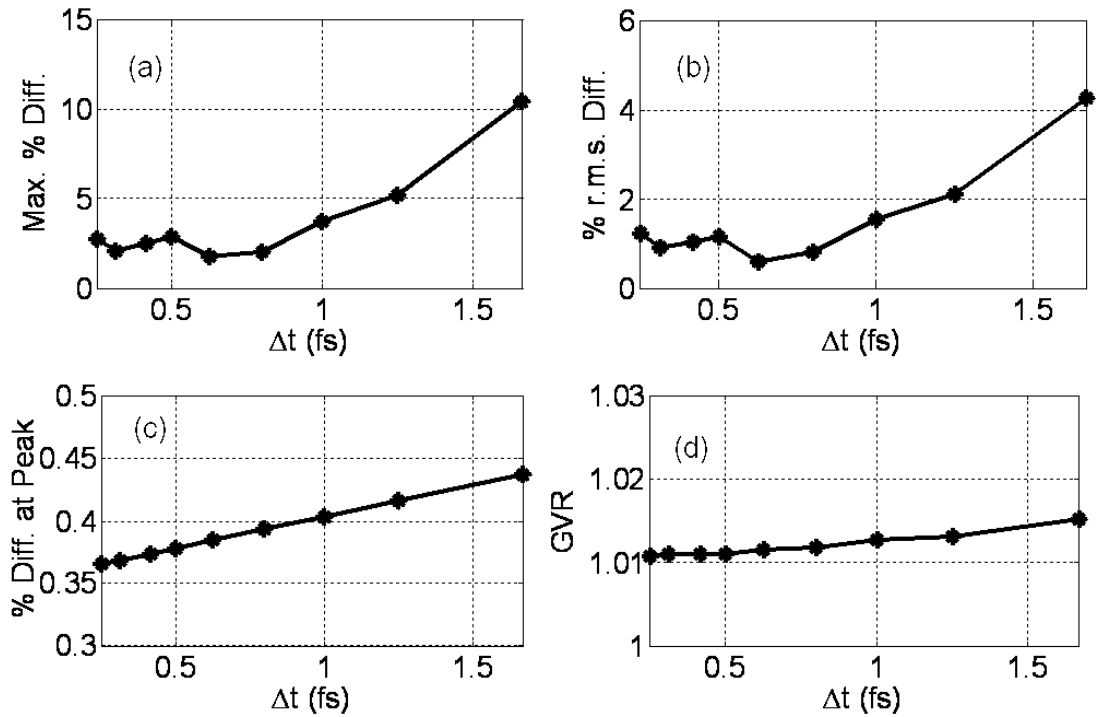


Figure 4.7 The effect of changing the time step size (Δt) on the convergence of the TD-BPM technique in comparison with the FDTD for a time pulse width of 25 fs (a) The percentage maximum difference (b) The percentage of root mean square of the difference (c) The percentage difference at peak, (d) the Group Velocity Ratio.

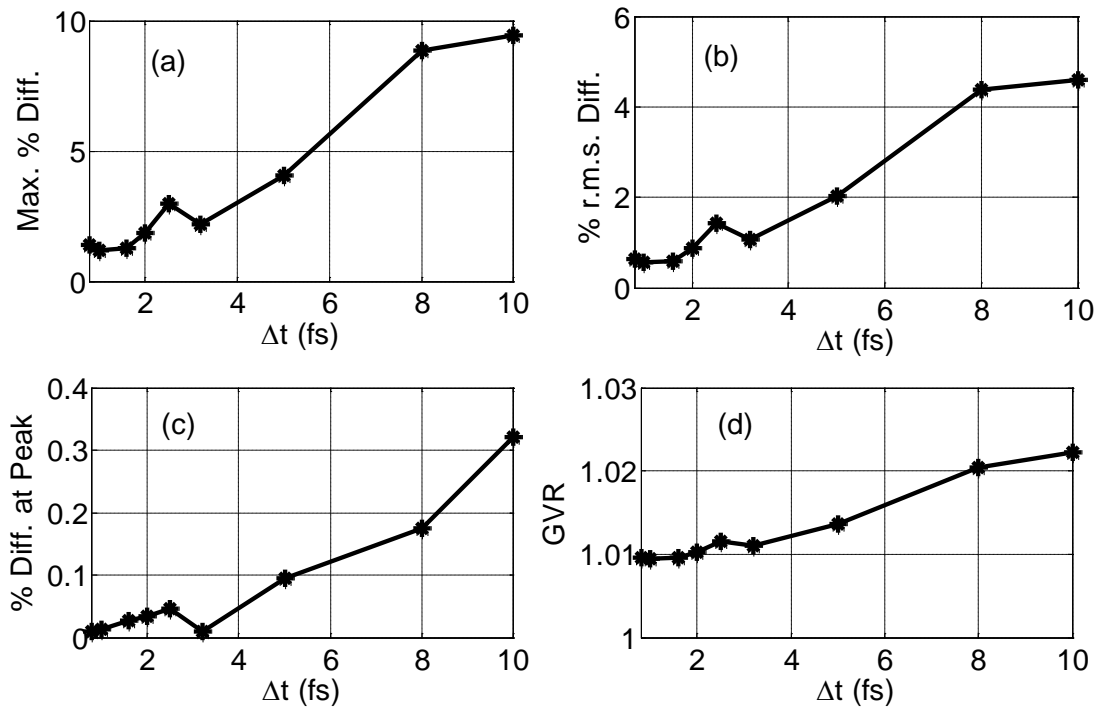


Figure 4.8 The same as of Figure 4.7 but with initial pulse width of $\sigma_{i0} = 100$ fs.

4.3.4.2 Propagation Step (Δz)

Figure 4.9 shows the effect of changing the propagation step size Δz of the TD-BPM on the percentage root mean square difference with fixed mesh size Δz of the FDTD for initial temporal pulse widths of 25 fs, 50 fs and 100 fs. In the TD-BPM, Padé order $p = 4$, and time step sizes $\Delta t = 0.4$ fs, 0.8 fs and 1.25 fs for 25 fs, 50 fs and 100 fs pulse, respectively were used; while Δx is kept the same as that of the FDTD.

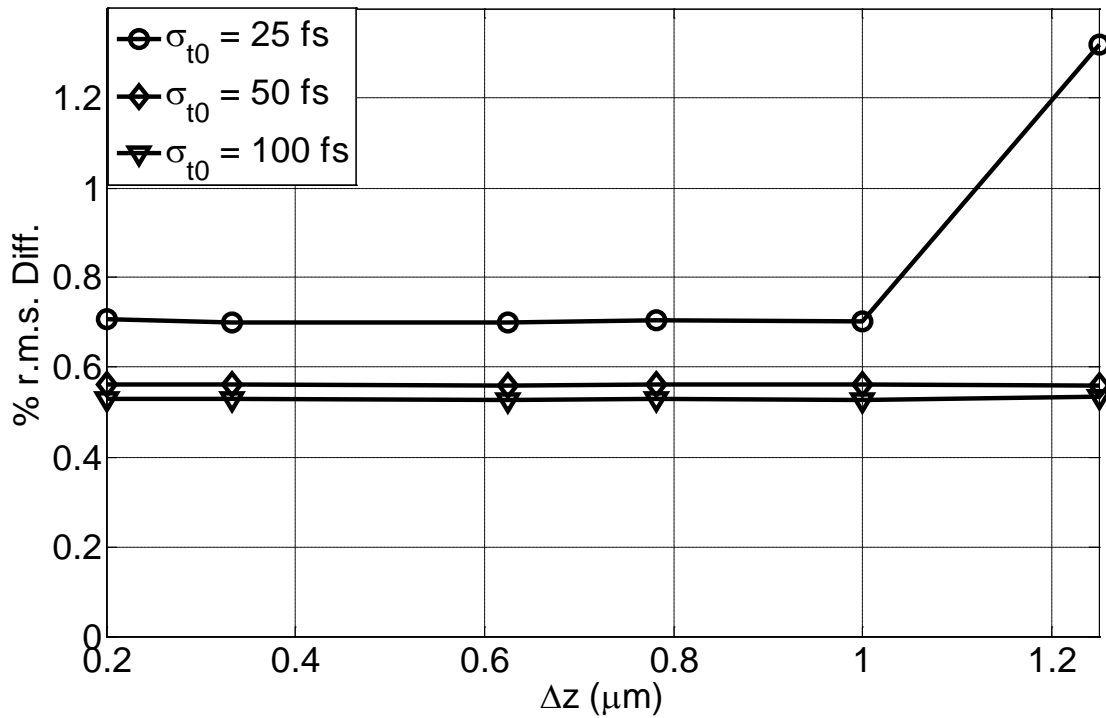


Figure 4.9 The effect of changing the propagation steps size (Δz) on the percentage root mean square difference of the technique in comparison with the FDTD for the propagation of a pulsed beam of 25 fs, 50 fs and 100 fs initial temporal waist inside a non-dispersive slab waveguide.

The figure shows that Δz can be increased to more than 64 times as those of the FDTD for an initial pulse widths of $\sigma_{t0} = 100$ fs and 50 fs, while it can be increased to 52 times for an initial pulse width of 25 fs without any change in the percentage difference.

4.3.4.3 Padé Order

Figure 4.10 shows the effect of changing the Padé order p on the percentage of root mean square difference between the two techniques for initial temporal pulse widths of 25 fs and 100 fs. In the TD-BPM, $\Delta z = 0.1 \mu\text{m}$ and time step size $\Delta t = 0.4 \text{ fs}$ and 1.25 fs for 25 fs and 100 fs pulse, respectively were used; while the other numerical parameters are kept the same as those of the FDTD.

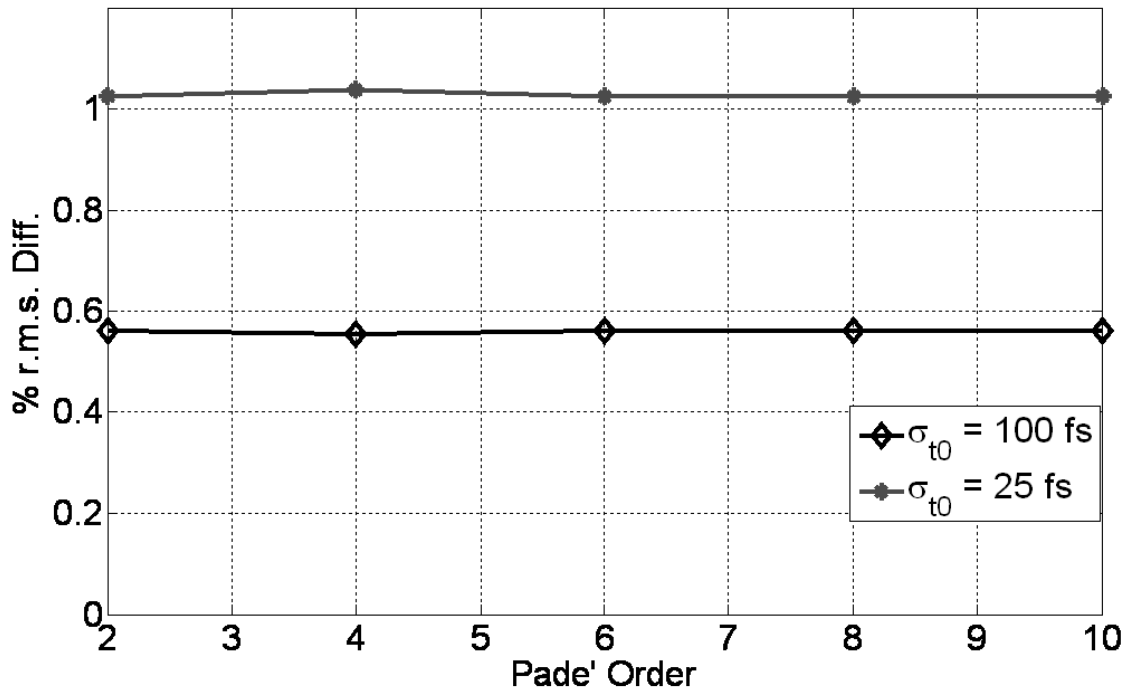


Figure 4.10 The same as of Figure 4.9 with the variation of the Padé order.

The figure shows that the percentage difference remains unchanged with the change of the Padé order p . A Padé order $p = 2$ gives the same percentage differences as higher orders. It is noted that the r.m.s. difference is reduced to 0.56% when the temporal pulse width increases to 100 fs. It is mentioned earlier that an initial pulse with 100 fs temporal-width has slower variation in comparison with the 25 fs pulse and this leads to a smaller error.

4.3.4.4 Computational Requirements

In this section, we compare the performance of the TD-BPM with the FDTD in terms of computational time and memory requirements using the implementation of the slab waveguide parameters used in the previous section. Two different cases were studied with the initial spatial pulse being the TE_0 mode and the temporal pulse of waists of $\sigma_{t0} = 25$ fs and $\sigma_{t0} = 100$ fs. The beam was propagated to a distance of $z = 100 \mu\text{m}$ using a Padé order of $p = 4$, a propagation step size of $\Delta z = 0.1 \mu\text{m}$, and $\Delta x = 0.1 \mu\text{m}$. The time steps of $\Delta t = 1.0$ fs for $\sigma_{t0} = 25$ fs and $\Delta t = 2.5$ fs for $\sigma_{t0} = 100$ fs were used. The FDTD parameters were $\Delta z = \lambda/80 = 0.019375 \mu\text{m}$ and $\Delta t = \Delta z/(2c_0) = 0.032314$ fs. It is mentioned earlier that the FDTD parameters are restricted with the fine mesh sizes and the CFL time criteria. In the TD-BPM implementations, different iterative techniques were used along with the direct method for inverting the matrices of the Padé operator described earlier. It has been noticed that all iterative solvers require almost the same computer memory space as the direct solver in the TD-BPM, but they require different computational time. The computational time taken by each algorithm depends upon the condition of the matrix. Figure 4.11 shows a comparison between the FDTD and the different solvers of the TD-BPM along the direction of propagation z for two different initial pulse-widths of 25 fs and 100 fs.

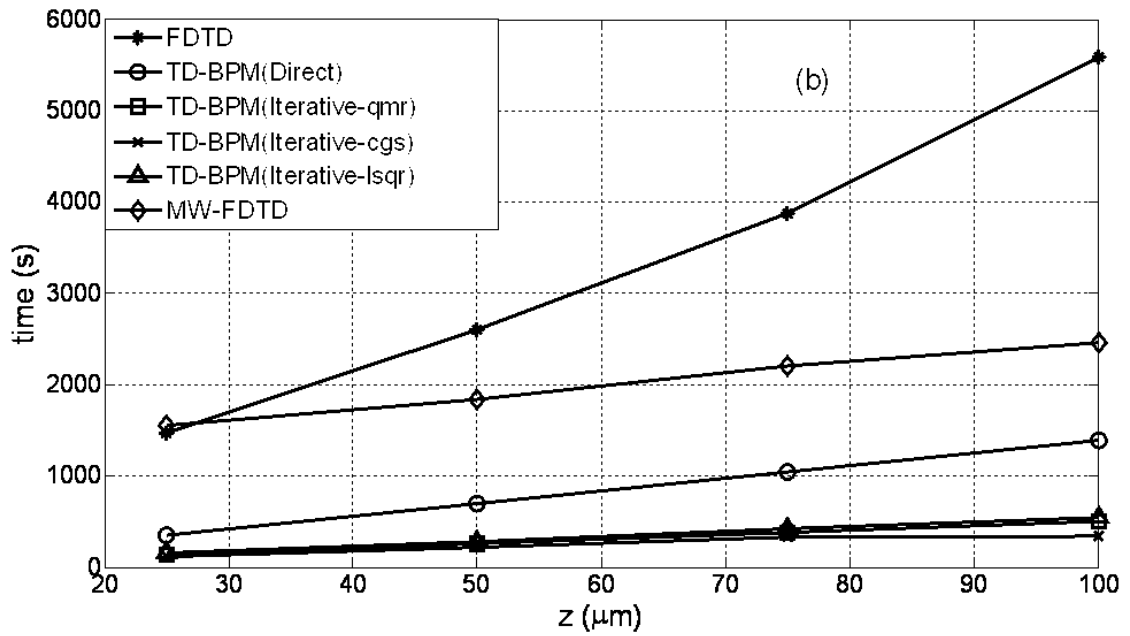
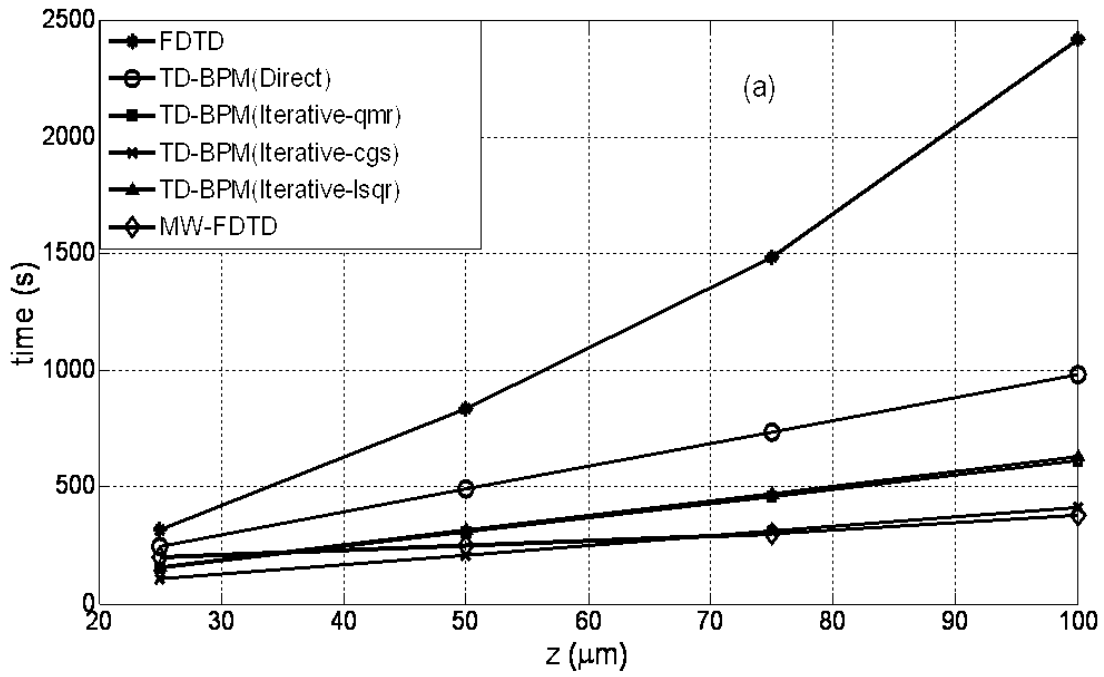


Figure 4.11 The total computational time of the FDTD and the TD-BPM using direct and iterative solvers for (a) 25 fs and (b) 100 fs pulsed beams as a function of propagation distance z .

The figure shows that the computational time in the TD-BPM methods increase linearly with the device length, while that in the FDTD changes nonlinearly with the device length. In iterative solvers the computational cost is reduced by a significant amount compared to that of the direct solver of the TD-BPM. The fastest convergence among the iterative techniques is demonstrated by the “CGS” with a speed increase factor of around 4-5 times the FDTD and double of the direct solver. Table 4.1 shows the convergence of the different iterative solvers with a default residual of 10^{-6} . The table shows that the convergence of the CGS is the fastest among the three selected iterative methods.

Table 4.1 Convergence of the Iterative Solvers of the TD-BPM operator for optical slab waveguide at minimum residual of 10^{-6} .

Iterative Methods	Number of Iteration	Residual
BICG	4	2.67×10^{-7}
BICGSTAB	2	2.84×10^{-7}
CGS	2	5.33×10^{-8}
QMR	4	2.67×10^{-7}
LSQR	3	9.022×10^{-7}
MINRES	3	2.84×10^{-7}
PCG	4	2.84×10^{-7}
SYMMLQ	3	2.84×10^{-7}
GMRES	4	2.67×10^{-7}

The results of Figure 4.11 also show that the FDTD computational time depends on the initial pulse width. As the initial width increases the required computational time increases. The figure also shows the FDTD when the spatial frame is moved with the group velocity to follow the interaction of the pulse along the z- direction [25 -26] and it is referred to here as the Moving Window FDTD (MW-FDTD). As discussed earlier that for many dielectric waveguide problems, such as the one in this example, it is difficult to know the group velocity in advance. Therefore, a dynamical numerical mechanism has been built to calculate the group velocity of the pulsed beam from the velocity of the pulse peak and then

the window was moved accordingly. It is worth mentioning at this point that the MW-FDTD faces numerical difficulty and instability in moving the spatial frame of the technique. This difficulty comes from the fast oscillation of the carrier frequency that makes the determination of the exact peak of the pulse difficult. If the exact group velocity cannot be determined, then the movement of the window gives instability during the course of propagation especially for long device interaction. The results for the MW-FDTD shown in figures 4.11 (a) and 4.11 (b) have been achieved after several numerical challenges using different techniques to stabilize the results. From Figure 4.11, one can notice that the iterative TD-BPM techniques and the MW-FDTD generally have faster computational time compared to the classical FDTD and the direct TD-BPM for 25 fs initial pulse width. The MW-FDTD has the best computational time with the iterative “cgs” TD-BPM comes next on the list. On the other hand, for 100 fs initial pulse width, the iterative techniques have similar computational time and they all have better performance with the increase of z as compared to the FDTD, the MW-FDTD and the direct TD-BPM.

Figure 4.12 shows the corresponding computer memory requirement of the FDTD, the MW-FDTD and the TD-BPM for 25 fs and 100 fs pulse beams as a function of device distance z . The figure shows that the memory requirement by the FDTD increases linearly with the size of the device, while it remains constant in the case of the TD-BPM and the MW-FDTD due to moving window concept. On the other hand, comparison between the TD-BPM and the MW-FDTD in terms of computer memory requirements shows that the TD-BPM is always superior to the MW-FDTD. For example, the MW-FDTD requires around 14 times more computer than the TD-BPM for $\sigma_{t0} = 25$ fs and around 65 times more computer

memory for $\sigma_{t0} = 100$ fs. In addition, at $z = 100 \mu\text{m}$, the TD-BPM requires around 35 and 78 times less memory than the FDTD for 25 fs and 100 fs initial pulse width, respectively.

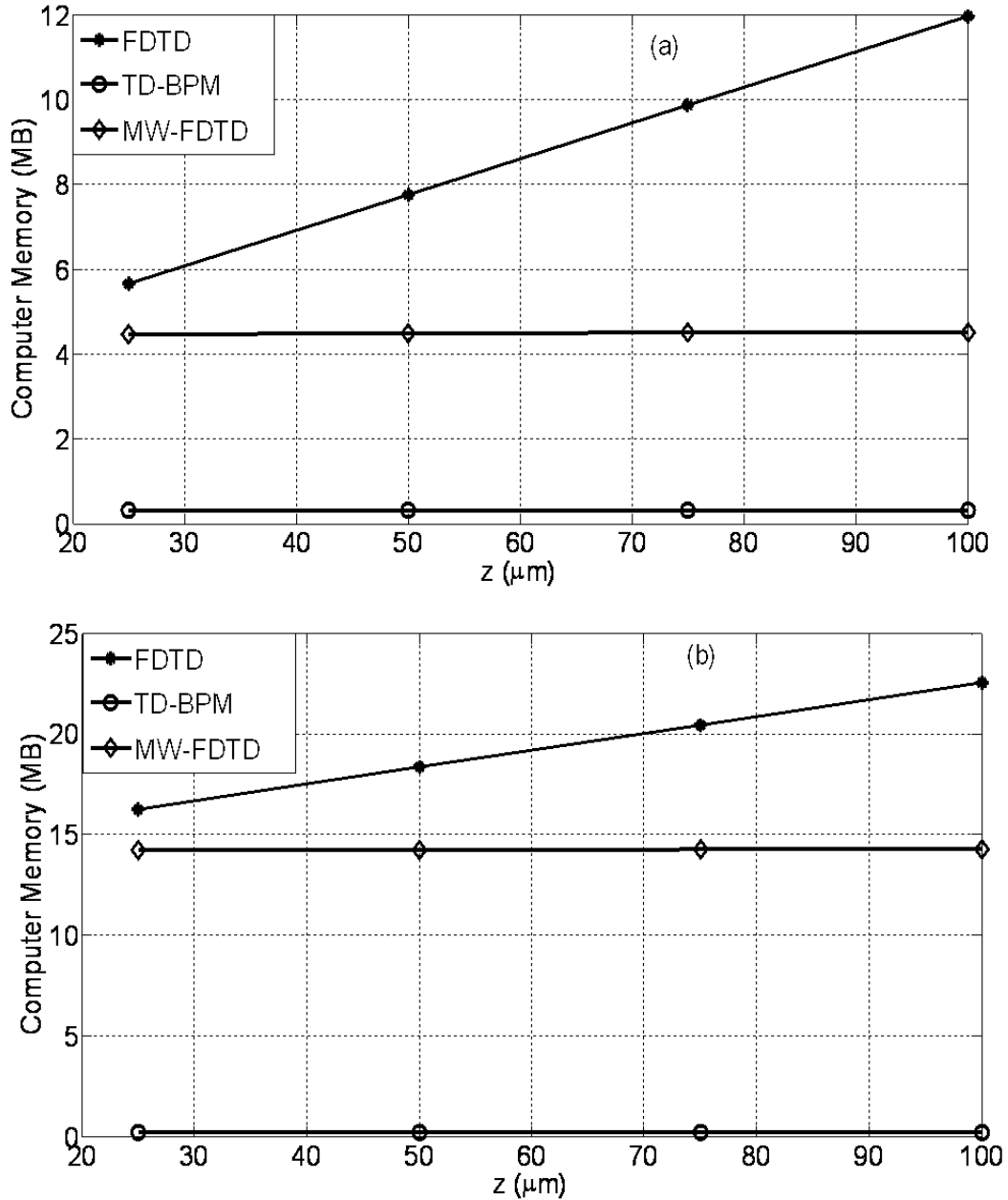


Figure 4.12 Computer memory requirement of the FDTD and the TD-BPM using direct and iterative solvers with (a) 25 fs and (b) 100fs initial pulsed beam widths.

All above implementations were performed using an Intel core i5 750, 2.67 GHz quad-core processor and 3 GB RAM.

4.4 Conclusion

In this chapter, detailed derivation of the non-paraxial TD-BPM for analyzing short and ultra short pulse propagation using Padé approximant technique and the methodology for obtaining the Padé quotient is shown. One dimensional numerical implementation has been performed using the TD-BPM, the FDTD and the MoL and their results were compared with each other. The TD-BPM has been also implemented in 2-D homogeneous medium and slab waveguide and the results have been verified with that of the FDTD. In addition, detailed performance tests were performed on the important numerical parameters of the TD-BPM and again the results were compared with the FDTD. Several iterative solvers have been tested in this technique to enhance the performance of the TD-BPM. Comparative study of the performance tests in terms of computational time and memory usage showed the TD-BPM to be very stable and accurate for various numerical parameters. The time step size and the longitudinal step size can be made several times larger than the FDTD sizes. It is also shown that using a number of iterative solvers for the solution of sparse linear systems of equations increased the convergence of the TD-BPM several folds. Therefore, it is concluded that the technique is very efficient in the analysis of short and ultra short pulse propagation in non-dispersive structures.

References

- [1] K. S. Yee, "Numerical solution of initial boundary value problems involving Maxwell's equations in isotropic media," *IEEE Trans. Antennas Propagat.*, vol. AP-14, pp. 302–307, May 1966.
- [2] R. Y. Chan and J. M. Liu, "Time-domain wave propagation in optical structure," *IEEE Photon. Technol. Lett.*, vol. 6, pp. 1001–1003, Aug. 1994.

- [3] G. H. Jin, J. Harari, J. P. Vilcot, and D. Decoster, "An improved time domain beam propagation method for integrated optics components," *IEEE Photon. Technol. Lett.*, vol. 9, pp. 348–350, Mar. 1997.
- [4] J. Zhenle, F. Junmei, and F. Enxin, "An explicit and stable time-domain method for simulation wave propagation in optical structures," *Micr. Opt. Technol. Lett.*, vol. 14, no. 4, pp. 249–252, March 1997.
- [5] F. Ma, "Slowly varying envelope simulation of optical waves in time domain with transparent and absorbing boundary conditions," *J. Lightwave. Technol.*, vol. 15, pp. 1974–1985, Oct. 1997.
- [6] L. Gomelsky and J. M. Liu, "Extension of beam propagation method to time dependent optical waveforms," *IEEE Photon. Technol. Lett.*, vol. 6, pp. 546–548, Apr. 1994.
- [7] H. M. Masoudi, M. A. AlSunaidi, and J. M. Arnold, "Efficient time-domain beam propagation method for modeling integrated optical devices," *J. Lightw. Technol.*, vol. 19, no. 5, pp. 759–771, May 2001.
- [8] H. M. Masoudi, M. A. AlSunaidi, and J. M. Arnold, "Time-domain finite-difference beam propagation method," *IEEE Photon. Technol. Lett.*, vol. 11, no. 10, pp. 1274–1276, Oct. 1999.
- [9] L. L. Bravo-Roger, K. Z. Nobrega, H. E. Hernandez-Figueroa, and A. P. Lopez-Barbero, "Spatio-temporal finite element propagator for ultrashort optical pulses," *IEEE Photon. Technol. Lett.*, vol. 16, no. 1, pp. 132–134, Jan. 2004.
- [10] H. M. Masoudi, "A Stable Time-Domain Beam Propagation Method for Modeling Ultrashort Optical Pulses" *IEEE Photonics Technology Letters*, vol. 19, No. 10, pp. 786-788, May 15, 2007.
- [11] F. A. Milinazzo, C. A. Zala, and G. H. Brooke, "Rational square-root approximations for parabolic equation algorithms," *J. Acoust. Soc. Amer.*, vol. 101, pp. 760-766, Feb. 1997.
- [12] P. L. Ho and Y. Y. Lu, "A stable bidirectional propagation method based on scattering operators," *IEEE Photon. Technol. Lett.*, vol. 13, no. 12, pp. 1316–1318, Dec. 2001.
- [13] Padé, H. "Sur la représentation approchée d'une fonction pour des fractions rationnelles", *Ann. Sci. Ecole Norm. Sup.* 16, vol. 9, pp. 1 – 93, 1892.
- [14] H. Cabannes, "Padé approximants Method and its applications to mechanics", Springer-Verlag, New York, 1976.

- [15] J. George A. Baker, "Essentials of Padé approximants." *New York: Academic Press*, 1975.
- [16] H. Rao, M. J. Steal, R. Scarmozzino, and R. M. Osgood, "Complex propagator for evanescent waves in bidirectional beam propagation method," *J. Lightw. Technol.*, vol. 18, no. 8, pp. 1155–1160, Aug. 2000.
- [17] P. L. Ho and Y. Y. Lu, "A stable bidirectional propagation method based on scattering operators," *IEEE Photon. Technol. Lett.*, vol. 13, no. 12, pp. 1316–1318, Dec. 2001.
- [18] Hua Zhang, Jianwei Mu, and Wei-Ping Huang, "Assessment of Rational Approximations for Square Root Operator in Bidirectional Beam Propagation Method" *J. Lightw. Technol.*, vol. 26, no. 5, pp. 600 - 607, March 2008.
- [19] Mohammad Ameeruddin, "Analysis of Waveguide Junctions and beam splitters using the Method of Lines with the Padé Approximants" *M.S. Thesis*, pp. 55, May 2004.
- [20] R. Barrett and M. Berry and T. F. Chan and J. Demmel and J. Donato and J. Dongarra and V. Eijkhout and R. Pozo and C. Romine and H. Van der Vorst, *Templates for the Solution of Linear Systems: Building Blocks for Iterative Methods*, 2nd Edition, SIAM, 1994.
- [21] Y. Saad, *Iterative Methods for Sparse Linear Systems*, 2nd ed., SIAM, 2003.
- [22] A. Taflove and S. C. Hagness, *Computational Electrodynamics: The Finite-Difference Time-Domain Method*. Norwood, MA: Artech, 2000.
- [23] R. Courant, K. Friedrichs and H. Lewy, "On the partial difference equations of mathematical physics", *IBM Journal*, March 1967, pp. 215-234, English translation of the 1928 German original.
- [24] Gavin P. Shorten Martin J. Burke, "The Application of Dynamic Time Warping to Measure the Accuracy of ECG Compression", *International Journal of Circuits, Systems and Signal Processing*, Issue 3, vol. 5, 2011.
- [25] Y. Pemper, R. Kastner and R. W. Ziolkowski "Hybrid Ray-FDTD Moving Coordinate Frame Approach for long range tracking of collimated", *PIER 30*, 1–32, 2001.
- [26] Y. Pemper, V. Lomakin, E. Heyman, R. Kastner and R. W. Ziolkowski, "Moving Coordinate frame FDTD analysis of long range tracking of pulsed fields in graded index waveguides", *PIER 26*, 133–164, 2000.

CHAPTER 5

MATERIAL DISPERSION MODELS

5.1 Introduction

Dispersion is a phenomenon that occurs when the phase velocity of a wave is dependent on frequency [1]. Dispersion can greatly affect short optical pulses. A short pulse is made up of a wide spectrum of frequencies all added together coherently, where each of them travels at different velocity. In a dispersive system, this gives rise to pulse spread. Pulse spread may also arise in non-dispersive material which is termed as intermodal dispersion or modal dispersion (sometimes referred to as modal distortion). Dispersion may also occur from the waveguide where it is called waveguide dispersion and this is usually weak compared to the other effects. This chapter describes the frequency response of optical material (material dispersion) and the different models usually used to approximate this behavior.

5.2 Material Dispersion

In optics, there are three sources of dispersion that arises from refraction, diffraction, and interference [2]. The first one is due to the variation of the refractive index with

frequency. The second one, diffraction, arises from the coupling of the wave vector direction and frequency that occurs at dielectric interfaces at non-normal incidence. The third has the origin in the interference of waves in periodic structures. The second and the third mechanisms can be adjusted and are usually used to counteract certain parts of the dispersion arising from materials.

There are several mathematical models that have been constructed to describe the frequency response of materials. The purpose of these models is to represent the macroscopic properties (e.g., dielectric constant) of the material with microscopic one (e.g., the atomic properties). The Debye, the Lorentz, the Cole-Cole and the Drude models are such models to represent the dielectric behavior of material within the frequency range of interest. The Debye model accounts for the dielectric relaxation and is commonly used to represent the frequency behavior of biological tissues and soil permittivities in wide frequency ranges. In Lorentz model, electrons are considered to be elastically bound with the nuclei which can be used to model non-metal and non-polar molecules, such as some optical materials and metamaterials [3]. The Cole-Cole models are better suited for some polymers, biological material and some dispersive dielectrics. The Drude model can be viewed as a special case of the Lorentz model wherever the restoring force of electrons of the atom to the nuclei is absent. Therefore, this model is useful to describe the behavior of metals at optical frequency. These models sometimes are interrelated to each other. Sometime it becomes difficult to extract the model parameters of the macroscopic dispersion relation for a material over the entire frequency range. In those cases, the parameters are frequently determined by fitting experimental data over the frequency range of interest. If the frequency range is not

too large, dispersion models with single term is enough. Otherwise, a model with multiple terms or combination of different models is sometimes necessary.

5.2.1 Debye Model

This dispersive medium model has a single pole. Derivation of the Debye model starts from the response of a dielectric to an applied DC electrical field [4]. Polarization takes time to follow the electric field. At steady state, it is given by

$$P(t) = \varepsilon_0 (\varepsilon - 1) E(t) - P_\infty e^{-t/\tau} \quad (5.1)$$

where P_∞ is the polarization in the steady state, $P(t)$ is the instantaneous polarization, and τ is the time constant. The exponential build up of the polarization provides the rate of buildup which can be expressed as

$$\frac{dP(t)}{dt} = \frac{1}{\tau} P_\infty e^{-t/\tau} \quad (5.2)$$

Replacing P_∞ from Eq. 5.2 into Eq. 5.1, we get

$$P(t) = \varepsilon_0 (\varepsilon - 1) E(t) - \tau \frac{dP(t)}{dt} \quad (5.3)$$

Taking the Fourier transform and rearranging,

$$\frac{P(\omega)}{\varepsilon_0 E(\omega)} = 1 + \chi(\omega) = \frac{\varepsilon - 1}{1 + j\omega\tau} \quad (5.4)$$

For the permittivity function to fit in the range of frequencies from zero to infinity, these conditions should be met

$$\varepsilon_r(0) = \varepsilon_s, \quad \varepsilon_r(\infty) = \varepsilon_\infty \quad (5.5)$$

where ϵ_∞ is the permittivity at infinite frequency and ϵ_s is the static permittivity at DC.

Therefore, the relation has to be modified to

$$\epsilon(\omega) = \epsilon_\infty + \frac{\epsilon_s - \epsilon_\infty}{1 - j\omega\tau} \quad (5.6)$$

where τ is the characteristic relaxation time of the medium named after the chemist Peter Debye. Dielectric relaxation refers to the relaxation response of a dielectric medium to an external electric field. Relaxation, in general, is a delay or lag in the response of a linear system, and therefore dielectric relaxation is measured relative to the expected linear steady state (equilibrium) dielectric values. In the case where the media is biological or water-based [5], [6], the dispersive debye model is of multiple relaxations of multiple species as given in the following equation

$$\epsilon(\omega) = \epsilon_\infty + \sum_{m=1}^M \frac{\epsilon_{sm} - \epsilon_\infty}{1 - j\omega\tau_m} + \frac{\sigma}{j\omega\epsilon_0} \quad (5.7)$$

Typical values of the debye model for water, methanol blood and muscle tissues are shown in Table 5.1 [7-10].

Table 5.1 Debye parameters of several dispersive materials.

Compound	ϵ_{s1}	τ_1 (ps)	ϵ_{s2}	τ_2 (ps)	ϵ_{s3}	τ_3 (ns)	ϵ_∞	σ (Sm ⁻¹)
Water	87.57	17.67	6.69	0.9	-	-	3.92	0.0
Methanol	32.5	51.5	5.91	7.09	4.9	1120	2.79	0.0
Blood	50.7	7.95	16.2	408	9835	73.5	6.5	0.7
Muscle	45.2	7.0	11.9	371	5018	66	6.5	0.2

The complex relative permittivity and the complex refractive index can be expressed in terms of their real and imaginary parts as [4]

$$\tilde{\epsilon} = \epsilon_1 + j\epsilon_2 = (n + j\kappa)^2 \quad (5.8)$$

The real part of the refractive index causes phase speed and the imaginary part indicates the amount of absorption. Equating the real and imaginary part of Eq. 5.8, the refractive index can be calculated using the following relation [4]

$$n = \sqrt{\frac{\sqrt{\epsilon_1^2 + \epsilon_2^2} + \epsilon_1}{2}} \quad (5.9)$$

The variation of the real and imaginary part of the relative permittivity and refractive index of human muscle tissue approximated by Debye model is shown in Figure 5.1.

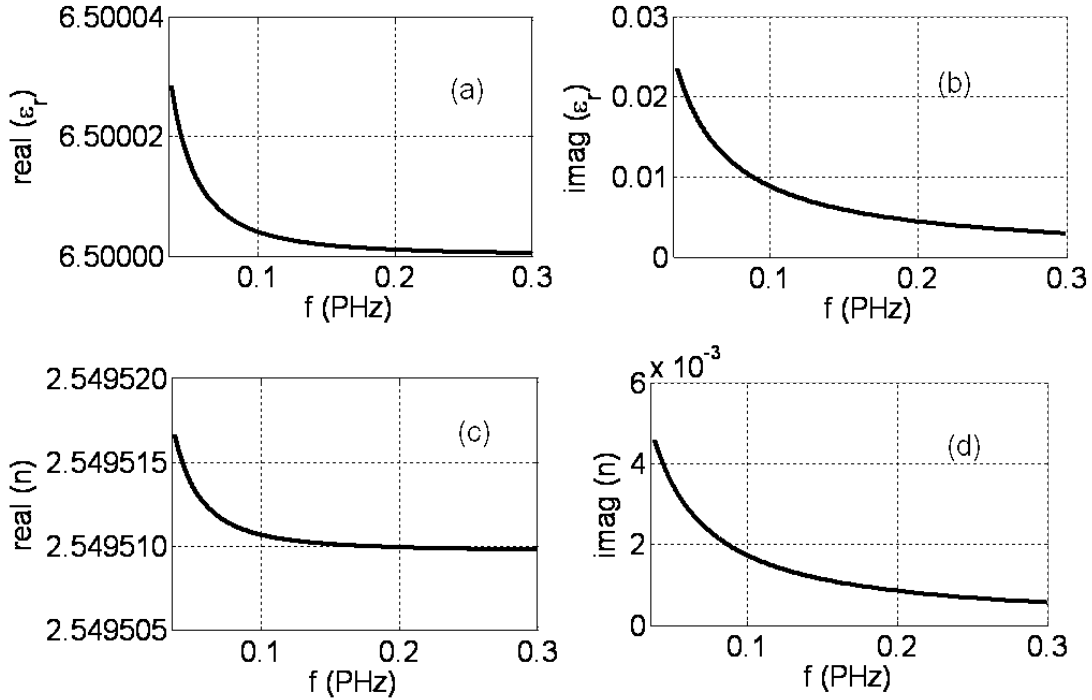


Figure 5.1 Frequency dependence of the real and imaginary part of the dielectric constant (a and b) and the same for refractive index (c and d) of human muscle tissue approximated by Debye model.

The figure shows that variation of the real part of the refractive index which causes the phase speed variation is slightly affected by the frequency variation. On the other hand,

the imaginary part of the refractive index that causes the absorption loss is highly frequency dependent.

5.2.2 Lorentz Model

The variation of the basic dipole moment of the system with the application of electric field is accounted by observing this electronic motion. Understanding this behavior leads to a model of the electric susceptibility of the medium and, hence, its permittivity. Lorentz model is based on classical mechanics and electromagnetic theory. Here the atom-field interactions are modeled by assuming an atom as a mass (the nucleus) connected to another smaller mass (the electron) by a spring as shown in Figure 5.2. In quantum mechanics viewpoint, this assumption is the dipole approximation of electron-atom interaction. Therefore, this perspective is quite valid [11].

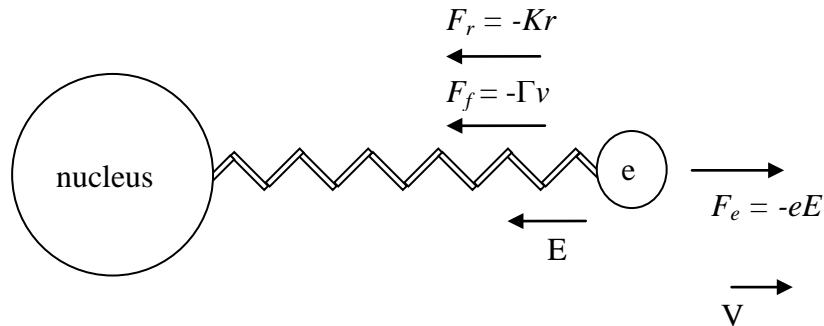


Figure 5.2 Forces affecting a free electron in Lorentz model.

The postulate that the force binding the two could be described by Hooke's Law, i.e., $\vec{F}_r = -K\vec{r} = -m\omega_0^2\vec{r}$, where K is the equivalent spring constant, \vec{r} is the displacement from equilibrium, m is the mass of electron and ω_0 is the resonant frequency. If Lorentz's system

comes into contact with an electric field, then the electron will simply be displaced from equilibrium. The oscillating electric field of the electromagnetic wave will set the electron into harmonic motion. Electrical force can be written as $\vec{F}_e = -e\vec{E}$, where e is the charge of electron and \vec{E} is the applied electric field vector. The effect of the magnetic field can be omitted because it is miniscule compared to the electric field. The possibility of damping is also considered in this model. The damping or friction loss can be written as:

$$\vec{F}_f = -m\Gamma \frac{\partial \vec{r}}{\partial t} = -m \frac{\vec{v}(t)}{\tau}, \quad \Gamma = \frac{1}{\tau},$$

where \vec{v} is the electron velocity and τ is the relaxation time of the electron. The damping or the friction loss Γ accounts for the radiation energy loss due to emission. So the faster the relaxation time, the higher is the friction loss. This damping loss also stands for the scattering or collisions, e.g. excited ions colliding with other ions in gas phase, oscillating electrons exciting vibrations in a material, etc. The binding force, the damping force and the electrical force can be related by the equation of motion as

$$m \cdot a - \vec{F}_f - \vec{F}_r = \vec{F}_e \quad (5.10)$$

where a is the acceleration of the electron. Each force can be replaced from the relations mentioned in the paragraph as

$$m \frac{\partial^2 \vec{r}(t)}{\partial t^2} + m\Gamma \frac{\partial \vec{r}(t)}{\partial t} + m\omega_0^2 \vec{r}(t) = -e\vec{E}(t) \quad (5.11)$$

Then Fourier Transform of this equation is to obtain the Fourier component at a single frequency ω

$$\left(-m\omega^2 - j\omega m\Gamma + m\omega_0^2\right) \vec{r}(\omega) = -e\vec{E}(\omega) \quad (5.12)$$

gives us the frequency dependent charge oscillation (and thus polarization). $\vec{r}(\omega)$ shows the features of the driven damped harmonic oscillator as

$$\vec{r}(\omega) = -\frac{e}{m} \frac{\vec{E}(\omega)}{(-\omega^2 - j\omega\Gamma + \omega_0^2)} \quad (5.13)$$

The attributes of this equation are as follow

1. Maximum amplitude when denominator minimum, when at $\omega \approx \omega_0$ (resonance)
2. For excitation at resonance ($\omega \approx \omega_0$) $\vec{r}(\omega)$ is entirely imaginary at resonance, 90 degree phase difference between \vec{E} and $\vec{r}(\omega)$.
3. At high frequencies ($\omega \gg \omega_0$) the amplitude $\vec{r}(\omega)$ vanishes.
4. At low frequencies ($\omega \ll \omega_0$) a finite amplitude is obtained.

Now we relate single atom displacement $\vec{r}(\omega)$ to single atom dipole moment as [4]

$$\vec{\mu}(\omega) = -e\vec{r}(\omega) \quad (5.14)$$

or

$$\vec{\mu}(\omega) = -\frac{e^2}{m} \frac{\vec{E}(\omega)}{(-\omega^2 - j\omega\Gamma + \omega_0^2)} \quad (5.15)$$

We now need to convert this single electron response to dipole moment per unit volume, P . To achieve this, the sum of dipole moment over all electrons in a volume V needs to be divided by the volume. If we have N valence electrons /m³, this gives NV electrons in volume V giving the polarization as

$$\vec{P}(\omega) = \frac{1}{V} \sum_{i=1}^{NV} \vec{\mu}_i(\omega) = N \langle \vec{\mu}(\omega) \rangle = \frac{Ne^2}{m} \frac{\vec{E}(\omega)}{(-\omega^2 - j\omega\Gamma + \omega_0^2)} \quad (5.16)$$

Susceptibility is defined as

$$\chi_e(\omega) = \frac{P(\omega)}{\varepsilon_0 E(\omega)} = \left(\frac{Ne^2}{m\varepsilon_0} \right) \frac{1}{(-\omega^2 - j\omega\Gamma + \omega_0^2)} \quad (5.17)$$

From which permittivity is given as [4]

$$\varepsilon_r = 1 + \chi_e(\omega) = 1 + \left(\frac{Ne^2}{m\varepsilon_0} \right) \frac{1}{(-\omega^2 - j\omega\Gamma + \omega_0^2)} \quad (5.18)$$

5.2.2.1 Lorentz Model of GaAs

GaAs is of particular interest for several reasons. It has a very fast turn-on time, that is, it becomes conductive almost immediately after photoexcitation. The electron mobility in GaAs is very high, about 8 times greater than that of silicon, and the lifetime of the photogenerated carriers is about 10 ns, compared to 10 ms for silicon. GaAs is extensively used in the applications of microwave integrated devices, infrared light emitting diodes, solar cells, laser diodes, optical windows [12] and THz spectroscopy (TRTS) [13].

We use the universal properties of electrons as: electron charge $e = 1.60217649 \times 10^{-19}$ C; effective mass of electron, $m_e = 9.10938188 \times 10^{-28}$ g; $\varepsilon_0 = 8.854187817 \times 10^{-12}$ and the properties of GaAs are: effective mass of each electron, $m = 0.063m_e$; at the Γ valley of conduction band of the energy band structure [14] and the relaxation time, $\tau = 1/\Gamma = 1 \times 10^{-12}$ s [15] in the Lorentz model. A rigorous study for obtaining the valence electron density is done in [14], from which it is understood that the valence electron density depends on many factors, such as, temperature, materials purity, doping profile, etc. A straight forward calculation can be done to have an approximate idea of the electron density from the atomic density of GaAs = 4.5×10^{28} atoms/m³ [14] and its valence electrons/atom = 4, as $N = 4 \times 4.5 \times 10^{28}$ electrons/m³ = 18.0×10^{28} electrons /m³. This yields the Lorentz model of GaAs as

$$\varepsilon_r = 1 + \frac{9.093164014 \times 10^{30}}{(-\omega^2 - j10^{12}\omega + \omega_0^2)} \quad (5.19)$$

To have the model to be fitted with the experimental values and to obtain the resonant frequency we use the Sellmeyer Equation [16]

$$n(\lambda) = \sqrt{A + \frac{B}{1 - C^2/\lambda^2}} \quad (5.20)$$

The empirical parameters A, B and C² are found in [16] as 8.950, 2.054 and 0.390, respectively from which resonant wavelength is at $\lambda_0 = 0.625 \mu\text{m}$. The electron concentration is adjusted to $N = 18.0 \times 10^{28.98}$ in order to obtain the resonant at that particular wavelength. This model now fits the experimental value of the refractive index of GaAs as $n = 3.5992551$ at $\lambda = 1.55 \mu\text{m}$ [17]. The variation of the real and imaginary part of the permittivity of GaAs with frequency and wavelength approximated by the Lorentz model is shown in Figure 5.3.

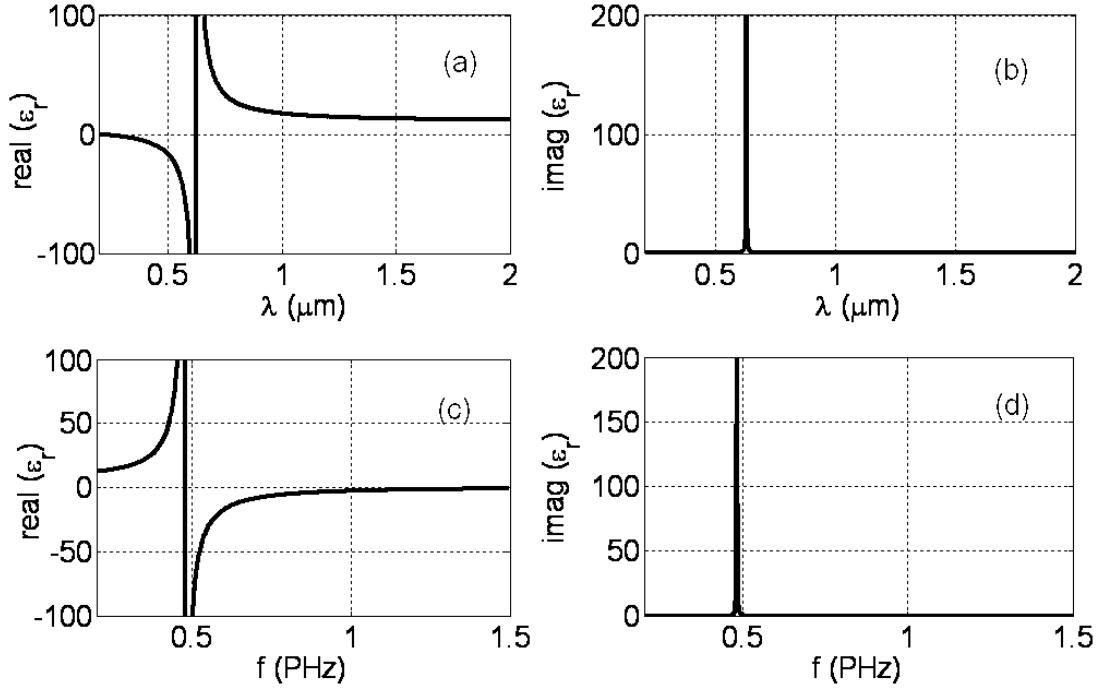


Figure 5.3 Wavelength λ dependence (a and b) and its corresponding frequency dependence (c and d) of the real and imaginary part of the relative permittivity of *GaAs* using Lorentz Model.

To fit the model over a frequency range of interest, it is found that in some cases the model needs to be composed of multispecies, as

$$\epsilon(\omega) = \epsilon_{\infty} + \sum_{i=1}^p \frac{\Delta\epsilon_i \omega_i^2}{\omega_i^2 + 2j\omega\delta_i - \omega^2} \quad (5.21)$$

where $\Delta\epsilon_i = \epsilon_{s,i} - \epsilon_{\infty}$ is the difference between static low frequency permittivity and the permittivity at the high frequency limit, $\epsilon(\infty)$, ω_i is the resonant frequency, and δ_i is the damping coefficient.

Typical values obtained from different sources used for different purposes in the thesis are given below. The Lorentz parameters obtained from the derivation of the model for *GaAs* are: $\epsilon_{\infty} = 1.0$, $\epsilon_s = 11.011$, $\omega_0 = 3.01384 \times 10^{15}$ rad/s and $\delta = 1.0 \times 10^{11}$ s⁻¹. With $\epsilon_{\infty} =$

1.5376, $\epsilon_s = 8.2944$, $\omega_0 = 0.66 \times 10^{16}$ rad/s and $\delta = 1.0 \times 10^{13}$ s⁻¹, a very good agreement is achieved with the single species for modeling *AlGaAs* [18]. In addition to these parameters and for convenient numerical testing purposes, some nonphysical parameters are sometimes used as: $\epsilon_\infty = 2.25$, $\epsilon_s = 5.25$, $\omega_0 = 4.0 \times 10^{14}$ rad/s and $\delta = 2.0 \times 10^9$ s⁻¹ to provide rapid variation in the ultra short pulse propagation over a short distance.

5.2.2.2 Ultra Short Pulses in GaAs

In optics, an ultra short pulse of light is an electromagnetic pulse whose time duration is in the order of femto second (10^{-15} s) range. Because of the progress in the generation, amplification and measurements of ultra short pulses [19], this time scale becomes accessible. Due to large energy concentration, this topic encompasses the study of interaction of intense laser with matter, as well as transient response of atoms and molecules and basic properties of the fs radiation itself [19-21]. Right after the invention of the laser in the 1960s, the scientific community was working on producing short light pulses in lasers. In the 70's progress in laser physics opened the door for pico-second pulse generation and continued in 80's to achieve femto second pulse [19]. Femto second technology opened up new fascinating possibilities based on some unique properties of ultra short light pulses which include [19 - 21]

- Energy can be concentrated in a temporal interval as short as *fs* which corresponds to a few optical cycles in the visible range.
- Pulse peak power can be extremely large even at moderate pulse energies. e.g. for 100 fs pulses an energy of 1 nJ exhibits an average power of 10 MW. Focusing this pulse to a $100 \mu\text{m}^2$ spot will generate an intensity of 20 TW/cm².

- The geometrical length of a femto second pulse amounts only to several μm . Such a coherence length is usually associated with incoherent light. The essential difference is that incoherent light is generally spread over a much longer distance.

Faster data transfer and processing is possible by utilizing this faster carrier frequency and subsequent higher bandwidths. A variety of reversible as well as irreversible nonlinear processes become accessible due to the large intensities of fs pulses. There are proposals to use such pulses for laser fusion [22]. Because of the large energy concentration in a very short duration, it is possible to utilize nonlinear processes in fiber and other optical-electronic devices.

The ultrashort pulse plays interesting roles in material dispersion of *GaAs*. As the pulse duration decreases, the frequency content increases, hence the refractive index range of variation increases. Figure 5.4 shows the refractive index of *GaAs* variation with the angular frequency for different pulse widths.

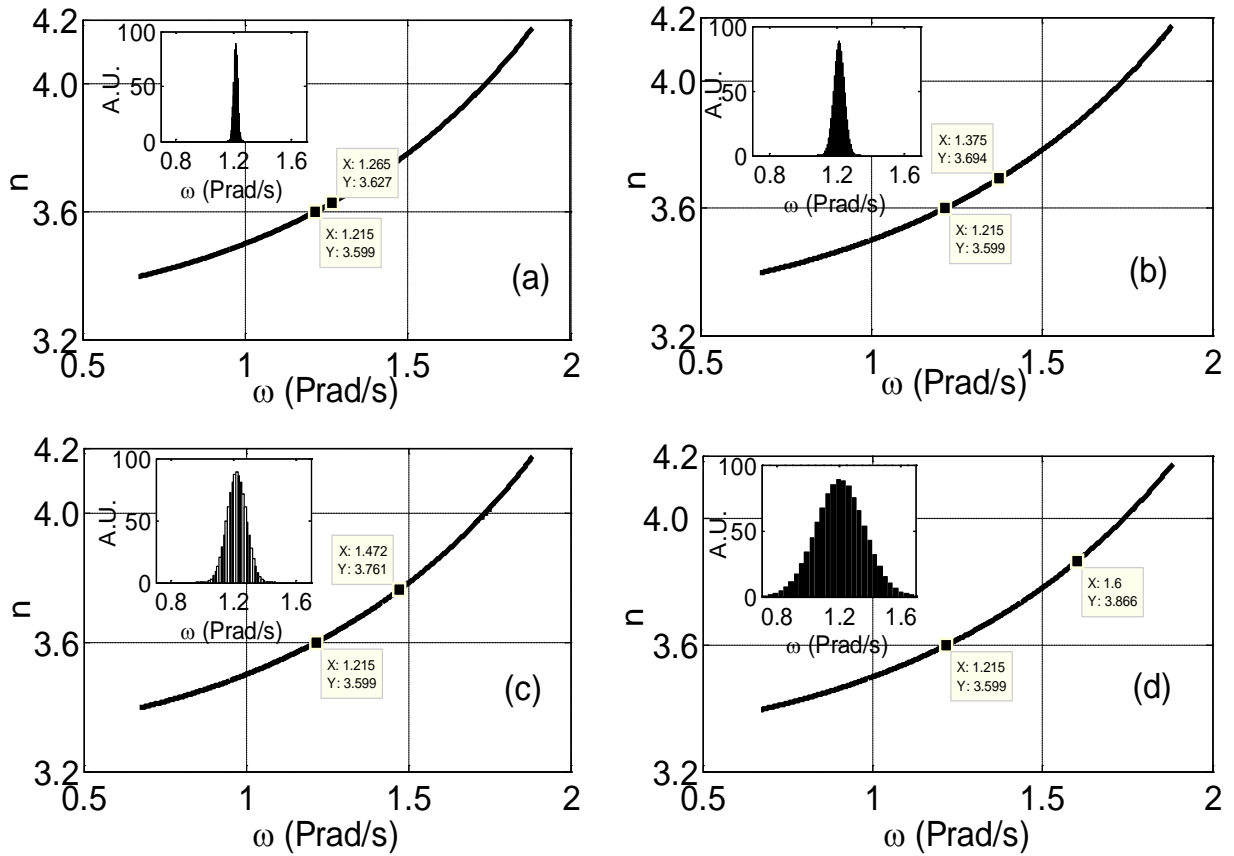


Figure 5.4 Operating refractive index of GaAs for Gaussian pulse with spread of (a) 120 fs, (b) 50 fs, (c) 25 fs, (d) 10 fs and their frequency spectrum (inset figures).

Four short pulses with a Gaussian temporal profile of waists of 120 fs, 50 fs, 25 fs and 10 fs were considered in the figure to investigate the change of refractive index due to their broad frequency band. It has been shown in the inset figures of each subplot that as the temporal waist is decreased the frequency content increases. The shorter pulse, which contains a larger frequency spectrum and hence causing larger variation of the refractive index in the material, will experience a varied velocity for each of the frequency within the pulse. The propagation of short pulses in dispersive material causes attenuation to some frequencies, in addition to the pulse spread due to the group velocity of the pulse. The

spreading of pulses cause pulse splitting in certain situations, and hence, distortion to the original shape of the pulse.

5.2.3 Drude Model

In this model it is assumed that the conduction electrons are not bound to the atom giving the postulate that $\omega_0 = 0$ in the Lorentz model. This assumption is somewhat valid for highly conductive materials, such as metal. The dispersion of a metal has frequently been taken into account using the Drude model. The permittivity expression of this model is

$$\varepsilon(\omega) = 1 + \frac{\omega_p^2}{j\Gamma\omega - \omega^2} \quad (5.22)$$

where the plasma frequency ω_p is defined as $\omega_p = \sqrt{\frac{Ne^2}{\varepsilon_0 m}}$.

5.3 Summary

Dispersive behavior of different optical materials has been represented using Debye, Lorentz and Drude models. Detailed mathematical formulation of these models have been derived and the modeling parameters of Water, Methanol, Human tissue, *GaAs* and *AlGaAs* have been presented in this chapter. The variation of the refractive index of *GaAs* with the frequency content of ultra short pulse has been also analyzed.

References

- [1] M. Born and E. Wolf, *Principles of Optics*, Cambridge University Press, Cambridge, pp. 14-24, 1999.

- [2] I. Walmsley, L. Waxer, C. Dorrer, "The role of dispersion in ultrafast optics, Ian Walmsley, *Review of Scientific Inst.*, vol. 72, no. 1, pp. 1-29, 2001.
- [3] F.L. Teixeira, W.C. Chew, M. Straka, M. L. Oristaglio, and T. Wang, "Finite-difference time-domain simulation of ground penetrating radar on dispersive, inhomogeneous, and conductive soils," *IEEE Trans. Geosci. Remote Sens.*, vol. 36, no. 6, pp. 1928-1937, 1998.
- [4] G. G. Raju, "Dielectrics in Electric Fields", Marcel Dekker, New York, 2003.
- [5] W. D. Hurt, "Multiterm Debye dispersion relations for permittivity of muscle," *IEEE Trans. Biomed. Eng.*, vol. BME-32, no. 1, pp. 60–64, 1985.
- [6] O. P. Gandhi and C. M. Furse, "Currents induced in the human body for exposure to ultrawideband electromagnetic pulses," *IEEE Trans. Electromagn. Compat.*, vol. 39, no. 2, pp. 174–180, 1997.
- [7] R. Buchner, J. Barthel, and J. Stauber, "The dielectric relaxation of water between 0° C and 35° C," *Chem. Phys.*, vol. 306, pp. 57–63, 1999.
- [8] Young, J.L, "On the Time Integration of Maxwell's Equations Associated With Debye Relaxation Processes", *IEEE Ant. Prop.*, vol. 55, no. 8, Aug. 2007.
- [9] Gabriel S, Lau R W and Gabriel C "Parametric Models for the Dielectric spectrum of tissues " *Phys. Med. Biol.* vol. 41, issue 11, Nov. 1996.
- [10] Neven Simicevic "FDTD computation of human eye exposure to ultra-wideband electromagnetic pulses" *Phys. Med. Biol.* 53, pp. 1795–1809, 2008.
- [11] Peter W. Milloni and Joseph H. Eberly. *Lasers*, pages 27--33. John Wiley and Sons, 1988.
- [12] M. R. Brozel, G. E. Stillman *Properties of Gallium Arsenide*. IEEE Inspec, London, 1996.
- [13] M. C. Beard, G. M. Turner, and C. A. Schmuttenmaer, "Transient photoconductivity in GaAs as measured by time-resolved THz spectroscopy." *Physical Review B.*, 62, 15764, 2000.
- [14] M.J. Howes and D.V. Morgan "Gallium Arsenide Materials, Devices and Circuits" pp.10, John & Wiley Sons, Dec. 1986.
- [15] Vaardingerbroek, M. T.; Kuypers, W.; Acket, G. A. "Energy relaxation time of hot electrons in GaAs" *Physics Letters A*, Volume 28, Issue 2, p. 155-156, Sep. 2002.

- [16] Sadao Adachi, "GaAs and related materials" World Scientific Publishing Co., Singapore, 1994.
- [17] Sadao Adachi, "Properties of Semiconductor Alloys", Group-IV, III-V, and II-VI Semiconductors" pp. 317, John & Wiley Sons, 2009.
- [18] M. A. Alsunaidi, F. S. Alhajiri, and H. M. Masoudi, " A FDTD Algorithm for the analysis of Short Optical Pulse second harmonic Generation in Dispersive Medium", *Microwave and Optical Techn. Lett.*, vol. 51, no. 4, April 2009.
- [19] Jean-Claude Diels, Wolfgang Rudolph, *Ultrashort Laser Pulse Phenomena: Fundamentals, Techniques, and Applications on a Femtosecond Time Scale*, Accademic Press, (2006).
- [20] J. Orear. Physik. Carl hansen Berlag., Munchen, Vienna, Austria, 1982.
- [21] R. A. Serway, C. J. Moses, and C.A. Moyer, *Modern Physics*, Saunders College Publishers, Philadelphia, PA, 1989.
- [22] R. R. Alfano and S. L. Shapiro, "Observation of self-phase modulation and small-scale filaments in crystals and glasses", *Phys. Rev. Lett.* 24 (11), pp.592, 1970.
- [23] Theodore S. Rappaport , "Wireless Communications: Principles and Practice" 2nd ed., Prentice-Hall, 2002.

CHAPTER 6

DISPERSIVE TIME DOMAIN NUMERICAL TECHNIQUES

6.1 Introduction

While one often describes a material by some constant (frequency independent) value of the permittivity and permeability, in reality all material properties are frequency dependent or alternatively can be said to be dispersive in nature, as we discussed in the previous chapter. The ionosphere, biological tissues, crystalline structures, ferrites, optical fibers, and radar-absorbing materials are dispersive [1]. Dispersive or time-varying media can be easily tackled in time-domain analysis [2 - 3]. In general, a time discretization strategy may involve either explicit or implicit updates. The explicit updates, such as the FDTD [4 - 5], are matrix-free and with low computational complexity. However, its memory requirements scale linearly with the number of unknowns. On the other hand, implicit updates, such as, the TD-BPM [6 - 10] or the implicit FDTD of the ADI or the LOD, are able to overcome the maximum time step bound imposed by the Courant stability limit [11 - 12]. However, they

require the solution of a linear system at every time step. This chapter shows the derivation of the TD-BPM and the FDTD in order to account for material dispersion. Their numerical implementation to model 2-D optical devices, and also their accuracy and performance tests are presented. The main objective of these implementations will remain in the framework of short and ultra short pulse propagation in dispersive material.

6.2 The Dispersive FDTD

In dispersive medium, the constitutive equation relating the electric field and the electric flux density D is expressed as a convolution integral between E and the inverse Fourier transformed frequency dependent permittivity. The direct implementation of the convolution requires the storage of the entire past time. In Trapezoidal Recursive Convolution (TRC) [13] and its improved Piecewise Linear Recursive Convolution (PLRC) [14 - 15], a recursive accumulator is used whereby storage of only few previous time steps is necessary. These techniques are applicable only to linear dispersive material. Other popular implementations for the convolution also exist with the z -transform (ZT) [16 - 17] whereby the transfer function in frequency domain is converted to the z -domain. The frequency dependent constitutive equation in dispersive media can also be expressed as ordinary differential equation (ODE) in time involving D and E by the inverse Fourier transform, which is commonly referred as the Auxiliary Differential Equation (ADE) approach [18 - 19]. It is observed that the ADE-based implicit methods require less CPU time than the TRC, PLRC and ZT based implicit techniques [20 - 21]. In this section, the derivation of the explicit FDTD and later on the TD-BPM are accomplished using the ADE technique.

The equations in 2-D for the Transverse Electric (TE) field can be obtained for dispersive material from the coupled partial differential equations given in Eq. 3.5 of chapter 3 as [5]

$$\frac{\partial D_y}{\partial t} = \frac{\partial H_x}{\partial z} - \frac{\partial H_z}{\partial x} \quad (6.1a)$$

$$D(\omega) = \epsilon_0 \epsilon_r(\omega) \cdot E(\omega) \quad (6.1b)$$

$$\frac{\partial H_x}{\partial t} = \frac{1}{\mu_0} \frac{\partial E_y}{\partial z} \quad (6.1c)$$

$$\frac{\partial H_z}{\partial t} = -\frac{1}{\mu_0} \frac{\partial E_y}{\partial x} \quad (6.1d)$$

A similar formulation can be followed to obtain the TM case. Following the numerical procedure described in chapter 3 and using the central Finite Difference (FD) approximation of the 1st order derivative, Eq. 6.1a can be written as

$$D_y \Big|_{i,k}^{n+1/2} = D_y \Big|_{i,k}^{n-1/2} + \frac{\Delta t}{\Delta z} \left(H_x \Big|_{i,k+1/2}^n - H_x \Big|_{i,k-1/2}^n \right) - \frac{\Delta t}{\Delta x} \left(H_z \Big|_{i+1/2,k}^n - H_z \Big|_{i-1/2,k}^n \right) \quad (6.2)$$

Here we have used the notations used in Eq. 3.15. To account for the dispersive property of the material, it is necessary to have the dispersion model in their time domain formulations. Three different types of dispersive models have been described in chapter 5. The inverse fourier transform of the Debye, the Lorentz and the Drude models from chapter 5 are respectively given as

$$D_y + \tau \frac{dD_y}{dt} = \epsilon_s E_y + \tau \epsilon_\infty \frac{dE_y}{dt} \quad (\text{Debye}) \quad (6.3a)$$

$$\omega_0^2 D_y + 2\delta \frac{dD_y}{dt} + \frac{d^2 D_y}{dt^2} = \omega_0^2 \epsilon_s E_y + 2\delta \epsilon_\infty \frac{dE_y}{dt} + \epsilon_\infty \frac{d^2 E_y}{dt^2} \quad (\text{Lorentz}) \quad (6.3b)$$

$$\frac{d^2 D_y}{dt^2} - \Gamma \frac{dD_y}{dt} = \frac{d^2 E_y}{dt^2} - \Gamma E_y + \omega_p^2 \frac{dE_y}{dt} \quad (\text{Drude}) \quad (6.3c)$$

The above equations provide the scope to obtain the electric field, which is eventually necessary to calculate the magnetic fields. The updates of the electric field for the models mentioned above, using again the central FD approximations, are

$$E_y \Big|_{i,k}^{n+1/2} = \frac{2}{\tau \epsilon_\infty} \left[\begin{array}{l} \frac{\tau}{2\Delta t} D_y \Big|_{i,k}^{n+1/2} + D_y \Big|_{i,k}^{n-1/2} + \frac{\tau}{2\Delta t} D_y \Big|_{i,k}^{n-3/2} \\ - \epsilon_s E_y \Big|_{i,k}^{n-1/2} + \frac{\tau \epsilon_\infty}{2\Delta t} E_y \Big|_{i,k}^{n-3/2} \end{array} \right] \quad (6.4a)$$

$$E_y \Big|_{i,k}^{n+1/2} = \frac{1}{\epsilon_\infty (1 + \Delta t \delta)} \left[\begin{array}{l} (1 + \Delta t \delta) D_y \Big|_{i,k}^{n+1/2} + (-2 + \Delta t^2 \omega_0^2) D_y \Big|_{i,k}^{n-1/2} \\ + (1 - \Delta t \delta) D_y \Big|_{i,k}^{n-3/2} + (2\epsilon_\infty - \Delta t^2 \omega_0^2 \epsilon_s) E_y \Big|_{i,k}^{n-1/2} \\ + \epsilon_\infty (-1 + \Delta t \delta) E_y \Big|_{i,k}^{n-3/2} \end{array} \right] \quad (6.4b)$$

$$E_y \Big|_{i,k}^{n+1/2} = D_y \Big|_{i,k}^{n+1/2} - \frac{4}{2 - \Delta t \Gamma} D_y \Big|_{i,k}^{n-1/2} + \frac{2 + \Delta t \Gamma}{2 - \Delta t \Gamma} D_y \Big|_{i,k}^{n-3/2} \\ + \frac{2\Delta t^2 \omega_p^2 - 4}{2 - \Delta t \Gamma} E_y \Big|_{i,k}^{n-1/2} - E_y \Big|_{i,k}^{n-3/2} \quad (6.4c)$$

It is to be noted from the above equations that for calculating E_y in the new time step $(n+1/2)$ at any mesh point, the values of fields E_y and D_y at the two previous time steps of $(n-1/2)$ and $(n-3/2)$, namely $E_y^{n-1/2}$, $E_y^{n-3/2}$, $D_y^{n-1/2}$ and $D_y^{n-3/2}$ are required. Table 6.1 shows a summary for the coefficients of Eq. 6.4.

Table 6.1 Coefficients of Debye, Lorentz and Drude model used for $E_y|_{i,k}^{n+1/2}$ calculation in FDTD of Eq. 6.4.

Variables	$D_y _{i,k}^{n+1/2}$	$D_y _{i,k}^{n-1/2}$	$D_y _{i,k}^{n-3/2}$	$E_y _{i,k}^{n-1/2}$	$E_y _{i,k}^{n-3/2}$
Debye Coefficients	$\frac{1}{\Delta t \epsilon_\infty}$	$\frac{2}{\tau \epsilon_\infty}$	$\frac{1}{\Delta t \epsilon_\infty}$	$-\frac{2\epsilon_s}{\tau \epsilon_\infty}$	$\frac{1}{\Delta t}$
Lorentz Coefficients	$\frac{1}{\epsilon_\infty}$	$\frac{-2 + \Delta t^2 \omega_0^2}{\epsilon_\infty (1 + \Delta t \delta)}$	$\frac{1 - \Delta t \delta}{\epsilon_\infty (1 + \Delta t \delta)}$	$\frac{2 - \Delta t^2 \omega_0^2 \epsilon_s}{\epsilon_\infty (1 + \Delta t \delta)}$	$\frac{-1 + \Delta t \delta}{\epsilon_\infty (1 + \Delta t \delta)}$
Drude Coefficients	1	$-\frac{4}{2 - \Delta t \Gamma}$	$\frac{2 + \Delta t \Gamma}{2 - \Delta t \Gamma}$	$\frac{2\Delta t^2 \omega_p^2}{2 - \Delta t \Gamma}$	-1

The updates for the H-fields are obtained from Eq. 6.1c and Eq. 6.1d as

$$H_x|_{i,k+1/2}^{n+1} = H_x|_{i,k}^n + \frac{\Delta t}{\mu_0 \Delta z} \left(E_y|_{i,k+1}^{n+1/2} - E_y|_{i,k}^{n+1/2} \right) \quad (6.5)$$

$$H_z|_{i+1/2,k}^{n+1} = H_z|_{i,k}^n - \frac{\Delta t}{\mu_0 \Delta x} \left(E_y|_{i+1,k}^{n+1/2} - E_y|_{i,k}^{n+1/2} \right) \quad (6.6)$$

The computational sequence of the dispersive FDTD can be summarized in the flow chart shown in Figure 6.1.

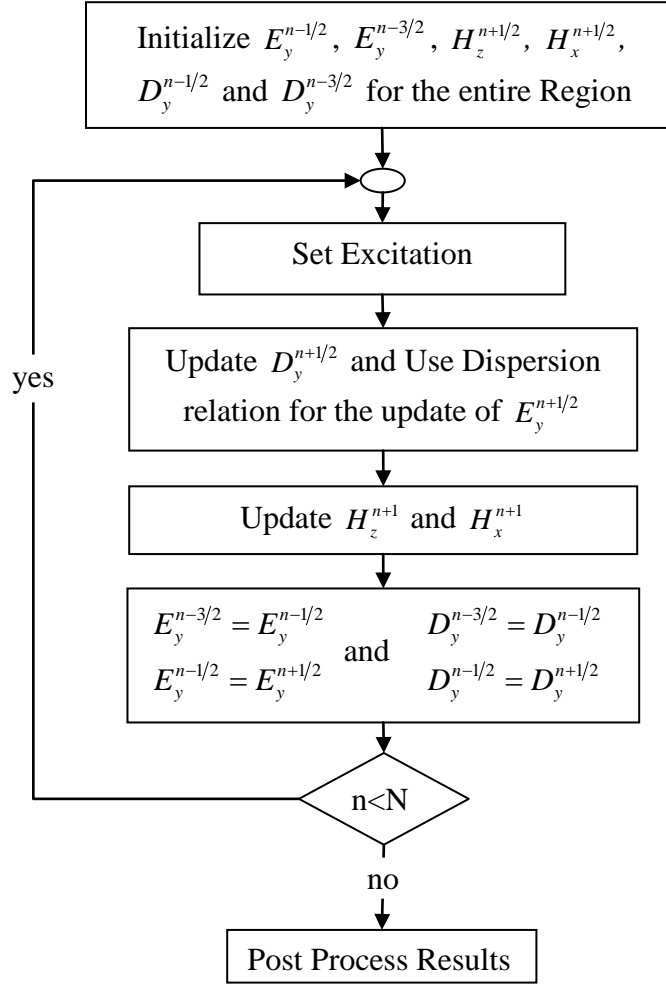


Figure 6.1 The flow chart of the dispersive FDTD algorithm.

6.3 The Dispersive TD-BPM

In this section, we formulate the TD-BPM described in chapter 4 to model structures containing dispersive material. Starting with the general 2-D wave equation for the TE case

(Eq. 2.10)

$$\frac{\partial^2 E_y}{\partial z^2} + \frac{\partial^2 E_y}{\partial x^2} - \frac{1}{\mu_0} \frac{\partial^2 D_y}{\partial t^2} = 0 \quad (6.7)$$

Here we assume that the device is uniform and infinitely stretched along the y- direction, so that there is no variation of field in the y-direction. Extracting a carrier from the fields by assuming $E_y = \psi(t)e^{j\omega t}$ and $D_y = \phi(t)e^{j\omega t}$. The removal of the fast carrier allows one to track a slowly varying envelope of a pulsed wave directly in the time domain and thus, the converged solution could be obtained with a moderate time step size [13 - 14]. Upon the substitution of these assumptions in Eq. 6.7, the following equation can be written

$$\frac{\partial^2 \psi}{\partial z^2} + \frac{\partial^2 \psi}{\partial x^2} - \frac{1}{\mu_0} \left(\frac{\partial^2 \phi}{\partial t^2} + 2j\omega \frac{\partial \phi}{\partial t} - \omega^2 \phi \right) = 0 \quad (6.8)$$

Using the same steps used above, the dispersive equation of 6.3 can be written as

$$(1 + j\omega\tau)\phi(t) + \tau \frac{d\phi(t)}{dt} = (\epsilon_s + j\omega\tau\epsilon_\infty)\psi(t) + \tau\epsilon_\infty \frac{d\psi(t)}{dt} \quad (\text{Debye}) \quad (6.9a)$$

$$\left(\frac{d^2\phi(t)}{dt^2} + 2j\omega \frac{d\phi(t)}{dt} - \omega^2\phi(t) \right) + 2\delta \left(\frac{d\phi(t)}{dt} + j\omega\phi(t) \right) + \omega^2\phi(t) = \epsilon_\infty \left(\frac{d^2\psi(t)}{dt^2} + 2j\omega \frac{d\psi(t)}{dt} - \omega^2\psi(t) \right) + 2\delta\epsilon_\infty \left(\frac{d\psi(t)}{dt} + j\omega\psi(t) \right) + \omega_0^2\epsilon_s\psi(t) \quad (\text{Lorentz}) \quad (6.9b)$$

$$\left(\frac{d^2\phi(t)}{dt^2} + 2j\omega \frac{d\phi(t)}{dt} - \omega^2\phi(t) \right) - \Gamma \left(\frac{d\phi(t)}{dt} + j\omega\phi(t) \right) = \left(\frac{d^2\psi(t)}{dt^2} + 2j\omega \frac{d\psi(t)}{dt} - \omega^2\psi(t) \right) - \Gamma \left(\frac{d\psi(t)}{dt} + j\omega\psi(t) \right) + \omega_p^2\psi(t) \quad (\text{Drude}) \quad (6.9c)$$

The time derivatives of Eq. 6.8 and Eq. 6.9 can be discretized using the central FD approximations. Then, the discretized equations of Eq. 6.9 give the following relation between φ and ψ as

$$Q \varphi_i = R \psi_i \quad (6.10)$$

where i represents the discretization along time, Q and R are tri-diagonal matrices and the coefficients of these matrices are given in Tables 6.2, 6.3 and 6.4 for the three dispersive models discussed before.

Table 6.2: The coefficients of Q and R matrices for the Debye model.

	Diagonal	Below the diagonal	Above the diagonal
Q	$1 + j\tau\omega$	$\frac{\tau}{2\Delta t}$	$-\frac{\tau}{2\Delta t}$
R	$\varepsilon_s + j\tau\varepsilon_\infty\omega$	$\frac{\tau\varepsilon_\infty}{2\Delta t}$	$-\frac{\tau\varepsilon_\infty}{2\Delta t}$

Table 6.3: The coefficients of Q and R matrices for the Lorentz model

	Diagonal	Below the diagonal	Above the diagonal
Q	$-\frac{2}{\Delta t^2} + (\omega_0^2 + 2j\omega\delta - \omega^2)$	$\frac{1}{\Delta t^2} + \frac{\delta + j\omega}{\Delta t}$	$\frac{1}{\Delta t^2} - \frac{\delta + j\omega}{\Delta t}$
R	$-\frac{2}{\Delta t^2} + (\omega_0^2\varepsilon_s + 2j\omega\delta\varepsilon_\infty - \omega^2\varepsilon_\infty)$	$\frac{\varepsilon_\infty}{\Delta t^2} + \frac{\varepsilon_\infty(\delta + j\omega)}{\Delta t}$	$\frac{\varepsilon_\infty}{\Delta t^2} - \frac{\varepsilon_\infty(\delta + j\omega)}{\Delta t}$

Table 6.4: The Coefficients of Q and R matrices for the Drude model

	Diagonal	Below the diagonal	Above the diagonal
Q	$-\frac{2}{\Delta t^2} + (j\omega\Gamma - \omega^2)$	$\frac{1}{\Delta t^2} + \frac{\Gamma + j2\omega}{2\Delta t}$	$\frac{1}{\Delta t^2} - \frac{\Gamma + j2\omega}{2\Delta t}$
R	$-\frac{2}{\Delta t^2} + \omega_p^2 + j\omega\Gamma - \omega^2$	$\frac{1}{\Delta t^2} + \frac{\Gamma + j2\omega}{2\Delta t}$	$\frac{1}{\Delta t^2} - \frac{\Gamma + j2\omega}{2\Delta t}$

Eq. 6.10 can be also written as

$$\varphi_i = Q^{-1}R\psi_i = A\psi_i \quad (6.11)$$

where $A = Q^{-1}R$. Upon the substitution of Eq. 6.11 in Eq. 6.8, we arrive the following equation written in terms of ψ as

$$\frac{\partial^2 \psi_i}{\partial z^2} + \frac{\partial^2 \psi_i}{\partial x^2} - AP\psi_i = 0 \quad (6.12)$$

where the diagonal, right-off-diagonal and left-off-diagonal elements of the tri-diagonal P matrix are $\frac{1}{\mu_0} \left(\frac{2}{\Delta t^2} + \omega^2 \right)$, $-\frac{1}{\mu_0} \left(\frac{1}{\Delta t^2} + j \frac{\omega}{\Delta t} \right)$ and $\frac{1}{\mu_0} \left(\frac{1}{\Delta t^2} - j \frac{\omega}{\Delta t} \right)$, respectively. If we define the pseudodifferential square-root operator L_d in a similar approach that we did earlier in chapter 4 as

$$L_d^2 \psi_i = \left[\frac{\partial^2}{\partial x^2} - T \right] \psi_i \quad (6.13)$$

The dense matrix T is expressed as

$$T = PA \quad (6.14)$$

Applying again the FD approximations to the spatial derivatives in L_d , given in Eq. 6.13, the matrix operator L_d in its discrete form can be written as a sparse matrix as

$$L_d^2 = \begin{bmatrix} T+S_{d1} & S_{d2} & 0 & \cdots & 0 \\ S_{d2} & T+S_{d1} & S_{d2} & \ddots & \\ 0 & \ddots & \ddots & \ddots & 0 \\ & \ddots & S_{d2} & T+S_{d1} & S_{d2} \\ 0 & & 0 & S_{d2} & T+S_{d1} \end{bmatrix} \quad (6.15)$$

S_{d1} and S_{d2} are diagonal matrices with the elements of $-2/\Delta x^2$ and $1/\Delta x^2$, respectively.

The size of the tri-diagonal block matrix L_d^2 is M_x by M_x , where M_x is the number of the spatial discretization points along x . The size of each block is M_t by M_t , where M_t is the number of temporal discretization points. Therefore, the size of matrix L_d^2 will be $M_x \times M_t$ by $M_x \times M_t$.

Then Eq. 6.12 can be written as

$$\left\{ \frac{\partial}{\partial z} + L_d \right\} \left\{ \frac{\partial}{\partial z} - L_d \right\} \psi_{i,m} = 0 \quad (6.16)$$

where m represents the discretization along the x -direction. For forward propagation, the solution can be written as

$$\psi_{i,m}(z) = e^{-j L_d z} \psi_{i,m}(0) \quad (6.17)$$

where, $\psi_{i,m}(0)$ is the initial field. The implementation of Eq. 6.17 is very similar to the implementation of Eq. 4.7 with the addition of the dispersive information. In principle, the exponential of the square root operator L_d of Eq. 6.15 can be solved either using the MoL approach, as mentioned in Eq. 2.32 of chapter 2, or using the techniques mentioned in chapter 4. However, the MoL approach is very costly because it requires finding the eigenvalues and eigenvectors in addition to the inversion of a large matrix.

6.4 Implementations

In order to test the performance of the formulation described before, the two methods (the FDTD and the TD-BPM) have been implemented to model the propagation of short and ultra short pulse propagation in dispersive one dimensional, two dimensional homogeneous and waveguide problems. The following implementations use Lorentz model as a representative of dispersion, while the implementation of the other two models should produce similar results. The choice of Lorentz model in this work is due to the fact that the dispersive *GaAs* and *AlGaAs* materials can be represented using this model of dispersion.

6.4.1 One Dimensional Implementation

In this section, the propagation of a 1-D Gaussian pulse in a dispersive medium that has a Lorentz model is considered. The parameters for the dispersive material considered are: $\delta=2.0 \times 10^9 \text{ s}^{-1}$, $\epsilon_\infty = 2.25$, $\epsilon_s = 5.25$, $\omega_0 = 4.0 \times 10^{14} \text{ rad/s}$ and $\lambda_c = 2.19 \text{ }\mu\text{m}$ [11]. The initial Gaussian pulse width was taken to be $\sigma_{t0} = 25 \text{ fs}$, and the pulse was propagated to a distance of $z = 126 \text{ }\mu\text{m}$. The operator given in Eq. 6.16 was also implemented and solved using the MoL approach for comparison purposes. The numerical parameters used for the TD-BPM in the simulation are: $p = 2$, $\Delta z = 0.05 \text{ }\mu\text{m}$, and $\Delta t = 0.80 \text{ fs}$, while the corresponding numerical parameters used for the FDTD are: $\Delta z = \lambda_c / 80 = 0.027375 \text{ }\mu\text{m}$, and $\Delta t = 0.0456566 \text{ fs}$. Figure 6.2 (a) and (b) show the temporal shape of the propagated pulse at $z = 55 \text{ }\mu\text{m}$ and $z = 126 \text{ }\mu\text{m}$, respectively, using the TD-BPM, the FDTD and the MoL techniques. The figures show the close agreement of the three results. The initial pulse shows a significant spread during the propagation in the dispersive material. It is to be noted that the temporal step size

Δt for the TD-BPM is more than 17 times larger than the corresponding Δt used for the FDTD.

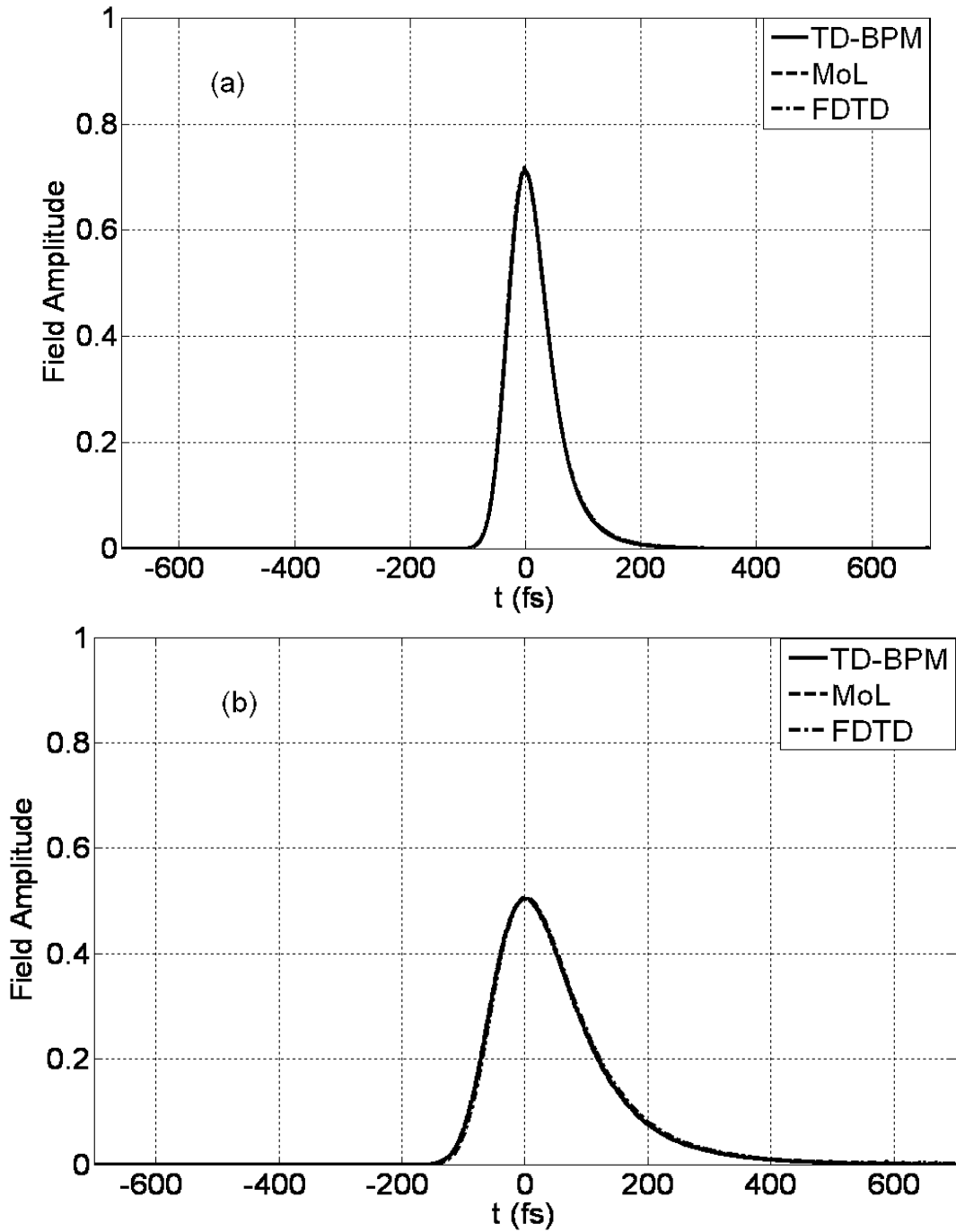


Figure 6.2 The propagation of the Gaussian pulse at (a) $z = 55 \mu\text{m}$ and (b) $z = 126 \mu\text{m}$ in a 1-D dispersive medium represented by Lorentz model using the MoL, the TD-BPM and the FDTD.

6.4.2 Two Dimensional Implementation

In this section, the implementation of the time domain numerical techniques of the TD-BPM and the FDTD for the investigation of dispersive homogeneous and 2-D waveguide problems will be discussed.

6.4.2.1 Homogeneous Medium

First the propagation of a pulsed Gaussian beam in a homogeneous *AlGaAs* dispersive medium has been investigated. The medium is approximated by a Lorentz model with the following parameters: $\delta=1.0\times 10^{13}\text{s}^{-1}$, $\epsilon_{\infty} = 1.5376$, $\epsilon_s = 8.2944$, $\omega_0 = 6.6\times 10^{15}$ rad/s and $\lambda_c = 1.064$ μm [24]. The initial temporal waist and the spatial waist of the Gaussian beam were $\sigma_{t0} = 20$ fs and $w_0 = 3.0$ μm , respectively. The TD-BPM numerical parameters used in the following simulation are: $p = 4$, $\Delta z = 0.1$ μm , $\Delta x = 0.1$ μm and $\Delta t = 0.75$ fs. The numerical parameters used in the FDTD simulation are: $\Delta z = \lambda/80 = 0.0133$ μm , $\Delta x = 0.1$ μm and $\Delta t = \Delta z/(2c_0) = 0.02218$ fs. In the FDTD simulation, Δt is upper bounded by the stability criterion of CFL given in [5]. Figure 6.3 shows the evolution of the pulsed beam at several propagation distances of $z = 12.5$ μm , 25.0 μm and 50.0 μm . The figure shows that the pulse diffracts in the spatial direction due to the homogeneity of the material, while it spreads due to material dispersion. The energy of the pulse is reduced due to the effect of the damping coefficient in the medium. The results obtained by the TD-BPM are compared with the results obtained using the FDTD. Figure 6.4 shows the time profile of the pulse in the middle of the spatial computational window x using both methods. It can be seen from the figure that the two techniques produce very similar results. It is to be noticed again that the time step size Δt used in this simulation is more than 33 times that of the FDTD.

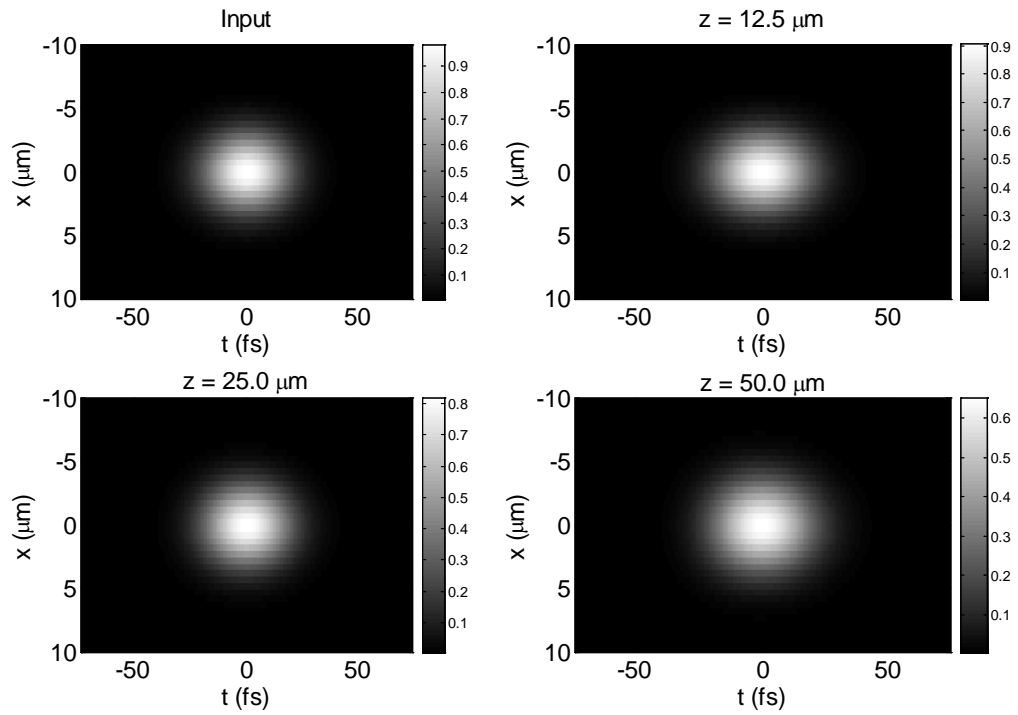


Figure 6.3 The evolution of the pulsed Gaussian optical beam in a homogeneous 2D dispersive medium using the non-paraxial TD-BPM for an initial pulse width of $\sigma_0 = 20$ fs.

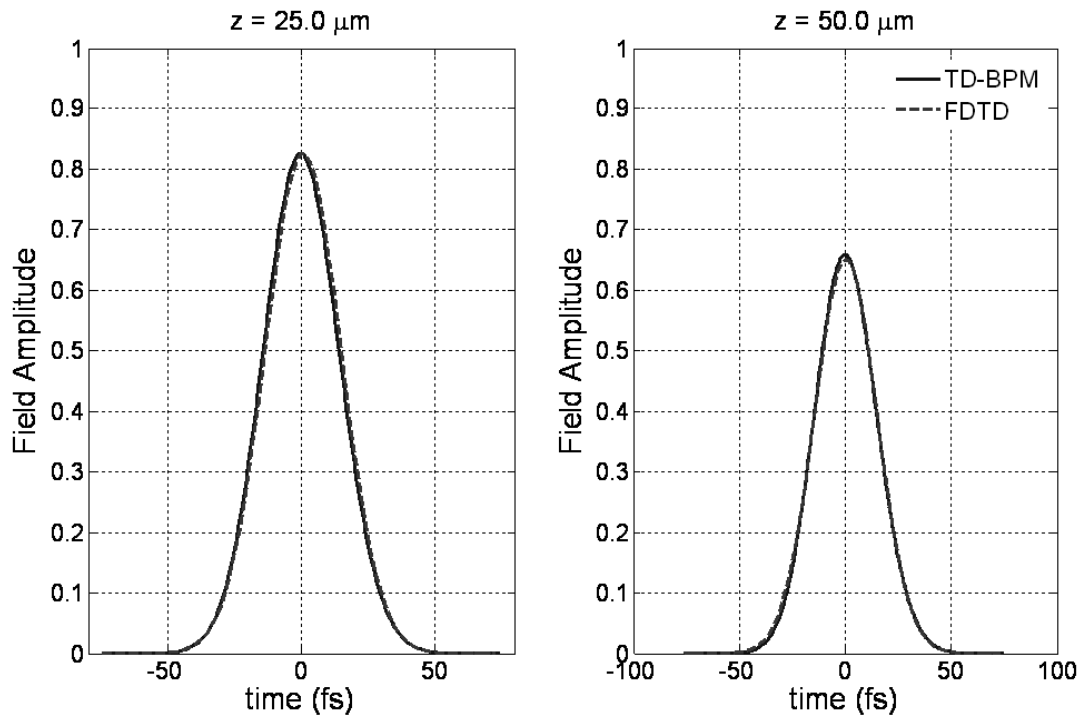


Figure 6.4 The temporal profile of the propagated pulsed beam in a homogeneous 2D dispersive medium at $z = 25.0 \mu\text{m}$ and $z = 50.0 \mu\text{m}$ using the non-paraxial TD-BPM and the FDTD.

6.4.2.2 Slab Waveguide

In this section, the propagation of pulsed optical beams in a dispersive symmetric slab waveguide is considered. The waveguide has a core of dispersive material of Lorentz type while the substrate and the superstrate are of non-dispersive silica material. The superstrate, the core and the substrate widths were taken to be $2.5 \mu\text{m}$, $1.0 \mu\text{m}$ and $2.5 \mu\text{m}$, respectively. The substrate refractive index is 1.52. The core dispersive medium is approximated by a Lorentz model with the following parameters: $\delta=2.0 \times 10^9 \text{ s}^{-1}$, $\epsilon_{\infty} = 2.25$, $\epsilon_s = 5.25$, $\omega_0 = 8.0 \times 10^{14} \text{ rad/s}$, and $\lambda_c = 3.0 \mu\text{m}$. The refractive index of the core at this wavelength is 3.172. The initial pulsed beam has a Gaussian temporal pulse of waist $\sigma_{t0} = 50 \text{ fs}$ with the TE_0 spatial mode profile. The propagation step size was taken to be $\Delta z = 0.1 \mu\text{m}$, $p = 4$, $\Delta x = 0.1 \mu\text{m}$ and $\Delta t = 1.25 \text{ fs}$ for the TD-BPM. Figure 6.5 shows the propagated pulsed beam at $z = 4.0 \mu\text{m}$, $8.0 \mu\text{m}$, 12.0 and $16.0 \mu\text{m}$ along the propagation direction inside the waveguide using the non-paraxial TD-BPM. Figure 6.5 shows that the optical pulse preserved its spatial guided mode profile along the x - direction while the temporal profile has spread within a very short distance due to the high variation of the refractive index in the core within the frequency spectrum of the initial pulse. The overall intensity of the pulsed beam has been reduced, as can be seen from the figure, due to the effect of the damping coefficient in the medium. The results obtained by the TD-BPM are compared with that of the FDTD in Figure 6.7. The parameters for the FDTD are: $\Delta z = \lambda_c/80 = 0.0375 \mu\text{m}$, $\Delta x = 0.1 \mu\text{m}$ and $\Delta t = \Delta z/(2c_0) = 0.0625433 \text{ fs}$. In the FDTD simulation Δt , again, is upper bounded by the CFL stability criterion which is 19 times smaller than that used for the TD-BPM. The high attenuation and the temporal spread indicate the strong interaction of the pulsed beam with the dispersive material. Figure 6.6 describes the temporal pulse shape right in the middle of

the waveguide for both the TD-BPM and the FDTD. It is clear from the figure that the two techniques produce very similar results.

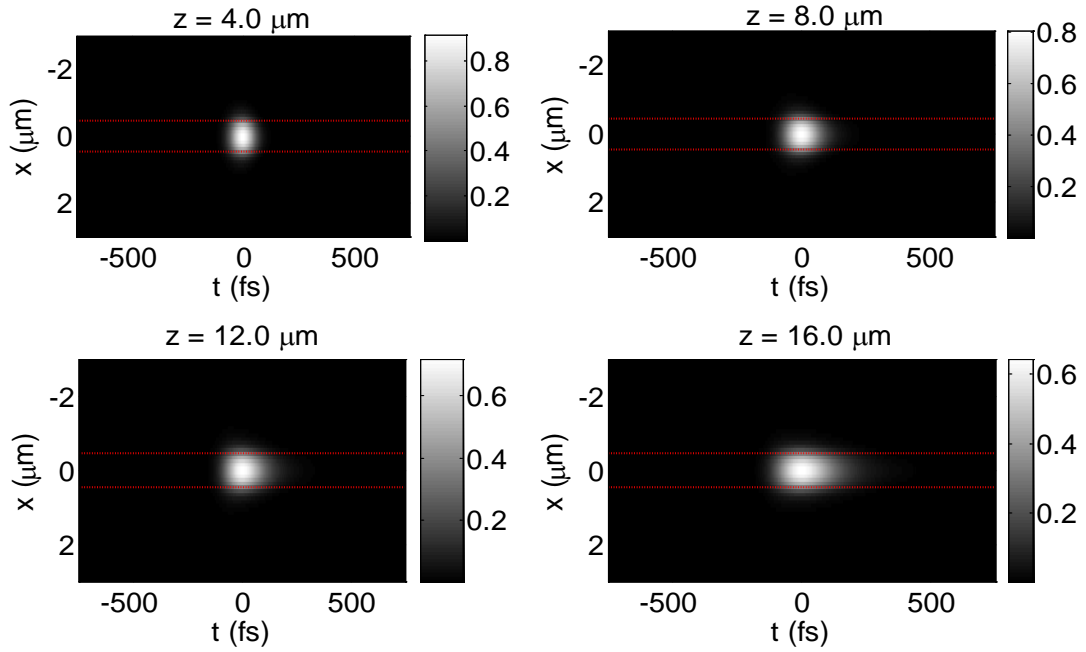


Figure 6.5 Propagation of the TE₀ pulsed optical beam in the dispersive slab waveguide using the TD-BPM at several propagation distances. The two horizontal lines show the positions of the core layer of the slab.

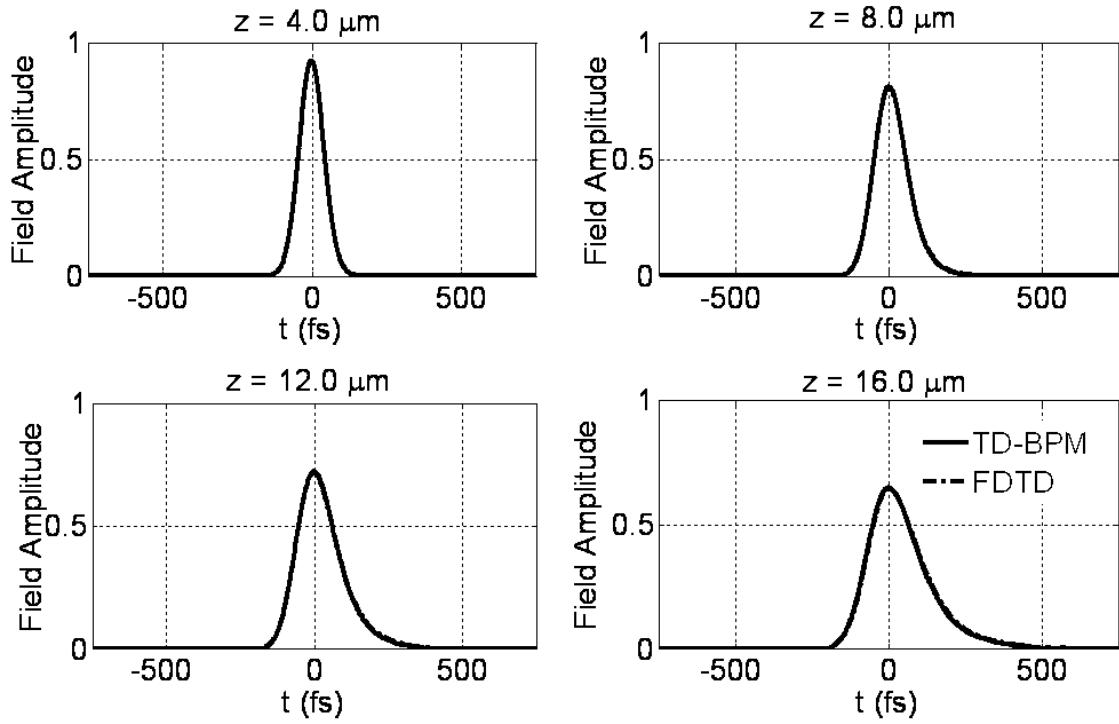


Figure 6.6 Comparison between the TD-BPM and the FDTD results of the temporal profile of the propagated pulse with $\sigma_{t0} = 50$ fs at several distances along the direction of z inside the dispersive slab waveguide.

6.5 Performance of the TD-BPM

In previous sections, comparison between the TD-BPM and the FDTD was done based on graphical inspection. In this section, quantitative and detailed comparisons of these two methods are performed rigorously. The material dispersion structures used in this work do not have closed form analytical expressions; therefore the FDTD result is taken as a reference in the following comparison. The maximum percentage difference, the percentage root mean square difference, the percentage difference at peak of the pulse and the ratio of the group velocities obtained by these two methods are calculated. Definitions of all these quantities are presented in chapter four (section 4.3.4).

It is to be noted that the accuracy analysis for dispersive structures are different from those seen in chapter 4. The strength of material dispersion in addition to the duration of the initial pulse width plays major roles on the numerical parameters of the TD-BPM and the FDTD. Therefore, in the following analysis three different cases are considered to fully explore the limit for the numerical parameters. The first and second cases use a dispersive *GaAs* symmetric slab waveguide that has a relatively strong dispersion relation that has the following parameters: a substrate and a superstrate refractive index of $n = 3.4$. The dispersion relation of the *GaAs*-based core is again fitted to Lorentz model with $\delta = 5.0 \times 10^{11} \text{ s}^{-1}$, $\epsilon_{\infty} = 1.0$, $\epsilon_s = 11.011$, $\omega_0 = 3.014 \times 10^{15} \text{ rad/s}$ and $\lambda_c = 1.55 \text{ }\mu\text{m}$. The substrate and superstrate are $2.5 \text{ }\mu\text{m}$ thick each, while the slab width is $1.0 \text{ }\mu\text{m}$. The calculated effective refractive index is $n_{eff} = 3.558445$. In these cases we study the effect of changing the initial pulse width using $\sigma_{t0} = 25 \text{ fs}$ and 100 fs . The third case uses a 25 fs pulsed beam propagation in a relatively weak dispersive *AlGaAs* core material with a substrate and superstrate of refractive index of $n = 2.706$. The dispersion relation of the *AlGaAs*-based core is also fitted to Lorentz model with $\delta = 1.0 \times 10^{13} \text{ s}^{-1}$, $\epsilon_{\infty} = 1.5357$, $\epsilon_s = 8.2944$, $\omega_0 = 6.6 \times 10^{15} \text{ rad/s}$, and $\lambda_c = 1.064 \text{ }\mu\text{m}$. The calculated effective refractive index is $n_{eff} = 2.9406$. In each case, the initial pulsed beam is formed using the spatial profile of the TE_0 and the temporal pulse of the Gaussian profile. The parameters for the FDTD are: $\Delta z = \lambda_c/80 = 0.0194 \text{ }\mu\text{m}$, $\Delta t = \Delta z/(2c_0) = 0.0323 \text{ fs}$ for the first two cases and $\Delta z = \lambda_c/80 = 0.0133 \text{ }\mu\text{m}$, $\Delta t = 0.02218 \text{ fs}$ for the third case and $\Delta x = 0.1 \text{ }\mu\text{m}$ for all the cases considered. The pulses were propagated to a distance of $z = 100 \text{ }\mu\text{m}$.

6.5.1 Time step (Δt)

In this part the effect of changing the time step size Δt is studied for the three different cases described earlier. Figure 6.7, 6.8 and 6.9 show the effect of the time step size Δt on the percentage maximum difference, the percentage root mean square of the difference, the percentage difference at peak of the pulse and the group velocity ratio of the FDTD and the TD-BPM for the three cases. In TD-BPM, $\Delta z = 0.1 \mu\text{m}$, and a Padé order $p = 4$ were used. The comparison between the three figures suggest that the TD-BPM method has a relatively large difference compared to the FDTD if the dispersion model has a strong dispersion profile and the initial pulse is in the ultra short range as in Figure 6.7. It is interesting to note, from Figure 6.8, that the method converges to small difference around $\Delta t = 3 - 4 \text{ fs}$, which means that the time step is around 93 - 124 times that used in the FDTD. The same observation can be noticed for the 25 fs pulse in Figure 6.9, for a small difference of around $\Delta t = 0.5 \text{ fs}$, for example, the time step size is 23 times the step sized used for the FDTD.

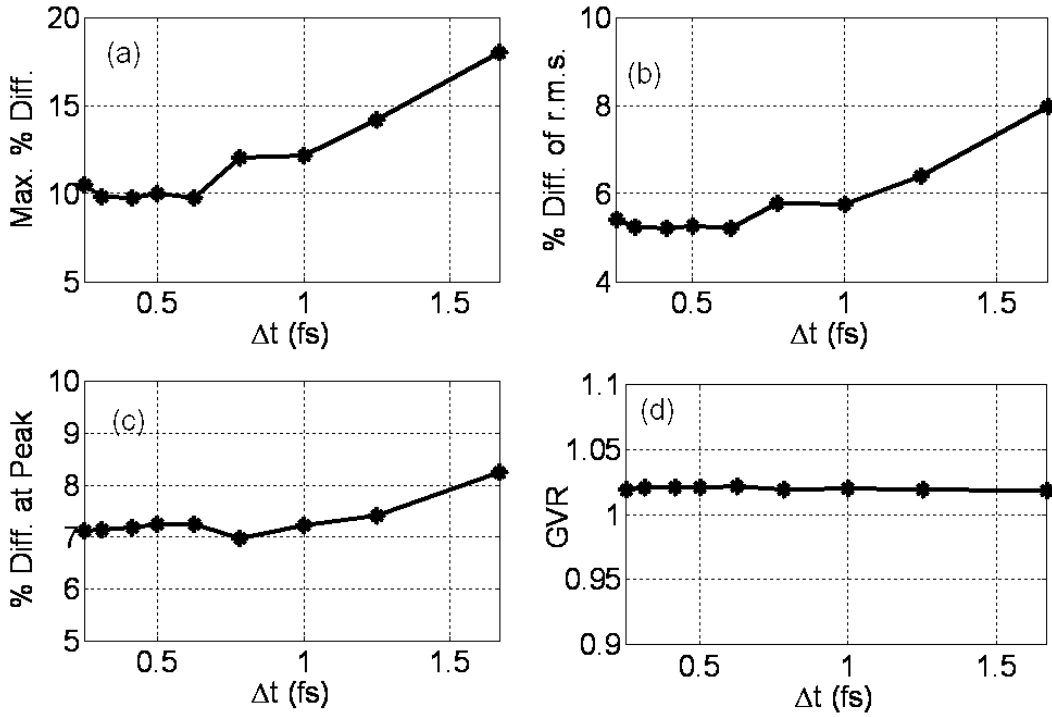


Figure 6.7 The effect of changing the time step size (Δt) on the accuracy of the technique in comparison with the FDTD (a) The percentage maximum difference (b) The percentage of root mean square of the difference (c) The percentage difference at peak, (d) Group Velocity Ratio for the propagation of a pulsed beam of 25 fs temporal waist inside a *GaAs* dispersive slab waveguide.

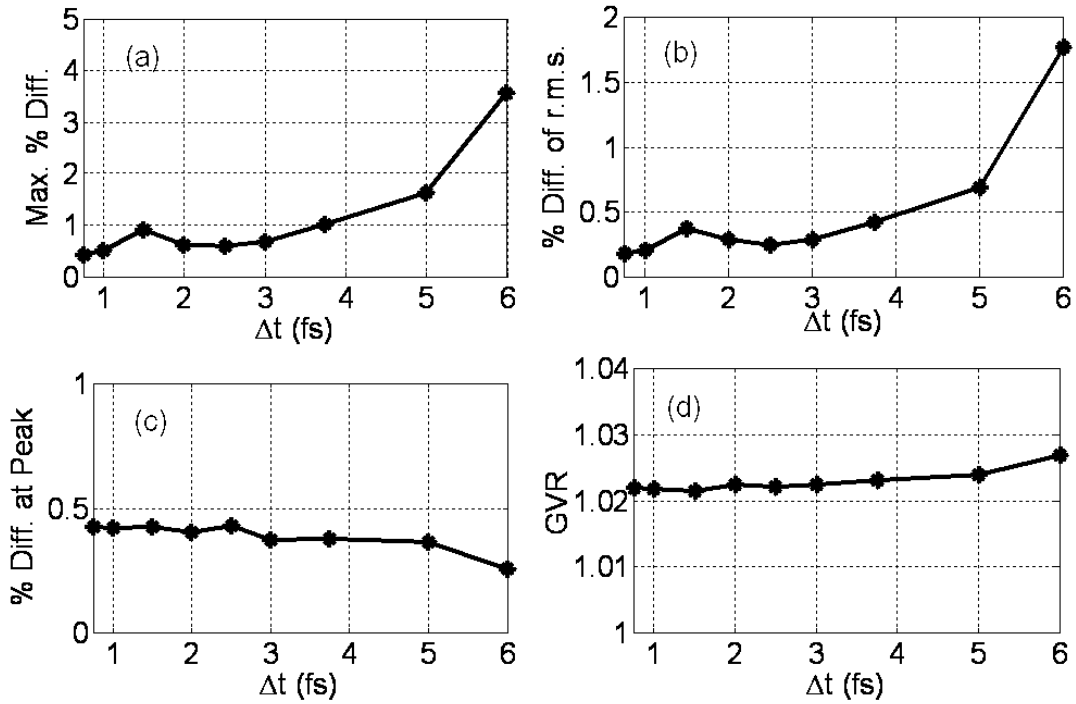


Figure 6.8 The same as in Figure 6.7 but with an initial temporal pulse waist of $\sigma_{t0} = 100$ fs.

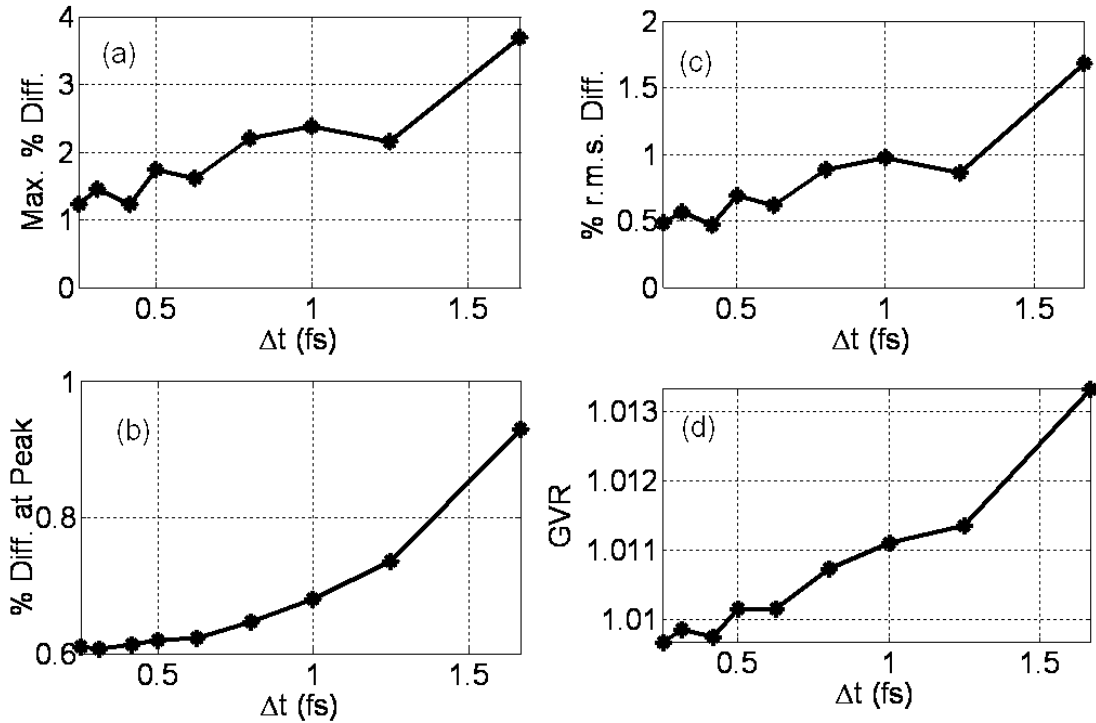


Figure 6.9 The same as in Figure 6.7 but with *AlGaAs* dispersive core waveguide whose Lorentz model parameters were given in the text.

It is to be noticed that the shape of the maximum percentage difference and percentage r.m.s. difference are the same. For this reason, the effect of Padé order and propagation step size is investigated by considering only the percentage r.m.s. difference.

6.5.2 Propagation step (Δz)

Figure 6.10 shows the effect of the variation of the propagation step size on the percentage root mean square difference between the two methods for all the three cases. Padé order $p = 4$ and time step sizes of $\Delta t = 0.4167$ fs and 1.25 fs for 25 fs and 100 fs pulse, respectively were used as numerical parameters for the TD-BPM.

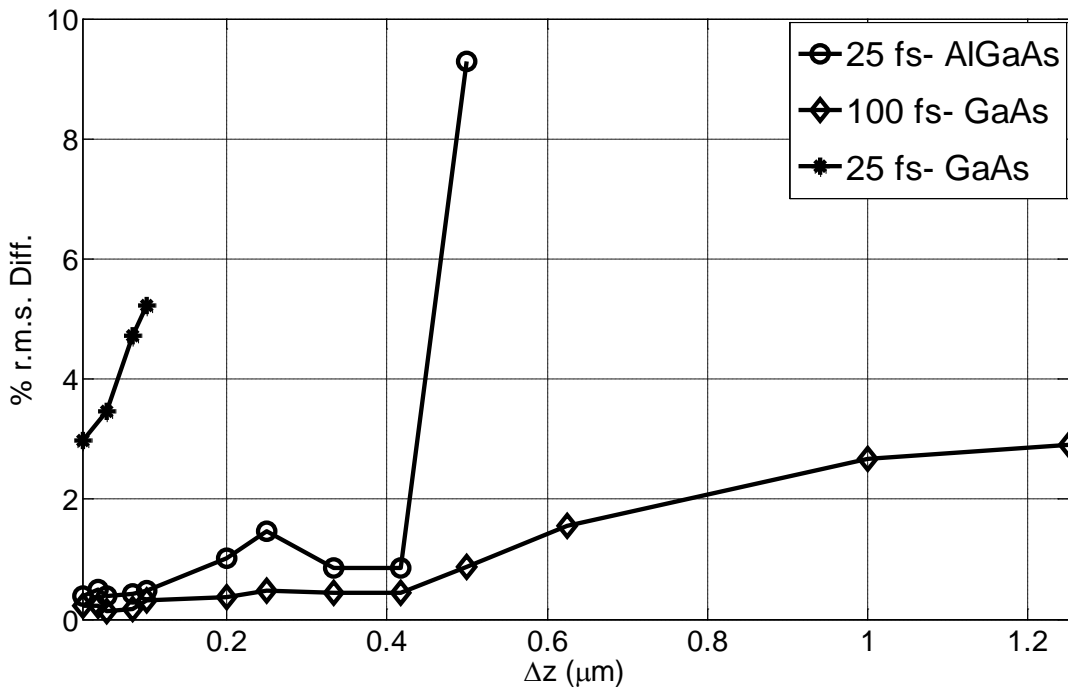


Figure 6.10 The effect of changing the propagation step size (Δz) on the percentage root mean square difference of the technique in comparison with the FDTD for the propagation of a pulsed beam of 25 fs and 100 fs temporal waist inside a strongly dispersive *GaAs* and a weakly dispersive *AlGaAs* dispersive slab waveguide.

The figure illustrates that the method is very stable even for large propagation step sizes (30 – 45 times higher than that of the FDTD) for short pulse width propagation in strongly dispersive material and for ultra short pulse propagation in weakly dispersive material. On the other hand, the difference for the 25 fs in *GaAs* core is a bit on the high side as compared to the other two cases. The following test may help to explain this difference.

6.5.3 Padé Order

Figure 6.11 shows the effect of varying the Padé order p on the percentage root mean square difference between the two methods for all the three cases. In TD-BPM, $\Delta z = 0.1 \mu\text{m}$ and time steps $\Delta t = 0.4167 \text{ fs}$ and $\Delta t = 1.25 \text{ fs}$ for 25 fs and 100 fs pulse widths were used,

respectively. At a Padé order of 8 or more, for ultra short pulse of 25 fs case in strongly dispersive material of *GaAs*, the r.m.s. difference becomes small. For the short 100 fs case in strongly dispersive material and for the ultra short 25 fs pulse case in weakly dispersive material of *AlGaAs*, a difference level of less than 1% is achieved even at Padé order of 2 and 4, respectively.

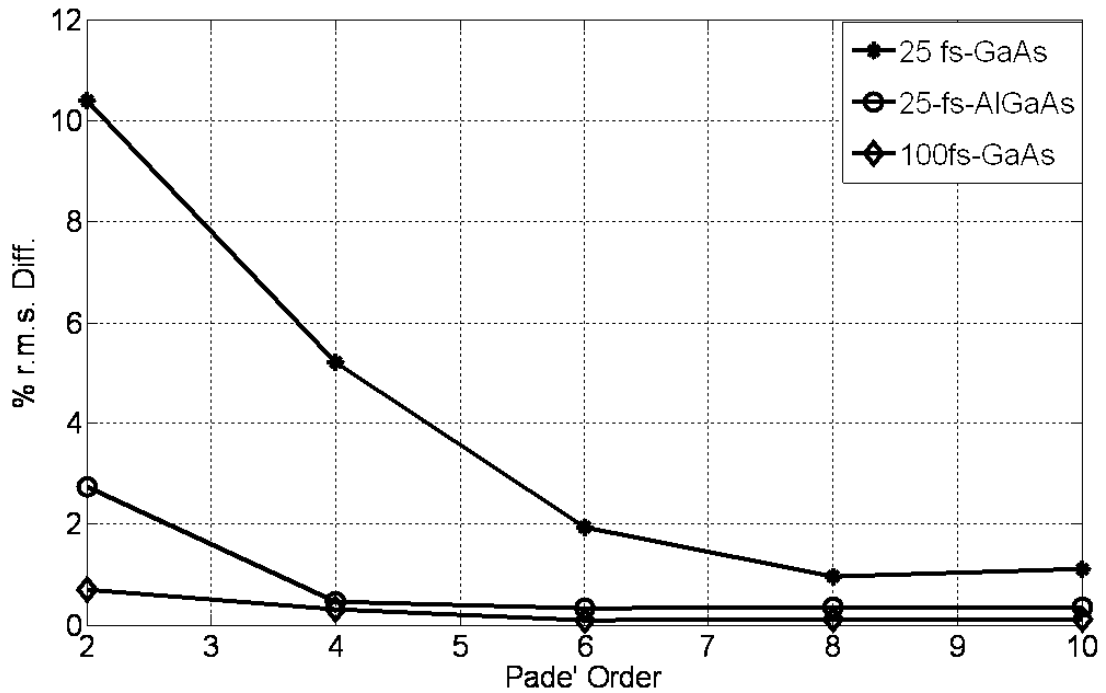


Figure 6.11 The effect of changing Padé order on the accuracy of the TD-BPM in comparison with the FDTD for the propagation of a pulsed beam of 25 fs and 100 fs temporal waist inside a strongly dispersive *GaAs* and a weakly dispersive *AlGaAs* dispersive slab waveguide.

It can be understood from the above performance tests that high accuracy is achieved using the TD-BPM with very low computational cost for ultrashort pulse propagation in weakly dispersive material and for short pulse propagation in strongly dispersive material. However, for the 25 fs ultrashort pulse propagation in the strongly dispersive *GaAs*, a Padé order of $p =$

8 or higher, $\Delta z = 0.05 \mu\text{m}$ and $\Delta t = 0.5 \text{ fs}$ or less results in sufficiently low differences, which eventually requires a longer computational cost.

6.6 The Performance of the FDTD

Since the dispersive problems considered in this thesis do not have analytical solutions, convergence of the FDTD parameters is examined in this section. For this purpose, the same waveguide parameters of the previous section have been taken into account. The TD-BPM parameters used are: Padé order $p = 8$, $\Delta z = 0.05 \mu\text{m}$ and $\Delta t = 0.5 \text{ fs}$, while for the FDTD $\Delta z = \lambda_c/80 = 0.019375 \mu\text{m}$ is kept fixed when $\Delta t/\Delta t_{CFL}$ was varied from 0.5 to 0.95. When $\Delta t/\Delta t_{CFL}$ is unity the method becomes unstable. Figure 6.12 shows the effect of the assessment parameters used earlier on varying $\Delta t/\Delta t_{CFL}$. The figure shows that the FDTD requires 0.8 the CFL limit for convergence.

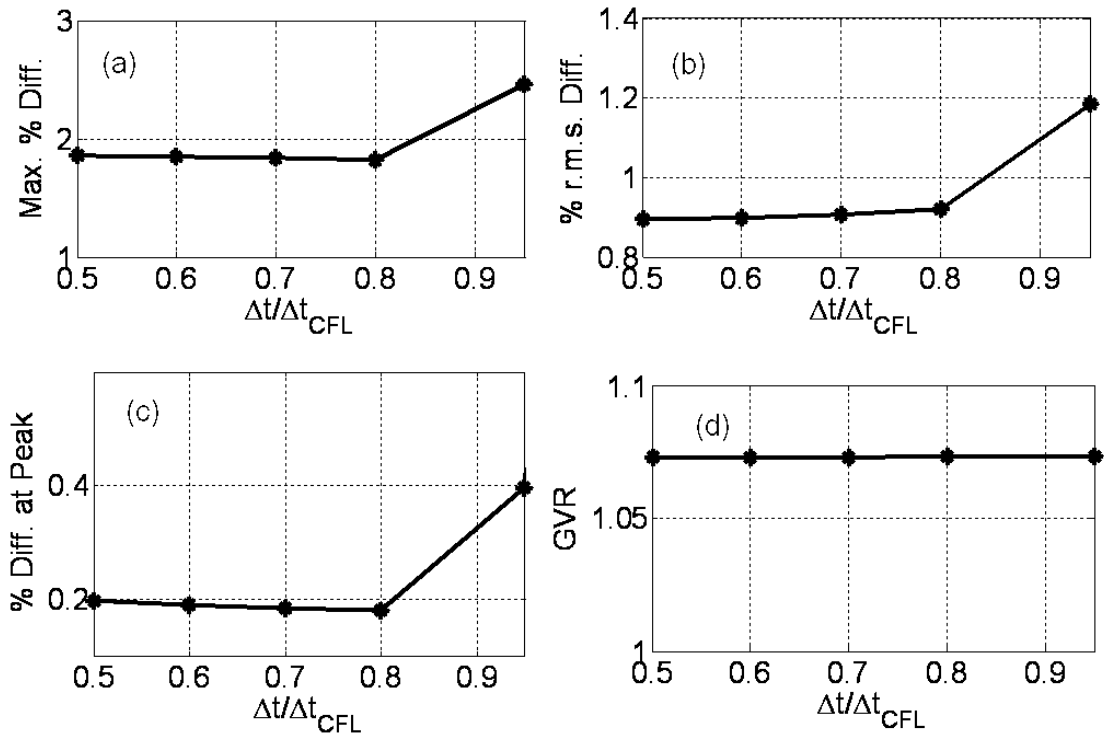


Figure 6.12 The effect of changing the time step size Δt on the accuracy of the FDTD in comparison with the TD-BPM (a) The percentage maximum difference (b) The percentage of root mean square of the difference (c) The percentage difference at peak, (d) Group Velocity Ratio for the propagation of a pulsed beam of 25 fs temporal waist inside a GaAs dispersive slab waveguide.

Figure 6.13 also shows the same analysis for the variation of the FDTD mesh size Δz , when $\Delta t / \Delta t_{CFL}$ is fixed to the values that keep the method stable as Δz is varied.

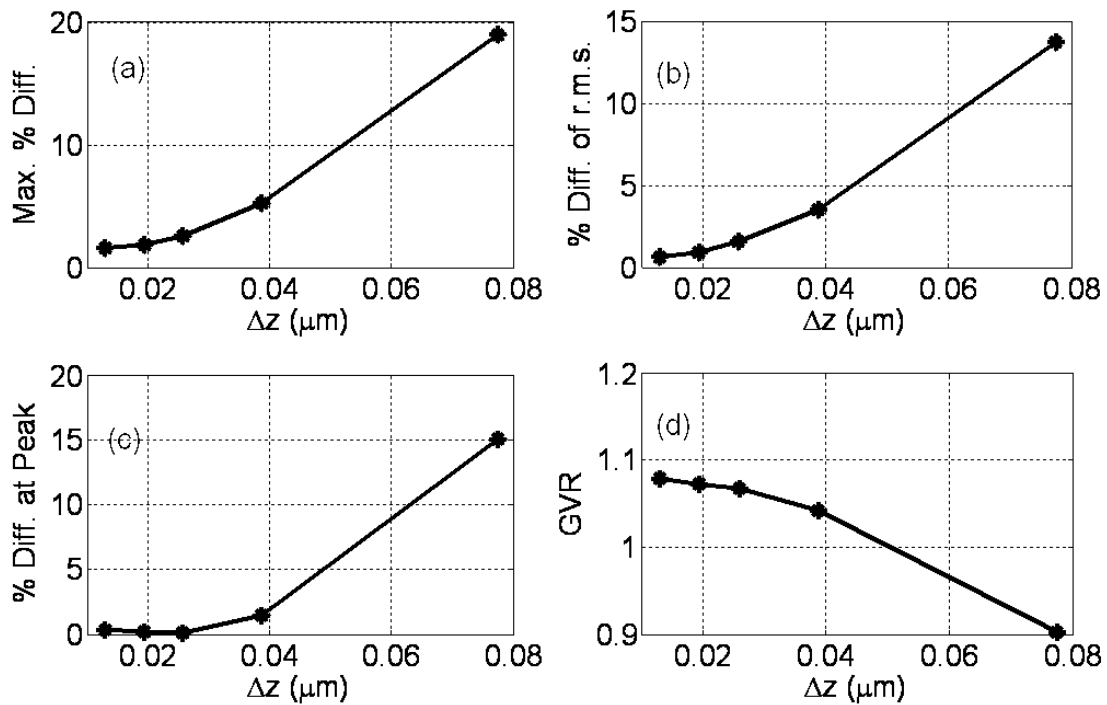


Figure 6.13 The same as of Figure 6.12 with the variation of the FDTD mesh size Δz .

Figure 6.13 shows that the FDTD requires very small values of Δz for convergence. For example when $\Delta z = 0.1 \mu\text{m}$, by which almost all the TD-BPM analysis were performed, the method becomes unstable. It is to be noted that fine mesh gridding refers to small time steps as well.

6.7 Computational Resource Requirement

In this section, the two methods are examined in terms of the computational resources required. The parameters used here have the same previous values, for Figure 6.7, except for the following. The pulsed beam was propagated to a distance of $z = 300 \mu\text{m}$ using Padé order, $p = 4$, propagation step size $\Delta z = 0.1 \mu\text{m}$, $\Delta x = 0.1 \mu\text{m}$ and time step sizes $\Delta t = 2.5 \text{ fs}$ and $\Delta t = 1.0 \text{ fs}$ for 100 fs and 25 fs, respectively. In the TD-BPM implementation different iterative

solvers discussed in chapter 4 have been used, such as the “QMR”, the “CGS” and the “LSQR” along with the direct method of implementing the Padé operator. It has been noticed that all the iterative solvers require almost the same computer memory space as the direct solver. However, they require different computational times for convergence. Figure 6.14 shows the computational time for 100 fs using the FDTD, the Moving Window (MW-FDTD) the iterative and the direct methods of the TD-BPM.

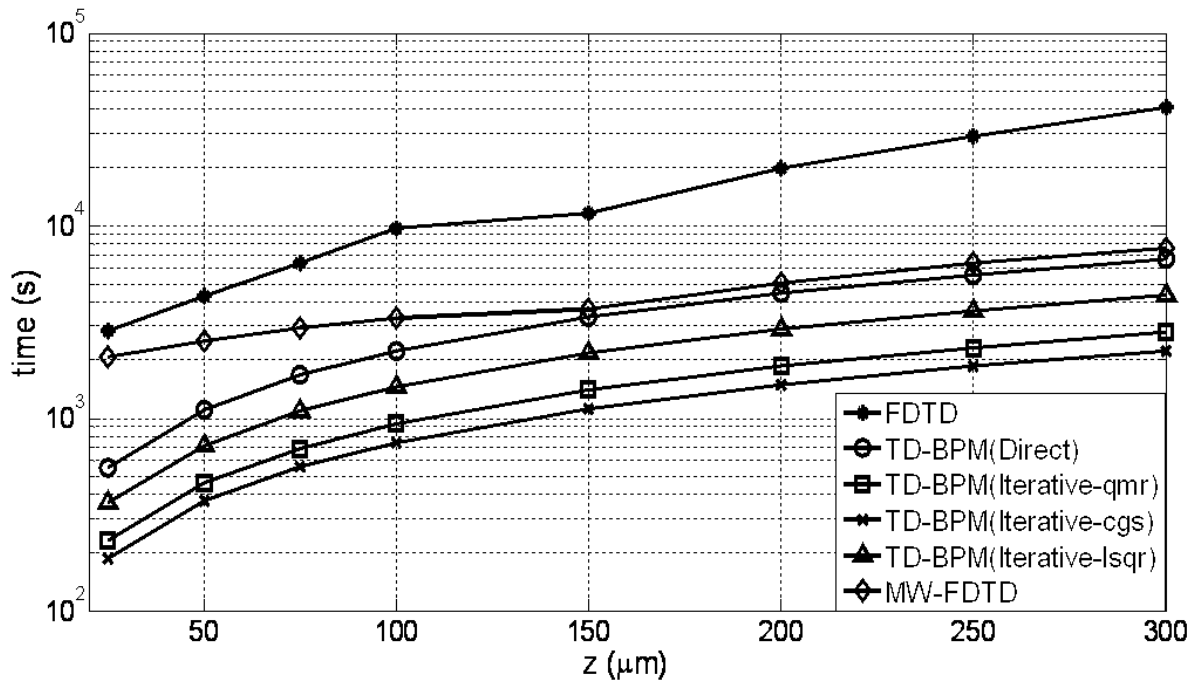


Figure 6.14 Computational time of the dispersive FDTD and the dispersive TD-BPM using the direct and the iterative solvers for the propagation of 100 fs pulsed beam in *GaAs* dispersive slab waveguide.

The figure shows that both the TD-BPM direct and the iterative techniques require less computational time than that of the FDTD and the MW-FDTD. The “CGS” always requires least computational time compared to any of the other techniques. Figure 6.15 shows the computational time for the 25 fs propagation inside *AlGaAs* dispersive waveguide using the same techniques.

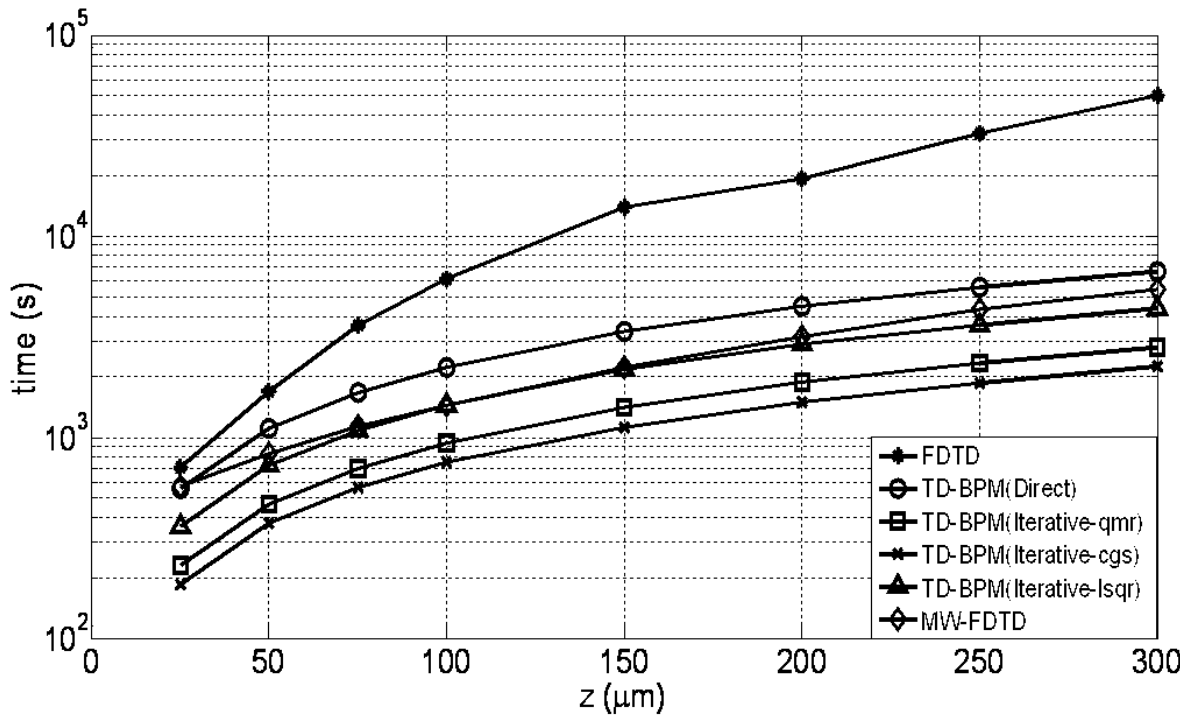


Figure 6.15 Computational time of the dispersive FDTD and the dispersive TD-BPM using the direct and the iterative solvers for the propagation of 25 fs pulsed beam in dispersive *AlGaAs* slab waveguide.

The figure shows that iterative solvers of the TD-BPM require less computational time than that of the FDTD and the MW-FDTD. At $z = 300 \mu\text{m}$ the “CGS” is around 22 times faster than the FDTD. Figure 6.16 shows the computer memory requirement by the time domain methods for the above two cases. The figures show that the proportionate increase of the memory consumption with the device size in the case of the FDTD is higher than the constant memory consumption of the TD-BPM using the direct or the iterative techniques. This is due to the fact that the TD-BPM is a unidirectional technique that follows the propagation of the pulse and thus requires less computational resources.

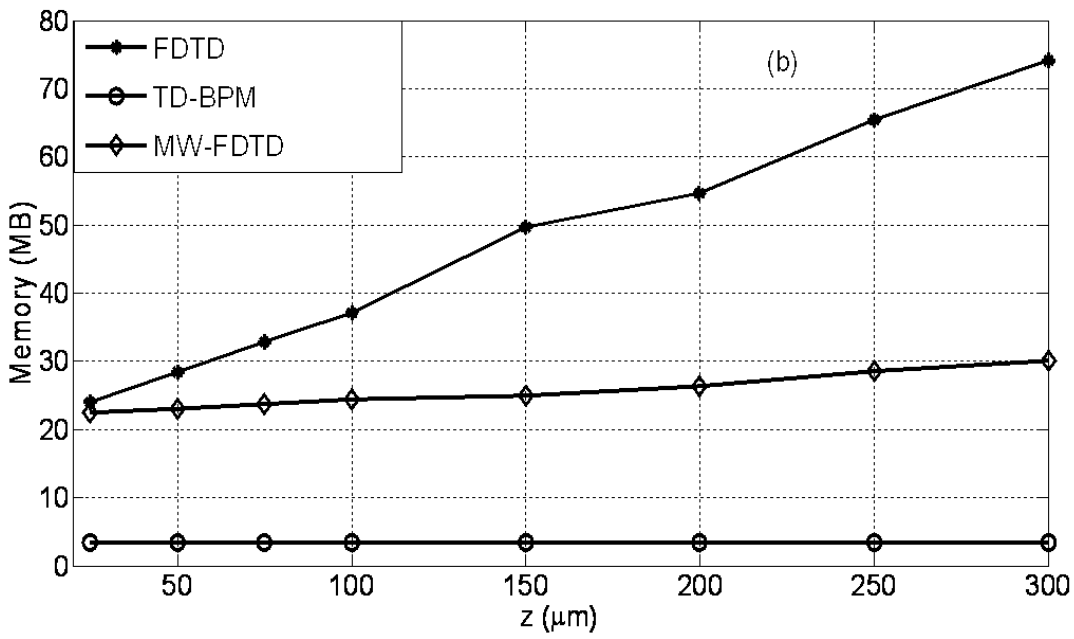
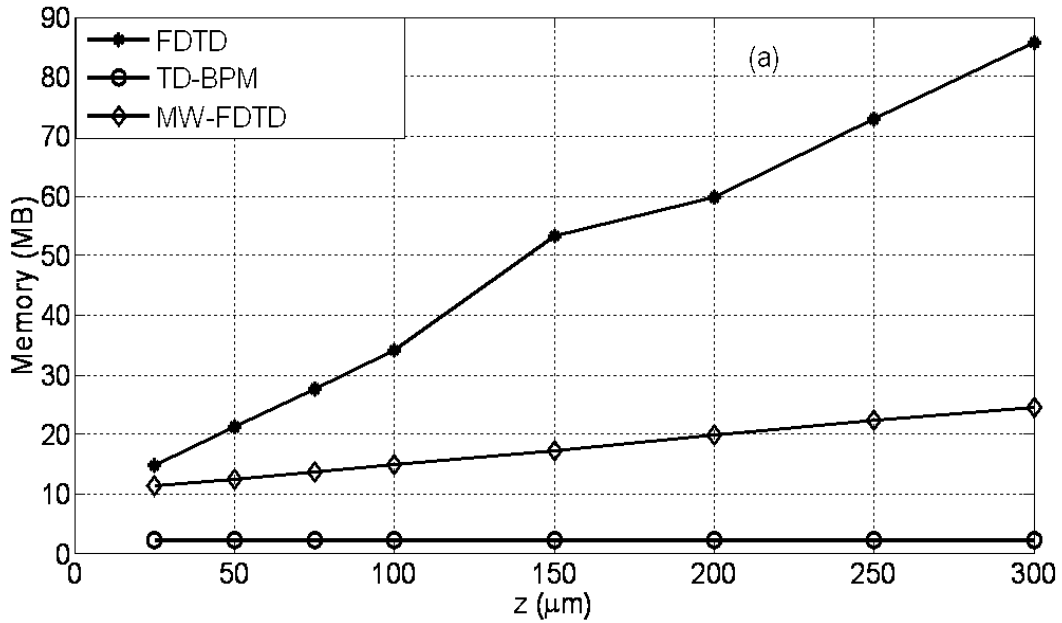


Figure 6.16 Memory usage by the dispersive FDTD and the dispersive TD-BPM using direct and iterative solvers with (a) 25 fs and (b) 100 fs pulsed beam.

Notes on the convergence of the dispersive TD-BPM

It has been noticed that the convergence and the accuracy of the dispersive TD-BPM is dependent on the time step size Δt used. Other numerical parameters (e.g., p and Δz) also play a role in the convergence of the dispersive TD-BPM. As Δt decreases, as expected, the accuracy increases. For weakly dispersive material Δt can be relaxed to relatively large values, as compared to the FDTD step size, even for ultra short initial pulse duration. For strong dispersive material Δt can be relaxed if the initial pulse duration is in the short range (e.g., 100 fs). Moreover, for ultra short pulse durations, Δt must be decreased to small values. Several numerical experiments showed that the size of Δt has an impact on the shape of the dense matrix T in Eq. 6.14 and as a result the operator matrix L_d . In the range of $\Delta t \approx 1.0$ fs or higher, the matrix T approaches a tri-diagonal matrix with the rest of the elements being very small values (e. g. 10^{-14}) where they have little influence on the accuracy of the method and hence can be eliminated. One such numerical experiment is shown in Figure 6.17. In this experiment $\Delta t = 2.5$ fs was used and the field amplitude at $z = 50 \mu\text{m}$ and $100 \mu\text{m}$ are obtained by the TD-BPM using both the full exact matrix and the manipulated tridiagonal approximate matrix of the dispersive matrix operator. The results are compared with that of the FDTD in terms of percentage difference of field amplitudes.

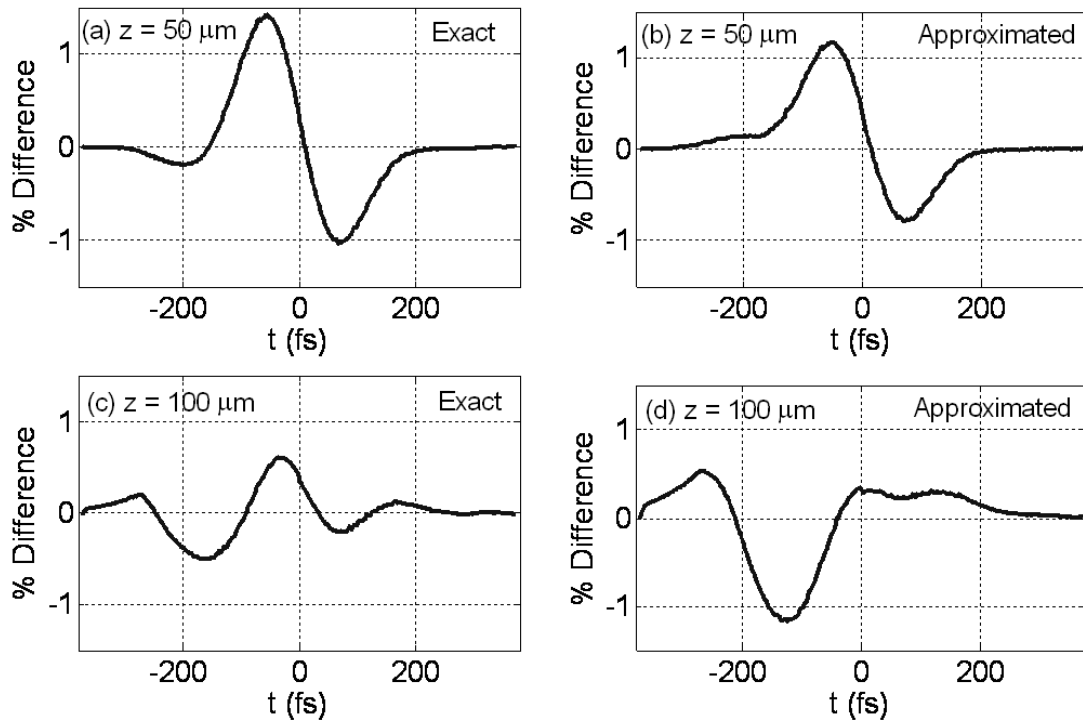


Figure 6.17 The effect on the percentage difference between the FDTD and the TD-BPM using the exact operator (a and c) and an approximated operator (b and d) at $z = 50 \mu\text{m}$ (a and b) and at $z = 100 \mu\text{m}$ (c and d) for the propagation of a pulsed beam of 100 fs temporal waist inside a *GaAs* dispersive slab waveguide.

It is clear from the figure that the percentage difference does not change much, if the approximate tridiagonal matrix of the dispersive TD-BPM operator is used. It is noted that the approximated TD-BPM consumes similar computational resources (time and memory) to those of the non-dispersive TD-BPM discussed in chapter 4. In addition, as it is known that the dispersive matrix L_d needs to be well conditioned for the convergence of iterative solvers, with large Δt provides faster convergence for these solvers. Therefore, the comparative results of the computational time and memory requirements shown earlier will be different with faster convergence and less memory requirements. On the other hand, for ultrashort pulse duration in strongly dispersive material sufficient discretized points are necessary to define the fast variations of the pulse profile. One possible solution to relax the time step size

Δt for ultra short pulses is to use higher order approximation of the finite difference method. If Δt is relaxed, then the dense matrix may produce banded dispersive matrix (e.g., tridiagonal or pentadiagonal) after eliminating small values, as discussed before, hence the efficiency can be improved.

6.8 Conclusion

Detailed mathematical formulations and numerical implementations of the TD-BPM have been shown for different dispersive devices. The chapter also shows the formulation and the implementation of the FDTD to study dispersive devices. One dimensional ultra short pulse propagation in dispersive media has been implemented by the TD-BPM and verified by the FDTD and the MoL. Excellent comparative results were observed. Short and ultra short pulsed beam propagation inside homogeneous dispersive medium, dispersive slab waveguide were also implemented and the results have been verified by the FDTD. The performance of the TD-BPM in terms of various accuracy measuring quantities has been analyzed rigorously with the variation of different numerical parameters, such as the time step size Δt , the propagation step size Δz and the Padé order p . Analysis shows that the TD-BPM is very stable, accurate and efficient technique for the analysis of short as well as ultra short propagation in dispersive material. Some results indicate that the time step size Δt for the TD-BPM is much larger than that needed for the FDTD (e.g., 23 - 123 times). Similar observations has been noticed for the propagation step size Δz . Propagation of ultra short optical pulses in a strongly dispersive material requires smaller time step sizes and higher Padé orders for convergence. For small values of Δt , the TD-BPM becomes less efficient compared to the FDTD due to the size of the main matrix of the operator. It has been noticed

that as Δt increases to the range of 1 fs the dispersive matrix L_d becomes similar to its corresponding non-dispersive one, and hence the dispersive TD-BPM technique shows similar efficiency to that of the non-dispersive TD-BPM discussed in chapter 4.

References

- [1] D. Werner and R. Mittra, *Frontiers in Electromagnetics*, Piscataway, NJ, IEEE Press, chapter 16, 1999.
- [2] E. K. Miller, "Time-domain modeling in Electromagnetics," *J. Electromagn. Waves Applicat.*, vol. 8, no. 9/10, pp. 1125–1172, 1994.
- [3] F. L. Teixeira, *Time-Domain Analysis*, J. Webster, Ed. New York: Wiley, Wiley Encyclopedia of Electrical and Electronics Engineering Online, 2001.
- [4] K. S. Yee, "Numerical solution of initial boundary value problems involving Maxwell's equations in isotropic media," *IEEE Trans. Antennas Propagat.*, vol. AP-14, pp. 302–307, May 1966.
- [5] A. Taflove and S. C. Hagness, *Computational Electrodynamics: The Finite-Difference Time-Domain Method*. Norwood, MA: Artech, 2000.
- [6] H. M. Masoudi, M. A. AlSunaidi, and J. M. Arnold, "Efficient time-domain beam propagation method for modeling integrated optical devices," *J. Lightw. Technol.*, vol. 19, no. 5, pp. 759–771, May 2001.
- [7] H. M. Masoudi, M. A. AlSunaidi, and J. M. Arnold, "Time-domain finite-difference beam propagation method," *IEEE Photon. Technol. Lett.*, vol. 11, no. 10, pp. 1274–1276, Oct. 1999.
- [8] M. Koshiba, Y. Tsuji, and M. Hikari, "Time-domain beam propagation method and its application to photonics crystal circuits," *J. Lightw. Technol.*, vol. 18, no. 1, pp. 102–110, Jan. 2000.
- [9] J. Shibayama, A. Yamahira, T. Mugita, J. Yamauchi, and H. Nakano, "A finite-difference time-domain beam-propagation method for TE- and TM-wave analyses," *J. Lightw. Technol.*, vol. 21, no. 7, pp. 1709–1715, Jul. 2003.
- [10] H. M. Masoudi, "A Stable Time-Domain Beam Propagation Method for Modeling Ultrashort Optical Pulses" *IEEE Photonics Technology Letters*, Vol. 19, No. 10, pp.

786-788, May 15, 2007.

- [11] S. Wang and F. L. Teixeira, "Some remarks on the stability of time-domain electromagnetic simulations," *IEEE Trans. Antennas Propag.* Vol. 52, pp. 895-898, 2004.
- [12] R. Courant, K. Friedrichs and H. Lewy, "On the partial difference equations of mathematical physics", *IBM Journal*, pp. 215-234, English translation of the 1928 German original, March 1967.
- [13] D. H. Lam, "Finite difference methods for transient signal propagation in stratified layered media," Ph.D. dissertation, The Ohio State Univ., Columbus, 1974.
- [14] D. F. Kelley and R. J. Luebbers, "Piecewise linear recursive convolution for dispersive media using FDTD," *IEEE Trans. Antennas Propag.*, vol. 44, pp. 792–797, Jun. 1996.
- [15] Luebbers R. J., D. Steich and K. Kunz, "FDTD calculation of scattering from frequency-dependent materials" *IEEE Trans. Antennas and Propagation*, vol. 41, pp. 1249 – 1257, 1993.
- [16] D. M. Sullivan, "Frequency dependent FDTD methods using z transforms," *IEEE Trans. Antennas Propag.*, vol. 40, pp. 1223–1230, 1992.
- [17] D. M. Sullivan, "z-transform theory and the FDTD method," *IEEE Trans. Antennas Propag.*, vol. 44, pp. 28–34, 1996.
- [18] R. K. Joseph, S. C. Hagness, and A. Taflove, "Direct time integration of Maxwell's equations in linear dispersive media with absorption for scattering and propagation of femtosecond electromagnetic pulses," *Opt. Lett.*, vol. 16, no. 18, pp. 1412–1414, 1991.
- [19] O. P. Gandhi, B. Q. Gao, and J. Y. Chen, "A frequency-dependent finite difference time-domain formulation for general dispersive media," *IEEE Trans. Microw. Theory Tech.*, vol. 41, no. 4, pp. 658–665, 1993.
- [20] J. Shibayama, A. Nomura, R. Ando, J. Yamauchi, and H. Nakano, "A frequency dependent LOD-FDTD Method and its application to the analyses of plasmonic waveguide devices", *IEEE Journal of Quantum Electronics*, vol. 46, no. 1, pp. 40–49, January, 2010.
- [21] K.-Y. Jung and F. L. Teixeira, "Multispecies ADI-FDTD algorithm for nanoscale three-dimensional photonic metallic structures," *IEEE Photon. Technol. Lett.*, vol. 19, no. 8, pp. 586–588, Apr. 2007.
- [22] P.-L. Liu, U. Zhao, and RS. Choa, "Slow-wave finite-difference beam propagation

method," *IEEE Photon. Technol. Lett.*, vol. 7, pp. 89CL892, Aug. 1995.

- [23] G. H. An, J. Haran, 1. P. Vilcot, and D. Decoster, "An improved time-domain beam propagation method for integrated optics components," *IEEE Photon. Technol. Lett.*, vol. 9, pp. 348-350, Mar. 1997.
- [24] M. A. Alsunaidi, F. S. Alhajiri, and H. M. Masoudi, " A FDTD Algorithm for the analysis of Short Optical Pulse second harmonic Generation in Dispersive Medium", *Microwave and Optical Techn. Lett.*, vol. 51, no. 4, April 2009.

CHAPTER 7

DISPERSIVE DIRECTIONAL COUPLER ANALYSIS

7.1 Introduction

The Optical Directional Coupler (ODC) forms the basis for many important elements used in photonic structures, such as optical power splitters, nonlinear optical switches and WDM filter devices. The basic structure of the ODC is placing two cores in close proximity so that the electric field can be coupled from one core to the other. Coupled optical waveguide structure shows potential of being used as an all optical switch, which in turn, provides the carriers to manage the new and competitive dense wavelength division multiplexing (DWDM) networks. This type of network eventually provides the increasing demand for high bandwidth. In recent years considerable research work has been conducted on twin core fiber for switching applications [1-3]. The operation of CW of the ODC is well documented in the literature. Under special conditions, when CW light is launched in one waveguide it can completely couple into the other waveguide. The same light couples back to

the original waveguide using the same mechanism as long as they are close to each other. Complete power exchange is only possible between modes with equal propagation constants for each waveguide in isolation. This condition is called phase matching or “synchronism”. In other words, all guided modes (for more than one) of two identical waveguides are mutually in phase, and therefore can couple to each other at all wavelengths. Non-identical waveguides can have coupling between modes whose phases are accidentally synchronized for certain wavelengths [4]. On the other hand, few studies have touched on the analysis of short pulse propagation in the ODC and little is known for pulse propagation in dispersive ODC. One of the underlying challenges behind the design of coupled waveguide structures is intermodal dispersion [5] which causes pulse spreading and even splitting of the pulse and as a result a loss of information [6]. This is the dispersion that takes place between the two dominant modes of the directional coupler structure. This intermodal dispersion is severe for the propagation of short and ultrashort pulses which have broad frequency spectra. The material dispersion adds another challenge in designing ODC, as the dispersive material has varied refractive indices over a large frequency spectrum for short pulses. Thus, it is essential to distinguish between the effect of material dispersion and intermodal dispersion in the case of short pulse propagation. One may recognize the complicated behavior of pulse propagation in dispersive directional coupler devices, due to the involvement of several variables in the mechanism of power exchange between the two waveguides. This behavior is completely different from the usual CW case. Therefore, it requires reliable and accurate numerical tools to investigate the complicated phenomenon of short pulse propagation in dispersive directional coupler devices. In this chapter, we use the previously discussed

numerical tools (the FDTD and the TD-BPM) for the analysis of short and ultrashort pulse propagation in a dispersive directional coupler.

7.2 Background

It has been predicted in 1995 [4] that the intermodal dispersion can break up short pulses launched in directional couplers. Later on, this break up phenomenon has been observed experimentally [7]. When a pulse is launched in one waveguide of the directional coupler structure, the two normal modes (supermodes) of the structure are excited equally at the input. If the initial pulse duration is smaller than the group delay difference along the length of interaction between the two supermodes, the two modes walk away from each other over propagation length of the coupler and they exit from each waveguide output as two splitted pulses of equal amplitudes. The total input power will be divided equally on the four pulses and the power exchange mechanism stops. [8]. Coupled mode theory can be used to describe the interaction of pulse propagation in non-dispersive directional coupler using an approximate one-dimensional approach. Considering weakly coupled waveguides, the electric field can be written as a sum of the fields in each waveguides as

$$E(x, y, z, t) = A_1(z, t)B_1(x, y)e^{-j(\omega_0 t - \beta_0 z)} + A_2(z, t)B_2(x, y)e^{-j(\omega_0 t - \beta_0 z)} \quad (7.1)$$

where z is the direction of propagation, A_1 and A_2 are the slowly varying envelopes of the modes of the waveguides in separation, B_1 and B_2 are the transverse spatial field profiles for each waveguides, β_0 is the propagation constant and ω_0 is the central carrier frequency of the pulse. The two coupled equations can be formulated as [7]

$$i \left(\frac{\partial A_1}{\partial z} + \frac{1}{v_g} \frac{\partial A_1}{\partial t} + C'' \frac{\partial A_2}{\partial t} \right) - \frac{k''}{2} \frac{\partial^2 A_1}{\partial t^2} + C A_2 - \frac{C''}{2} \frac{\partial^2 A_2}{\partial t^2} = 0 \quad (7.2)$$

$$i \left(\frac{\partial A_2}{\partial z} + \frac{1}{v_g} \frac{\partial A_2}{\partial t} + C'' \frac{\partial A_1}{\partial t} \right) - \frac{k''}{2} \frac{\partial^2 A_2}{\partial t^2} + C A_1 - \frac{C''}{2} \frac{\partial^2 A_1}{\partial t^2} = 0 \quad (7.3)$$

where the propagation constant β , when expanded around the carrier frequency ω_0 gives

$$\begin{aligned} \beta(\omega) &= \beta(\omega_0) + \Delta\omega \left. \frac{d\beta}{d\omega} \right|_{\omega_0} + \frac{(\Delta\omega)^2}{2} \left. \frac{d^2\beta}{d\omega^2} \right|_{\omega_0} + \dots \\ &= \beta(\omega_0) + \frac{\Delta\omega}{v_g} + \frac{(\Delta\omega)^2}{2} k'' + \dots \end{aligned} \quad (7.4)$$

where v_g and k'' are the group velocity and group velocity dispersion, respectively. The group velocity dispersion (GVD) k'' is responsible for pulse broadening [9 - 12]. When a pulse is launched in an optical waveguide, it behaves differently for the sign of k'' . For normal dispersion regimes (wavelengths where $k'' > 0$) high frequency component of optical pulse (blue shifted) travel slower than the low frequency component (red shifted). Opposite action happens for the anomalous dispersion regime (wavelengths where $k'' < 0$). Similarly, the coupling coefficient C that depends on the overlap between the spatial fields B_1 and B_2 , can be expanded around the carrier frequency ω_0 as

$$C(\omega) = C(\omega_0) + \Delta\omega C'(\omega_0) + \frac{(\Delta\omega)^2}{2} C''(\omega_0) \quad (7.5)$$

Where $C' = \frac{dC}{d\omega}$ and $C'' = \frac{d^2C}{d\omega^2}$ are respectively the first order and the second order coupling coefficient dispersion terms. Using the normal mode expansion [8] we can write

$$C = \frac{\beta^e - \beta^o}{2} \quad (7.6)$$

and

$$\beta = \frac{\beta^e + \beta^o}{2} \quad (7.7)$$

where β^e and β^o are the propagation constants of the even and the odd modes of the structure, respectively. The intermodal dispersion is given as

$$\delta_\tau = \tau^e - \tau^o = 2 \frac{dC}{d\omega} \quad (7.8)$$

This is actually the group delay difference between the two modes per unit length.

7.3 Numerical Implementations

In this section, both TD techniques of the TD-BPM and the FDTD, discussed in the previous chapters, have been used to analyze the propagation of pulsed optical beams in a dispersive directional coupler. The objective of this analysis is to study the effect of material dispersion on the mechanism of coupling when excited by short and ultra short pulses. Figure 7.1 shows the geometry of the dispersive directional coupler structure with a separation of s . The directional coupler shown consists of both dispersive and non-dispersive layers.

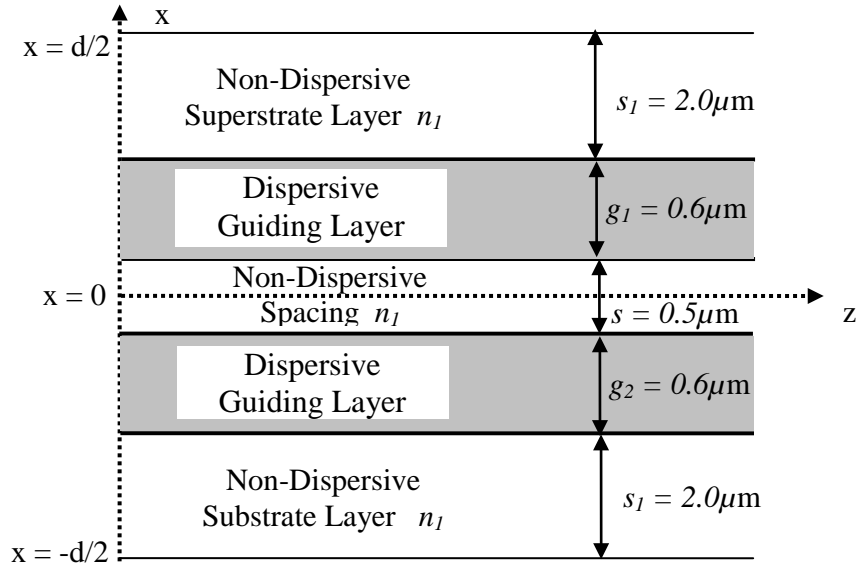


Figure 7.1 The Dispersive Directional Coupler Geometry

The core refractive index of the device having a dispersive material is approximated by the Lorentz model surrounded by non-dispersive materials with a refractive index of 3.4. The Lorentz model approximates the dispersive property of *GaAs*, used in chapter 6, with $\epsilon_\infty = 1.0$, $\epsilon_s = 11.011$, $\omega_0 = 3.0138425 \times 10^{15}$ rad/s and $\delta = 5.0 \times 10^{11}$ s⁻¹. It is to be noticed that these parameters are the same parameters used to test the performance of the TD-BPM and the FDTD of chapter 6. As it has been noticed before that the dispersive parameters of this waveguide suggests that it has relatively strong dispersion relation at the center-carrier wavelength. The operating carrier wavelength is $\lambda_c = 1.55$ μm . In all of the simulation results that follows again a Gaussian pulsed beam in time of the form $\psi(x, z = 0, \tau) = \psi_0(x) \exp(-\tau^2/\sigma_\tau^2)$ is launched as an input field, excited at $z = 0$ in one of the waveguides, while a zero field is assumed at the second waveguide. Here $\psi_0(x)$ is the spatial profile in the x -direction taken as the TE₀ mode of a single waveguide of the

directional coupler structure. Each waveguide is single mode at the central carrier wavelength λ_c .

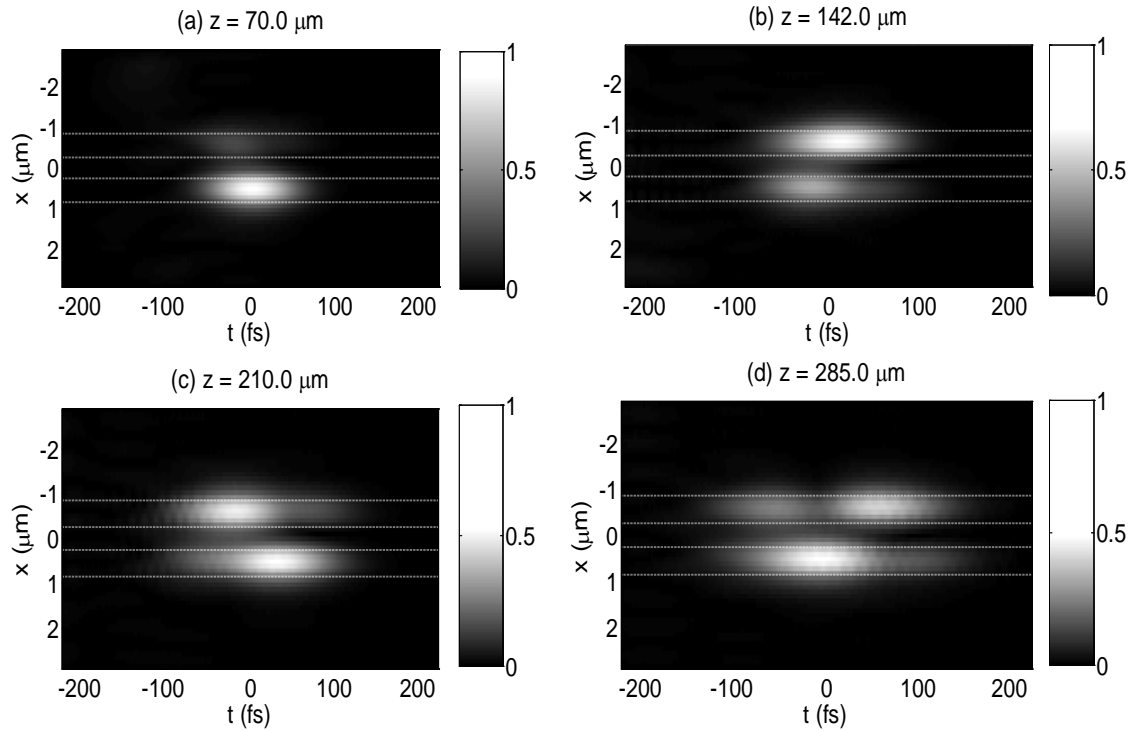


Figure 7.2 Evolution of the pulsed optical beam with an initial pulse width of 50 fs inside the dispersive directional-coupler structure of Figure 7.1 at several distances along the longitudinal direction. The horizontal lines show the position of the two waveguide boundaries.

Figure 7.2 shows the evolution of the pulsed beam in the spatio-temporal window of the TD-BPM for a 50 fs initial pulse width at several propagation distances. The input (not shown here) has been launched in the upper waveguide. The figure shows the exchange of power of the pulsed beam between the two waveguides along the propagation direction. The figure also shows the pulse splits into two pulses in the input waveguide as can be seen in Figure 7.2 (d). Figure 7.3 and 7.4 show the time profiles of the propagated pulsed beam inside the dispersive directional coupler for two different initial pulse widths of 25 fs and 120

fs respectively, using the TD-BPM and the FDTD techniques. The profiles shown are taken at the middle of the two waveguides indicated by WG_1 (where the input was launched) and WG_2 (the other waveguide). The figures show the time profiles of the pulse at two distances of $z = L_c/2$ and $L_c = 57.27 \mu\text{m}$, where L_c is the CW coupling length. The numerical parameters used for these simulation results are: $\Delta z = \lambda/80 = 0.019375 \mu\text{m}$ and $\Delta t = \Delta z / (2c_0)$ to meet the CFL criteria for the FDTD. The TD-BPM parameters are $\Delta z = 0.05 \mu\text{m}$, $p = 8$ and $\Delta t = 0.40$ fs and 1.8 fs for $\sigma_{t0} = 25$ fs and 120 fs respectively, while $\Delta x = 0.1 \mu\text{m}$ for both techniques.

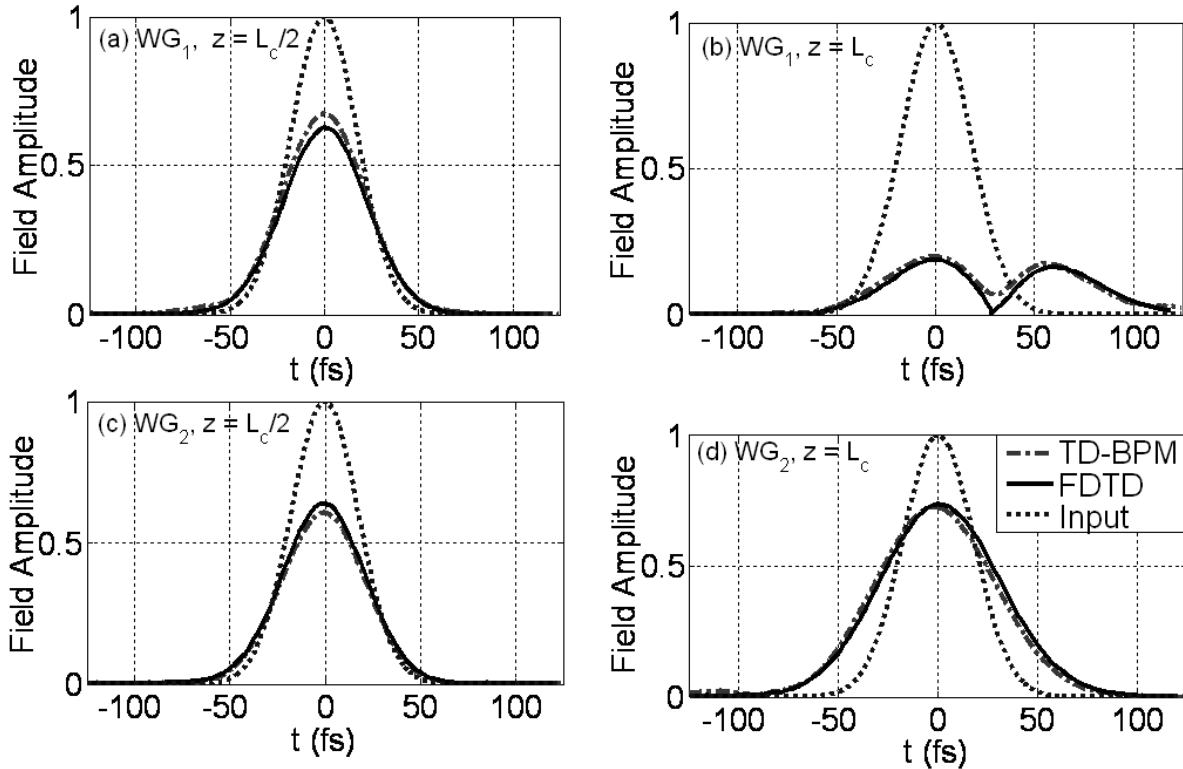


Figure 7.3 Temporal profiles at two distances along the z direction in the two waveguides of a directional coupler for an initial pulse-width of 25 fs using the TD-BPM and the FDTD. WG_1 is the waveguide where the input has been launched.

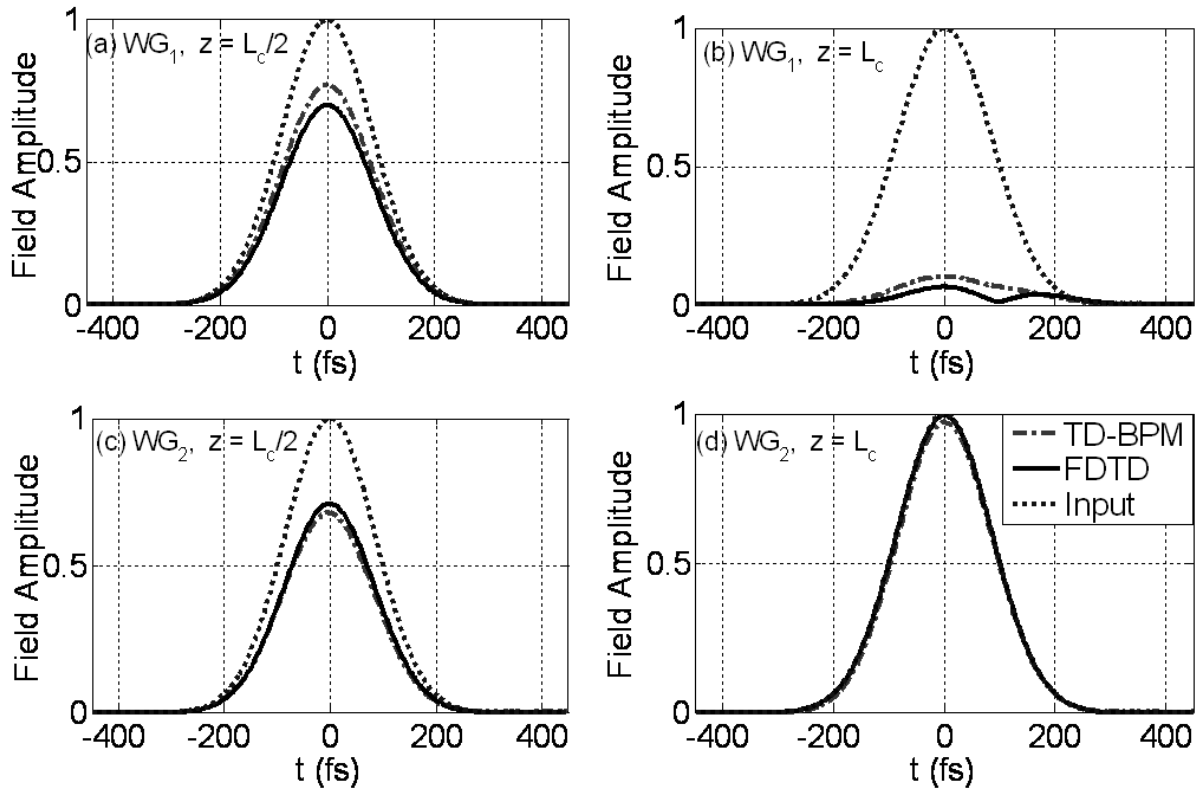


Figure 7.4 The same as of Figure 7.3 but for an input beam of 120 fs temporal pulse-width.

Comparison between the two figures show that the interaction of ultra short pulses of 25 fs range with the dispersive material gives rise to attenuated pulse energy in addition to pulse spread and hence the pulse splits as shown in Figure 7.3(b). Short pulses in the range of 120 fs has little change in comparison to the input at this distance compared to the ultra short pulses in the range of 25 fs as the power exchange takes place along the directional coupler structure. The effect on short pulses is seen to take place at longer distances than those of ultra short ones as will be discussed in detail in the following section.

7.4 Material and Intermodal Dispersions Analysis

To understand the complicated behavior of the interaction of ultra short pulse propagation inside a dispersive directional coupler, we compare the propagation of different initial pulse widths over a distance of several coupling lengths. The distance of $z = 286.3 \mu\text{m}$ is around five times the coupling length of the CW operation of the directional coupler. In addition, several numerical experiments have been performed to distinguish between the material dispersion effects from those of the intermodal dispersion effects. Figure 7.5, 7.6 and 7.7 show the normalized power versus the propagation distances z of the two waveguides of the directional coupler for CW and for different initial pulse-widths. Curves starting with a normalized power of one belong to the upper half of the computational window with respect to x indicated by WG_1 , where the input was launched. Curves starting with a zero normalized power belong to the lower half of the computational window that contains the unexcited waveguide indicated by WG_2 . Figure 7.5 shows the normalized power inside the waveguides for the 120 fs initial pulse width inside dispersive and non-dispersive DC structures. The corresponding CW normalized power of the non-dispersive DC structure has been included in the figure as a reference.

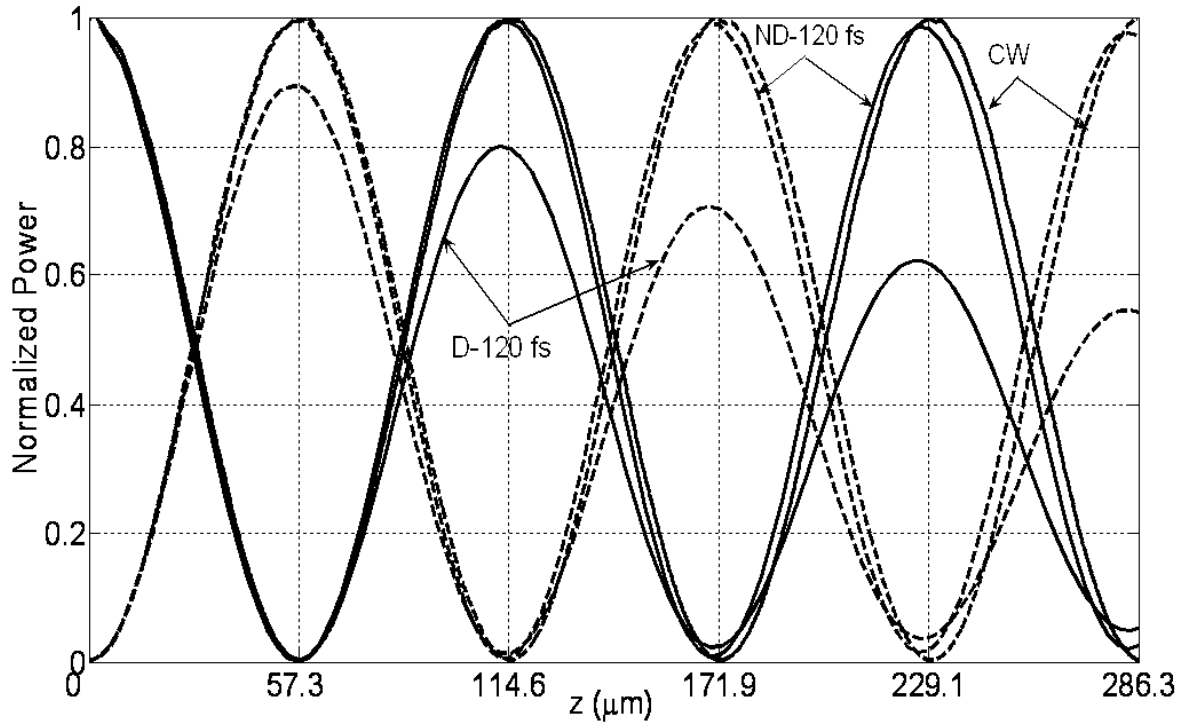


Figure 7.5 Normalized power inside the upper and lower waveguides of the directional coupler along the direction of propagation for CW and 120 fs initial pulse-width. Solid lines belong to the upper waveguide (WG_1) where the input was launched and dashed lines belong to the lower waveguide (WG_2). D means dispersive and ND means non-dispersive.

For this case, material dispersion has a strong effect on the behavior of power exchange, especially at large distances. The effect of material dispersion on the propagation of 120 fs pulse can be seen very clearly in the figure. Figure 7.6 shows a comparison between the dispersive DC (indicated by D) and the non-dispersive (indicated by ND) DC, when the material dispersion of two waveguides is turned-off for an input of 50 fs initial pulse width.

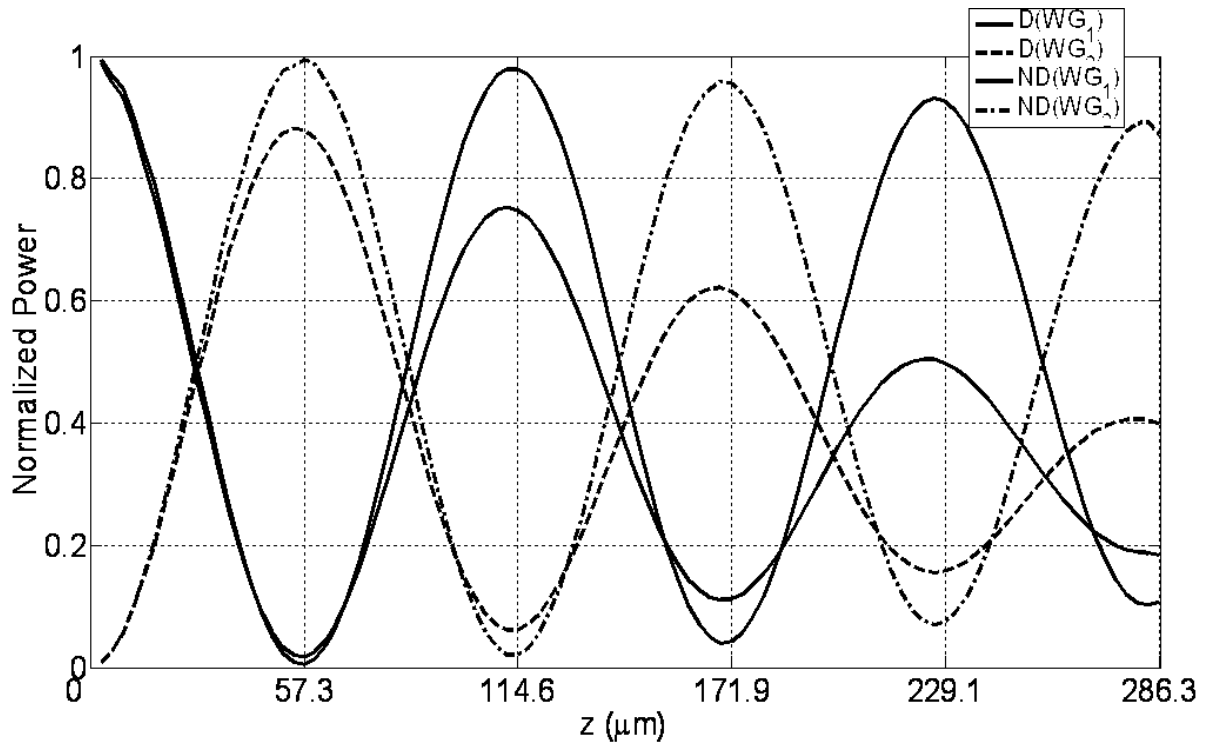


Figure 7.6 The same as in Figure 7.5 but for an initial pulse width of 50 fs.

The figure shows clearly the effect of material dispersion on the propagation of 50 fs pulse. The amount of power exchange between the two waveguides is seen to decrease along the direction of propagation where the reduction for the dispersive case is much larger than that of the non-dispersive case. It is to be noted that the reduction of power exchange is also accompanied by a reduction of power loss in the intermodal dispersion case. Figure 7.7 shows the same simulation as in Figure 7.6, but for the shorter pulse width of 25 fs. Similar conclusions can be drawn from Figure 7.7 as those of 50 fs, but with more reduction in power exchange between the two waveguides.

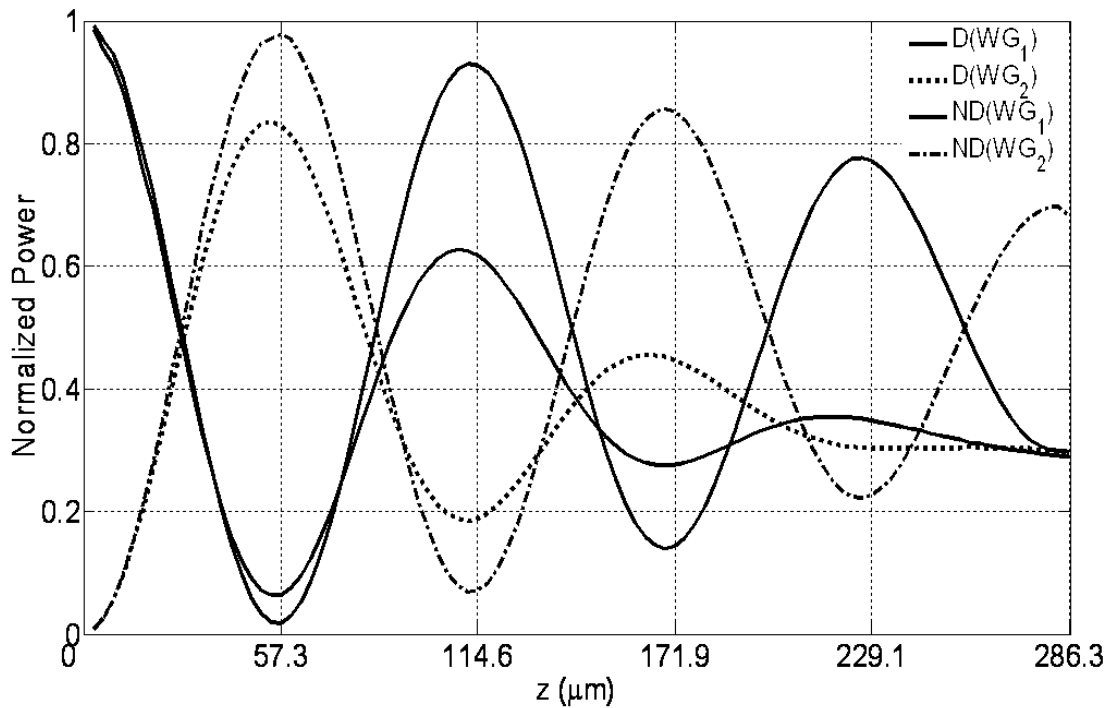


Figure 7.7 The same as in Figure 7.6 but for an initial pulse width of 25 fs.

As we have discussed in the previous chapter, material dispersion causes group velocity dispersion and losses in the material. To study the effect of losses due to dispersive material, Figures 7.8 and 7.9 show a comparison between the normalized power for dispersive material in the case of $\delta = 5.0 \times 10^{11} \text{ s}^{-1}$ (as given before) and when $\delta = 0$ (zero loss) for initial pulse widths of 50 fs and 25 fs of Figures 7.6 and 7.7, respectively. At $z = 286.3 \text{ } \mu\text{m}$, there is roughly 40% loss in energy within the device as can be seen from the figures.

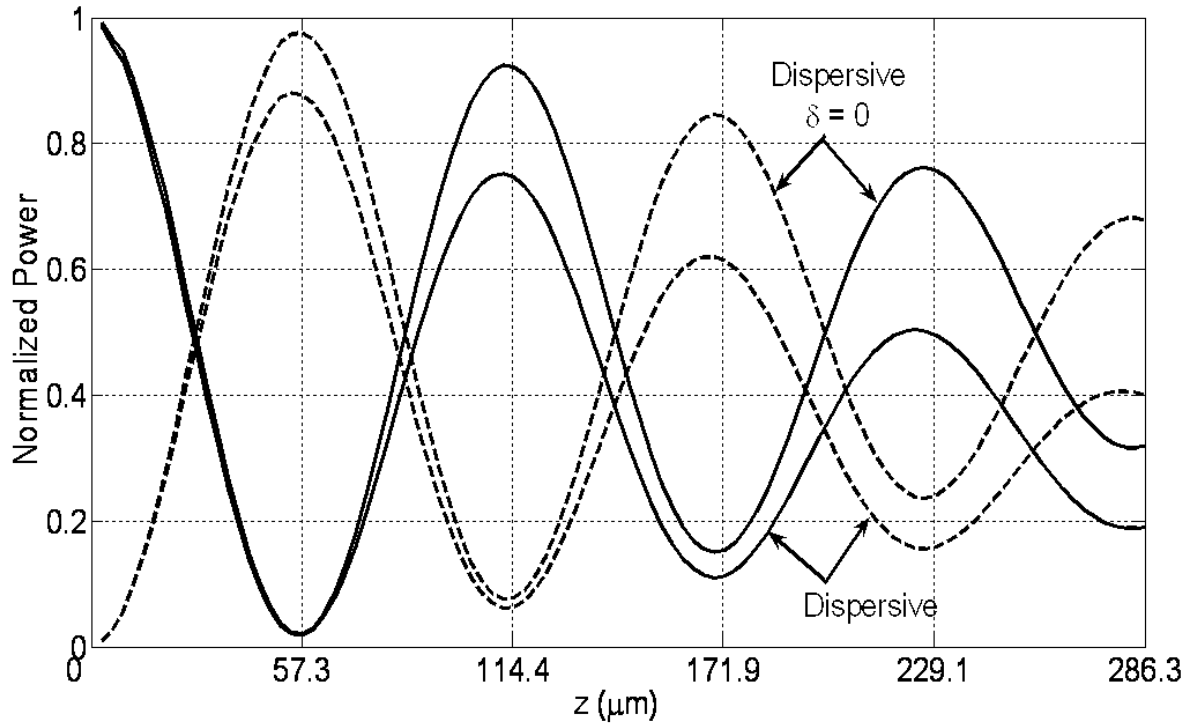


Figure 7.8 The same as in Figure 7.6, but for $\delta = 0$.

Comparison between Figures 7.8 and 7.9 along with the previous analysis of Figure 7.5, leads us to conclude that the energy loss at this central carrier wavelength is not affected greatly by the initial pulse width duration. This is due to the fact that the central carrier wavelength of the pulsed beams are relatively far from the resonance of the imaginary part of the dielectric constant of *GaAs*, as can be seen in Figure 5.3 (b) and (d). Although the central carrier wavelength is far from resonance, this has a large impact on the propagation of the pulse in the dispersive DC structure.

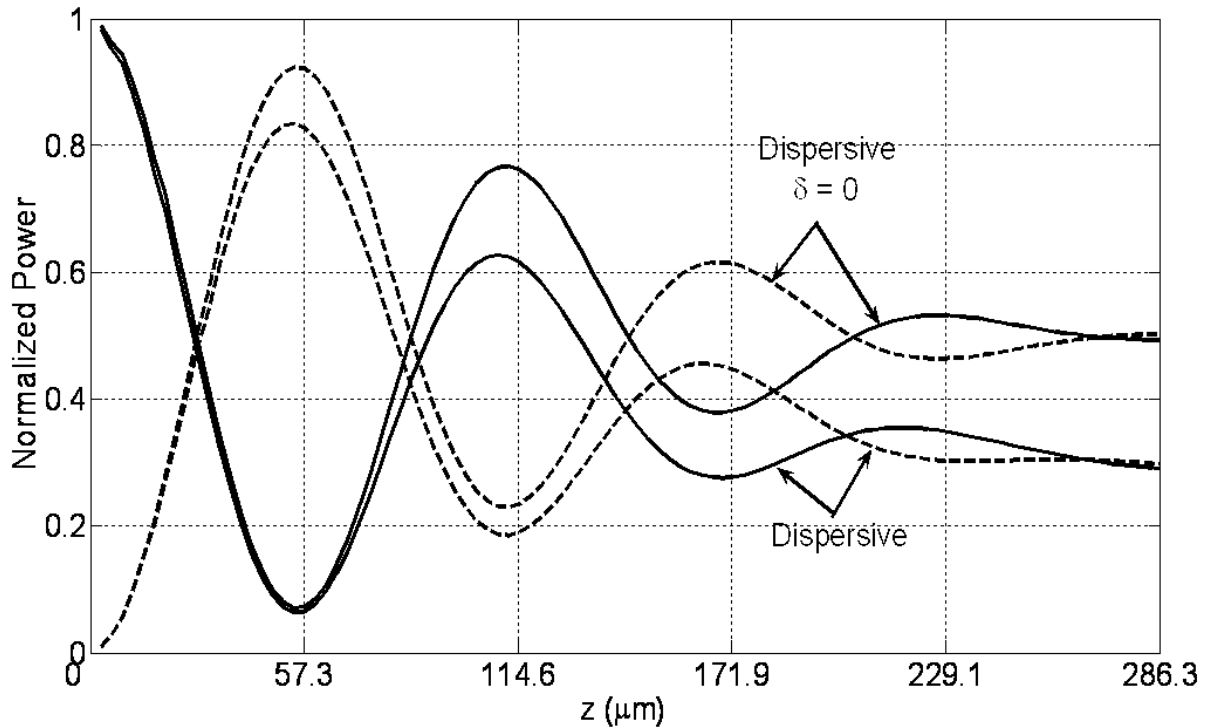


Figure 7.9 The same as in Figure 7.7, but for $\delta = 0$.

7.5 Pulse Spread Due to Material and Intermodal Dispersions

It is well known that as the initial pulse duration decreases the frequency content increases. Thus, an ultra short pulse in the range of 25 fs which contains a wide band of frequencies around the central carrier frequency, where the CW directional coupler was designed with. This central frequency is no longer the only dominant frequency in the operation of the structure at this pulse duration scale. The expanded frequency content is expected to have a dramatic effect on the operation of the normal directional coupler. On the other hand, these effects and interactions are very involved and difficult to predict using analytical based techniques, such as the coupled mode theory or the normal mode theory. In order to assess and study the effect of an increase in the frequency content of the pulse and to

measure the effect of material dispersion, we examine the pulse spread for both the dispersive and the non-dispersive cases of the two waveguides. This means that the first case considers the presence of material dispersion while the second case considers the absence of it. We measure the change in the width of the pulse as a function of propagation distance. Figure 7.10 shows the relative pulse width increase, in percent with respect to the input pulse duration, in both waveguides for non-dispersive and dispersive structures with 25 fs and 50 fs initial pulse widths considered before.

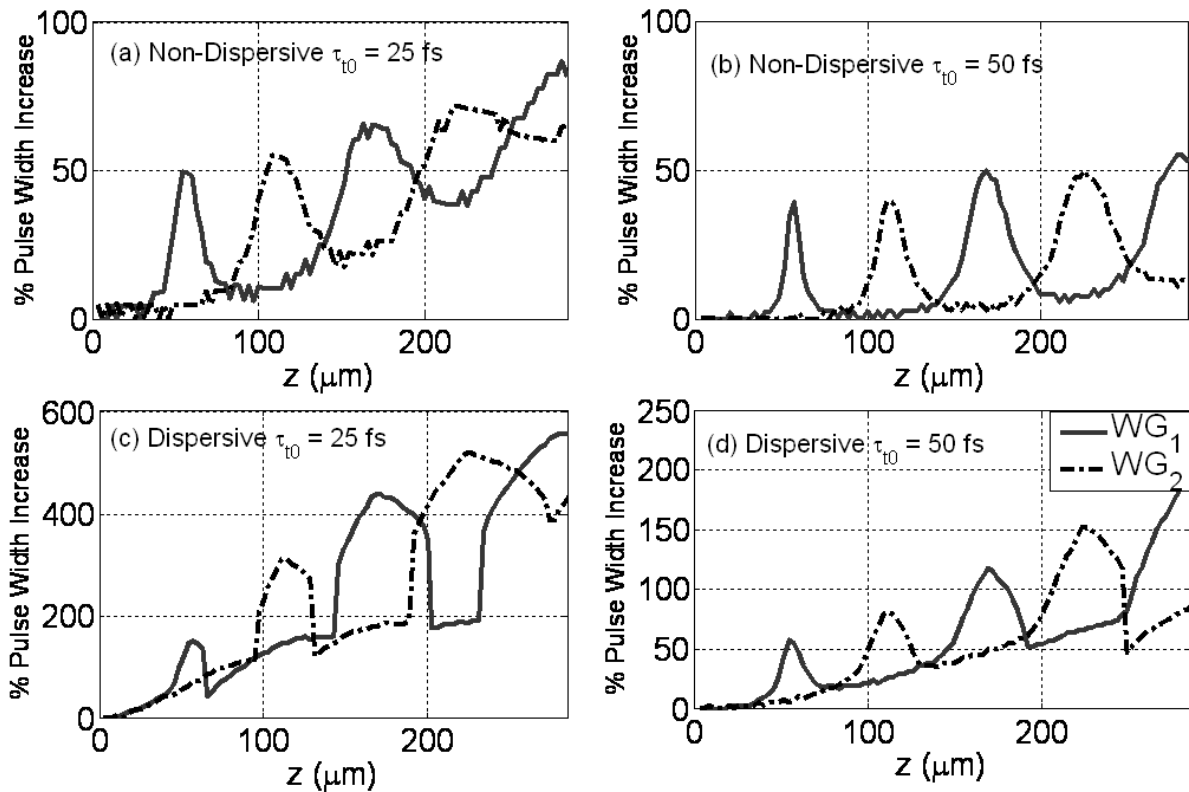


Figure 7.10 Relative pulse width increase in percent for the propagation of 50 fs and 25 fs pulses in dispersive and non-dispersive directional couplers.

The upper two plots are almost similar to those of Figure 8 in [13], which uses the non-paraxial TD-BPM in a non-dispersive DC structure. Generally the figure shows two observations. First, it can be noticed that as the initial pulse duration decreases, the relative

pulse spread increases. The second is the oscillatory behavior of the relative pulse change in both waveguides. One has to notice that waveguide dispersion is small compared to other dispersion effects presented here. Comparison between the dispersive and the non-dispersive cases gives a clear indication of the effect of material dispersion on the pulse spread during propagation. For 50 fs initial pulse width material dispersion produced 3.5 times the relative increase in pulse spread compared to the non-dispersive case at $z = 286.3 \mu\text{m}$. For the shorter pulse of initial pulse width of 25 fs, the relative increase of pulse spread is double this number. For the dispersive case with a pulse width of 25 fs a large pulse spread up to around 600% within $5L_c$ is predicted.

Using Fast Fourier Transform (FFT) to examine the frequency content of pulses gives a different perspective and information compared to the time domain. Figure 7.11 and 7.12 show the frequency spectrum of the input temporal pulse of 25 fs and 50 fs launched at the 1st waveguide along with that of the output temporal pulse of the two dispersive and non-dispersive waveguides of the DC at $z = 5L_c = 286.3 \mu\text{m}$. General observation show that the dominant frequencies launched at the input have changed positions during propagation, with the creation of new dominant frequencies of two peaks and sometimes three peaks as seen in Figure 7.11 (d), for example. This splits and the interaction of several dominant frequencies during the course of propagation is the main cause of pulse spread and pulse breakup. Comparison between Figure 7.2 (d) (pulse profile at $z = 286.3 \mu\text{m}$) with its corresponding fourier spectrum in Figure 7.12 (d), show that the two peaks in WG_1 belongs to the two pulses and the single peak in WG_2 belongs to the single pulse.

It appears that the existence of material dispersion accelerates the creation of new dominant frequencies; hence it results in further pulse spread compared to the pulse spread due to intermodal dispersion alone.

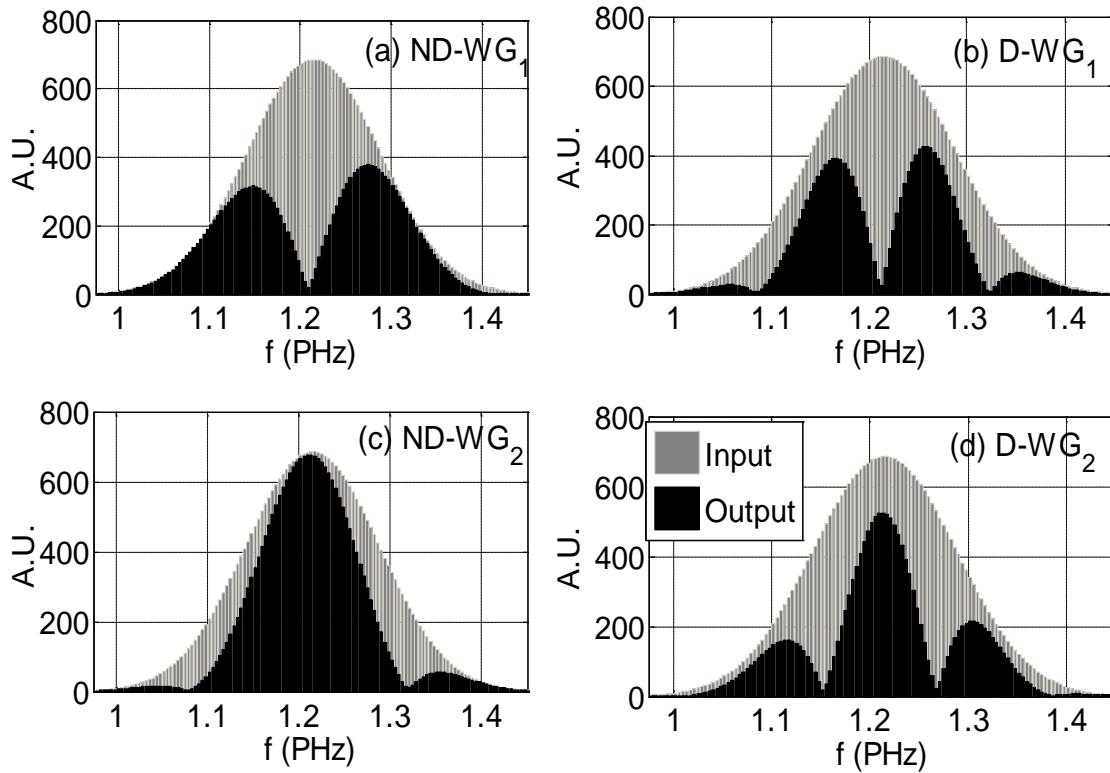


Figure 7.11 Frequency Spectrum of the input of 25 fs temporal pulse and the pulsed beams of a *GaAs* directional coupler having non-dispersive medium (ND) and Lorentz dispersive medium at $z = 5L_c = 286.3 \mu\text{m}$.

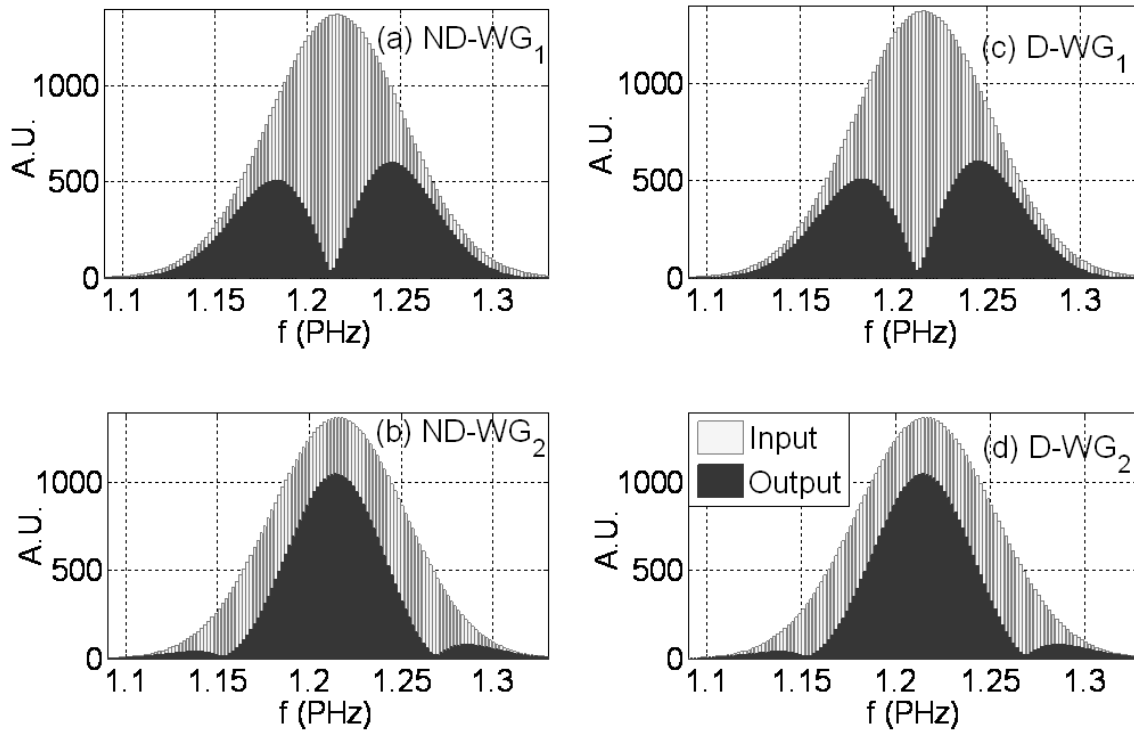


Figure 7.12 The same as in Figure 7.11 with temporal pulse of 50 fs.

7.6 Conclusion

In this chapter we employed the time domain techniques described in the previous chapters to study the propagation of short and ultra short pulsed optical beams inside a dispersive directional coupler. For short optical pulse durations, spatio-temporal coupling effect, which increases with the decrease of pulse width, has a profound impact on the interaction of pulses with the material and the structure. It has been observed that the existence of material dispersion gives rise to pulse spread in addition to the pulse spread due to intermodal dispersion. The power exchange mechanism between the two waveguides was seen to depart drastically from the usual CW. The study in this chapter is concentrated on the differences between the existence of material dispersion and the absence of it for the purpose

of quantifying the effect of dispersion in a guided structure. In this study we showed and calculated the exact amount of pulse spread due to each dispersive effect separately. As the initial pulse decreases, the pulse spread in a dispersive DC structure increases and eventually the pulse breaks up. The existence of material dispersion accelerates the pulse spread profoundly. The mechanism of splitting pulses may cause distortion in certain applications, but may lead to a desirable effect for other applications.

References

- [1] K. Saitoh, Y. Sato, and M. Koshiba, "Coupling characteristics of dual-core photonic crystal fiber couplers", *Opt. Express*, 11, pp. 3188-3195, 2003.
- [2] M. J. Potasek and Y. Yang, "Multiterabit-per-second all-optical switching in a nonlinear directional coupler", *IEEE J. Selected Topics in Quantum Electron*, 8, pp. 714-721, 2002.
- [3] S. Trillo, S. Wabnitz, E. M. Wright, and G. I. Stegeman, "Soliton switching in fiber nonlinear directional couplers," *Optics Letters*., 13, pp. 672–674, 1988.
- [4] Marcuse, D. *Theory of Dielectric Waveguides*, Academic Press, San Diego, 1991.
- [5] Kin S. Chiang, "Intermodal dispersion in two-core optical fibers", vol. 20, no. 9, *Optics Letters*, pp. 997-999, May 1, 1995.
- [6] S. Droulias, M. Manousakis and K. Hizanidis, "Switching dynamics in nonlinear directional fiber couplers with intermodal dispersion", *Opt. Commun.*, vol.240, pp.209- 219, 2004.
- [7] Kin Seng Chiang, "Coupled-Mode Equations for Pulse Switching in Parallel Waveguides", *IEEE Journal of Quantum Electronics*, vol. 33, no. 6, pp. 950-954, June 1997.
- [8] Kin Seng Chiang, "Theory of Pulse Propagation in Optical Directional Couplers", *Journal of Nonlinear Optical Physics & Materials*, vol. 14, No. 2, pp. 133—147, 2005.
- [9] G. P. Agrawal, *Lightwave Technology: Components and Devices*, John Wiley& Sons, Inc., 2004.

- [10] G. P Agrawal, “*Nonlinear Fiber Optics, 3rd edition*”, Academic press, 2001.
- [11] Marcuse, D. *Theory of Dielectric Waveguides*, Academic Press, San Diego, 1991.
- [12] Snyder, A. W., Love, J. D., *Optical Waveguide Theory*, Chapman and Hall, London, 1983.
- [13] Husain M. Masoudi, “Analysis of ultra short pulse propagation in optical directional coupler structures”, *Optical Quant. Electron*, vol. 41, pp. 397-408, 2009.

CHAPTER 8

CONCLUSION AND FUTURE WORK PLAN

8.1 Conclusion

The work done in this thesis is intended to study the interaction of short and ultra short pulses with dispersive material using the non-paraxial TD-BPM. A systematic modeling of the method has been shown starting from the CW to time domain and from non-dispersive to dispersive applications. Alongside this objective, the FDTD has been also formulated and implemented in non-dispersive and dispersive devices of different dimensions of 1-D and 2-D. At each stage, results obtained by the TD-BPM have been compared with its FDTD counterparts. Prior to the implementation of the method in a dispersive material, it was tested in terms of its accuracy, stability, convergence and performance for non-dispersive optical devices. It was observed that the developed TD-BPM method is unconditionally stable, accurate and converges even when large time steps (Δt) and large propagation steps (Δz) are used. In addition, the method was implemented along with several iterative solvers to speed up the execution time of the technique. It was shown that

the performance of the method, in terms of computational time and computer memory usage, using both the direct and iterative solver is much better than the FDTD when used as a unidirectional technique.

Detailed mathematical modeling and implementations to the non-paraxial TD-BPM have been performed for short and ultra short pulse propagation inside a dispersive 1-D and 2-D homogeneous medium and an optical slab waveguide. The graphical and quantitative analyses were performed by comparing the results obtained by the method with its FDTD counterparts. It was observed again that the method is free from CFL criteria, very stable and accurate in modeling short and ultra short pulse propagation in dispersive structures. High accuracy with this method can be achieved requiring very low computational cost and resources for short pulse interaction in highly dispersive and ultra short pulse interaction in weakly dispersive materials. Applications of ultra short pulse propagation in highly dispersive material can also be performed using this technique, but requires higher computational cost and resources. It has been also noticed that if the temporal step size is relaxed to the order of ≈ 1 fs, then the matrix that contains the dispersive information in the operator of the TD-BPM can be approximated as a tridiagonal matrix by eliminating other small coefficients without jeopardizing accuracy. As a result, the non-paraxial dispersive TD-BPM efficiency becomes similar to its non-dispersive counterpart.

Directional couplers consisting of dispersive and non-dispersive material have been analyzed fully using the time domain techniques for short and ultra short pulse interaction. A non-paraxial TD-BPM has been developed for analyzing the coupling behavior of this device in

the time domain. Complicated effects, such as pulse spread, distortion and splitting were calculated accurately along the device direction. Detailed analyses were performed to differentiate the effect due to intermodal dispersion from these due to material dispersion. It was observed that for ultra short pulse interaction inside a strongly dispersive *GaAs* DC causes very large pulse spread, which eventually results in pulse splitting. It was also found that material dispersion has a strong effect on the pulse spread phenomenon as compared to the intermodal dispersion of the directional coupler.

8.2 Future Work Plan

The TD-BPM is understood to be a promising implicit numerical tool for analyzing optical devices. So far the applicability of this method is tested in non-dispersive optical devices. In this thesis the applicability of the method in dispersive optical devices of Lorentz profile has been tested. The introduction of an iterative solver has made the method robust and more efficient. The analysis of this method in this thesis has just started to explore a number of interesting practical problems. Here is a limited list of possible future work.

1. Expanding the FD approximation of the time derivatives using higher orders, e.g., fourth order, may lead to further relaxed time step sizes. As it has been discussed in chapter 6, that when Δt approaches $1 fs$ most of the elements of the dense dispersive matrix become very small and can be neglected with little effects on accuracy of the method. The main operator matrix will become pentadiagonal, and hence makes the efficiency of the dispersive TD-BPM comparable to the non-dispersive counterpart.

2. There are a number of techniques in the literature depend on the idea of the split step of the main operator. Splitting the time variation from the spatial variation in the operator will have again a great impact on the efficiency of the method [1].
3. The work in this thesis can be easily extended to other important dispersive models of Debye, Drude and Cole-Cole.
4. The method should be useful to study a number of problems in surface plasmons and metamaterials applications [2 - 4].
5. The extension of the TD-BPM to non-linear material of $\chi^{(2)}$ and $\chi^{(3)}$ to study propagation of short and ultra short pulsed optical beams in such materials would be very useful. This would be also useful to analyze long distance temporal soliton interactions.
6. If the efficiency of the method improves through split-step techniques discussed in (2) above, extension to 3-D would be another interesting implementation that helps to understand a number of complicated 3-D problems.
7. The extension of the method to bidirectional problems to account for reflections would again be very interesting in many applications such as Y-junctions, Bragg gratings and photonic crystals.

References

- [1] Ning-Ning Feng, Gui-Rong Zhou, and Wei-Ping Huang, "An Efficient Split-Step Time-Domain Beam-Propagation Method for Modeling of Optical Waveguide Devices", *Journal of Lightwave Technology*, vol. 23, no. 6, June 2005.
- [2] Wuenschell, J.; Hong Koo Kim, "Excitation and propagation of surface plasmons in a metallic nanoslit Structure" vol. 7, Issue 2, pp. 229 – 236, *IEEE Transactions on*

nanotechnology, 2008.

- [3] Yan Zhao; Yang Hao, “Finite Difference Time Domain Study of Guided modes in nano-plasmonic waveguides”, *IEEE Transactions on Antenna and Propagation*, vol. 55, Issue 11, pp. 3070 – 3077, 2007.
 - [4] Kantartzis, N.V., Sounas, D.L., Antonopoulos, C.S., Tsiboukis, T.D., “A Wideband ADI-FDTD Algorithm for the Design of Double Negative Metamaterial-Based Waveguides and Antenna Substrates”, *IEEE Transactions on Magnetics*, vol. 43, Iss. 4 , pp. 1329 – 1332, 2007.
-

APPENDIX

Algorithms of Iterative Solvers

A.1 Conjugate Gradient Squared (CGS)

This method was developed by Sonneveld in 1984 [1] to gain a faster convergence than the biconjugate gradient (BCG). The algorithm of this method can be summarized as

1. *Compute* $r_0 := b - Ax_0$, r_0^* arbitrary
2. *Set* $p_0 := u_0 := r_0$
3. *for* $j = 1, 2, 3, \dots$ *Until Convergence Do*
4. $\alpha_j = (r_j, r_0^*) / (Ap_j, r_0^*)$
5. $q_j = u_j - \alpha_j Ap_j$
6. $x_{j+1} = x_j + \alpha_j (u_j + q_j)$
7. $r_{j+1} = r_j - \alpha_j A (u_j + q_j)$
8. $\beta_j = (r_{j+1}, r_0^*) / (r_j, r_0^*)$
9. $u_{j+1} = r_{j+1} + \beta_j q_j$
10. $p_{j+1} = u_{j+1} + \beta_j (q_j + \beta_j p_j)$
11. *EndDo*

Figure A.1 Algorithm of Conjugate Gradient Squared (CGS)

The iteration starts with the initial guess x_0 of the unknown x , computes few auxiliary vectors along with the residual vector r and continues until r reaches a tolerance. The Euclidean inner product mentioned in step 4 and 8 can be represented in matrix notation as $(x, y) = y^H x$, where y^H is the Hermitian matrix of y . This algorithm works quite well in many cases. But very high variations of the residual vectors often cause the residual norms computed from the result of line 7 of the above algorithm to become inaccurate.

A.2 Least Square (lsqr)

This method solves the equivalent linear system $A^T A x = A^T b$ to overcome the nonsymmetric linear system [2]. This method uses the conjugate gradient (CG) algorithm to solve the equivalent linear system. The algorithm is of this method is as

1. *Compute* $r_0 = b - Ax_0$, $z_0 = A^T r_0$, $p_0 = z_0$
2. *for* $i = 1, 2, 3, \dots$ *Until Convergence Do*
3. $w = Ap_i$
4. $\alpha_i = \|z_i\|_2^2 / \|w_i\|_2^2$
5. $x_{i+1} = x_i + \alpha_i p_i$
6. $r_{i+1} = r_i - \alpha_i w_i$
7. $z_{i+1} = A^T r_{i+1}$
8. $\beta_i = \|z_{i+1}\|_2^2 / \|z_i\|_2^2$
9. $p_{i+1} = z_{i+1} + \beta_i p_i$
10. *EndDo*

Figure A.2 Algorithm of Least Square (lsqr)

In this algorithm z_i is the residual vector which has to be minimized. In step 4 and 8, α_i and β_i is calculated using the vector norm defined as $\|x\|_p^q = \left(\sum_{i=1}^n |x_i|^p \right)^{\frac{q}{p}}$. This algorithm is characterized by slow convergence to problems arising from the partial differential equations (PDEs). Preconditioning should improve performance somewhat, but normal equations are also difficult to precondition.

A.3 Quasi-Minimal Residual (QMR)

This method is based on the projection processes onto Krylov subspaces, which are considered currently to be among the most important iterative processes [3 - 4]. The main idea behind this algorithm is to solve the reduced tridiagonal system in a least squares sense. Since the constructed basis for the Krylov subspace is bi-orthogonal, the obtained solution is viewed as a quasi-minimal residual solution, which explains the name. Additionally, QMR uses look-ahead techniques to avoid breakdowns in the underlying Lanczos process, which makes it robust. The algorithm is of this method is as

1. Compute $r_0 = b - Ax_0$, $\beta_1 = \delta_1 = 0$, $\gamma_1 := \|r_0\|_2$, $w_1 = v_1 = r_0/\gamma_1$, $w_0 = v_0 = 0$
2. *Until Convergence Do*
3. *For $j = 1, 2, \dots, m$, Do*
4. $\alpha_j = (Av_j, w_j)$,
5. $\hat{v}_{j+1} = Av_j - \alpha_j v_j - \beta_j v_{j-1}$
6. $\hat{w}_{j+1} = A^T w_j - \alpha_j w_j - \delta_j w_{j-1}$
7. $\delta_{j+1} = \left| (\hat{v}_{j+1}, \hat{w}_{j+1}) \right|^{1/2}$
8. $\beta_{j+1} = (\hat{v}_{j+1}, \hat{w}_{j+1}) / \delta_{j+1}$, *If $\delta_{j+1} = 0$ Stop*
9. $w_{j+1} = \hat{w}_{j+1} / \beta_{j+1}$
10. $v_{j+1} = \hat{v}_{j+1} / \delta_{j+1}$
11. *EndDo*
12. *Formulate the tridiagonal matrix T_m*
13. *Compute $y_m = T_m^{-1}(\beta e_1)$ and $x_m = x_0 + V_m y_m$*
14. *Compute the quasi residual norm $J(y) = \|\beta e_1 - \bar{T}_m y\|_2$*
15. *If $J(y)$ is small enough then stop*
16. *EndDo*

Figure A.3 Algorithm of Quasi-Minimal Residual (QMR)

The Lanczos vectors V, W are formed using the generated elements $v_1, \dots, v_m, w_1, \dots, w_m$ that are used in step 13. The tri-diagonal matrix in step in step 12 is formulated using the elements generated in step 4,7 and 8 as

$$T_m = \begin{bmatrix} \alpha_1 & \beta_2 & & & \\ \delta_2 & \alpha_2 & \beta_3 & & \\ & & & & \\ & & \delta_{m-1} & \alpha_{m-1} & \beta_m \\ & & & \delta_m & \alpha_m \end{bmatrix} \quad (\text{A.1})$$

The $(m+1) \times m$ sized tridiagonal matrix \bar{T}_m is formed using

$$\bar{T}_m = \begin{bmatrix} T_m \\ e_m^T \end{bmatrix} \quad (\text{A.2})$$

where e_m^T is the transpose of the m -th column of the $(m+1) \times m$ identity matrix.

References

- [1] J. Ortega, "Orderings for conjugate gradient preconditionings", *SIAM Journal on Optimization*, pp. 565-582, 1991.
- [2] C. C. Paige and M. A. Saunders, LSQR: An algorithm for sparse linear equations and sparse least squares, *ACM Trans. Math. Soft.*, 8 , pp. 43–71, 1982.
- [3] R. Freund and N. Nachtigal, QMR: A quasi-minimal residual method for non-Hermitian linear systems, *Numerical Math.*, 60, pp. 315–339, 1991.
- [4] R. W. Freund and N. M. Nachtigal, An implementation of the QMR method based on coupled two-term recurrences, *Tech. Rep. 92.15, RIACS, NASA Ames, Ames, CA*, 1992.

VITA

Name : Mohammad Shahed Akond

Nationality : Bangladeshi

Date of Birth : September 9, 1975.

Permanent Address : 4, Kumartuly, Islampur, Dhaka-1100, Bangladesh.

Tel. +880-2-7395346, email: s_akond@yahoo.com.

Degrees : **Master of Science** in Electrical & Electronic Engineering from Dhaka University of Engineering & Technology (DUET) (Aug. 2002 – Aug. 2004).

Bachelor of Science in Electrical & Electronic Engineering from Bangladesh University of Engineering & Technology (BUET) (June. 1994 – Sep. 1999).

Experiences : **Lecturer B** in Electrical Engineering Department of King Fahd University of Petroleum & Minerals (KFUPM) (Aug. 2005 – Feb. 2011).

Research Assistant in Electrical Engineering Department of King Fahd University of Petroleum & Minerals (KFUPM) (Sep. 2004 – Aug. 2005).

Assistant Professor in Electrical and Electronic Engineering Department of Dhaka University of Engineering & Technology (DUET) (Feb. 2004 – Sep. 2004).

Lecturer in Electrical and Electronic Engineering Department of Dhaka University of Engineering & Technology (DUET) (Oct. 2000 – Feb. 2004).

Assistant Engineer of Transvent International Ltd. (April 2000 – Oct. 2000).